UNIVERSITAT DE LES ILLES BALEARS
DEPARTAMENT DE FISICA

Polarization Properties of Vertical-Cavity Surface-Emitting Lasers

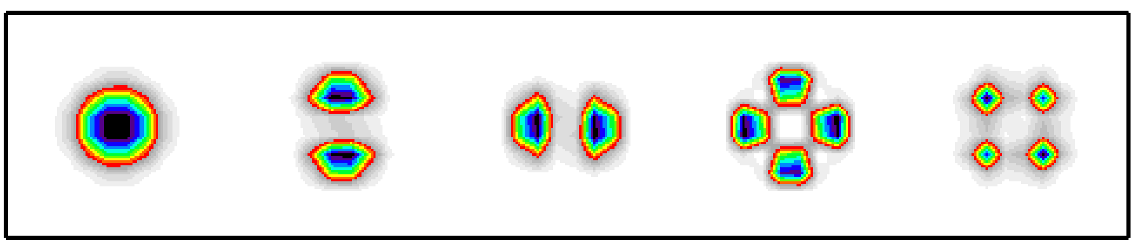

Memoria presentada por José María Martín Regalado para optar al Grado de Doctor en Ciencias Físicas por la Universitat de les Illes Balears.

Maximino San Miguel Ruibal, catedrático la Universitat de les Illes Balears y Salvador Balle Monjo, profesor titular de la misma Universidad,

CERTIFICAN

Que la presente memoria, titulada "POLARIZATION PROPERTIES OF VERTICAL-CAVITY SURFACE-EMITTING LASERS", ha sido realizada por José María Martín Regalado bajo su dirección en este Departamento, y que concluye la Tesis que presenta para optar al grado de Doctor en Ciencias Físicas.

Y, para que así conste, firman la presente en Palma de Mallorca a 17 de Septiembre de 1997.

Maximino San Miguel　　　　　　Salvador Balle

A mis padres,
a mi hermana,
y a Nuria

"Por un inmortal poder,
todas las cosas lejanas o cercanas
están ocultamente ligadas entre sí,
de modo que no puedes arrancar una flor
sin perturbar las estrellas."

Agradecimientos

Trás cerca ya de cuatro años en esta Universidad son muchas las personas que, directa o indirectamente, han contribuido a que este proyecto llegue a buen fin. Vaya por delante mi más sincero y profundo agradecimiento a todas ellas.

En primer lugar, al profesor Maxi San Miguel, por su excelente trabajo en la dirección de esta Tesis. Él puso a mi alcance las personas y los medios necesarios para que este trabajo de investigación saliese adelante siempre con éxito, permitiéndome también participar de sus conocimientos — no sólo sobre VCSELs — en seminarios y reuniones informales, llegando al punto de no darme descanso ni en las salas de espera de los aeropuertos. Me gustaría también resaltar su capacidad humana y agradecerle todo el apoyo moral que me ha ofrecido en los momentos más duros de mi, hasta ahora, corta carrera, así como su amistad, la confianza que ha depositado en mi persona, su buen humor y, como no, el apodo de *Fofi*.

Al doctor Salvador Balle, por ser un buen profesor, mejor co-director de tesis, e inigualable amigo. Tuve la suerte, o no!, de compartir con él la adicción por sustancias como la cafeina y la nicotina, motivo suficiente para, cuando asistiamos juntos a los congresos, compartir la misma habitación y en contadas ocasiones hasta la misma cama. Entre cafés, Coca-colas, pitillos, y algun que otro "pardal!", él me introdujo en el complejo mundo de los láseres de semiconductor y su modelización, me ayudó en el manejo del IDL, en el análisis de resultados, en la preparación de experimentos, en ...., bueno, en una larga lista de cosas imposible de enumerar en estas líneas.

Al profesor N. B. Abraham, del Bryn Mawr College, por su inestimable participación en la mayoría de mis trabajos de investigación, tanto teóricos como experimentales, en los que aportó ideas y sugerencias muy valiosas. Personalmente, le considero un gran científico, con una capacidad de trabajo infinita, un humor y un saber estar envidiables, y lo mejor de todo, una enorme calidad humana.

Al profesor Jorge J. Rocca y al doctor Juan Chilla, de la Colorado State University, por la oportunidad que me brindaron para realizar la parte experimental de este trabajo aún conociendo mi falta de experiencia. También agradecer de todo corazón a sus respectivas esposas, Carmen y Graciela, por su hospitalidad y amabilidad, así como al grupo de compañeros y amigos que dejé en aquellas tierras y que hicieron más confortable mi estancia en Colorado: Juanjo, Cesar, Fernando, Chris, Verdurita, Giorgui, Aine Dalu, y Olivier Chomette.

Al profesor Luis Pesquera y al doctor Angel Valle, de la Universidad de Cantabria, y al profesor Ramón Vilaseca y al doctor Carles Serrat, de la Universidad Politécnica de Catalunya, por las interminables discusiones sobre VCSELs en las sobremesas y *coffee-breaks* de los cursos y congresos en los que coincidimos; al doctor Franco Prati, de la Universitá degli Studi di Milano, por su colaboración en mis primeros estudios sobre los VCSELs; al doctor Nikolai Senkov, del Lebedev Institute de Moscú, por su paciencia en la complicada tarea de aleccionar a un *proyecto* de experimental como soy; al doctor G. van Tartwijk, actualmente en la University of Rochester, por ayudarme a explorar los entresijos del modelo de dos niveles aplicado a los láseres de semiconductor entre Mahou y Mahou (hombre!); y al doctor Salva Fernandez Casares, de la Politécnica de Madrid, por encender la mecha de mi carrera científica.

Un saludo muy especial para todos los profesores y compañeros del *mundillo* de los láseres de semiconductor en España quienes, en una u otra ocasión, nos hemos reunido en la capital cántabra para aprender sobre el tema: al profesor Luis Pesquera, de nuevo, por su fenomenal organización de los cursos; a los profesores Ignacio Esquivias, Manuel López-Amo, J. M. Lopez-Higuera, y Ramón Vilaseca, por sus excepcionales cursos de introducción a temas tan diferentes como los láseres de pozo cuántico, los amplificadores ópticos, la óptica integrada, etc.; a José Revuelta y Juanma, por enseñarme los encantos y la cultura gastronómica de su tierra; y a Bea, Julia y Marita, por su grata compañía durante las noches de farra en el casco antiguo.

Quiero también dar las gracias a los compañeros/as del grupo de Palma: a Claudio Mirasso (y familia), excelente *gourmet* con quien comparto los colores de mi equipo de futbol (força Barça!!!); a Margalida Victoria Homar, con quien me une una gran amistad forjada durante estos años a base de cafés, dias de playa y películas de cine; a Pere Colet, por su eficiencia en la organización de eventos de carácter científico y no tan científico, así como por su excelente labor al frente de la red informática y del servicio de *catering*; a Tomás Sintes y su hermana Ali, Rafael *"Loquito"* Salazar, Cristobal López, Han *"Flying Dutchman"* van der Lem, y Andreas Gahl, por soportar mis *marujadas* durante el tiempo que estuve conviviendo con ellos; a Miguel Hoyuelos, Marco Santagiustina y Rafa Gallego, por enseñarme que el *poker* es cosa de hombres; y al resto de profesores, doctores y estudiantes por su gran calidad personal: Raúl Toral (y familia), Emilio Hernández (y familia), Jorge Tredicce, Aurora Vicens (y *"Coletito"*), Oreste Piro (y familia), Julyan Cartwright, Raúl Montagne (y familia), Víctor Martínez y Cati Mayol.

También quiero expresar mi gratitud al resto del personal de esta Casa empezando por los habitantes de la agencia EFE: a Alberto *"el tiburon de Illetes"* Alvarez, por su sentido del humor y cordura y que, por mi culpa, se dejó literalmente *la piel* en Estrenc; a Benja, que con su peculiar sentido del humor pudo ser un perfecto compañero de fatigas los viernes por la noche; a Moncho, eterno rival futbolero; a Jean Michel, por enseñarme a cazar medusas en Na Foradada; y a Alvaro por sus filosóficas tertulias durante las comidas. No puedo dejarme en el tintero a aquellos miembros del PAS que, de un modo u otro, han aportado también su granito de arena: a Maribel y Micaela, de Contabilidad; a Gloria, la *secre* del Departamento; a Clara y Micaela, de la Biblioteca; a Juana y Cati, del servicio de limpieza; y a los conserjes del edificio Mateu Orfila: Rafael, "Mestre" Jaume, Joan, Antonia, y Sion.

Como buen catalán, también estoy profundamente agradecido a las Instituciones que han aportado la financiación económica necesaria para la realización del trabajo: la Comisión Interministerial de Ciencia y Tecnología (CICYT), proyectos TIC93/0744 y TIC95/0563; y la Unión Europea, proyectos CHRX-CT94-0594 y FMRX-CT96-0077. En particular, esta tesis se ha realizado con el soporte económico de una beca predoctoral del Programa de Formación de Personal Investigador, financiada por la CICYT, y que he disfrutado desde el 01/01/1994 hasta el 30/09/1997.

Finalmente, quiero agradecer desde lo más profundo de mi corazón a mi familia más directa por su amor, su comprensión y su constante apoyo durante los cuatro años que pasé fuera de casa. A ellos, mis padres, mi hermana Ana y Nuria (la "*shati*"), les dedico esta Tesis.

Contents

Resumen

El desarrollo de los láseres de semiconductor desde su aparición a principios de los años 60 hasta la actualidad ha estado fuertemente ligado a la industria de las telecomunicaciones. El constante aumento del tráfico de voz y datos en el mundo ha forzado el cambio de los sistemas de comunicación convencionales basados en hilos de cobre por otros capaces de transportar grandes cantidades de información, a velocidades de transmisión elevadas ($\geq$ 1 Gbit/s) y sin necesidad de repetidores. Estos nuevos sistemas, que forman actualmente la columna vertebral de las redes de comunicación mundiales, se basan en la transmisión de pulsos de luz a través de fibra óptica y utilizan láseres de semiconductor como emisores.

Paralelamente, el progreso en el campo de la optoelectrónica ha permitido la introducción de los diodos láser en aplicaciones industriales — procesado de materiales, tratamiento de superficies — y en el mundo de la medicina — diagnóstico médico, cirugía —. Además, el abaratamiento de los procesos de producción de estos dispositivos ha facilitado el desarrollo de equipos que se han incorporado rápidamente a nuestras vidas: compact-disc (CD), lectores de barras, CD-ROM, impresoras láser, punteros láser, etc.

La relevancia de los láseres de semiconductor hoy día se refleja claramente en su mercado de ventas, valorado en el año 1996 en cerca de $ 1.62 millardos y con una previsión de crecimiento del 18.5% para 1997 [1]. De este nada despreciable volumen de negocios, el 59% correspondió a las ventas de láseres en el sector de las telecomunicaciones, el 31% al sector de almacenamiento óptico de datos, mientras que el restante 10% correspondió a otras aplicaciones.

El diodo láser más utilizado en la actualidad es el llamado láser de emisión lateral. En su forma básica consiste en una doble heterounión p^+pn, donde dos capas de semiconductor de dopaje tipo p^+ y n, respectivamente, encierran una capa tipo p de material activo con menor gap y mayor índice de refracción que sus vecinas. La cavidad resonante, de varios cientos de micras de longitud, se consigue al cortar y pulir dos caras de la oblea dando lugar a caras parcialmente reflejantes por donde escapa la radiación láser (emisión lateral). A pesar de sus excelentes prestaciones ópticas y eléctricas, factores como la divergencia y el perfil elíptico del haz, el carácter generalmente multimodo de la emisión, la imposibilidad de realizar test iniciales antes de separar la oblea en chips, así como la limitación en la integración monolítica de los dispositivos en circuitos electro-ópticos, han conducido a la búsqueda de estructuras de láseres de semiconductor alternativas.

En este sentido, las investigaciones se han encaminado hacia el desarrollo de dispositivos más pequeños, baratos y fiables, llamados microláseres y caracterizados por la corta longitud de su cavidad resonante (del orden de la longitud de onda de emisión). Un primer paso hacia el microláser es el Láser de Cavidad Vertical y Emisión Superficial o VCSEL[2]. El primer VCSEL fue demostrado por el Profesor Iga y sus colaboradores a finales de los años 70 en el Tokyo Institute of Technology. La estruc-

[1]Según datos de la empresa consultora *Strategies Unlimited*

[2]Vertical-Cavity Surface-Emitting Laser

tura básica de ese primer VCSEL era muy parecida a la del láser de emisión lateral convencional, esto es, consistía en una capa de material activo encerrada entre dos capas epitaxiales p y n, respectivamente. Sin embargo, la cavidad resonante, ahora de unas decenas de micras de longitud, se formaba al crecer dos espejos metálicos sobre la superficie de las capas epitaxiales, de forma que la luz se emitía en la dirección perpendicular a la superficie de la oblea.

Aunque la idea del VCSEL era muy prometedora, fue abandonada hasta finales de los años 80 debido a las elevadas corrientes umbrales (~ 1 A) que eran necesarias para su operación en modo continuo (CW). Sin embargo, el refinamiento en el diseño de estos dispositivos durante los últimos 10 años gracias al uso de técnicas de crecimiento epitaxial como la deposición química metalorgánica en fase vapor (MOCVD)[3] y la epitaxia por haz molecular (MBE)[4], ha permitido mejorar sus prestaciones ópticas y eléctricas haciendo posible su comercialización desde 1993.

En su configuración actual, los VCSELs consisten en dos espejos dieléctricos de multicapa (espejos DBR[5]) que encierran una región espaciadora de unas pocas micras de longitud, la cual contiene a su vez una o varias estructuras de pozo cuántico que actuan como medio activo. Estos nuevos dispositivos, con corrientes umbrales de pocos miliamperios, potencias ópticas de varios miliwatts, operación en un único modo longitudinal, y haces circulares y poco divergentes, se están convirtiendo en atractivos sustitutos de los láseres de emisión lateral en compact disks, lectores de barras, aplicaciones de almacenamiento de datos, punteros láser, medicina, etc. Además, están considerados a ser los componentes clave en los sistemas futuros de comunicaciones por fibra óptica debido la alta eficiencia de acoplamiento haz-fibra. La naturaleza plana de los VCSELs permitirá su uso tanto en circuitos integrados optoelectrónicos como en aplicaciones de procesado de señal e imagen, reconocimiento de patrones, almacenamiento holográfico, conmutación activada por luz, etc. Por otro lado, su elevada escala de integración en forma de matrices dos-dimensionales los hace ideales para aplicaciones de alta potencia — impresión láser, bombeo de láseres de estado solido, comunicaciones en el espacio libre — o bien de procesado o interconexión óptica en paralelo — ordenadores ópticos, pantallas ópticas —.

A pesar del atractivo futuro de los VCSELs, estos dispositivos presentan en la actualidad una extremada sensibilidad a los efectos térmicos así como inestabilidades de polarización y de modos transversales que degradan la calidad del haz de luz emitido. La motivación principal del trabajo es la ausencia de una explicación fundamental para este tipo de fenómenos, con la casi única excepción del modelo desarrollado por San Miguel, Feng y Moloney (SFM) en 1995 para VCSELs de pozo cuántico sin tensionar. A lo largo de esta Tesis exploraremos las posibilidades de dicho modelo mediante análisis teóricos, simulaciones numéricas y experimentos con el objetivo de determinar el papel jugado por ciertos mecanismos físicos — tales como la dispersión saturable (o factor α), las anisotropías del VCSEL, los procesos de relajación de spin, la presencia de campos magnéticos, o la temperatura — en las propiedades de

[3]Metal-Organic Chemical-Vapor Deposition
[4]Molecular Beam Epitaxy
[5]Distributed Bragg Reflectors

polarización y de modos transversales de estos dispositivos.

La selección del estado de polarización y la dinámica de modos transversales en los VCSELs son dos cuestiones que han sido tratadas exhaustivamente en los últimos años, y que se revisan ampliamente en el Capítulo 1 de esta Tesis tras una breve introducción.

El Capítulo 2 presenta medidas experimentales de las propiedades ópticas y eléctricas de VCSELs guiados por ganancia — características de Luz-Corriente-Tensión (LIV)[6], características Luz-Corriente en función de la polarización, espectros ópticos, espectros ópticos resueltos en tiempo, etc. — así como un estudio de la respuesta térmica de los dispositivos. Los resultados obtenidos sirven para determinar el rango de valores de sus parámetros característicos tales como la corriente umbral y su dependencia con la temperatura, la resistencia térmica, el tiempo de respuesta térmica, la birefringencia, la orientación de la polarización, etc.

El Capítulo 3 esta dedicado a la deducción del modelo SFM. Este modelo es utilizado en los Capítulos posteriores para el estudio de la dinámica de polarización en VCSELs y considera el acoplamiento del vector campo óptico a las dos transiciones permitidas entre la banda de conducción y la banda de huecos pesados en un pozo cuántico sin tensionar. Las ecuaciones de evolución para las componentes de polarización circular dextrógira y levógira del vector campo óptico se deducen a partir de las ecuaciones de Maxwell para el caso de un VCSEL guiado por ganancia. Las ecuaciones de evolución para las densidades de momentos dipolares inducidos (polarización material) y de portadores en cada transición permitida, se deducen utilizando el formalismo de la matriz densidad suponiendo el medio semiconductor como un medio de dos niveles. Los efectos espaciales están incluidos a través de los términos de difracción óptica y de difusión de portadores. Dentro de este formalismo, la dinámica de polarización y de modos transversales está descrita en términos de dos conjuntos de ecuaciones de Maxwell-Bloch para láseres de dos niveles que están acoplados entre sí mediante procesos de relajación de spin. El Capítulo finaliza con una discusión de las limitaciones de la aproximación de "láser de dos niveles" en la descripción de la dinámica de láseres de semiconductor.

En el Capítulo 4 se analizan los mecanismos que dan lugar a la selección del estado de polarización en el modo fundamental del VCSEL. La operación monomodo del dispositivo permite deducir un conjunto de ecuaciones de balance a partir del modelo original, donde se incorporan las anisotropías características del VCSEL: la birefringencia y el dicroismo. Este modelo más simple permite encontrar expresiones analíticas para las soluciones estacionarias con polarización lineal y elíptica. Seguidamente, el análisis de la estabilidad de estas soluciones permite predecir los diferentes comportamientos de polarización característicos cuando se varía la corriente aplicada al láser — emisión estable en una única polarización lineal, conmutación entre polarizaciones lineales, coexistencia de polarizaciones lineales ortogonales, y emisión en polarización elíptica — en función de la birefringencia del dispositivo. Estos resultados son corroborados con simulaciones numéricas de las ecuaciones del modelo y comparados con los resultados experimentales de la bibliografía. El Capítulo finaliza

[6]Light-Intensity-Voltage characteristics

con el estudio numérico del efecto de la inyección de luz linealmente polarizada en el VCSEL sobre su estado de polarización, y muestra la existencia de biestabilidad y de conmutación de polarización causados por cambios en la intensidad y en la frecuencia de la señal óptica inyectada. Los resultados de este Capítulo coinciden cualitativamente con las medidas experimentales poniendo de manifiesto la posible relevancia de la dispersión saturable y de los procesos de relajación de spin en la selección del estado de polarización en los VCSELs.

En el Capítulo 5 extendemos el modelo de las ecuaciones de balance para estudiar los efectos de la aplicación de un campo magnético axial sobre el estado de polarización del VCSEL. Para VCSELs perfectamente isótropos mostramos que la emisión ocurre en forma de polarización lineal rotante como consecuencia de la birefringencia circular inducida por el campo magnético (efecto Zeeman). Sin embargo, cuando se tienen en cuenta las anisotropías lineales propias de estos dispositivos, se encuentra que el estado de polarización de la luz emitida depende fuertemente del valor de la birefringencia circular inducida, que es función de la intensidad del campo magnético aplicado. Para campos magnéticos débiles (birefringencia circular mucho menor que la birefringencia lineal) observamos el mismo tipo de fenomenología que en el Capítulo 4 al variar la corriente inyectada — emisión estable y conmutación de polarización — pero ahora entre estados con polarización elíptica cuya elipticidad depende tanto de la corriente como de la intensidad del campo magnético aplicado. En la región de campos magnéticos moderados (birefringencia circular comparable a la birefringencia lineal), la emisión ocurre principalmente en estados de polarización con dos componentes espectrales primarias que se caracterizan por una trayectoria cerrada sobre la esfera de Poincaré y que denominamos soluciones de “dos frecuencias”. En el límite de campos magnéticos fuertes mostramos que la emisión ocurre en la forma de polarización elíptica rotante, un estado de polarización casi lineal cuya orientación cambia en el tiempo con una frecuencia que depende de la intensidad del campo magnético aplicado. Motivados por este último resultado, exploramos al final del Capítulo la posibilidad de generar pulsos ópticos rápidos a velocidades de GHz mediante la aplicación de un campo magnético externo a un VCSEL casi isótropo, con aplicaciones en comunicaciones ópticas y generación óptica de reloj.

En el Capítulo 6 presentamos un estudio experimental en VCSELs guiados por ganancia con el fin de discriminar entre los efectos producidos por los cambios en la corriente de inyección y aquellos producidos por cambios en la temperatura de la zona activa (efectos térmicos inducidos por la corriente aplicada) sobre el estado de polarización dentro del modo transversal fundamental del VCSEL. El estudio se basa en dos series de medidas Luz-Corriente (variando en cada una la temperatura del sustrato) realizadas bajo condiciones térmicas diferentes. En la primera serie, la larga duración de la rampa de corriente aplicada (~ 1 s) permite que la temperatura de la zona activa del dispositivo se actualice para cada valor de la corriente. En este caso, la conmutación de polarización observada en los dispositivos puede ser atribuida o bien verse influenciada por el calentamiento del VCSEL inducido por la corriente. En la segunda serie de medidas, la temperatura de la región activa se mantiene constante mediante el uso de rampas de corriente de duración corta (~ 100 ns) comparada con el tiempo de respuesta térmica del VCSEL (~ 1 μs). La observación de conmutación de polarización en esta segunda serie de medidas elimina la posible explicación térmica de dicho fenómeno e indica la existencia de mecanismos asociados con los cambios de la corriente (como los estudiados en el Capítulo 4) que afectan la seleción del estado de polarización. La dependencia lineal observada experimentalmente entre la corriente de conmutación y la temperatura del sustrato se explica en términos de los resultados del Capítulo 4, permitiendo estimar los valores de la constante de relajación de spin y de la anisotropía de ganancia intrínseca del VCSEL estudiado.

En el Capítulo 7 estudiamos la selección del estado de polarización en conjunto con la dinámica de modos transversales en VCSELs circulares guiados por ganancia a partir de simulaciones numéricas del modelo general deducido en el Capítulo 3. En primer lugar, estudiamos las propiedades de polarización durante el encendido del láser. Seguidamente, presentamos resultados de características Luz-Corriente y espectros ópticos que muestran las inestabilidades típicas de estos dispositivos a medida que se aumenta la corriente aplicada: *i)* estabilidad o conmutación de polarización durante la operación dentro del modo fundamental, *ii)* aparición del primer modo transversal con polarización ortogonal al modo fundamental, y *iii)* coexistencia de ambas polarizaciones a corrientes superiores. El Capítulo concluye con la presentación de resultados que muestran la sensibilidad de las inestabilidades de modos transversales y de polarización en VCSELs a los mecanismos de relajación de spin.

El Capítulo 8 presenta el resumen y las conclusiones de este trabajo.

Chapter 1

Introduction

Semiconductor lasers are nowadays quite common in our lives. These devices, also known as diode lasers, are the key components in compact-disk (CD) audio players, supermarket bar-code scanners, CD-ROMs and laser printers in our home and office computer equipment, etc.. While optical data storage applications represented roughly 31 % of the diode laser sales market in 1996, semiconductor laser sales for telecommunication applications accounted for $960 million in the same year, corresponding to 59% of the diode laser market [1].

The dominance of the telecommunication segment in the diode laser market should not be surprising since it has been driven by the increasing voice and data traffic around the world. The reason is that fiber-based optical networks, where laser diodes are used as emitters, have become the backbone of worldwide communication systems since, as compared to conventional copper-wire communication systems, they allow the transport of information over much longer distances without repeaters, and at higher data rates ($\geq$ 1 Gbit/s).

Furthermore, the relevance of semiconductor lasers has rapidly increased along with progress in the opto-electronics field, leading to the development of new applications such as second harmonic generation, material processing and surface treatment, pumping of solid state lasers, pumping of Er-doped fiber amplifiers, medical diagnostics and surgery [2], interferometry, sensing, communications within computer systems, optical interconnects, photonic switching, etc., corresponding to the remaining 10% of the diode laser market in 1996.

Semiconductor lasers became widely available in the early 1980s. However, these first commercial diode lasers, known as edge-emitting lasers, still have several shortcomings: divergents beams, elliptical beam profiles, multimode emission, limited monolithic integration of lasers into electro-optical circuits, etc. As a consequence, new semiconductor laser structures have been developed in order to improve on the characteristics of edge emitters. Research has addressed the development of smaller, cheaper, and more reliable devices, generally referred to as microlasers [3].

A semiconductor microlaser is a laser diode with a very short resonant cavity — of the order of the emission wavelength — for which only one cavity mode overlaps the semiconductor gain profile. A first step towards the semiconductor microlasers is the Vertical Cavity Surface Emitting Laser (VCSEL) [4, 5], which is the topic of this work. A VCSEL was first demonstrated by Prof. Iga and co-workers at the Tokyo Institute of Technology in the late 1970s [6]. The basic structure consisted of a bulk active layer cladded by two epitaxial p- and n- layers. A few μm long resonant cavity was formed by attaching metal mirrors to the top and bottom epitaxial surfaces such that light was emitted perpendicular to the wafer.

Although the idea of a VCSEL was very promising, it was almost abandoned until 1987 since CW operation was prevented due to the high threshold currents ($\sim$ 1 A). However, VCSEL designs have been refined over the past 10 years with the use of epitaxial growth techniques such as metal-organic chemical-vapor deposition (MOCVD) and molecular beam epitaxy (MBE), and they are commercially available since 1993.

In their present configurations, VCSELs consist of two dielectric mirror stacks (DBR mirrors) surrounding a spacer region of few microns long, which contains one or several quantum well structures as the gain medium. Present VCSELs — with threshold currents of few milliamps, maximum output powers of the order of several milliwatts, circular and low divergent beams, single-longitudinal mode emission, etc. — have become attractive substitutes of edge-emitting lasers for applications such as CD players, barcode scanning, optical data storage, lasers pointers, etc. In addition, VCSELs are considered to be the key components in future fiber-optic communication because of the high coupling efficiency between the VCSEL beam profile and the fiber core. The planar nature of VCSELs will allow them to be used in opto-electronic integrated circuits [7]. On the other hand, the large-scale of integration into two-dimensional arrays [8] will allow VCSELs to find applications in areas such as image/signal processing, pattern recognition, holographic storage, light-activated switching, laser printing, solid-state and microchip laser pumping, optical displays, free-space communications, etc. [9, 10].

Hence, it is widely expected that VCSELs will replace edge-emitting lasers in the near future. However, despite the attractive optical and electrical characteristics of present VCSELs, they are still strongly sensitive to temperature changes. Moreover, some VCSELs also display polarization and transverse mode instabilities which degrade the quality of the output beam. This thesis is devoted to the study of the physical mechanisms leading to such instabilities.

In the following sections I will briefly review the basic features of semiconductor lasers and the main characteristics of two widely used types of semiconductor lasers: the edge-emitter and the VCSEL. Then, I will show published results reporting the characteristic polarization and transverse mode behavior of these devices, including a brief review of the models and the explanations given to the experimental results. In particular, I will focus on the models for the selection of the polarization state in VCSELs. I finish this Chapter with a list of criticisms of these models, and the outline of the work.

1.1 Basics of semiconductor lasers

Semiconductor physics depends on the existence of a gap of forbidden energies, typically from 0.1 to 3 eV, which lies between the valence band of bonding electrons and the conduction band of “free” electrons. Such a relative small bandgap allows for several thermal and optical interaction processes that alter the concentration of charge carriers in the semiconductor material and hence modify the optical and electrical properties.

Charge carriers in a semiconductor can be generated either by thermal excitation or by the absorption of a photon whose energy is bigger than the bandgap energy. In both cases, a valence band electron is excited to the conduction band leaving behind a vacancy which effectively behaves as positively charged free particle (hole). Conduction band electrons and valence band holes (electron-hole pairs) can suffer the reverse process in either of two different ways: nonradiative recombinations — such as Auger recombinations, recombinations at defects, and surface recombinations—, when the electron-hole energy is finally released into lattice phonons (heat); and radiative recombinations, when the energy is released as photons. Radiative recombinations are predominant in direct-gap semiconductors and can be either spontaneous or stimulated. Spontaneously generated photons are emitted in random directions and with arbitrary phases, such that the emitted light is incoherent. However, when the electron-hole recombination is stimulated by a photon of energy $h\nu$ existing in the semiconductor material, the result is the coherent amplification of the incoming photon such that the photon energy after the recombination increases in $h\nu$, keeping the phase and the propagation direction of the incoming photon.

Stimulated emission processes are the basis of lasers. However, stimulated emission processes have to compete with photon absorption processes in order to produce coherent optical amplification (optical gain). Therefore, the interesting quantity is the net rate of stimulated emission, r_{st}, namely the difference between the stimulated photon rate and the absorption rate. For a given photon energy, $E=E_c-E_v=h\nu$, r_{st} is proportional to the difference between the occupation probabilities of the electrons in the conduction band with energy E_c, $f_c(E_c)$, and the electrons in the valence band with energy E_v, $f_v(E_v)$. Such occupation probabilities follow Fermi-Dirac statistics ($f_i(E_i) = (exp[(E_i - E_{fi})/k_BT] + 1)^{-1}$, $i = c, v$), where E_{fc} and E_{fv} are the quasi-Fermi levels for the conduction and valence band, respectively, k_B is the Boltzman constant, and T is the absolute temperature. The condition at which the rates of photon absorption and stimulated emission are equal at a given photon energy, $r_{st}=0$, is known as transparency. Beyond transparency, because net stimulated emission occurs, the occupation probability in the conduction band at energy E_c is larger than the occupation probability in the valence band at energy E_v, $f_c > f_v$, a condition known as population inversion.

The simplest semiconductor structure in which population inversion can be achieved is an ordinary *p-n* junction formed by a *p*–type region grown in contact with a *n*–type region from the same direct-gap semiconductor material (homostructure). When the *p-n* junction is forward biased, electrons and holes, which are the majority carriers in the *n*- and *p*–type regions, respectively, flow towards the depletion region of the junction (active region) where the population inversion condition can be achieved depending on the forward bias value. Although the first diode lasers were based on this type of homostructure, today most practical lasers employ either a double heterostructure [11] or a quantum-well heterostructure [12].

Double heterostructure lasers (DH) consist of cladding a thin (100 to 200 nm thick) active layer of a given semiconductor material between two or more layers of different semiconductor materials but with approximately the same lattice constant as the active layer (See Fig. 1.1(left)). The main advantages of the semiconductor heterostructure over the homostructure are that it provides (*i*) better carrier confinement, since the potential barriers at the heterojunctions prevent the outflow of electrons (holes) to the *p*–type (*n*–type) region, while the bandgap difference helps the injected carriers to be confined at the active region, as shown in Fig. 1.1(right); and (*ii*) better optical confinement, since the cladding layers have a smaller refractive index than the active layer, forming a dielectric waveguide which confines the generated photons in the vicinity of the active region through the physical mechanism of total internal reflection.

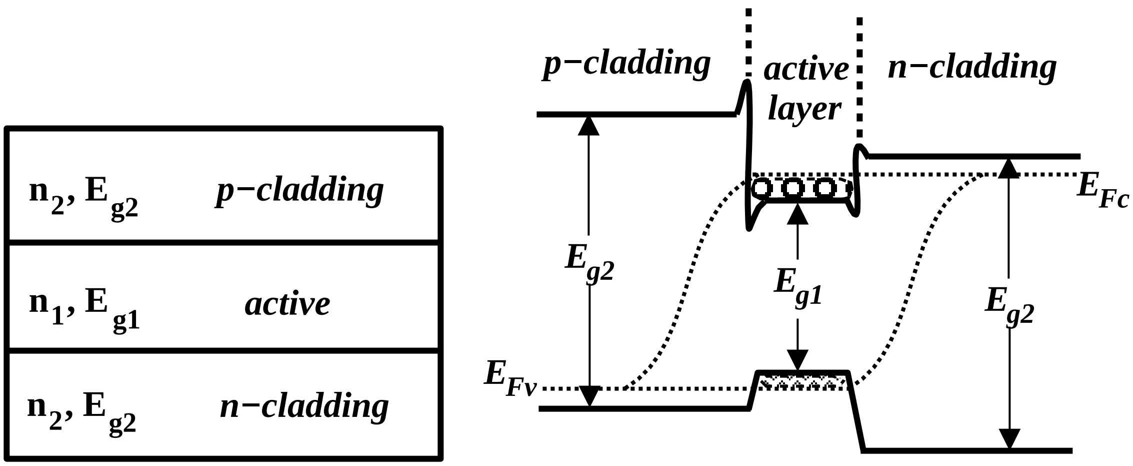

Figure 1.1: (left) Three-layer slab-waveguide heterostructure: $n_1 > n_2$, $E_{g1} < E_{g2}$. (right) Energy band diagram of a DH-laser under forward bias.

A single quantum-well laser [12] is similar to a conventional bulk heterostructure, but with the active layer only a few nanometers wide (< 20 nm), which requires sophisticated growth techniques such as MOCVD or MBE. In a quantum well, carriers are confined along the direction normal to the quantum-well plane (quantization direction), and their energy and density of states become quantized. Coherent radiation occurs by stimulated electron-hole recombination between the quantized sub-bands of the conduction and valence bands. Because of the thin heterostructure, carriers are tightly confined, resulting in a better efficiency than in bulk laser diodes, and thus in lower threshold devices. However, optical confinement requires the addition of separate confinement heterostructure (SCH) layers with a refractive index in between that of the cladding layers and the wells. Multiple quantum wells can also be produced by alternating narrow layers with low and high bandgaps, which allows for higher powers. Fig. 1.2 shows the band structure of a single- (left) and a multi-quantum (right) well structure.

Hence, a semiconductor medium can be used as an active medium to emit light by stimulated emission processes. The remaining requirement to have a laser diode is a resonant cavity to provide an adequate optical feedback mechanism for frequency selection, in other words, to define the frequencies (modes) to be amplified. Depending on the type of resonant cavity, semiconductor lasers can be classified into six main categories, as shown in Fig. 1.3. In conventional semiconductor lasers, known as edge-emitting lasers (a), the resonator is a Fabry-Perot cavity of partially reflecting facets formed by cleaving the wafer along parallel crystal planes to create flat mirror facets. Some edge-emitting lasers use a different wavelength selector consisting of a periodic index perturbation directly integrated along the laser structure [13], namely the Distributed Feedback (DFB) laser (b) [14], when the grating region is built into the pumped part of the gain region; and the Distributed Bragg Reflector (DBR) lasers (c) [15], when the grating replaces the usual cleaved mirror on one or both

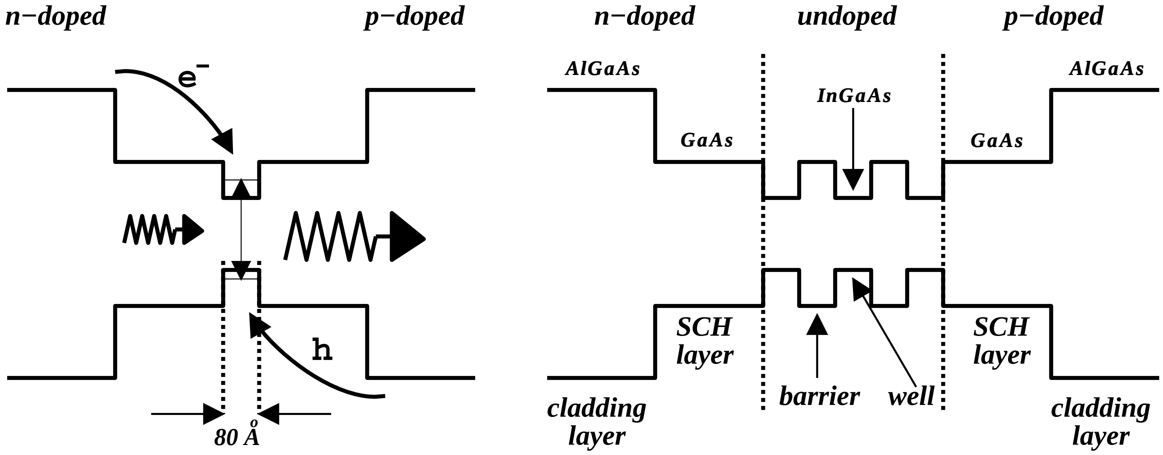

Figure 1.2: Band structure of a single (left) and a multi-quantum (right) well heterostructure. Stimulated transitions occur between the quantized subbands of the wells.

sides of the resonator. Other geometries are also used in which the light is emitted normal to the surface of the wafer, such as a conventional edge-emitting lasers with a 45^o etched mirror (d) [16] or a DBR laser using a second-order grating (e) [17]. A completely different approach to obtain surface emission is the VCSEL (f) [4]. In these lasers, the cavity is vertical and the mirrors, typically quarter-wave DBRs, are parallel to the wafer surface. It is worth noting that in quantum-well VCSELs the quantization direction coincides with the emission direction while in the other classes of quantum-well laser diodes is always perpendicular.

The emission characteristics of laser diodes as a function of the bias voltage are common to all devices. At low values of the applied voltage (or current), the carrier density in the active layer is small, so photon absorption is dominant over amplification and the laser diode mainly emits spontaneous light. Transparency is achieved for a bias voltage equal to the active layer energy gap (if zero series resistance is assumed). For increasing bias voltage, the carrier population is inverted so net optical gain occurs over a small spectral region given by $(\mathrm{E}_{fc}\text{-}\mathrm{E}_{fv})/h > \nu > \mathrm{E}_g/h$, known as the amplifier bandwidth. But while there is net amplification in the medium, it is not enough to overcome the transmission losses at the facets, so the emission is still incoherent — amplified spontaneous emission — but spectrally filtered by the Fabry-Perot etalon. Coherent laser light is emitted only when the net optical gain overcomes both the internal losses (any optical loss within the laser cavity which does not yield a generation of carriers within the active region, such as light scattering, free carrier absorption, etc.) and the mirror losses (transmission through the mirrors) at a particular resonant frequency of a cavity mode. When gain and losses are balanced, this is called the threshold condition. The carrier density satisfying the threshold condition is called the threshold carrier density. Equivalently, the applied voltage (current) providing such a carrier density is known as the threshold voltage, V_{th} (current, I_{th}). Above threshold, the carrier density remains almost clamped to its threshold value and the population of excess injected carriers is transformed into stimulated radiation within the selected cavity mode(s). The output power (L) in-

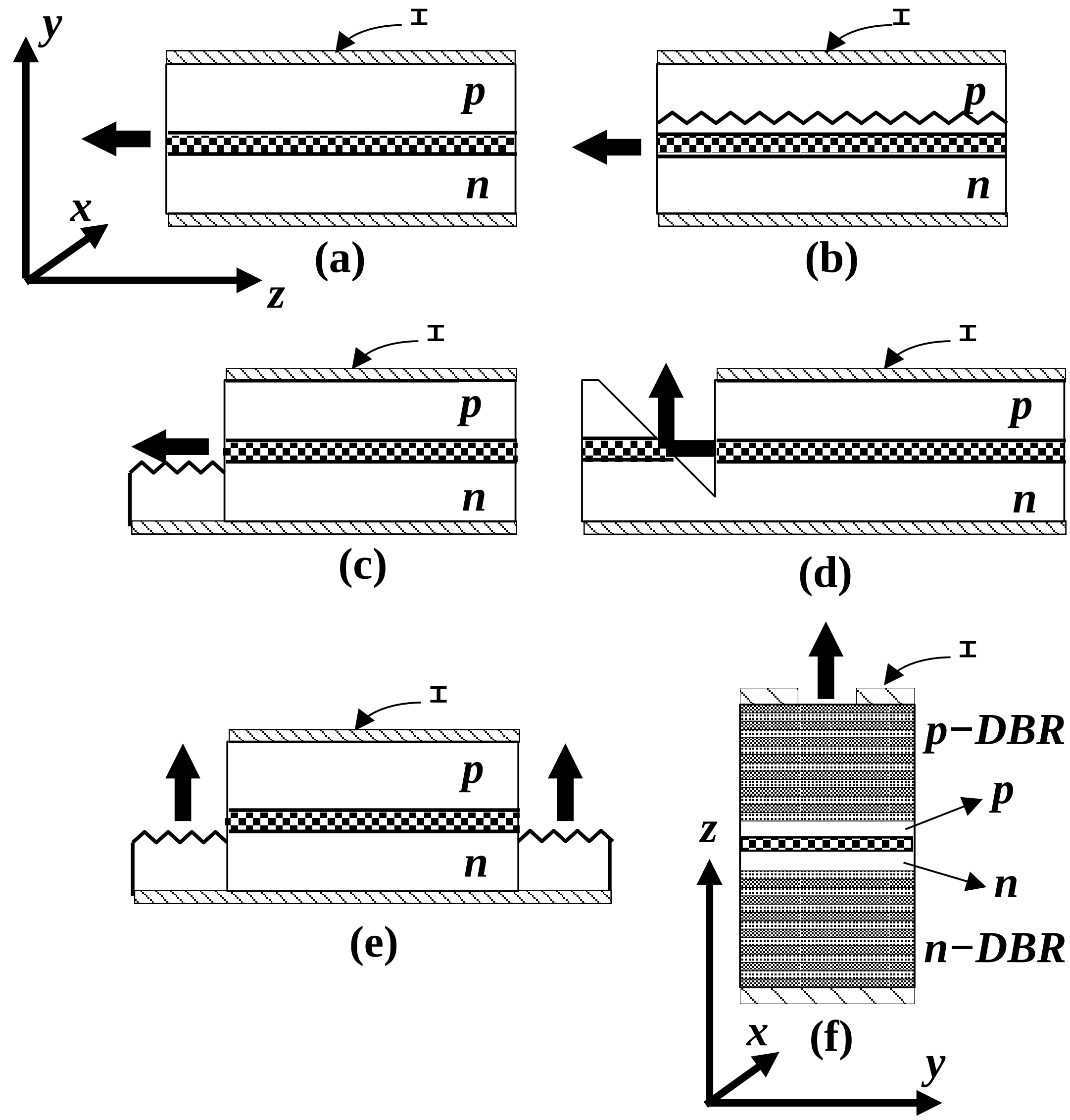

Figure 1.3: Semiconductor laser cavities: (a) conventional edge-emitting, (b) DFB, (c) DBR, (d) edge-emitting laser with a 45^o etched mirror, (e) DBR laser using a second-order grating, (f) VCSEL.

creases linearly with the applied current (I), and the slope of the L-I characteristics is a measure of the external quantum efficiency, typically 0.2 -0.5 W/A.

The emission spectrum might consist of one (single-mode) or several (multi-mode) narrow peaks — each one hundreds of MHz wide, typically — which correspond to the Fabry-Perot empty cavity modes modified by the active medium. The number of simultaneously lasing cavity modes will depend on the width of the gain spectrum, the spectral separation between adjacent longitudinal modes, and the applied current. However, the emission wavelength of the laser will depend on the type of semiconductor material used as the laser medium [18]. Blue-green visible lasers are based on the ZnSe family on GaAs substrates, such as ZnSSe and ZnCdSe. Red visible lasers, operating between 620 and 690 nm, are based on $Ga_{1-x}In_xP$ or $(Al_xGa_{1-x})_yIn_{1-y}P$ on GaAs substrates. Laser diodes based on $Al_xGa_{1-x}As$ technology grown on GaAs substrates emit at relatively higher wavelengths, from 750 to 870 nm, depending on the aluminum concentration [1]. The other common group of lasers is based on $In_xGa_{1-x}As$ grown on GaAs substrate or $In_{1-x}Ga_xAs_{1-y}P_y$ on InP substrates, having emission wavelengths in the near infrared area (980 to 1650 nm) [2]. Longer wavelength regions, from 1.7 to 4.4 μm, are covered by InGaAsSb lasers on GaSb substrates [3].

1.2 Edge-emitting lasers

In conventional semiconductor lasers, the laser cavity is obtained by cleaving the wafer on which the laser diode is built, which creates a Fabry-Perot cavity several hundreds of micrometers long, with partially reflecting facets at which light is emitted from the edge of the chip (z-direction, parallel to the surface of the wafer). Transverse confinement (y-direction) of carriers and photons is typically provided by a double heterostructure. In addition, laser action is laterally (x-direction) limited to a stripe of the active layer, typically, a few microns wide. Lateral optical confinement is achieved by either concentrating the current flow (and hence the laser gain) in the stripe (gain-guiding) [19], or fabricating the stripe with a higher refractive index (index-guiding). As a result of the combined lateral and transverse confinements, the laser output beam of edge-emitting lasers has elliptic shape and is strongly divergent.

Index-guided lasers have a built-in lateral waveguide where the high refractive index region coincides with the stripe used for current injection. As a consequence of the optimal carrier and field confinement, index-guided lasers display stable operation on the fundamental transverse mode at high injection currents, so they are commonly used for applications such as laser printers and CD players. Depending on the refractive index step of the lateral waveguide, Δn, index-guided lasers can be classified as weakly [20] ($\Delta n \sim 5 \cdot 10^{-3}$) and strongly [21] ($\Delta n \sim 5 \cdot 10^{-2}$) index-guided devices. In some weakly index-guided structures, the active region waveguide thickness is varied by growing it over a channel or a ridge in the substrate, as in the inverted-rib waveguide laser. In mesa-stripe lasers, as shown in Fig. 1.4(a), the stripe is edged. In buried-heterostructure lasers, Fig. 1.4(b), the active region is buried such that the optical field is strongly confined not only in the transverse but also in the lateral direction, providing strong index-guiding of the optical mode.

Gain-guiding mechanism does not confine the light as tightly as index-guiding, so the beam quality is not as good. A common gain-guided stripe laser is shown in Fig. 1.4(c). The injected current is limited to the active region by making the side regions non-conducting using proton implantation. The main shortcoming of gain-guided emitters is the onset of higher-order transverse modes when the laser is operated at high currents, which results in non-linearities or 'kinks' in the Light-

[1] AlGaAs lasers are commonly used in a wide range of applications, including CD players, short-distance fiber-optic communications, optical data storage and laser printing.

[2] These longer-wavelength diode lasers are used almost entirely for communication applications, since they cover the minimum dispersion wavelength (1310 nm) and the minimum attenuation wavelength (1550 nm) of optical fibers.

[3] These lasers have applications in pollutant detection, eye safe devices, etc.

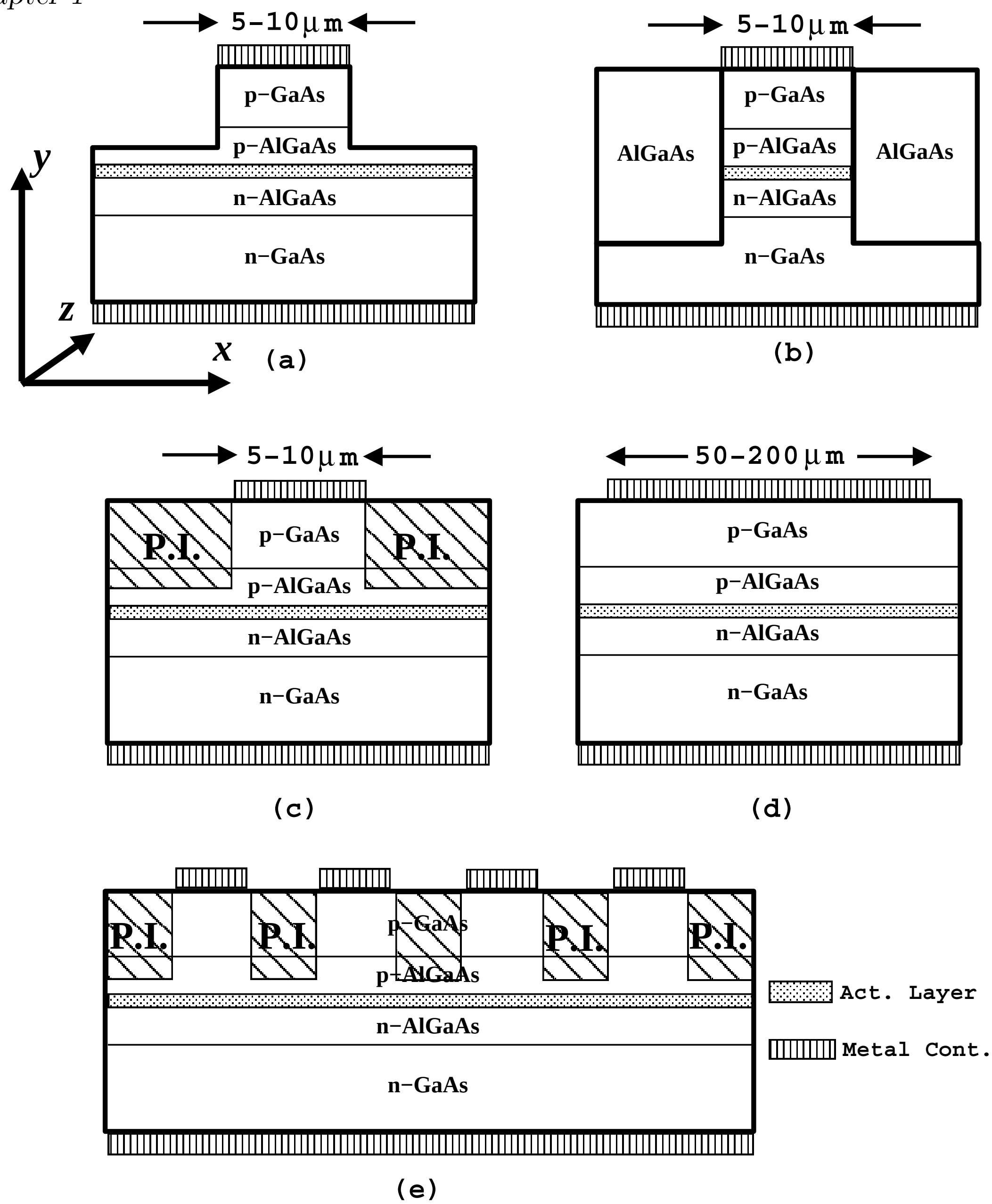

Figure 1.4: Edge-emitting lasers (a) mesa-stripe, (b) buried heterostructure, (c) gain-guided, (d) broad-area, (e) gain-guided array.

Intensity (LI) characteristic [22] and filamentation of the output beam.

Typical threshold currents for commercial, bulk, narrow-stripe, index-guided lasers are 30-60 mA, with CW output powers up to 50 mW. Narrow stripe gain-guided lasers have roughly 50% higher thresholds and similar output powers. Maximum power levels increase in proportion to the volume in the active layer. Broad-area lasers [23], based on this principle, can generate 1 W output power for a 100 μm wide stripe with typical thresholds of 0.5 A. The high optical power provided by these lasers is spread over a large active area, thus reducing the likelihood of catastrophic facet damage caused by heating and the subsequent melting of the cleaved facet mirrors. A typical broad-area laser structure is shown in Fig. 1.4(d). Despite the simple structure and the possibility to obtain high output powers, broad-area lasers present many disadvantages as a consequence of their gain-guiding nature such as high threshold currents and poor spatio-temporal optical characteristics (erratic beam filamentation), which limit their practical application for communication purposes.

High power, coherent lasers can be achieved if the active area is divided into a series of narrow, closely spaced, parallel stripes giving rise to a laser array. The relatively small separation between the adjacent lasers allows for coupling from both the optical field and the carriers of adjacent emitters which, under certain circumstances, can establish a definite phase relation between the lasers of the array resulting in the emission of narrow, high-power, coherent beams (phase-locked arrays). Depending on the type of lateral waveguiding mechanism, laser arrays are classified as gain-guided [24] (Fig. 1.4(e)), index-guided [25], and index-antiguided [26] arrays.

1.3 Vertical-Cavity Surface-Emitting Lasers

The first Vertical-Cavity Surface-Emitting Laser consisted of a short gain region (few microns long) of bulk semiconductor material cladded by highly refracting gold mirrors parallel to the top and bottom surfaces of the semiconductor wafer [6]. This original configuration has been modified in order to develop more efficient and reliable devices.

Present VCSELs have the original metal mirrors replaced by Distributed Bragg Reflectors (DBR) [27]. A DBR mirror consists of alternating semiconductor layers of quarter-wave thick high- and low-refractive index. Because of the short active region, VCSELs have low round-trip gain as compared with conventional edge-emitting lasers (hundreds of microns long), so tens of these pairs of layers need to be stacked together in order to achieve a high overall reflectivity ($\sim$ 99.9 %). The DBR mirrors clad a gain region which contains one or several quantum-wells. The quantum-well structures are placed at the antinodes of the standing wave of the resonant longitudinal mode for which the VCSEL is designed, since this enhances the modal gain [28]. Therefore, spacing layers are needed to adjust the cavity length to a integer multiple of the emission wavelength of the VCSEL. Fig. 1.5 shows the standing wave intensity distribution in the central region of a VCSEL (left) and a typical reflectivity spectrum (right) for a GaAs MQW laser wafer [29].

VCSEL wafers (Fig. 1.6(a)) are fabricated by a fully monolithic process, using MOCVD and MBE growth techniques. Transverse confinement can be achieved by either gain- or index-guiding as in conventional edge-emitting lasers [5, 30]. In gain-guided VCSELs (Fig. 1.6(b)), proton-implantation is generally used to produce a high-resistance region which funnels the injected carriers into the active region (current confinement) [31]-[33]. The high gain region generated at the center of the proton-implanted region provides optical confinement. Index-guided VCSELs use either mesa-etching, buried heterostructure, or native oxide processes to produce a transverse refractive index profile to allow optical waveguiding. Air-posted VCSELs (Fig. 1.6(c)) are fabricated by a self-aligned process using metal masks with SiO_2 win-

Figure 1.5: (left) Standing wave intensity distribution in the central region of a VCSEL. H and L denote high and low refractive index layers respectively; (right) Typical reflectivity spectrum of a GaAs MQW laser wafer (after Ref. [29] ©IEEE 1991).

dows protecting the laser aperture during reactive ion etching [34]. These air-posted devices have strong waveguiding because the large refractive index difference between the heterostructure and the air (Δn$\sim$1). Weakly index-guided VCSELs can be built, e.g., by regrowing a cladding layer around the air-posted structure with a lower refractive index than the active region (Fig. 1.6(d)) [35, 36]. This structure, referred to as buried heterostructure, allows simultaneous current and optical confinement. An alternative way of producing index-guided devices is through a native oxide process, in which a specific layer of AlAs in the VCSEL structure is selectively transformed into a native oxide which has a low refractive index and a high resistivity [37].

The effective cavity length in VCSELs is of the order of one to a few times the emission wavelength. Hence, the longitudinal eigenmodes of the VCSEL cavity have tens of nanometers spacing between them. Since the gain bandwidth is similar to the mode spacing only one longitudinal mode falls within the gain spectrum. Therefore, VCSELs are single longitudinal mode devices even under dynamical operation.

As a consequence of this feature, the electrical and optical characteristics of VCSELs are strongly sensitive to thermal effects. Fig. 1.7(left) shows the temperature dependence of the current and voltage thresholds for a typical VCSEL [38]. The voltage threshold increases monotonically with decreasing temperature due presumably to the potential barriers at the multiple p-heterointerfaces [38]. The threshold current shows a parabolic dependence which is unique to VCSELs. The reason for such a unique behavior lies on the different thermal red shift rates of the cavity mode frequency and the gain peak frequency. The resonant frequency of the cavity mode red shifts at roughly 0.6 $\overset{o}{A}/^{o}$C(see Fig. 1.8(left)) because heating changes the cavity length and changes the index of refraction through changes in the carrier number [38]-

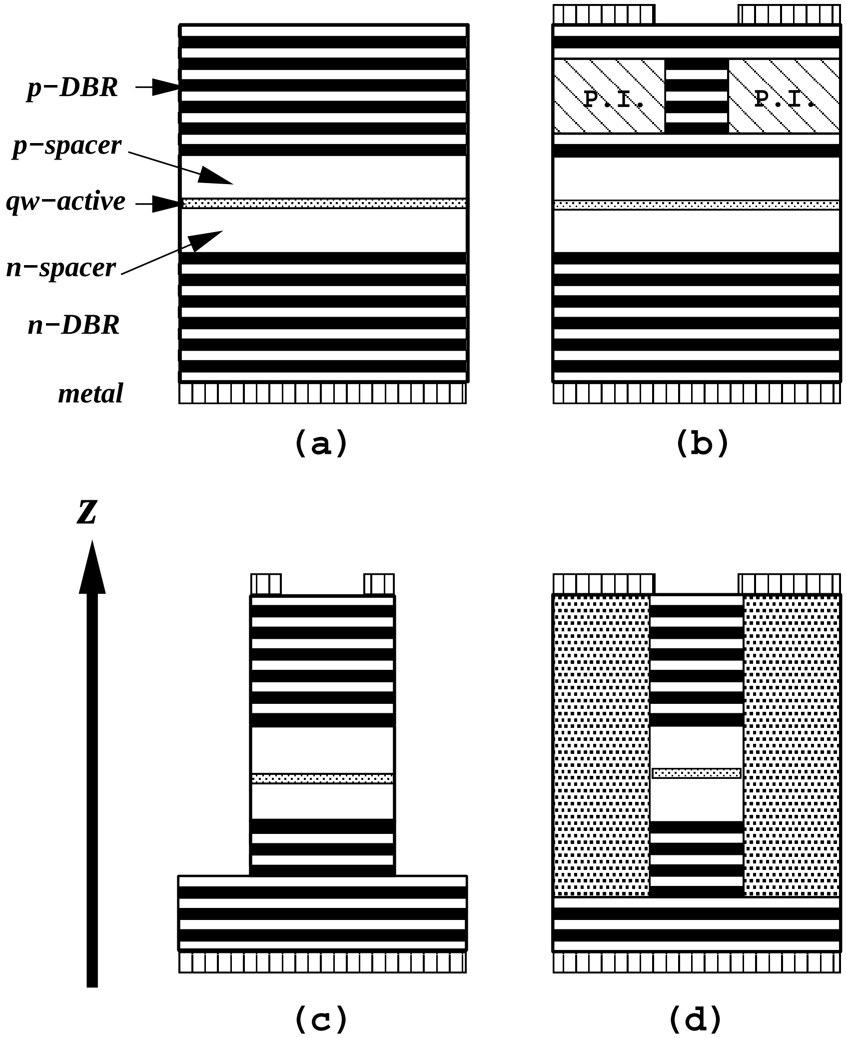

Figure 1.6: VCSEL structures: (a) VCSEL wafer; (b) gain-guided; (c) air-posted; (d) buried heterostructure.

[40]. The gain profile red shifts at 3.3 $\mathring{A}/^o$C mainly because of bandgap shrinkage with increasing temperature [38, 41, 42]. Therefore, considering that present VCSELs are designed such that the cavity resonance is on the long wavelength side of the gain spectrum at low temperatures — red shifted from the gain peak—, an increase in the heat sink temperature brings the gain peak towards the cavity resonance. As a consequence, there is a decrease of the threshold current with increasing temperature. The temperature at which minimum threshold occurs corresponds to the temperature at which the cavity resonance and the gain peak frequencies coincide. For larger temperatures, the mismatch of the frequencies reduces the gain of the lasing mode leading to an increase in the threshold current.

The same thermal effect is responsible for the reversible extinction of the output light in VCSELs with increasing current (see Fig. 1.7(right)). For a constant substrate temperature, increasing the operating current produces internal heating of the device (self-heating). Initially, although the temperature rise may bring the

Figure 1.7: (left) Temperature dependence of the current (circles) and voltage (squares) threshold for a 20 μm emitting window (after Ref. [38] ©AIP 1992).; (right) Light-Intensity (LI) characteristics for an 8 μs diameter VCSEL (after Ref. [40] ©IEEE 1993).

gain peak towards the cavity resonance, after the cavity mode frequency matches the gain peak frequency a further increase of the injection current increases the mode mismatch. Therefore, the gain available for laser action is reduced giving rise to a thermal induced saturation of the output light. When the mode mismatch is such that the internal losses overcome the effective modal gain, lasing stops. Thus, VCSELs are extremely sensitive to temperature changes and self-heating of the devices is the limiting factor in their operation.

The main source of temperature rise in VCSEL is the series resistance in the DBR mirrors which arises from the impedance to carrier transport caused by the energy

Figure 1.8: (left) Peak wavelength of the VCSEL emission plotted against substrate temperature. The response is linear, with a rate of change of 0.63 $\mathring{A}/^{o}$C; (right) Fundamental mode emission wavelength as a function of the dissipated power in the device. The wavelength shifts linearly at a rate 1.0 $\mathring{A}$/mW (after Ref. [40] ©IEEE 1993).

barriers at the heterointerfaces. High reflectivity mirrors require sharp interfaces that increase their series resistance. This results in high operating voltages and correspondingly high dissipated powers occur during CW operation of the device. For most applications, the effects of temperature changes on the device must be minimized. Several ways have been proposed: *i)* to reduce the series resistance of the VCSELs with techniques such as continuous-grading of the DBR heterointerfaces [43], or doping of the DBR interface regions [44, 45]; *ii)* to improve the current flow through the mirrors [46]; and *iii)* to improve the heat flow away from the VCSEL with the addition of a diamond heat-sink to the top of the device [40]. Although these techniques make VCSELs less sensitive to temperature during CW operation, thermal effects are not completely eliminated.

1.4 Polarization and transverse mode characteristics of VCSELs

Due to the previously mentioned technological interest in VCSELs, considerable research effort has been devoted in recent years to understand their fundamental properties. Among them, the selection of the polarization state and the transverse mode dynamics are two questions which have been extensively studied both experimentally and theoretically by several research groups [31],[47]-[94].

Pattern formation in the transverse profile of the VCSEL beam has received considerable attention because these devices easily have a rather large Fresnel number which favors the appearance of transverse patterns [31, 47, 48]. Studies of the mode profile in the near field and/or far field have been combined with spectral information taken at low [31] and high resolution [47]-[50] in order to analyze the transverse mode structure of VCSELs. It turns out from these measurements that VCSELs mode structure is very similar to that of edge-emitting lasers [31], namely each longitudinal mode of the VCSEL cavity has an associated set of transverse modes with different transverse profiles and frequencies.

Transverse modes of typical VCSELs are nearly Gauss-Laguerre or Gauss-Hermite (TEM) modes (see Appendix A). The fundamental transverse mode, commonly termed as the TEM_{00} mode, has a Gaussian beam pattern. Each higher-order mode presents a subset of transverse modes with equal emission frequency but different transverse profiles. For example, the first-order transverse mode has the TEM_{01} and the TEM_{10} modes, and their combination can give, if properly phased, two doughnut modes with opposite helicity but equal intensity distribution in the transverse plane [51]. Even though it is expected that the first-order TEM_{01} and TEM_{10} modes would be frequency degenerate [4], high resolution measurements show that in real VCSELs these modes have different emission frequencies [49, 50]. Such a symmetry breaking has been attributed to the uniaxial material strain which induces astigmatism in the VCSEL cavity [49, 52].

The sequence of appearance of transverse modes in VCSELs with increasing cur-

[4]Based on symmetry arguments

Figure 1.9: Transverse mode structure of a mesa VCSEL. The figure shows the near-field patterns of the dominant modes at different currents: (a) below threshold at 1 mA, (b) at threshold, (c) TEM_{00} at 6.3 mA, (d) TEM_{10} at 7.4 mA, (e) TEM_{01} at 7.5 mA, (f) TEM_{10} + TEM_{01} at 15 mA (after Ref. [50] ©AIP 1996).

rent is, typically, similar for many structures. Emission in the fundamental Gaussian transverse mode occurs for current values just above the threshold while high-order transverse modes can be successively excited as the current is increased; see for example Refs. [31, 47, 53]-[59] for gain-guided, Refs. [35, 36] for buried heterostructure, Refs. [50, 60] for mesa-contact, Ref. [48] for narrow (< 4 μm) air-posts, and Refs. [37, 48, 61, 62] for narrow (< 4 μm) oxidized VCSELs. Fig. 1.9 shows the near field patterns of the dominant modes at different current values of a 12 μm aperture mesa VCSEL [50]. Below threshold (a), the spontaneous emission is nearly uniform across the whole aperture. At threshold (b), the fundamental transverse mode emerges above the spontaneous emission background. At 6.5 mA (c), emission still occurs on the Gaussian TEM_{00} mode. Beyond 7.2 mA, a TEM_{10} mode (d) and a TEM_{10} mode (e) are simultaneously excited and coexist with the fundamental transverse mode. For increasing current (f), the fundamental mode is strongly suppressed, and the output pattern resembles a doughnut.

Exceptions to such a common transverse mode behavior are some strongly index-guided VCSELs [37, 61, 62] which are reported to start lasing in a mode higher than the fundamental one. It has been also reported experimentally that the onset of transverse modes can be affected by the relative detuning of the cavity resonance from the gain peak [63] — higher-order lasing modes are favored for the condition that the fundamental cavity resonance wavelength is longer than the gain peak wavelength, while the fundamental mode is favored when the fundamental cavity resonance has a shorter wavelength than that of the gain peak —.

Michalzik and Ebeling have performed an extensive theoretical study of the conditions affecting the onset of transverse modes in circular gain- and index-guided VCSELs [64]. It turns out from this study that the transverse mode spacing is not significantly different for both guiding mechanisms. In addition, they show that the effective modal gain difference between the fundamental and the first-order transverse modes *i*) is one order of magnitude larger for gain-guided than for index-guided devices with the same characteristics; *ii*) it decreases with the active region diameter in both gain- and index-guided VCSELs; *iii*) it increases as the refractive-index step of the waveguide decreases in index-guided VCSELs. Hence, they conclude that: *i*) gain-guided VCSELs provide a better transverse side-mode suppression ratio than index-guided lasers of comparable active region diameter; *ii*) the current at which the VCSEL goes into the multi-transverse mode regime decreases with increasing the active region diameter for both guiding mechanisms; *iii*) the larger the index step in index-guided VCSELs the smaller the active region diameter should be for single-mode operation. The influence of laser heating and spatial-hole burning were both disregarded in this work although these effects can quantitatively affect the results, as pointed out in Ref. [54].

Modeling the transverse properties of VCSELs has been an important topic. Much of the work has been focused on index-guided VCSELs because the modes of these lasers are defined by the built-in waveguide. Sarma and coworkers investigated the modal gain characteristics of index-guided VCSELs and proposed a design criteria for stable fundamental mode operation, namely, to use small devices (radius $\sim 3\ \mu$m) with a small current confinement region and a relative small index step [65]. Shore and coworkers have focused their work on the analysis of the the role of spatial hole burning in the transverse mode selection from the dynamical point of view [66, 67]. Steady-state numerical analysis of a self-consistent model including carrier diffusion, nonlinear dispersion and thermal effects has been used to study the transverse mode properties in gain-guided VCSELs by Zhang and Peterman [68].

We now deal with the polarization properties of VCSELs. Most of present devices are fabricated on [001]-oriented semiconductor substrates (emission direction), and are reported to emit linearly polarized light with a preference for polarization orientation along the [110] and [1$\bar{1}$0] crystalline axes [69] (transverse plane). This is a surprising result since the high degree of transverse symmetry of the circular VCSEL cavity and the cubic crystal [5] imposes no constraint on either type of polarization (linear, circular, elliptical) or the preference of the polarization direction. The unique explanation given for such a polarization behavior is the presence of linear anisotropies in the VCSEL cavity which break the transverse symmetry.

High resolution spectral measurements have shown that the transverse modes of the VCSEL have different emission frequencies depending on their polarization [49]. This feature indicates the presence of linear birefringence (or linear phase anisotropy) in the VCSEL cavity which breaks the frequency degeneracy of the transverse modes

[5] Quantum-wells oriented along the [001]-direction have in-plane crystalline symmetry.

Figure 1.10: Histogram of measured birefringence between the lasing (narrower peak) and non-lasing (wider peak) fundamental TEM_{00} modes measured at 1.4 I_{th} for a set of 39 VCSELs (after Ref. [72] ©APS 1997).

with orthogonal polarization. Birefringence is typically measured by means of the frequency splitting between the orthogonally polarized components of the fundamental transverse mode close to threshold. In some cases the two frequencies are unresolved within experimental accuracy ($<$ 2-3 GHz) [47, 58]. In other cases the reported frequency splittings are about 10-12 GHz [60, 70, 71] while a wide range, from 5 to 20 GHz, has also been reported [72] (see Fig. 1.10).

Woerdman and coworkers have developed an experimental all-optical technique, referred to as the *hot-spot technique*, to manipulate the VCSEL birefringence almost at will in either a reversible [73] or a permanent [74] way. Using this technique, this group has performed a systematic experimental study of VCSEL anisotropies which has allowed them to identify the physical mechanisms giving rise to the transverse symmetry breaking. From these studies, it turns out that the dominant anisotropy in VCSELs is linear birefringence between the preferred crystal axes, which is caused by stress and strain acting via the elasto-optic effect [73], and by internal electric fields acting via the electro-optic effect [72]. An explanation of most of their experimental results has been given within a linear coupled-mode theory including linear birefringence and dichroism [75]. However, the discrepancy between some experimental data and the linear model, such as the birefringence measurements as a function of the hot-spot induced temperature in Ref. [75], indicates the relevance of the non-linear gain dynamics, as has been recently demonstrated in [76, 77].

Figure 1.11: Polarized LI characteristics for VCSELs showing: (left, above) polarization stability (after Ref. [60] ©IEEE 1994); (right,above) polarization switching (after Ref. [70] ©AIP 1993); (left, below) hysteresis of the switching current (after Ref. [81] ©IEE 1995); (right, below) polarization coexistence (after Ref. [58] ©AIP 1994).

Even though several VCSELs display stable linearly polarization emission at any current value close to threshold [60, 69] (Fig. 1.11(left,above)), the polarization state of the emitted light sometimes depends on the injected current [78]. Many experiments [47, 58, 70, 71, 79, 80] have shown that VCSELs may switch from emitting linearly polarized light to emitting polarized light of the orthogonal linear polarization as the current is changed above the lasing threshold, a phenomenon known as polarization switching (Fig. 1.11(right,above)). Some authors have also reported polarization bistability [70, 81] and hysteresis of the switching current [81] (Fig. 1.11(left,below)). Emission on both linearly polarized modes (polarization coexistence) with different emission frequencies [58, 60] (Fig. 1.11(right,below)), as well as in both linearly polarized modes with the same emission frequency (elliptically polarized light) [82] have also been reported. All these polarization behaviors are observed to occur close to threshold within the fundamental transverse mode regime.

For higher injection currents, the excitation of higher-order transverse modes may be accompanied by changes in the polarization state of the output light. A commonly observed feature in VCSELs is that the first-order transverse mode tends to lase in the polarization orthogonal to that of the fundamental TEM_{00} mode [31, 47, 56, 58, 60, 80, 83]. For higher currents, the power in the dominant polarization typically saturates while the power in the orthogonal polarization rapidly increases [47, 56, 58, 80]. Abrupt polarization switching between higher-order modes has also been observed [58].

As an example, Fig. 1.12 shows the LIV characteristics (left) and the emission spectra (right) for a 12 μm aperture mesa VCSEL emitting at 840 nm [50]. The device, with a threshold current of 3.9 mA, operates on the fundamental mode up to 7.2 mA as inferred from the optical spectrum. At 6.3 mA, the abrupt drop in the linear $\hat{x}$-polarized light power indicates a polarization switching to linear $\hat{y}$-polarized light [6]. The birefringence induced frequency splitting is measured to be roughly 7 GHz. At 7.4 mA, the $\hat{x}$-polarized light power increases abruptly. At this current, the optical spectrum reveals the coexistence of a dominant $\hat{y}$-TEM_{00} mode, a relatively weak $\hat{x}$-TEM_{10} mode, and a much weaker $\hat{y}$-TEM_{01} mode. Thus, the first-order mode starts lasing mainly in the polarization orthogonal to the fundamental mode. As the current is slightly increased to 7.5 mA, the fundamental mode polarization flips back to $\hat{x}$ but the same mode structure is observed in the first-order mode, which is 85 GHz from the fundamental mode. At 8.1 mA, coexistence of the fundamental and the first-order transverse modes in both linear polarizations occurs. Beyond 13 mA, the fundamental mode is strongly attenuated, probably due to spatial hole burning, and the power is mainly carried by the TEM_{10} and the TEM_{01} modes in both polarizations. At this current level, the output pattern appears to form a $\hat{x}$- and a $\hat{y}$-doughnut modes (see Fig. 1.9(f)).

Stable polarization characteristics are required for VCSELs in polarization sensitive applications such as magneto-optic disk memory and coherent detection systems. Polarization mode control of VCSELs is also important for low noise transmission systems including optical interconnects because polarization fluctuations cause excess intensity noise even under fundamental transverse mode operation [84, 85]. Furthermore, polarization must be controlled for VCSEL arrays in 2-D applications.

To control the polarization state of the VCSELs, symmetry in the plane of the quantum well has to be broken. This is commonly carried out by introducing anisotropy of optical gain or loss to the laser medium [7]. Several polarization control methods have been discussed and reported ([86] and references therein), such as asymmetric cavity geometries [60], asymmetric stress produced from an elliptical etched hole [87], anisotropic gain from a fractional layer superlattice [88], and quantum-wells layers grown on misoriented substrates [89, 90]. Nevertheless, a better understanding of the physical mechanisms that influence the polarization behavior in the fundamental transverse mode of VCSELs may be useful to achieve improved or alternative methods of polarization control.

In this context, K. Choquette and coworkers have proposed a possible mechanism

[6] Notice that we have changed in the text the notation of the linearly polarized states in the figure: s by $\hat{x}$, and p by $\hat{y}$

[7] It has been shown that a difference in the modal gain/loss of 10 cm^{-1} between the polarization modes is enough to provide complete polarization stability [85].

Figure 1.12: (left) LIV characteristics and (right) emission spectra of a 12 μm aperture mesa VCSEL. s and p ($\hat{x}$ and $\hat{y}$ in the text, respectively) indicates linearly polarized emission along two orthogonal directions of the transverse plane (after Ref. [50] ©AIP 1996).

for the selection of the polarization state in VCSELs [58, 79] based on the results of a careful study of the polarization behavior of these devices as the mean of the frequencies of the two linearly polarized modes is shifted from one side of the gain curve to the other and as the strain induced anisotropies are varied, changing both the frequency splitting and the gain differences for the modes [79]. The authors argue that, since the material gain is a function of the wavelength, the birefringence induced splitting of the polarization cavity resonances yields different gain coefficients for the orthogonal linearly polarized modes. Such a gain difference, which is sufficient to suppresses the polarization mode with weaker gain and thus select the one with higher gain, depends on the relative spectral alignment between the cavity resonances and the gain peak, and therefore its value changes as the current is injected into the VCSEL because of self-heating. Hence, they conclude that *(i)* stable polarization emission occurs when the gain difference favors the same polarization mode for any current value; *(ii)* polarization switching is observed when there is an exchange of the relative gain of the two polarized modes as the current is increased; and *(iii)* coexistence of both linearly polarized states occurs when the gain difference is small as a consequence of a small birefringence.

However, several points are worth noting in the above explanation:

- On the one hand, since the frequency splitting between orthogonal linearly polarized states is often very small as compared to the width of the gain curve (below or of the order of 20 GHz as compared to 20 nm or more, respectively), the gain differences may be minute, so polarization switching in the fundamental mode should be difficult to observe. Moreover, polarization bistability [70] and hysteresis of the switching current [81] observed in some experiments, are not consistent with the above phenomenological explanation.

- On the other hand, one would expect stable polarization emission if the temperature of the device is kept constant. However, a recent experiment (see Chap. 6) has shown that polarization switching may also be present under constant active region temperature.

- The phenomenological explanation given by Choquette *et al.* comes from intuitive consideration of the competition of the intensities of the modes with orthogonal polarizations, but disregards phase effects. In this context, theoretical work has been performed by Shore and collaborators who have studied the polarization state selection in index-guided VCSELs [91]-[94]. Their model includes birefringence and carrier diffusion and is used to describe the dynamical evolution of the modal amplitudes of the built-in waveguide modes, which are coupled to the total population number. Such a model predicts polarization switching within the fundamental mode [91]-[93] and within the first higher-order transverse modes [94] as a consequence of spatial hole burning, which changes the modal gain between the linearly polarized modes as the current increases. However, their studies neglect the phase of the optical fields which may lead to similar and/or additional polarization state selection mechanisms. For example, in cases of two mode interaction, competition and coexistence of frequency nondegenerate modes occurs as a consequence of the phase sensitive dynamics [95, 96].

- Polarization switching is a well known phenomenon in gas lasers. It has been conclusively demonstrated that the predominant effect causing the switching in these lasers (with small birefringence relative to the gain linewidth) is not the gain differential, but the presence of saturable dispersion from the anomalous index of refraction of the transitions [97]-[99]. Studies of third-order Lamb theories with equal gains for the two linear polarizations found that birefringence together with saturable dispersion is sufficient to explain many of the experimentally observed phenomena. Saturable dispersion is also present in semiconductor lasers through the linewidth enhancement α-factor [100]-[102], which produces coupling of the modulus and the phase of the optical field. The effects of the α-factor are known to be much more important for semiconductor lasers than detuning is for gas lasers.

- From a fundamental point of view, the polarization state of light emitted by a laser depends on both the angular momentum of the quantum states involved in the material transitions and on the laser cavity. Emission of a quantum of light (a photon) with right (left) circular polarization corresponds to a transition in which the projection of the total material angular momentum on the direction of propagation changes by +1 (−1) in units of $\hbar$. However, the anisotropies, geometry and waveguiding effects of the cavity can lead to a preference for a particular polarization state of the laser light. These two ingredients can compete or be complementary, their relative importance depending on the type of laser. Different atomic gas lasers emit linearly, circularly or elliptically polarized light, and these polarization states have been identified with different atomic or molecular optical transitions [99], [103]-[110]. Conventional edge emitting semiconductor lasers usually emit TE linearly polarized light due to the geometrical design of the laser cavity, although special engineering of the geometries, reflectivities, or the crystal stresses can favor TM linearly polarized light. The situation in [001]-oriented quantum-well VCSELs is more subtle due to the high degree of transverse symmetry of the circular VCSEL cavity and the isotropic gain properties in the quantum-well plane. Therefore, both ingredients, namely the quantum states involved in the allowed transitions and the anisotropic properties of the VCSEL cavity, should play an important role in the determination of the polarization properties of VCSELs.

In the spirit of the previous points, a fundamental model was developed by San Miguel, Feng, and Moloney in 1995, which considers the polarization of the laser field by including the magnetic sublevels of the conduction and valence bands in unstrained quantum-well VCSEL media. The SFM model [112], as it is widely termed, is one of the building blocks of this thesis.

1.5 Outline

The selection of the polarization state and the transverse mode dynamics in VCSELs are two linked questions which have been extensively addressed in recent years. Theoretical studies on these topics have disregarded both the phase sensitive effects and the quantum nature of the polarization in lasers, which are known to be important in other kinds of lasers. Armed with the knowledge and the experience obtained in gas lasers along almost thirty years, we seek in this thesis a fundamental explanation for the polarization and transverse mode phenomena observed in VCSELs by considering the fundamental aspects of the physics of semiconductors through the SFM model. Theoretical analysis, numerical simulations and experiments will be combined to investigate the role of physical mechanisms — such as the saturable dispersion (or α-factor), the VCSEL anisotropies, the spin-flip relaxation processes, and the temperature — on the polarization and the transverse mode properties of unstrained quantum-well VCSELs.

Although optical and electrical characterization of VCSELs have been extensively addressed, Chap. 2 presents experimental measurements of the electrical and optical properties of proton-implanted VCSELs and compares them to the experimental data reported elsewhere. Results for Light-Current-Voltage characteristics and spectral measurements as a function of the device temperature are shown for several devices with different active region sizes. These measurements are used to determine the characteristic parameters of the devices under study: the threshold current and its dependence with temperature, the thermal resistance, the characteristic thermal time, the birefringence, the polarization orientation, etc.

In order to study the polarization dynamics in VCSELs, Chap. 3 is devoted to the derivation of the SFM model that considers the coupling of the vector optical field to the two allowed transitions between the conduction band and the heavy hole band in unstrained quantum-well media. The evolution equation for the vector optical field of circularly polarized components is derived from Maxwell's equations for a gain-guided VCSEL, and includes transverse effects through the optical diffraction term. The evolution equations for the material dipole densities and the carrier densities for each transition are derived using a density matrix formalism, and extended spatially in the transverse plane by considering carrier diffusion. Coupling between the circularly left and right polarized transitions is assumed to occur via spin-flip relaxation processes. Within this framework, introduced by San Miguel, Feng, and Moloney in Ref. [112], the polarization and transverse mode dynamics of VCSELs are described in terms of two coupled sets of semiclassical two-level Maxwell-Bloch equations, one for each circularly polarized transition (SFM[8]. The chapter is finished with a general discussion of the limitations of two-level Maxwell-Bloch type of approach in the description of semiconductor dynamics.

In Chap. 4, we analyze the polarization state selection in fundamental transverse-mode of VCSELs. The single-mode operation of the device allows the derivation of a rate equation model (from the general model developed in Chap. 3) which includes the characteristic cavity anisotropies of VCSELs, birefringence and dichroism, as well as the saturable dispersion through the α-factor. Such a simpler model permits us to find analytical expressions for the allowed linearly and elliptically polarized steady-state solutions. The stability analysis of these solutions allows us to predict the different polarization behaviors as the VCSEL current is changed — stable linearly polarized emission, polarization switching, polarization coexistence, and elliptically polarized emission — as a function of the VCSEL anisotropies. All these results are corroborated by numerical simulations of the model equations [113]-[116]. We finish the chapter by studying the effect of a linearly polarized optical beam injected into the VCSEL which shows the existence of bistability and polarization switchings caused by changes in the intensity and the detuning of the injected optical signal [116]. All these results, in good agreement with experimental findings, show the possible relevance of the saturable dispersion and the spin-flip relaxation processes on the polarization state selection in VCSELs.

In Chap. 5, we extend the previous rate-equation model to study the effects of an axial magnetic field on the polarization state of a VCSEL. For perfectly isotropic VCSELs we show that emission always occurs in the form of rotating-linearly polarized light as a consequence of the circular birefringence induced by the magnetic field (Zeeman effect). Nevertheless, when linear anisotropies are taken into account, it is found that the polarization state of the emitted light strongly depends on the value of the magnetically-induced circular birefringence, which depends on the magnetic

[8] SFM model stands for San Miguel-Feng-Moloney model as well as Spin-Flip-Model [111] model

field strength. For weak magnetic fields (circular birefringence smaller than linear birefringence), we observe that the zero magnetic field preference for linearly polarized emission is converted into a preference for elliptically polarized emission, whose current-dependent ellipticity is in good agreement with the experimental measurements in Ref. [82]. In the parameter range of moderate magnetic fields (circular and linear birefringences are of the same order), we show that emission typically occurs in the form of "two-frequency" states (solutions involving emission of two primary spectral components) which are characterized by a close trajectory on the Poincare sphere. In the limit of very strong magnetic fields we show that the emission occurs in the form of rotating elliptically polarized light, a special case of almost linearly polarized emission in which the output power in each linear polarization mode is modulated at a frequency that depends on the strength of the external magnetic field [117]. Motivated by the latter results, we present at the end of the Chapter the possibility of generating fast optical polarized pulses at GHz rates by applying an axial magnetic field to an almost isotropic VCSEL, with applications in optical communications and optical clock generation [118].

In Chap. 6, we report a experimental study in gain-guided VCSELs in order to discriminate between the effects produced by changes in the injection current and those produced by changes in temperature (from the current-induced self-heating) on the polarization state of a VCSEL operating in the fundamental transverse mode regime. We first perform CW Light-Current measurements using a current ramp duration of a few seconds that allows the active region temperature to change for each value of the injected current and dissipated power. In these measurements, the polarization switching observed in the device can be influenced by the thermal-induced shift of the cavity resonances relative to the gain peak as a consequence of VCSEL self-heating [79]. We next perform Light-Current measurements in which the current ramp last for a time that is short compared to the thermal response time of the VCSEL ($\sim 1\ \mu$s) so that the temperature of the active region stays constant during the scan. The fact that polarization switching still occurs at constant active region temperature indicates the existence of additional mechanisms causing the selection of the polarization state associated with the current scanning [119]. This temperature-independent polarization switching phenomenon is explained in terms of the rate equation model and its results in Chap. 4, while the fitting of the experimental data allows us to estimate the value of the spin-flip relaxation rate.

In Chap. 7, we analyze the polarization and transverse mode competition for circular proton-implanted VCSELs, using the continuous transverse model presented in Chap. 3. We first study the polarization properties during the turn-on of the VCSEL. Next, polarization stability and polarization switching within the fundamental transverse mode are shown as the current is scanned for two different situations in which the gain of the linearly polarized modes is different. New polarization instabilities are observed at higher injection currents related to the onset of higher-order modes. The first-order transverse mode always starts lasing orthogonally polarized to the fundamental one in good agreement with experimental reports. At larger currents polarization coexistence with several active transverse modes is observed. We finally show that these results are sensitive to the strength of the coupling between carrier populations associated with different circular polarizations of light (spin relaxation rate) [120, 121].

Chap. 8 contains a summary and the conclusions of this work.

Chapter 2

Determination of VCSEL characteristics

Abstract [1]

This Chapter reports an experimental characterization of optical and electrical characteristics of gain-guided VCSELs. These basic properties give first-hand experience with the system and phenomena for which the theoretical model of Chap. 3 has been developed. The ranges of parameters measured will be used in the studies in the remaining Chapters.

[1]The experimental results presented in this chapter were obtained during my visit to the Center for Optoelectronic Computing Systems and the Department of Electrical Engineering of the Colorado State University, Fort Collins, Colorado, USA.

The VCSELs that were studied for the experimental results reported in this chapter are commercial proton-implanted top-surface emitting AlGaAs/GaAs multi-quantum-well devices emitting at 850 nm and produced by VIXEL Corporation [122]. The optical cavity is formed by a pair of graded-step AlAs/AlGaAs distributed Bragg reflectors with 19 periods for the p-doped upper mirror and 29 periods for the n-doped bottom mirror. The active region consists of three GaAs/AlGaAs quantum wells which are each 80 $\mathring{A}$ long, separated by 80 $\mathring{A}$ long barriers. The transverse geometry and dimensions of the active layer are delimited by proton-implantation in the top DBR region, as depicted in Fig. 2.1(left), which allows for gain-guiding. The circular window in the top metal contact, whose diameter is smaller than the proton-implantation region, allows for spatial filtering [53].

Electrical and optical measurements were performed on linear arrays of independently addressable cylindrically symmetric devices. Four linear arrays with active region diameters of 15, 18, 22 and 24 μm and contact window diameters of 12, 15, 18 and 20 μm, respectively, were available. To avoid confusion, we identify these devices from here on by their active region diameters. The linear arrays, each one having 35 devices, were encapsulated on a chip and bonded with gold wires. A schematic representation of the VCSEL chip is shown in Fig. 2.1(right).

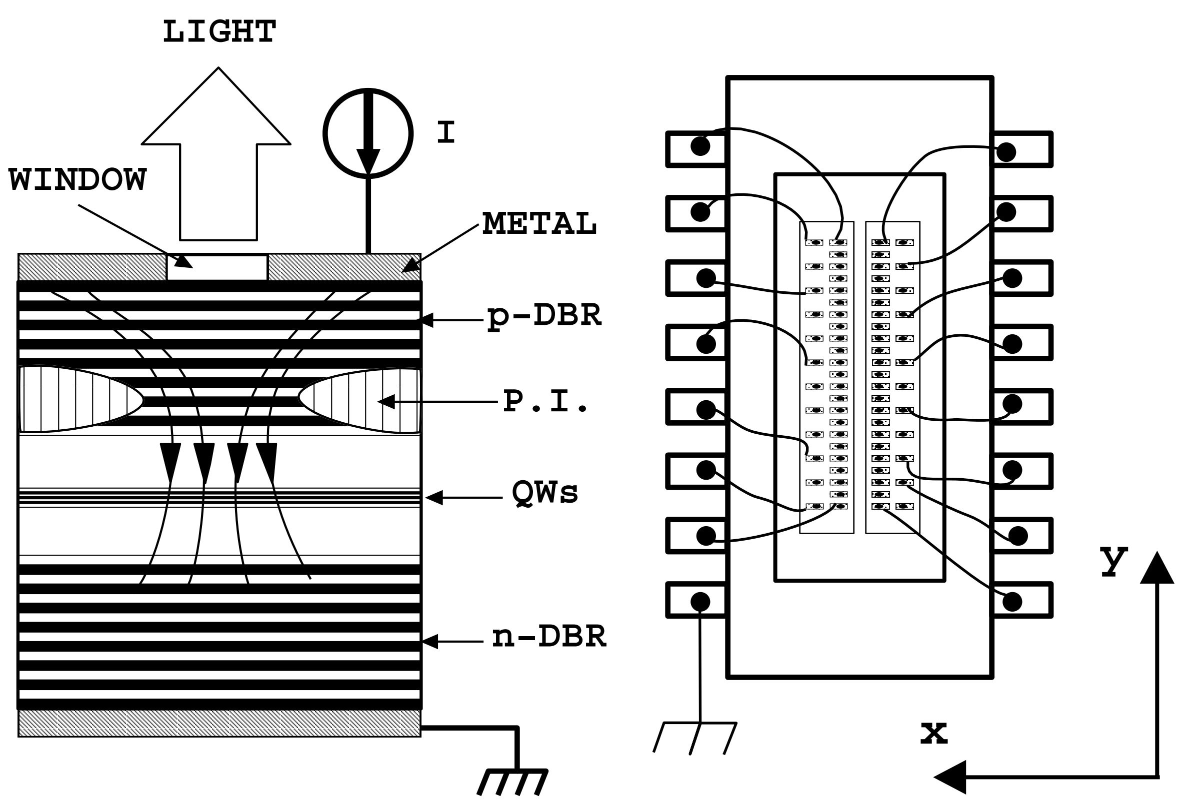

Figure 2.1: (left) Gain-guided VCSEL structure: the upper and lower DBR mirrors are doped p- and n-type, respectively; current is injected from the top surface through an annular contact into the active region, whose transverse dimensions are delineated by proton implantation; (right) VCSELs are bonded to the chip by soldering a gold wire from the VCSEL metal pad.

2.1 Light-Intensity-Voltage and spectral characteristics

For operation, the VCSEL chip is mounted on a Peltier thermo-cooler as indicated in Fig. 2.2 (left). The external current source for the Peltier element permits the control of the temperature of the wafer substrate, which is measured by means of a calibrated thermocouple.

The VCSELs are conditioned by a thermal annealing process before any electro-optical measurement is performed. In this "burn-in" process, as it is commonly termed, a train of current ramps is applied to each device over a long time (2 hours), which seems to homogenize the VCSEL active region and leads to the reproducible measurements.

CW Light-Intensity-Voltage (LIV) characteristics are measured for several devices using a HP-4145A Semiconductor Parameter Analyzer (SPA) connected as shown in the setup of Fig. 2.2(right). The SPA applies a voltage ramp to the VCSEL and simultaneously measures both the current through the junction and the VCSEL output power, the latter detected with a wide-area photodetector (PD) after the beam is collimated with a microlens (L).

Typical LIV characteristics for 15 μm active-region diameter VCSELs are shown in Fig. 2.3(left). The V-I characteristics, taken at room temperature, are similar for all three devices. The average threshold current, I_{th}, is 6 mA. The applied bias voltage at threshold, V_{th}, is roughly 1.82 V. The series resistance of the DBRs , R_s, can be estimated as the average value of dV/dI in a current range well above threshold [2]. We have measured a series resistance of 25 Ω over currents from 30 to 50 mA. For the 18 μm diameter VCSELs (Fig. 2.3(right)), we find similar V-I

[2] The total applied voltage to the VCSEL, V, is related to the injected current, I, as $V=\beta\cdot ln(I/I_o+1)+R_s\cdot I$, where I_o is the reverse saturation current, $\beta = kT/e$, k is the Boltzman constant, T is the temperature, e is the electron charge, and R_s is an intrinsic resistance in series with the VCSEL. Thus, the VCSEL resistance is $R_V=dV/dI=R_s+\beta/(I+I_o)$.

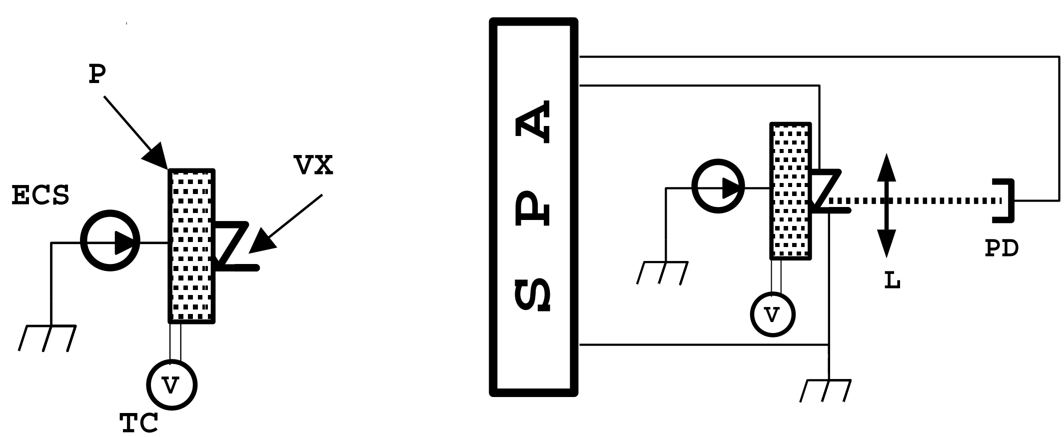

Figure 2.2: (left) Control of the substrate temperature: (VX) VCSEL chip, (P) Peltier, (TC) thermocouple, (ECS) Peltier external current source. (right) Setup for CW LIV measurements.

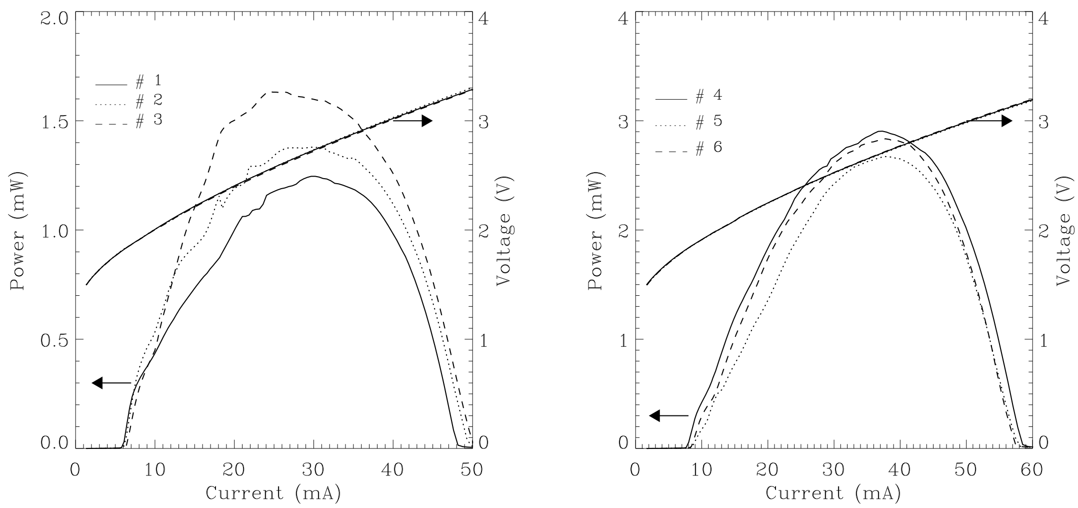

Figure 2.3: LIV characteristics for three different VCSELs with 15 μm (left) and 18 μm (right) diameters, respectively. Measurements are performed at room temperature.

characteristics but with I_{th}= 8 mA, V_{th} = 1.8 V, and R_s = 23 Ω (averaged between 30 and 60 mA). Such a small series resistance is a direct consequence of the use of graded DBR mirrors [43, 123].

We now look at the LI characteristics. For injection currents above the lasing threshold, the output power first increases linearly with increasing the applied current. The average slope is roughly the same for all the devices, 0.20 W/A. Kinks in the L-I characteristics occur due to the onset of higher order transverse modes. After a kink, the slope typically decreases. Around 25 mA (35 mA), the output power saturates for the 15 μm (18 μm) diameter VCSELs. At this current, the average maximum output power, P_{max}, is 1.4 mW (2.7 mW). Beyond the saturation regime, the output power drops very fast with increasing current as a consequence of heating in the device [39], and lasing action ceases at 50 mA (60 mA). This is a reversible process. The effects of the temperature on the electrical and optical characteristics of the VCSELs are the topic of the next Section.

The spectrum of the VCSEL emission is also measured using the setup shown in Fig. 2.4 (left). The VCSELs are CW biased using a DC current source. The output light is first collimated and then focused on the entrance slit of a half-meter, high-resolution monochromator (Jarrel Ash 82-020). A photo-multiplier (PMD), connected to a high-voltage (HV) source, is placed at the exit port of the monochromator. Since the PMD signal is very weak and noisy, the VCSEL output light is chopped at 1.5 kHz using an optical chopper driven by a controller (CC), and the weak signal is synchronously detected and amplified by a Stanford Research System SR510 lock-in amplifier.

The spectral behavior of a 15 μm diameter VCSEL is shown in Fig. 2.4 (right) for different values of the injection current. The device operates in a well defined single-longitudinal mode up to 10 mA. At 11.5 mA there is coexistence of the fundamental and the first of the higher-order transverse modes, the latter has a wavelength 0.25 nm shorter ($\approx$ 100 GHz). For increasing current, at 13.1 mA, the fundamental trans-

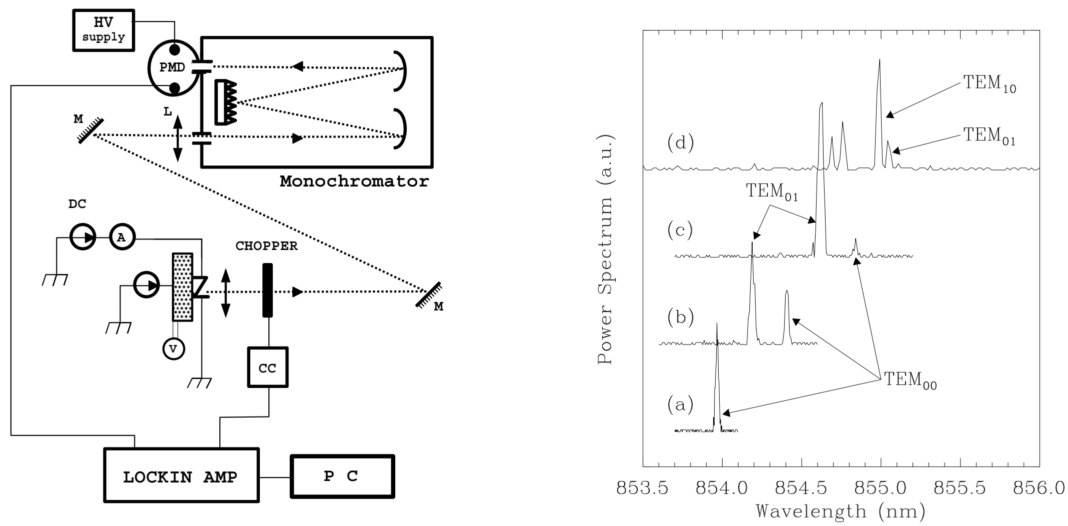

Figure 2.4: Setup (left) and results (right) for CW emission spectra (right) of 15 μm diameter VCSELs (device # 3 of Fig. 2.3 (left)). Measurements are performed at room temperature for different operating currents: (a) 8.4, (b) 11.5, (c) 13.1, (d) 18.3 mA. The monochromator resolution is 0.02 nm.

verse mode is suppressed and most of the optical power is emitted in the first-order transverse mode. As a consequence of the ohmic heating, the emission wavelength of each mode red shifts (towards longer wavelength) with increasing applied current at a rate of 0.2 nm/mA, in agreement with other reported values [56]. At higher currents several transverse modes coexist; for example, at 18.3 mA emission occurs on two higher-order modes separated by roughly 0.30 nm ($\approx$ 120 GHz). The first-order transverse mode, $\lambda \sim$ 855.0 nm, has two peaks corresponding to the TEM_{10} and TEM_{01} modes, which are separated 0.04 nm in wavelength ($\approx$ 15 GHz in frequency). The second-order mode, $\lambda \sim$ 854.7 nm, also presents two main peaks. At this current, the fundamental mode is completely suppressed.

2.2 Temperature effects

A systematic study of the temperature-dependent characteristics of our gain-guided VCSELs is reported in this section.

We first study the temperature dependence of I_{th}, V_{th} and P_{max} by performing LIV measurements under CW operation at different substrate temperatures. The L-I characteristics, depicted in Fig. 2.5 (left) for a 15 μm active region diameter VCSEL, seem to be very similar up to 15 mA within the range of temperatures studied (-25 to 45 ^{o}C). However, important differences are observed in the current and voltage thresholds. These magnitudes are shown in Fig. 2.5 (right) and the results can be compared with those in Fig. 1.7(left). The threshold voltage increases monotonically with decreasing temperature. Furthermore, the current threshold has a parabolic dependence with the minimum threshold around room temperature (20 ^{o}C). The inset in Fig. 2.5 (left) also shows that the maximum output power emitted by the VCSEL

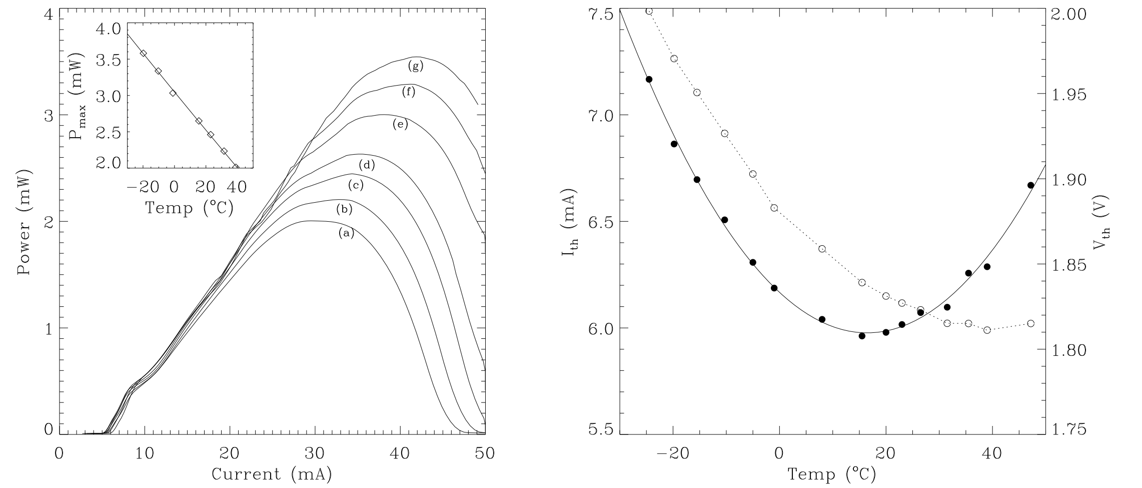

Figure 2.5: (left) L-I characteristic for a 15 μm active-region diameter VCSEL taken at different substrate temperatures (a) 39.0, (b) 31.5, (c) 23.0, (d) 15.5, (e) -1.0, (f) -10.3, and (g) -19.8 ^{o}C; the inset shows the dependence of the maximum output power emitted by the VCSEL for the labeled temperatures. (right) Dependence of the CW current (solid circles) and bias voltage (open circles) at the lasing threshold on the substrate temperature.

increases linearly with decreasing the substrate temperature. All these phenomena, which have been widely reported for other VCSELs [40, 38, 124, 125], can be explained in terms of the temperature dependences of the cavity mode resonances and the gain profile. The same thermal tuning mechanisms are responsible for the saturation of the output power and the lasing cutoff observed in the L-I characteristic at a fixed substrate temperature.

The temperature in the active region of the VCSEL, T_{act}, depends on both the substrate temperature, T_{sub}, and the local heating due to the electrical power dissipated by ohmic heating (Joule heating) as the current is increased, P_{dis}. For certain applications, such as those described in Chap. 6, it is important to estimate T_{act}. One way is to measure the thermal resistance of the VCSEL [126], R_{th}, which relates the active region temperature to the dissipated power, as

$$T_{act} = T_{sub} + R_{th} P_{dis} \ . \tag{2.1}$$

We have estimated this parameter for our AlGaAs devices using an indirect technique based on the dependence of the emission wavelength of the fundamental transverse mode on the dissipated power. The emission wavelength is measured during CW operation for different values of the injection current at fixed substrate temperature using the set up shown in Fig. 2.4. For each injection current value I, the dissipated power is calculated from the LIV characteristic as P_{dis}=I·V-P_{out}, where P_{out}(I) and V(I) are the power emitted as laser light and the laser voltage drop, respectively, at the given current. Results for different substrate temperatures are depicted in Fig. 2.6.

For constant T_{sub}, the emission wavelength exhibits a linear red shift as a function of the dissipated power with an average rate of dλ/dP_{dis}= 0.87 $\AA$/mW, as depicted in the upper inset of Fig. 2.6. The lower inset shows the dependence of the emission

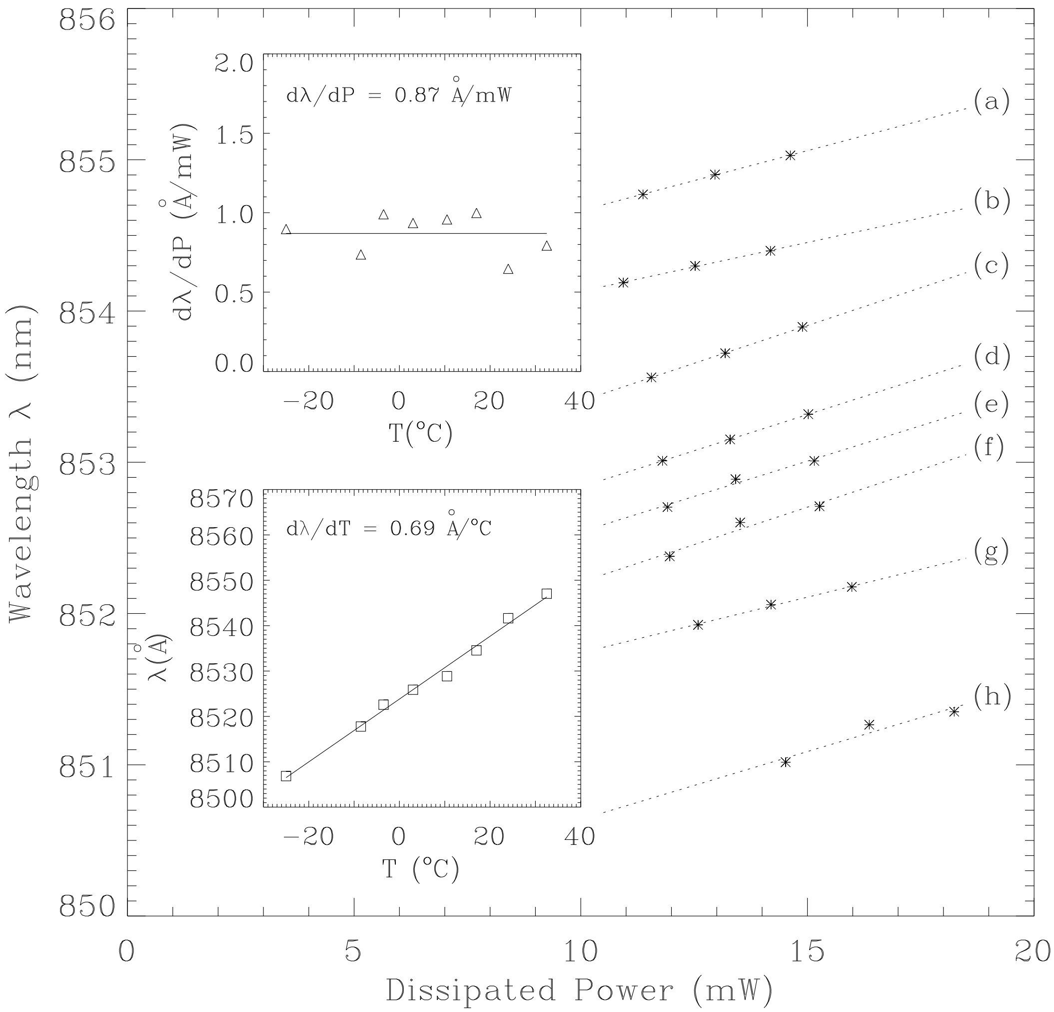

Figure 2.6: Peak wavelength of the fundamental transverse mode as a function of the dissipated power for different substrate temperatures (a) 32.0, (b) 24.0, (c) 17.0, (d) 10.5, (e) 3.0, (f) -3.5, (g) -8.5, and (h) -25.0 ^oC. The upper inset shows the average slope of the curves. The lower inset shows the dependence of the peak wavelength with the substrate temperature at constant dissipated power.

wavelength on the substrate temperature at a constant dissipated power (P_{dis}(I)=10 mW). The emission wavelength grows linearly with T_{sub} at a rate $d\lambda/dT = 0.69\ \mathring{A}/^oC$. Since the data represented in the lower inset is taken at constant dissipated power — so that the active region temperature only changes due to substrate temperature variations — we conclude that the emission wavelength is a good thermometer of the active layer temperature.

From the previous values, the thermal resistance of the VCSEL under study is

$$R_{th} = \frac{dT}{dP_{dis}} = \frac{dT}{d\lambda}\frac{d\lambda}{dP_{dis}} = 1.26\frac{^oC}{mW} \ . \tag{2.2}$$

Similar thermal resistance values are found for the other VCSELs. We point out

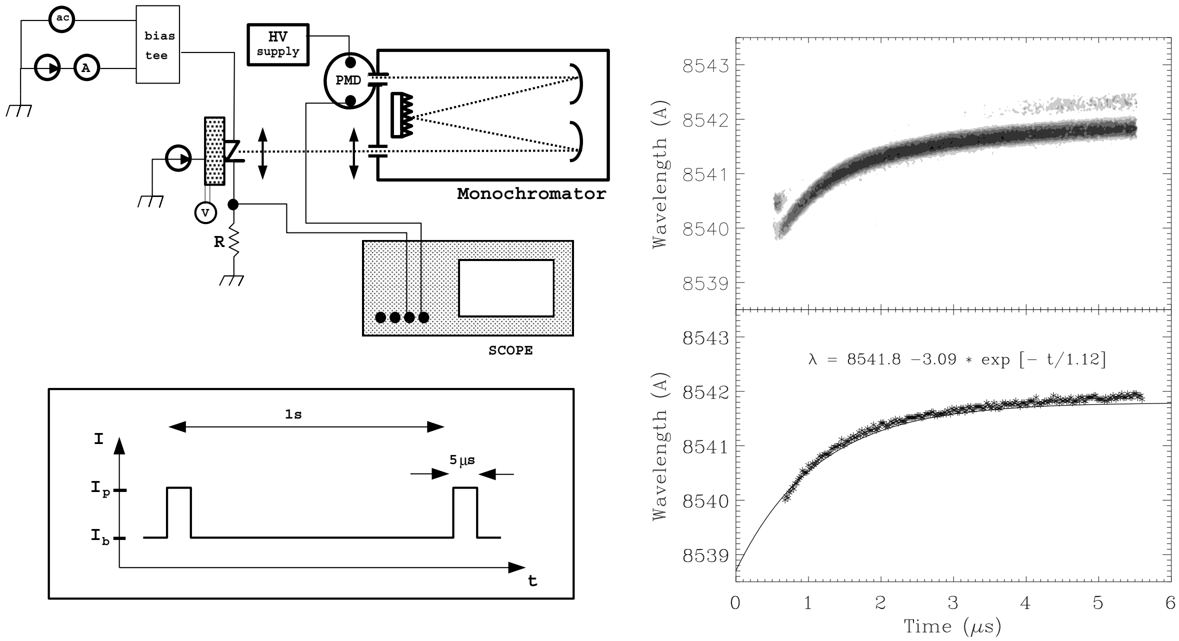

Figure 2.7: (left, above) Setup used to measure the thermal time constant. (left, below) Time trace of the current applied to the VCSEL. (right, above) Time-resolved optical spectrum. (right, below) Fitting of the emission peak wavelength, which shows an exponential dependence with a characteristic time of 1.12 μs. Measurements are performed at room temperature.

that although not many points were considered for this measurement, all the thermal parameters are in good agreement with previously reported values for similar AlGaAs/GaAs systems [40] (Results can be compared with those in Fig. 1.8).

One way to minimize the temperature rise induced by Joule heating is to operate the device under fast modulation at low-duty-cycle [39, 119, 127]. This idea is based on the fact that the thermal response of the VCSEL to an abrupt increase of the dissipated power is not instantaneous but takes a finite time. For example, for a square pulse current, the active region temperature exponentially approaches the steady-state temperature as [4, 39]

$$T_{act} = T_{sub} + \Delta T(P_{dis}) \left(1 - e^{-(t-t_0)/\tau_{th}}\right) \;, \tag{2.3}$$

where ΔT is the temperature raise corresponding to the power dissipated by the current pulse, t_0 is the pulse switch-on time, and τ_{th} is known as the thermal time constant.

In order to estimate the characteristic thermal time constant of our VCSELs we take advantage of the fact that the emission wavelength depends linearly on the temperature of the active layer. Then, it is straightforward to demonstrate that the emission wavelength will change in time as

$$\lambda = \lambda_f - \Delta\lambda e^{-(t-t_0)/\tau_{th}} \;. \tag{2.4}$$

where $\Delta\lambda$ is the emission wavelength red shift due to the active layer temperature raise, and λ_f is the steady-state emission wavelength.

Therefore, by monitoring the time evolution of the emission wavelength to a square current pulse, the characteristic thermal time can be measured. For this purpose, we use the setup shown in Fig. 2.7 (left,above). The VCSEL is biased by means of a DC current source (HP 6214A) and an AC voltage square pulse generator (Stanford Research Sys., DG535), connected to the VCSEL through a bias-tee network. The VCSEL applied current, measured through a load resistance R=20 Ω, is schematically depicted in Fig. 2.7 (left,below). It consists of a train of 5 μs long square pulses with a 1 Hz repetition rate [3]. The bias (I_b) and pulse (I_p) currents are 5.43 and 7.65 mA, respectively, and the threshold current is 6.15 mA. The VCSEL output light is collimated and focused on the entrance slit of a half-meter, high-resolution monochromator, using a PMD to detect the output light. The injected current and the PMD electric signals are displayed with a a high-resolution (2 Gsamples, 500 MHz bandpass) digital scope — triggered to the AC voltage source — and recorded in a PC.

Time-resolved spectra are measured as follows. The scan velocity of the monochromator grating is set to 2 $\overset{o}{A}$/min, such that every second during the measurement (every pulse) the central wavelength of the monochromator changes in 1/30 $\overset{o}{A}$. However, the central wavelength is effectively constant during each current pulse (5 μs), and therefore the PMD electric signal gives the temporal response of the VCSEL output at a fixed wavelength, $P(\lambda_0, t)$. Time-traces of the PMD signal are stored in the personal computer connected to the scope for every current pulse. This allows us to reconstruct the time resolved spectrum [4], which is shown in Fig. 2.7 (right,up). As expected, the emission wavelength red shifts exponentially in time with a characteristic time τ_{th}=1.12 μs, which corresponds to the thermal time constant, in good agreement with values reported previously [39]. From this measurement, we conclude that low-duty-cycle modulation of the VCSEL current using current ramps much shorter than the thermal time constant of the VCSEL, may allow operation at constant active region temperature. This technique will be used in Chap. 6 to study the polarization behavior of the VCSEL during fundamental transverse mode operation in order to avoid thermal effects [119].

2.3 Polarization characteristics

This Section is devoted to reporting the study of the polarization properties of our gain-guided VCSELs. First, we will present measurements of the distribution of linear polarization angles, finding that the polarization orientation exhibits a preference for two crystal directions in the transverse plane of the VCSEL. Next, polarized LI measurements will be shown revealing different (and uncorrelated) polarization behaviors depending on the VCSEL device. Finally, we will show results of the birefringence-induced frequency splitting for several devices.

---

[3] Notice that, since the period between pulses is much longer than the pulse width, the thermal response of the VCSEL is essentially the same as for a single pulse [128].

[4] Notice that $P(\lambda, t)$ is plotted as a histogram in Fig. 2.7(right,up) using a 256 grey scale, where white color corresponds to $P(\lambda, t)$=0.

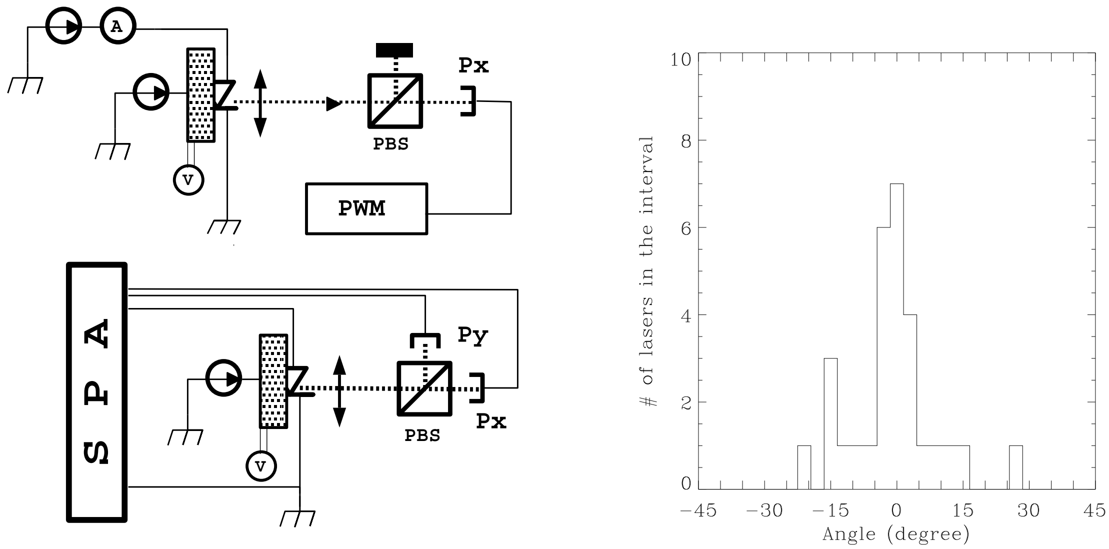

Figure 2.8: (left,above) Setup for the distribution of polarization angles, and (right) results. (left,below) Setup for polarized LIV measurements.

The polarization angle was measured (see Fig. 2.8 (left,above)) by rotating a polarizer beam-splitter (PBS) in front of a wide-area photodetector such that the transmitted polarization component, P_x, was maximized for a constant injection current just above the lasing threshold. Fig. 2.8 (right) shows the distribution of polarization angles for all the VCSELs available. In this figure, we identify the angles 0 and 90 of the polarizer with the directions $\hat{x}$ and $\hat{y}$ of the transvese plane of the VCSEL, respectively (see Fig. 2.1). The distribution is centered around the 0 angle of the polarizer which corresponds to either [110] or [$1\bar{1}0$] crystalline axis (we cannot distinguish between them). We thus infer that the light coming out from the VCSELs is typically linearly polarized and preferentially oriented along one of two orthogonal directions of the transverse plane of the wafer, in good agreement with previous reports [73].

We next studied the polarized LI characteristics in several 15 μm active region diameter VCSELs. The setup used, shown in Fig. 2.8(left,below), is similar to that of Fig. 2.3 but with the insertion of a Glan-Thomson polarizer which splits the output light from the VCSEL into two orthogonal linearly polarized components. The angle of the polarizer was adjusted until one of the polarization components was blocked during fundamental mode operation.

Fig. 2.9 shows the LI characteristics for four different devices taken at room temperature. The fundamental mode regime occurs for current values between 6 and 10 mA, approximately. The commonly observed behaviors as the current is increased are *i)* the dominance of one of the linear polarization components as the current is increased (Fig. 2.9 (a) and (b)), and *ii)* polarization switching (Fig. 2.9 (c)). For a few number of devices it was impossible to fully block one of the polarization components (Fig. 2.9 (d)) which indicates that, for these VCSELs, emission is not perfectly linearly polarized — e.g., one possibility is elliptically polarized emission [82] as a consequence of the misalignment between linear dichroism and linear birefringence axes [75, 129, 130] —.

For injection currents above the fundamental mode regime, polarization instabilities are commonly associated with the onset of higher-order modes. For the devices in Fig. 2.9 (a) and (b), the first-order transverse mode starts lasing with linear polarization perpendicular to that of the fundamental mode at roughly 10 and 15 mA, respectively. This polarization behavior has been widely reported [47, 60, 80, 83]. For the other two cases, the first-order transverse mode has the same polarization than the fundamental one. In the latter devices, Fig. 2.9 (c) and (d), abrupt drops of the dominant polarization component are observed for increasing current which are associated with the onset of higher order modes having the orthogonal polarization. These features were verified visually by looking at the expanded far field transverse profile of the laser beam using an infrared card as a detector.

The linearly polarized modes of the VCSEL also have different frequencies as a

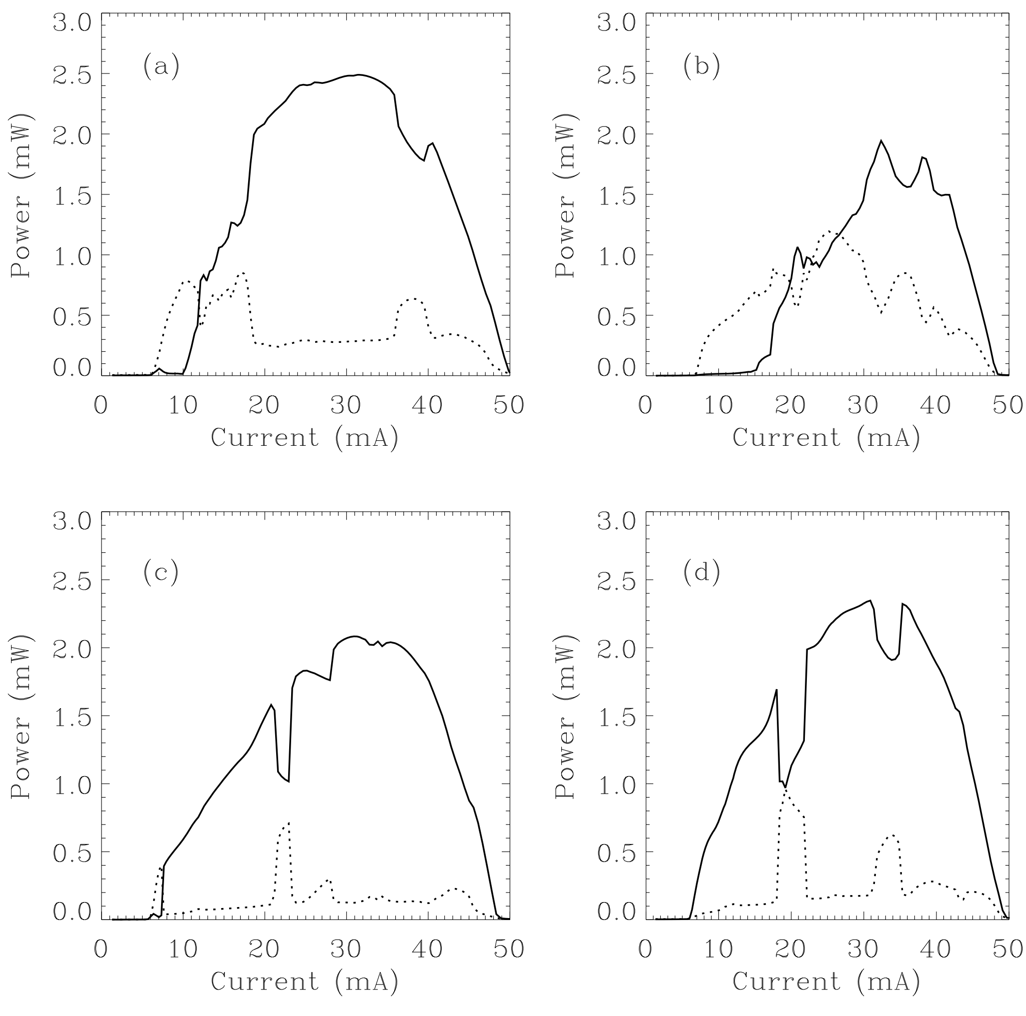

Figure 2.9: polarized LI characteristics for four different 15 μm diameter VCSELs. Solid (dashed) line stands for $\hat{x}$ ($\hat{y}$) polarization. The polarization angles for the $\hat{x}$ component are (a) -13^o, (b) -1 ^{o}, (c) 1^o, and (d) -3 ^{o}.

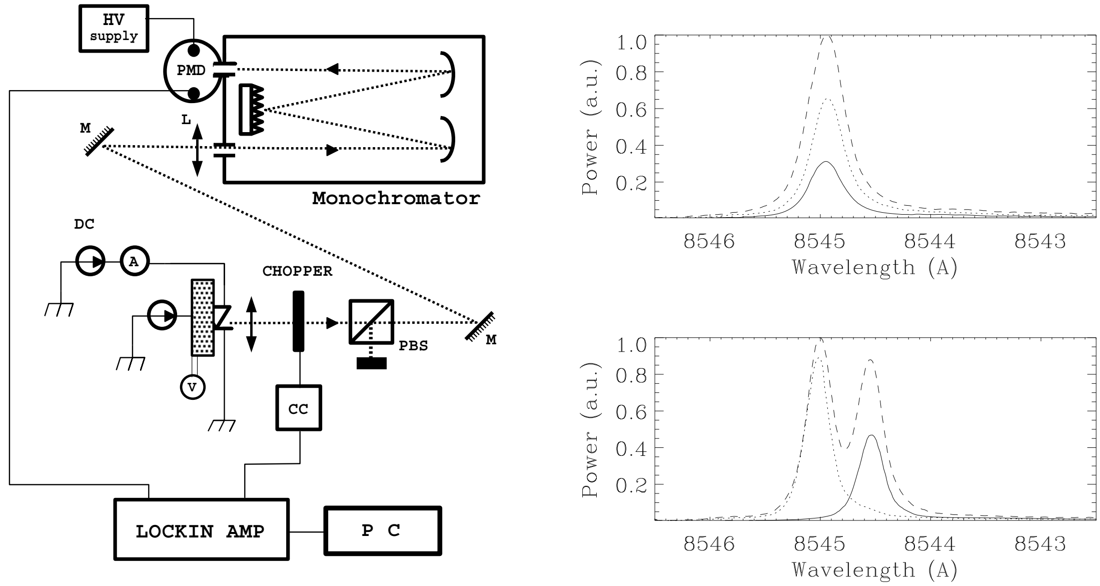

Figure 2.10: (left) Setup for birefringence measurements. For some devices the birefringence-induce splitting was in the range from 0.4 to 0.7 $\mathring{A}$ (right,below), while for the rest the splitting was unresolved (right,above). Solid (dotted) line stands for $\hat{x}$ ($\hat{y}$) polarization, while the dashed line corresponds to the total optical spectrum.

consequence of the birefringence of the crystal [49]. The frequency splitting between these orthogonally polarized components of the VCSEL output was measured with a high resolution monochromator using the setup of Fig. 2.10 (left). Birefringence measurements were performed at room temperature for the 15 μm active region diameter devices for a fixed current value slightly below the lasing threshold. For many VCSELs, as shown in Fig. 2.10 (right,above)), the spectral splitting was below the spectral resolution (< 0.02 nm). However, when resolved, it was in the range from 0.4 to 0.7 $\mathring{A}$ (15 to 30 GHz). An example is shown in Fig. 2.10 (right,below), which corresponds to the VCSEL of Fig. 2.9(c). Finally, we point out that all the VCSELs exhibiting polarization switching within a given temperature range had a spectral splitting greater than 0.4 $\mathring{A}$.

Chapter 3

Modeling polarization dynamics in Quantum-Well VCSELs

Modeling the dynamics of laser systems is based on the proper description of how the radiation and the gain medium interact with each other within the laser cavity. The most general model for a matter-radiation system is fully quantum-mechanical. However, if quantum-fluctuations are neglected, a semiclassical treatment is possible based on the fact that the number of photons interacting with the gain medium — because of stimulated emission processes — is large. Within this semi-classical framework, the dynamical equation for the optical field vector, $\vec{\mathcal{E}}$, is derived from Maxwell equations taking into account the boundary conditions imposed by the laser cavity. However, the gain medium has to be treated quantum-mechanically.

The simplest quantum-mechanical description for the gain medium is to consider it as a collection of two-level atoms which are perturbed by an external optical field. A density-matrix formalism allows to derive dynamical equations for the nonlinear polarization induced by the optical field, $\vec{\mathcal{P}}$, and the population inversion of the medium, $\mathcal{N}$. These two equations, together with the classical equation for $\vec{\mathcal{E}}$ and supplemented with stochastic noise sources, form a set of nonlinear time-dependent equations, usually referred to as Maxwell-Bloch two-level model [131]-[133], which properly model laser dynamics in systems where optical transitions occur between almost constant energy levels (gas lasers, solid-state lasers, etc.).

However, the quantum-mechanical treatment of light-matter interaction processes in semiconductors is rather more complicated since optical transitions take place between band states with uneven, temperature dependent occupation. Moreover, the band structure and transition probabilities of the semiconductor are affected by many-body effects, such as Coulomb interaction, non-equilibrium distributions, etc. A density-matrix formalism can still be applied giving rise to the semiconductor Bloch equations which describe the material polarization and the population of the electrons and hole states in the bands as a function of the **k**-momentum [134]-[136]. However, their high complexity does not easily allow to study the dynamics of the system, and there is ongoing research towards developing simpler models which incorporate the main results of the microscopic theories in a phenomenological way [137, 138].

Nevertheless, considerable insight on semiconductor laser dynamics can be obtained if one assumes that most of the electronic transitions within the active layer take place between fix energy levels at the band edge. It is with this spirit that we will consider here, in first approximation, a two-level approach for the semiconductor quantum-well medium. Therefore, the scope of this Chapter is to derive dynamical equations for the laser variables in the case of an unstrained quantum-well, gain-guided VCSEL in the framework of a two-level Maxwell-Bloch formalism.

3.1 Dynamical equation for the optical field vector

In order to describe the light-matter interaction processes which occur in a Vertical-Cavity Surface-Emitting Laser, we start our discussion from the well known Maxwell's equations [139]:

$$\begin{aligned}
\nabla\times\vec{\mathcal{E}} &= -\partial_t\vec{\mathcal{B}}\,, && (3.1)\\
\nabla\times\vec{\mathcal{H}} &= \vec{\mathcal{J}}+\partial_t\vec{\mathcal{D}}\,, && (3.2)\\
\vec{\nabla}\,\vec{\mathcal{D}} &= \rho\,, && (3.3)\\
\vec{\nabla}\,\vec{\mathcal{B}} &= 0\,, && (3.4)
\end{aligned}$$

where $\vec{\mathcal{E}}$ and $\vec{\mathcal{H}}$ are the electric and magnetic field vectors, respectively, $\vec{\mathcal{D}}$ and $\vec{\mathcal{B}}$ are the corresponding electric and magnetic flux density vectors, ρ is the free-charge density, and $\vec{\mathcal{J}}$ is the free-current density vector. Eqs. (3.1)–(3.4) can be written in the frequency domain by using the Fourier transformation $F_\omega=\int_{-\infty}^{\infty}dt\ \mathrm{e}^{-\mathrm{i}\,\omega t}F(t)$ as[1]

$$\begin{aligned}
\nabla\times\vec{\mathcal{E}}_\omega &= -\mathrm{i}\,\omega\vec{\mathcal{B}}_\omega\,, && (3.5)\\
\nabla\times\vec{\mathcal{H}}_\omega &= \vec{\mathcal{J}}_\omega+\mathrm{i}\,\omega\vec{\mathcal{D}}_\omega\,, && (3.6)\\
\vec{\nabla}\,\vec{\mathcal{D}}_\omega &= 0\,, && (3.7)\\
\vec{\nabla}\,\vec{\mathcal{B}}_\omega &= 0\,, && (3.8)
\end{aligned}$$

where we have considered that $\rho_\omega\sim 0$ at optical frequencies.

The relationships between the field and flux density electromagnetic vectors strongly depend on the medium under consideration. Semiconductors are dielectric, non-magnetic media which obey Ohm's law. These characteristics can be written down as

$$\begin{aligned}
\vec{\mathcal{D}}_\omega &= \epsilon_o\vec{\mathcal{E}}_\omega+\vec{\mathcal{P}}_\omega\,, && (3.9)\\
\vec{\mathcal{B}}_\omega &= \mu_o\vec{\mathcal{H}}_\omega\,, && (3.10)\\
\vec{\mathcal{J}}_\omega &= \sigma_\omega\vec{\mathcal{E}}_\omega\,, && (3.11)
\end{aligned}$$

where ϵ_o is the vacuum permittivity, μ_o is the vacuum permeability, and σ_ω is, under isotropic conditions, a scalar conductivity. The material polarization $\vec{\mathcal{P}}_\omega$ is the induced dipole-moment density of the material having two contributions, a linear ($\vec{\mathcal{P}}^\ell$) and a nonlinear ($\vec{\mathcal{P}}^{\mathbf{n}\ell}_\omega$) terms

$$\vec{\mathcal{P}}_\omega = \vec{\mathcal{P}}^\ell+\vec{\mathcal{P}}^{\mathbf{n}\ell}_\omega\,. \qquad (3.12)$$

The linear polarization takes into account the dielectric nature of the unpumped semiconductor medium, and can be written in terms of a linear susceptibility χ^ℓ as

$$\vec{\mathcal{P}}^\ell=\epsilon_o\chi^\ell\vec{\mathcal{E}}_\omega\,, \qquad (3.13)$$

which is related to the background refractive index of the semiconductor, $n^2=1+\chi^\ell$.

[1]Notice that we use the $exp(+\mathrm{i}\,\omega t)$ basis.

The nonlinear part of the polarization accounts for the dipole-moment density induced by the optical field when the semiconductor is pumped. As for the linear part, it can be related to the optical field perturbing the medium as

$$\vec{\mathcal{P}}_\omega^{\mathbf{n}\ell} = \epsilon_o \chi_\omega^{\mathbf{n}\ell}(\mathcal{N})\vec{\mathcal{E}}_\omega \; , \tag{3.14}$$

where $\chi_\omega^{\mathbf{n}\ell}$ is a scalar nonlinear susceptibility which locally depends on the carrier density $\mathcal{N}$, and that takes into account both absorption/gain and dispersion in the semiconductor medium.

The wave equation for the evolution of the optical field $\vec{\mathcal{E}}_\omega$ is derived by applying the operator $\nabla\times$ to Eq. (3.5), using Eq. (3.6), the definitions given by Eqs. (3.9)–(3.14), and the general identity $\nabla\times(\nabla\times\vec{\mathcal{E}}_\omega) = \vec{\nabla}\,(\vec{\nabla}\,\vec{\mathcal{E}}_\omega) - \nabla^2\,\vec{\mathcal{E}}_\omega$. The evolution equation reads

$$\vec{\nabla}\,(\vec{\nabla}\,\vec{\mathcal{E}}_\omega) - \nabla^2\,\vec{\mathcal{E}}_\omega = \frac{\omega^2}{c^2}n^2(z)\vec{\mathcal{E}}_\omega - \mathrm{i}\,\frac{\omega\sigma_\omega}{\epsilon_o c^2}\vec{\mathcal{E}}_\omega + \frac{\omega^2}{c^2}\chi_\omega^{\mathbf{n}\ell}\vec{\mathcal{E}}_\omega \; , \tag{3.15}$$

where $c{=}1/\sqrt{\epsilon_o\mu_o}$ is the velocity of light in vacuum. The z-dependence of the refractive index in the first term of the right hand side (RHS) takes into account the refractive index distribution along the emission direction of the VCSEL (see Fig. 3.1(b)). The conductivity in the second term of the RHS takes into account internal loss mechanisms, e.g., scattering losses, which reduce the number of photons propagating back and forth within the laser cavity. The last term on the RHS takes into account the interaction of the optical field with the externally pumped medium through the nonlinear susceptibility $\chi_\omega^{\mathbf{n}\ell}(\mathcal{N})$.

In Chap. 1 we have seen that gain-guided VCSELs use a proton-implanted region in order to confine the injected carriers into a finite transverse region within the quantum-well layer. Therefore, the carrier density is not uniform in the plane of the quantum-well, $\mathcal{N}(x,y)$, so the optical field is also non uniform. Such a broken transverse invariance of the pumped VCSEL implies the condition $\vec{\nabla}\cdot\vec{\mathcal{E}}_\omega \neq 0$.

$\vec{\nabla}\cdot\vec{\mathcal{E}}_\omega$ can be evaluated taking into account Eq. (3.7) and the definitions given by Eqs. (3.9)-(3.14),

$$\vec{\nabla}\cdot\vec{\mathcal{E}}_\omega \;=\; -\vec{\mathcal{E}}_\omega\cdot\vec{\nabla}\,\left[\ell n\left(n^2(z)+\chi_\omega^{\mathbf{n}\ell}(x,y,z)\right)\right] \approx -\frac{\vec{\mathcal{E}}_\omega}{n^2(z)}\left[\,d_z\,n^2(z)\vec{z}\,\right] \; , \tag{3.16}$$

where we have taken into account that, for gain-guided VCSELs, the value of $\chi_\omega^{\mathbf{n}\ell}(x,y,z)$ is very small as compared with the value of $n(z)$, and that $\chi_\omega^{\mathbf{n}\ell}(x,y,z)$ varies in length scales ($\sim$ proton implanted region) much larger than those for $n(z)$ ($\sim$ quantum-well width). Eq. (3.16) admits solutions

$$\vec{\mathcal{E}}_\omega(x,y,z) = \mathcal{A}(z)\mathcal{E}_\omega(x,y)\;\vec{a_\perp} \; , \tag{3.17}$$

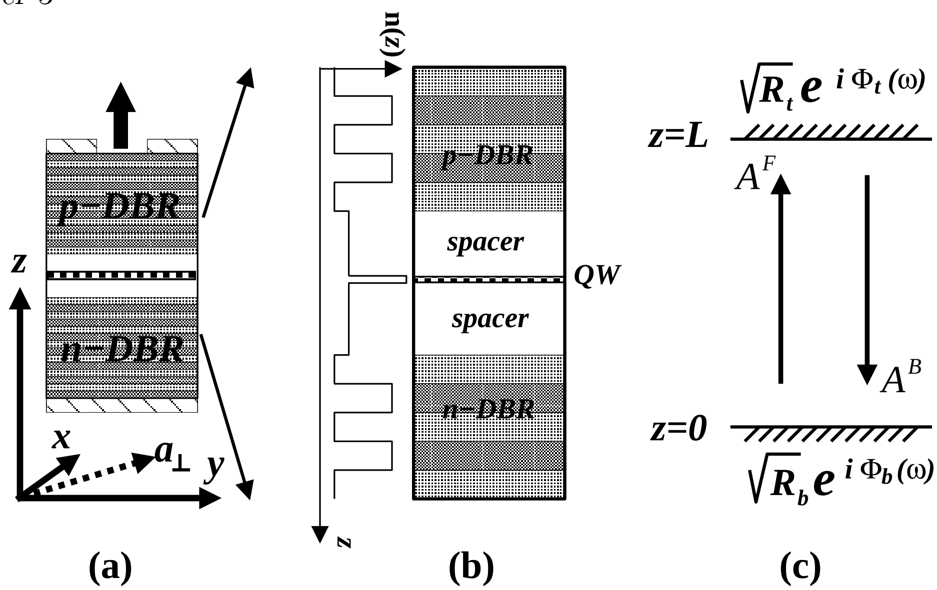

Figure 3.1: (a) VCSEL geometry, (b) Expanded region showing the longitudinal distribution of refractive index, (c) Schematic representation of the forward and backward plane-waves in the equivalent VCSEL cavity.

for which $\vec{\nabla}\cdot\vec{\mathcal{E}}_\omega \approx 0$, where $\vec{a_\perp}$ is an arbitrary vector in the plane of the quantum-well layer, which is perpendicular to the emission direction $\vec{z}$ ($\vec{a_\perp}\cdot\vec{z} = 0$), as schematically depicted in Fig. 3.1(a). Eq. (3.17) represents the family of linearly polarized modes of the VCSEL. The propagation equation for these modes is the scalar equation

$$\mathcal{E}_\omega d_z^2\,\mathcal{A} + \mathcal{A}\nabla_\perp^2\mathcal{E}_\omega + \frac{\omega^2}{c^2}n^2(z)\mathcal{A}\mathcal{E}_\omega - \mathrm{i}\,\frac{\omega\sigma_\omega}{\epsilon_o c^2}\mathcal{A}\mathcal{E}_\omega + \frac{\omega^2}{c^2}\chi_\omega^{\mathbf{n}\ell}\mathcal{A}\mathcal{E}_\omega = 0\,, \tag{3.18}$$

where $\mathcal{A}(z)$ and $\mathcal{E}_\omega(x,y)$ are the longitudinal and transverse components of the optical field, respectively.

In order to solve Eq. (3.18), the boundary conditions imposed by the cavity have to be considered. Fig. 3.1(b) shows the vertical cross section of the VCSEL which looks like a Fabry-Perot type laser of cavity length[2] L, and top and bottom distributed Bragg reflectors [3]. For practical purposes — we want to develop a mean-field dynamical model for $\mathcal{E}_\omega$, disregarding the propagation problem of the optical field along the emission direction — it is convenient to define an equivalent Fabry-Perot cavity for the VCSEL where the DBR reflectors are treated as effective plane mirrors [140] with complex top and bottom mirror reflectivities [4] given by $\sqrt{R_t}e^{\mathrm{i}\,\Phi_t(\omega)}$ and $\sqrt{R_b}e^{\mathrm{i}\,\Phi_b(\omega)}$,

[2] $L = L_{qw} + 2L_{sp}$, where L_{qw} is the quantum-well length, and L_{sp} is the spacer layer length.

[3] Each DBR layer width is $\lambda/4$, where λ is the Bragg wavelength, which is close to the VCSEL emission wavelength.

[4] Each DBR exhibits a complicated reflectivity spectrum but we approximate the complex top and bottom mirror reflectivities in the vicinity of the VCSEL emission wavelength by a constant reflectivity modulus, R_i ($\approx 99.99\%$), and a frequency dependent phase, $\Phi_i(\omega)$, which vanishes at the Bragg frequency [140].

respectively, and $n(z)$ is substituted by an effective refractive index [5], $n_e(\omega)$.

For the equivalent VCSEL cavity, $\mathcal{A}(z)$ can be generally written in terms of a forward ($\mathcal{A}^{\mathcal{F}}$) and a backward ($\mathcal{A}^{\mathcal{B}}$) plane-wave as

$$\mathcal{A}(z) = \mathcal{A}^{\mathcal{F}}\, \mathrm{e}^{\mathrm{i}\, q_w z} + \mathcal{A}^{\mathcal{B}}\, \mathrm{e}^{-\mathrm{i}\, q_w z} \;, \tag{3.19}$$

where q_w is a complex propagation constant. $\mathcal{A}(z)$ verifies the eigenvalue equation

$$\left[d_z^2 + q_w^2\right] \mathcal{A}(z) = 0 \;, \tag{3.20}$$

and the boundary conditions imposed by the equivalent VCSEL cavity

$$\begin{cases} \mathcal{A}^{\mathcal{F}} = \sqrt{R_b}\, \mathrm{e}^{\mathrm{i}\,\Phi_b(\omega)} \mathcal{A}^{\mathcal{B}} & \text{at } z = 0 \;, \\ \sqrt{R_t}\, \mathrm{e}^{\mathrm{i}\,\Phi_t(\omega)} \mathcal{A}^{\mathcal{F}}\, \mathrm{e}^{\mathrm{i}\, q_w L} = \mathcal{A}^{\mathcal{B}}\, \mathrm{e}^{-\mathrm{i}\, q_w L} & \text{at } z = L \;, \end{cases} \tag{3.21}$$

which can be rewritten as

$$\sqrt{R_t R_b}\, \mathrm{e}^{\mathrm{i}\,(2 q_w L + \Phi_t(\omega) + \Phi_b(\omega))} = 1 \;. \tag{3.22}$$

From Eq. (3.22), the allowed propagation constants are given by

$$q_{mw} = q_{mw}^r + \mathrm{i}\, q_{mw}^i = \frac{m\pi}{L_e(\omega)} - \mathrm{i}\, \frac{1}{2L} ln \left(\frac{1}{\sqrt{R_t R_b}} \right) \;, \tag{3.23}$$

where m is an integer number, and L_e is the effective cavity length defined as

$$L_e(\omega) = L + 2L_{pen}(\omega) = \frac{m\pi}{m\pi - (\Phi_t(\omega) + \Phi_b(\omega)/2)} L \;, \tag{3.24}$$

and L_{pen} is the averaged penetration depth in each DBR, which arises from the frequency dependence of the phase of the DBR reflectivity.

Therefore, the real part of the propagation constant, q_{mw}^r, shows that the longitudinal modes of the VCSEL are those whose wavelength is an integer submultiple of $2L_e$, and the imaginary part, q_{mw}^i, accounts for the distributed mirror losses in the Fabry-Perot cavity. It is worth noting that the propagation constants given by Eq. (3.23) correspond to the empty-cavity modes since they are modified when the VCSEL is pumped. However, they will be useful in the derivation.

Inserting Eq. (3.20) into Eq. (3.18), we obtain

$$\mathcal{A} \nabla_\perp^2 \mathcal{E}_\omega + \left(\beta_\omega^2 - q_{mw}^2\right) \mathcal{A}\mathcal{E}_\omega - \mathrm{i}\, \frac{\omega \sigma_\omega}{\epsilon_o c^2} \mathcal{A}\mathcal{E}_\omega + \frac{\omega^2}{c^2} \chi_\omega^{\mathbf{n}\ell} \mathcal{A}\mathcal{E}_\omega = 0 \;, \tag{3.25}$$

[5] We consider that the presence of the quantum-well in the spacer layer will not affect the field pattern $\mathcal{A}(z)$ because of its very small thickness.

where $\beta_\omega = \frac{\omega}{c} n_e$ is the real propagation constant of the longitudinal mode at which the VCSEL is designed for operation.

Multiplying Eq. (3.25) by $\mathcal{A}^*(z)$, and integrating along the z-direction, $(\int_0^L dz\,)$, we end up with the eigenvalue equation for the transverse component of the optical field, $\mathcal{E}_\omega(x, y)$, which reads

$$\nabla_\perp^2 \mathcal{E}_\omega + \left(\beta_\omega^2 - q_{mw}^2\right) \mathcal{E}_\omega - \mathrm{i}\, \frac{\omega \overline{\sigma_\omega}}{\epsilon_o c^2} \mathcal{E}_\omega + \frac{\omega^2}{c^2} \chi_\omega^{\mathbf{n}\ell} \Gamma_z \mathcal{E}_\omega = 0 \;, \tag{3.26}$$

where

$$\overline{\sigma_\omega} = \frac{\int_0^L dz\, \mathcal{A}^* \sigma_\omega \mathcal{A}}{\int_0^L dz\, |\mathcal{A}|^2} \;, \tag{3.27}$$

is the average (mean) conductivity along the z-direction, and

$$\Gamma_z = \frac{\int_{qw} dz\, |\mathcal{A}|^2}{\int_0^L dz\, |\mathcal{A}|^2} \;, \tag{3.28}$$

is the gain confinement factor, which arises because $\chi_\omega^{\mathbf{n}\ell}$ is only created within the quantum-well region of the VCSEL

$$\chi_\omega^{\mathbf{n}\ell}(x, y, z) = \begin{cases} 0 & \text{outside the quantum-well ,} \\ \chi_\omega^{\mathbf{n}\ell}(x, y) & \text{within the quantum-well .} \end{cases} \tag{3.29}$$

Next, we perform the Slowly Varying Amplitude Approximation to Eq. (3.26). For this reason, let's consider the empty cavity mode, m_o, closer to the VCSEL emission wavelength, λ, and let Ω be the carrier frequency corresponding to this mode, such that

$$\beta_\Omega = \frac{\Omega}{c} n_e = \frac{m_o \pi}{L_e(\Omega)} = q_{m_o\Omega}^r \;. \tag{3.30}$$

Developing β_ω^2 in Taylor series around Ω, we obtain

$$\beta_\omega^2 = \beta_\Omega^2 + 2\beta_\Omega \beta\,'_\Omega (\omega - \Omega) + O^2(\omega - \Omega) \approx \beta_\Omega^2 + 2\beta_\Omega \beta\,'_\Omega (\omega - \Omega) \;, \tag{3.31}$$

where $\beta\,'_\Omega = \frac{d\beta_\omega}{dw}|_{\omega=\Omega} = n_g/c$, and $n_g = n_e + \Omega \frac{dn_e}{dw}|_{\omega=\Omega}$ is the group index of the longitudinal mode considered. Hence, the propagation equation for the transverse component of the optical field of the m_o mode becomes

$$\nabla_\perp^2 \mathcal{E}_\omega + 2\beta_\Omega \beta\,'_\Omega (\omega - \Omega)\mathcal{E}_\omega + (\beta_\Omega^2 - q^2_{m_o\Omega})\mathcal{E}_\omega - \mathrm{i}\,\frac{\Omega\overline{\sigma_\Omega}}{\epsilon_o c^2}\mathcal{E}_\omega + \frac{\Omega^2\Gamma_z}{\epsilon_o c^2}\mathcal{P}^{n\ell}_\omega = 0\;, \quad (3.32)$$

where we have used the definition in Eq. (3.14). Taking into account Eqs. (3.23) and (3.30), we can approximate the third term of the left hand side of Eq. (3.32) as

$$(\beta_\Omega^2 - q^2_{m_o\Omega})\mathcal{E}_\omega = (\beta_\Omega + q_{m_o\Omega})(\beta_\Omega - q_{m_o\Omega})\mathcal{E}_\omega \approx \mathrm{i}\,2\beta_\Omega q^i_{m_o\Omega}\mathcal{E}_\omega\;, \quad (3.33)$$

where we have assumed that $q^r_{m\Omega} \gg q^i_{m\Omega}$. Defining

$$\sigma_T = \overline{\sigma_\Omega} + \frac{\epsilon_o c n_e}{2L} ln\left(\frac{1}{R_t R_b}\right)\;, \quad (3.34)$$

as the total conductivity, and $\nu = \omega - \Omega$ as a slow frequency around Ω, Eq. (3.32) now reads

$$\nabla_\perp^2 \mathcal{E}_\nu + 2\beta_\Omega \beta\,'_\Omega \nu \mathcal{E}_\nu - \mathrm{i}\,\frac{\Omega\sigma_T}{\epsilon_o c^2}\mathcal{E}_\nu + \frac{\Omega^2\Gamma_z}{\epsilon_o c^2}\mathcal{P}^{\mathbf{n}\ell}_\nu = 0\;. \quad (3.35)$$

Rewriting Eq. (3.35) in the time domain ($\mathrm{i}\,\nu \longrightarrow \partial_t$, $\mathcal{E}_\nu \to \mathcal{E}$, $\mathcal{P}^{\mathbf{n}\ell}_\nu \to \mathcal{P}$) and using the definitions for β_Ω and $\beta\,'_\Omega$, we end up with

$$\partial_t \mathcal{E} = -\kappa\mathcal{E} - \mathrm{i}\,\frac{c^2}{2\,\Omega n_e n_g}\nabla_\perp^2\mathcal{E} - \mathrm{i}\,\frac{\Omega\Gamma_z}{2\epsilon_o n_e n_g}\mathcal{P}\;, \quad (3.36)$$

where we have defined the optical field decay rate, κ, as [6]

$$\kappa = \frac{\sigma_T}{2\epsilon_o n_e n_g} = \frac{c}{2n_g}\left[\alpha_{in} + \frac{1}{2L} ln\left(\frac{1}{R_t R_b}\right)\right]\;, \quad (3.37)$$

with $\alpha_{in} = \overline{\sigma_\Omega}/(\epsilon_o c n_e)$ being the internal losses.

The first term on the RHS of Eq. (3.36) accounts for the optical field losses inside the cavity. The second term on the RHS accounts for optical field diffraction which leads to the selection of the transverse mode profiles and the associated frequencies. The last term in Eq. (3.36) is responsible for the material gain (real part) and the dispersion (imaginary part). We point out that, since the time scale of the evolution of the fields $\mathcal{E}(x,y)$ and $\mathcal{P}(x,y)$ is much slower than Ω^{-1}, these magnitudes correspond to the slowly-varying amplitudes of the optical field and the nonlinear polarization, respectively.

At this point we have to take into account that light emitted from VCSELs is, typically, linearly polarized with the vector field oriented along one of two orthogonal

[6] 2κ is the inverse of the photon lifetime in the cavity, $\tau_{ph} = (2\kappa)^{-1} \sim 1$ ps

crystal axis, which are both perpendicular to the emission direction $\vec{z}$. Let us define these directions in terms of two arbitrary orthogonal vectors, $\vec{x}$ and $\vec{y}$, which lie in the quantum-well plane. Eq. (3.36) becomes

$$\partial_t \mathcal{E}_i = -\kappa \mathcal{E}_i - \mathrm{i}\,\frac{c^2}{2\,\Omega n_e n_g} \nabla_\perp^2 \mathcal{E}_i - \mathrm{i}\,\frac{\Omega \Gamma_z}{2\epsilon_o n_e n_g} \mathcal{P}_i, \qquad i = x, y\ , \tag{3.38}$$

and the vector character of the optical field, as pointed out in Eq. (3.17), is finally recovered: $\vec{\mathcal{E}} = \mathcal{E}_x \vec{x} + \mathcal{E}_y \vec{y}$. For what follows, it is convenient to rewrite Eq. (3.38) in the basis of circularly polarized field components ($\mathcal{E}_\pm = (\mathcal{E}_x \pm \mathrm{i}\,\mathcal{E}_y)/\sqrt{2}$, and $\mathcal{P}_\pm = (\mathcal{P}_x \pm \mathrm{i}\,\mathcal{P}_y)/\sqrt{2}$), as

$$\partial_t \mathcal{E}_\pm = -\kappa \mathcal{E}_\pm - \mathrm{i}\,\frac{c^2}{2\,\Omega n_e n_g} \nabla_\perp^2 \mathcal{E}_\pm - \mathrm{i}\,\frac{\Omega \Gamma_z}{2\epsilon_o n_e n_g} \mathcal{P}_\pm\ , \tag{3.39}$$

3.2 Dynamical equations for the density-matrix elements in unstrained quantum-well media

The polarization state of laser light originates in the spin sublevels of the transitions involved in the lasing process. Different polarization states have been associated to different $J_1 \to J_2$ transitions in atomic systems, where J_i refers to the total angular momentum quantum number of the two atomic energy levels involved in the interaction with the optical field [103]-[110].

For semiconductors, the situations is rather more complicated. Semiconductor bands cannot be described "completely" by atomic symmetry properties since the atomic orbitals are coupled in the solid. However, for semiconductors with cubic symmetry, such as GaAs, it is possible to assign quantum numbers for the electron states at the band edge ($\mathbf{k}$=0) using the *tight-binding* approximation [134], this is, by relating the crystal states of a given symmetry to the the atomic states of the same symmetry.

In the element semiconductors of group IV, and also in the isoelectronic compound semiconductors of the groups III-V and II-IV, the valence band states at $\mathbf{k}$=0 are made up of three degenerate p-like states, while the conduction band consists of an s-like state. In an isolated atom, electron states from an s-type orbital have $J = \frac{1}{2}$, while electron states from p-type orbitals may have $J = \frac{3}{2}$ or $J = \frac{1}{2}$, where we have already considered that due to spin-orbit coupling the relevant quantum number of the electron states is the total angular momentum J. Therefore, the conduction band at the band edge has symmetry isomorphous to $J = \frac{1}{2}$ states, while the energy degenerate heavy-hole and light-hole valence bands have symmetry isomorphous to $J = \frac{3}{2}$ [141]. Due to spin-orbit interaction, the split-off valence band ($J = \frac{1}{2}$) is usually energetically well separated from the $J = \frac{3}{2}$ valence band near the band-edge (tenths of eV) so it will not be consider any further.

With these considerations, the energy band structure of III-V bulk semiconductor media can be calculated around the band-edge using the Luttinger Hamiltonian and

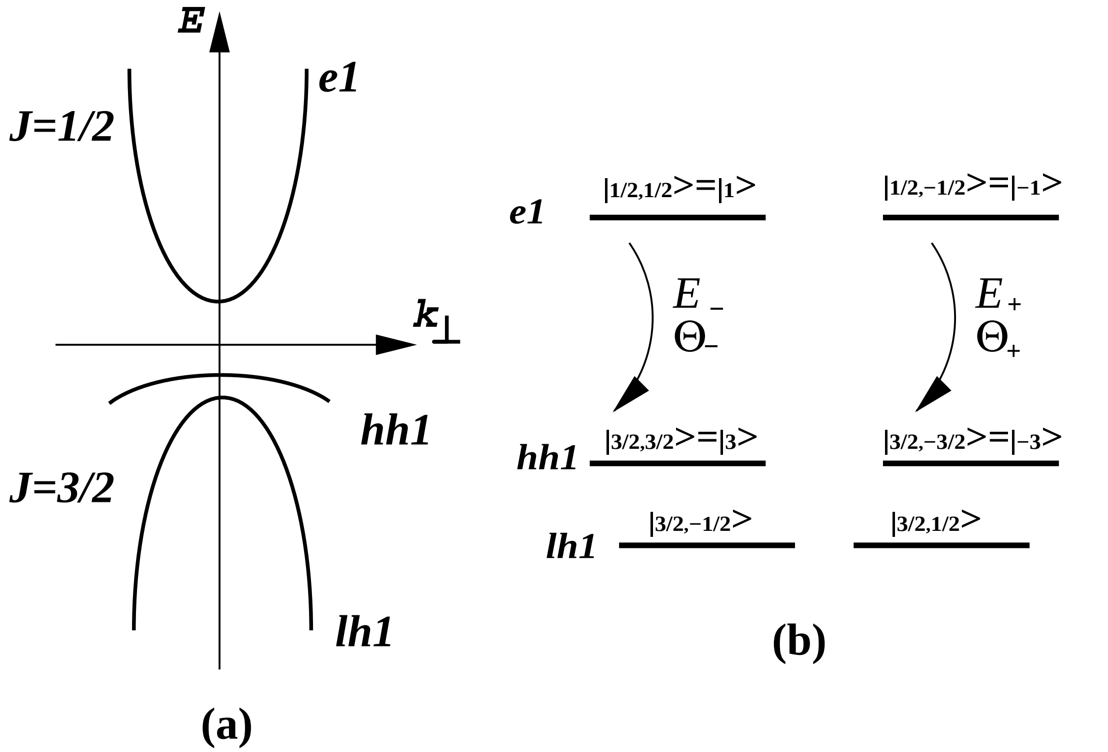

Figure 3.2: (a) Band structure of a III-V unstrained quantum-well semiconductor for the first allowed subbands. Here $\mathbf{k}_\perp$ is the modulus of the momentum vector orthogonal to $\mathbf{k}_z$; (b) Equivalent six-level model at the band-edge. States are labeled according to the quantum numbers $|J, J_z>$. For quantum-well VCSELs it is sufficient to take into account $e1$-$hh1$ transitions giving rise to the four-level system considered in the SFM model.

$\mathbf{k}\cdot\mathbf{p}$ theory [134, 135]. The heavy-hole (hh) and light-hole (lh) bands result degenerated at the band-edge, although this degeneracy is lifted for $\mathbf{k}\neq 0$ values due to the different effective hole masses.

The same formalism can be applied in III-V quantum-well semiconductors. In these structures, due to the carrier confinement along the quantization z-direction, k_z can only take finite values so the energy is quantized. However, for each allowed k_z value, energy subbands result due to the free motion in the $x-y$ plane ($e1$, $e2$, ..; $hh1$, $hh2$, ...; $lh1$, $lh2$, ...). In unstrained, narrow (<8 nm) quantum-wells, it is sufficient to consider the first conduction ($e1$), heavy-hole ($hh1$) and light-hole ($lh1$) subbands. In this case, it turns out from the band-structure calculation that the energy degeneracy of the $hh1$ and the $lh1$ subbands at the band-edge is removed [7]. In addition, band-mixing effects occur for $\mathbf{k}_\perp \neq 0$ [8].

However, the quantum-well band structure at the band edge ($\mathbf{k}_\perp$=0) reduces to the six-level system shown in Fig. 3.2(b), and can be labeled according to the J_z quantum number in the respective band: conduction subband states have $J_z = \pm\frac{1}{2}$, $hh1$ valence subband states have $J_z = \pm\frac{3}{2}$, and $lh1$ valence subband states have $J_z = \pm\frac{1}{2}$. Such a six-level scheme has been widely used in many theoretical [142]-

[7] Typically, tens of meV

[8] For states with $\mathbf{k}_\perp \neq 0$, J_z is no longer a good quantum number and the band states are a linear combination of states with different J_z (band-mixing).

[144] and experimental [145]-[147] studies of time-resolved luminiscence spectroscopy and photoluminiscence experiments in (001)-grown III-V semiconductor quantum-wells. In these experiments, polarized laser pulses are used to excite and distinguish different spin states of the interband transitions.

The possible optically allowed intraband transitions are those verifying the selection rule for the third component of the total angular momentum, $\Delta J_z = 0, \pm 1$. Transitions with $\Delta J_z = 1$ are associated with right-handed circularly polarized light, $E_+ \vec{a}_+ = E_+(\vec{x} + \mathrm{i}\,\vec{y}\,)/\sqrt{2}$; transitions with $\Delta J_z = -1$ are associated with left-handed circularly polarized light, $E_- \vec{a}_- = E_-(\vec{x} - \mathrm{i}\,\vec{y}\,)/\sqrt{2}$; when the component of the optical field parallel to the quantization direction does not vanish, $E_z \neq 0$, $\Delta J_z = 0$ transitions are also allowed. Since the quantization direction in quantum-well VCSELs coincides with the propagation direction of the optical field, the axial component of the optical field is very small (see Eq. (3.17)), so the most favored optical transitions are those for which $\Delta J_z = \pm 1$.

Therefore, in III-V unstrained quantum-well VCSELs a further simplification of the six-levels scheme is possible in the case of large $hh1$-$lh1$ splitting, since it is sufficient to investigate only the allowed transitions between the $hh1$-valence and the $e1$-conduction subbands [142, 143, 148, 149]. In this situation, the scheme reduces to a four-level system, which is the starting point of the SFM model. It is worth noting that the previous arguments are only valid at the band edge. However, a detailed analysis of band-mixing effects in the SFM model [150] indicates that they do not produce qualitative changes in the results that we will present in the remaining Chapters.

From here on, we use the notation $|\pm 1>$ for the conduction band states with $J_z = \pm\frac{1}{2}$, and $|\pm 3>$ for the $hh1$ band states with $J_z = \pm\frac{3}{2}$ (see Fig. 3.2(b)). Let us apply a matrix-density formalism to the four-level scheme. The time evolution equations of the density-matrix elements of a N energy levels laser are derived in Appendix B, and read

$$\dot{\rho}_{k,l} = \mathrm{i}\ \omega_{k,l}\ \rho_{k,l} - \frac{1}{\mathrm{i}\hbar}\ \vec{\mathbf{E}} \cdot \sum_{j=1}^{N} \left[\rho_{k,j}\ \vec{\Theta}_{j,l} - \rho_{j,l}\ \vec{\Theta}_{k,j}\right] \ , \tag{3.40}$$

where $\omega_{k,l}$ is the frequency difference between the levels k and l, $\vec{\mathbf{E}}$ is the optical field perturbing the medium, $\rho_{k,l} = \rho^*_{l,k}$ are the density-matrix elements, and $\vec{\Theta}_{k,l} = \vec{\Theta}^*_{l,k}$ are the dipole matrix elements [9].

Within the four-level scheme for quantum-well VCSELs, the dipole selection rules depend on the dot product $\vec{\mathbf{E}} \cdot \vec{\Theta}$, where $\vec{\mathbf{E}} = E_+ \vec{a}_+ + E_- \vec{a}_-$. Hence, the non-vanishing dipole elements are

$$\vec{\Theta}_{-1,-3} = \vec{\Theta}^*_{-3,-1} = \Theta^*_+ \vec{a}_+ \ , \tag{3.41}$$

for the σ_+-transition ($|-1> \rightarrow |-3>$), and

[9] See Appendix B for definitions.

$$\vec{\Theta}_{1,3} = \vec{\Theta}_{3,1} = \Theta_-^* \vec{a}_- \ , \tag{3.42}$$

for the σ_--transition ($|+1> \rightarrow |+3>$). In addition, there are 10 independent density-matrix elements whose time evolution equations read

$$
\begin{aligned}
\dot{\rho}_{1,1} &= -\frac{E_-}{\mathrm{i}\,\hbar} \left[\rho_{3,1}^* \,\Theta_- - \rho_{3,1}\,\Theta_-^*\right] = -\dot{\rho}_{3,3} \ , && (3.43)\\
\dot{\rho}_{-1,-1} &= -\frac{E_+}{\mathrm{i}\,\hbar} \left[\rho_{-3,-1}^* \,\Theta_+ - \rho_{-3,-1}\,\Theta_+^*\right] = -\rho_{-3,-3} \ , && (3.44)\\
\dot{\rho}_{3,1} &= -\mathrm{i}\ \omega_g\,\rho_{3,1} + \frac{\rho_{1,1}-\rho_{3,3}}{\mathrm{i}\,\hbar}\,E_-\,\Theta_- \ , && (3.45)\\
\dot{\rho}_{-3,-1} &= -\mathrm{i}\ \omega_g\,\rho_{-3,-1} + \frac{\rho_{-1,-1}-\rho_{-3,-3}}{\mathrm{i}\,\hbar}\,E_+\,\Theta_+ \ , && (3.46)\\
\dot{\rho}_{1,-1} &= -\frac{1}{\mathrm{i}\,\hbar}\left[\rho_{-3,1}^*\ \ E_+\,\Theta_+\ -\rho_{3,-1}\,E_-\,\Theta_-^*\right] \ , && (3.47)\\
\dot{\rho}_{3,-3} &= \frac{1}{\mathrm{i}\,\hbar}\left[\rho_{-3,1}^*\,E_-\,\Theta_-\ -\rho_{3,-1}\,E_+\,\Theta_+^*\right] \ , && (3.48)\\
\dot{\rho}_{3,-1} &= -\mathrm{i}\ \omega_g\,\rho_{3,-1} - \frac{1}{\mathrm{i}\,\hbar}\left[\rho_{3,-3}\,E_+\,\Theta_+\ -\rho_{1,-1}\,E_-\,\Theta_-\right] \ , && (3.49)\\
\dot{\rho}_{-3,1} &= -\mathrm{i}\ \omega_g\,\rho_{-3,1} - \frac{1}{\mathrm{i}\,\hbar}\left[\rho_{3,-3}^*\,E_-\,\Theta_-\ -\rho_{1,-1}^*\,E_+\,\Theta_+\right] \ , && (3.50)
\end{aligned}
$$

where we have taken that $\omega_{3,1} = \omega_{-3,-1} = \omega_{3,-1} = \omega_{-3,1} = -\omega_g$, where ω_g is the frequency difference between the upper and lower levels.

3.3 The semiclassical Four-Level Maxwell-Bloch equations

The diagonal matrix-density terms $\rho_{i,i}$ give the occupation probabilities of the energy levels. The population difference of the $\sigma_\pm$-transitions are defined as $d_\pm = (\rho_{\mp1,\mp1} - \rho_{\mp3,\mp3})$. The elements $\rho_{\mp3,\mp1}$ give the dipole polarization vector $\vec{p} = \hat{p}_+\vec{a}_+ + \hat{p}_-\vec{a}_-$ where we define $\hat{p}_\pm = \rho_{\mp3,\mp1}^*\Theta_\pm$. The rest of density-matrix coherences involved in Eqs. (3.47)-(3.50) are decoupled from $d_\pm$ and $\hat{p}_\pm$, so they will not be considered any further.

From Eqs. (3.43)-(3.46), we derive the evolution equations for the the population difference and dipole polarization variables, which read

$$
\begin{aligned}
\dot{\hat{p}}_\pm &= \mathrm{i}\ \omega_g\,\hat{p}_\pm - \frac{|\Theta_\pm|^2}{\mathrm{i}\,\hbar}\,d_\pm\,E_\pm \ , && (3.51)\\
\dot{d}_\pm &= -\frac{2}{\mathrm{i}\,\hbar}\,E_\pm\,\left[\hat{p}_\pm - \hat{p}_\pm^*\right] \ , && (3.52)
\end{aligned}
$$

Let be $\hat{p}_\pm = p_\pm \, \mathrm{e}^{\mathrm{i}\,\omega_g t}$ and $E_\pm = \mathcal{E}_\pm \, \mathrm{e}^{\mathrm{i}\,\Omega t} + \mathcal{E}^*_\pm \, \mathrm{e}^{-\mathrm{i}\,\Omega t}$, with $p_\pm$ and $\mathcal{E}_\pm$ being the slowly varying amplitudes of the dipole polarization and the optical field, respectively. For these slow variables, Eqs. (3.51)-(3.52) read

$$\dot{p}_\pm \approx -\frac{|\Theta_\pm|^2}{\mathrm{i}\,\hbar} \, d_\pm \, \mathcal{E}_\pm \; \mathrm{e}^{\mathrm{i}\,(\Omega-\omega_g)t} \, , \tag{3.53}$$

$$\dot{d}_\pm \approx \frac{2}{\mathrm{i}\,\hbar} \left[\mathcal{E}_\pm \, p^*_\pm \; \mathrm{e}^{\mathrm{i}\,(\Omega-\omega_g)t} - \mathcal{E}^*_\pm p_\pm \; \mathrm{e}^{-\mathrm{i}\,(\Omega-\omega_g)t} \right] \, , \tag{3.54}$$

where we have disregarded the terms containing $\mathrm{e}^{\pm\mathrm{i}\,2(\Omega+\omega_g)t}$ since they average to zero in the characteristic times for the evolution of the slow variables. This approximation is known as the Rotating Wave Approximation.

For the redefined material variables $\mathcal{P}_\pm(t) = p_\pm(t) \; \mathrm{e}^{-\mathrm{i}\,(\Omega-\omega_g)t}$ and $\mathcal{N}_\pm(t) - \mathcal{N}_0/2 = d_\pm(t)$, where $\mathcal{N}_0$ is the total population difference at transparency, the time evolution equations are

$$\dot{\mathcal{P}}_\pm(t) = -\gamma_\perp \mathcal{P}_\pm(t) + \mathrm{i}\,(\omega_g - \Omega)\mathcal{P}_\pm(t) - \frac{|\Theta_\pm|^2}{\mathrm{i}\,\hbar}(\mathcal{N}_\pm(t) - \mathcal{N}_0/2)\mathcal{E}_\pm(t) \, , \tag{3.55}$$

$$\dot{\mathcal{N}}_\pm(t) = \mathcal{C}/2 - \gamma_e \mathcal{N}_\pm - \gamma_j(\mathcal{N}_\pm - \mathcal{N}_\mp) + \frac{2}{\mathrm{i}\,\hbar}\left[\mathcal{E}_\pm \mathcal{P}^*_\pm - \mathcal{E}^*_\pm \mathcal{P}_\pm \right] \, . \tag{3.56}$$

Some phenomenological terms have been added to Eqs. (3.55) and (3.56). The first term on the RHS of Eq. (3.55) takes into account the relaxation processes suffered by the dipole, where $\gamma_\perp$ is the inverse of the polarization relaxation time $\tau_p \sim$ 50- 100 fs. The first term on the RHS of Eq. (3.56) is the total injection current density necessary for lasing, $\mathcal{C}$. The second term on the RHS of Eq. (3.56) accounts for the spontaneous and non-radiative processes which decrease the number of carriers, where $\gamma_e = \tau_e^{-1} \sim$ 1 ns^{-1} is the carrier decay rate.

The third term on the RHS of Eq. (3.56) takes into account coupling mechanisms between the two emission channels which mix the populations with opposite value of J_z. For our purposes the parameter γ_j can be understood as a phenomenological modeling of a variety of complicated microscopic processes, which are loosely termed spin-flip relaxation processes [151]. Several spin relaxation processes for electrons and holes have been identified in semiconductors [141], e.g., scattering by defects [147, 152], exchange interactions between electrons and holes [153], exciton–exciton exchange interactions [148], etc. From experimental measurements [145]–[148, 146] of spin relaxation times in quantum wells it is known that γ_j^{-1} is of the order of tens of picoseconds. Indirect evidence of the coupling between $\mathcal{N}_+$ and $\mathcal{N}_-$, as implied by spin-flip relaxation processes, might be given by anticorrelations of the two independent polarization components in RIN spectra [154]. More recently, an indirect measurement of γ_j in the context of the predictions of the model developed here has also been reported ($35 < \gamma_j(ns^{-1}) < 75$, [82]).

Equations (3.55) and (3.56) can be generalized considering the transverse dependence of $\mathcal{P}_\pm$ and $\mathcal{N}_\pm$ by including transverse carrier diffusion, with $\mathcal{D}$ being the diffusion constant. These generalized equations, supplemented by Eq. (3.39) for the optical field, become the whole set of Maxwell-Bloch equations describing laser action in the quantum-well VCSEL

$$
\begin{aligned}
\partial_t \mathcal{E}_\pm &= -\kappa \mathcal{E}_\pm - \mathrm{i}\,\frac{c^2}{2\,\Omega n_e n_g}\nabla_\perp^2 \mathcal{E}_\pm - \mathrm{i}\,\frac{\Omega\Gamma_z}{2\epsilon_o n_e n_g}\mathcal{P}_\pm\,, && (3.57)\\
\partial_t \mathcal{P}_\pm &= -\gamma_\perp[1-\mathrm{i}\,\theta]\,\mathcal{P}_\pm - \frac{|\Theta_\pm|^2}{\mathrm{i}\,\hbar}(\mathcal{N}_\pm - \mathcal{N}_0/2)\mathcal{E}_\pm\,, && (3.58)\\
\partial_t \mathcal{N}_\pm &= \mathcal{C}(x,y)/2 - \gamma_e \mathcal{N}_\pm - \gamma_j(\mathcal{N}_\pm - \mathcal{N}_\mp) + \mathcal{D}\nabla_\perp^2 \mathcal{N}_\pm \\
&\quad + \frac{2}{\mathrm{i}\,\hbar}\left[\mathcal{E}_\pm \mathcal{P}_\pm^* - \mathcal{E}_\pm^* \mathcal{P}_\pm\right]\,, && (3.59)
\end{aligned}
$$

where we have defined the normalized detuning as $\theta = (\omega_g - \Omega)/\gamma_\perp$. As we will show in the next section, the detuning parameter plays the role of the semiconductor α-factor [101] within the four-level model.

The frequency reference frame of the laser can be changed to one where the laser emission frequency is close to zero at threshold. The change of the reference frequency frame can be accomplished by defining

$$
\mathcal{E}_\pm(x,y;t) = \hat{\mathcal{E}}_\pm(x,y;t)e^{\mathrm{i}\,(\kappa\theta)t}\,, \qquad \mathcal{P}_\pm(x,y;t) = \hat{\mathcal{P}}_\pm(x,y;t)e^{\mathrm{i}\,(\kappa\theta)t}\,.
$$

In addition, it is useful to rescale the optical field variables to be proportional to the total photon number, $\#_{ph}$, which is given by the ratio of the total electromagnetic energy in the medium and the photon energy at frequency Ω

$$
\#_{ph} = \frac{2\epsilon_o {n_e}^2}{\hbar\Omega}\int_{-\infty}^{\infty} dx \int_{-\infty}^{\infty} dy\,|\hat{\mathcal{E}}_\pm(x,y)|^2\,.
$$

Therefore, defining the rescaled variables

$$
E_\pm = \sqrt{\frac{2n_g}{\Gamma_z n_e}}\sqrt{\frac{2\,\epsilon_o {n_e}^2}{\hbar\Omega}}\hat{\mathcal{E}}_\pm\,, \qquad P_\pm = -\mathrm{i}\sqrt{\frac{\Omega\Gamma_z}{\hbar\epsilon_o n_e n_g}}\hat{\mathcal{P}}_\pm\,,
$$

and

$$
N = \mathcal{N}_+ + \mathcal{N}_-\,, \qquad n = \mathcal{N}_+ - \mathcal{N}_-\,, \qquad N_0 = \mathcal{N}_0\,,
$$

the model can be finally written as

$$
\begin{aligned}
\partial_t E_\pm(x,y;t) &= -\kappa(1+\mathrm{i}\,\theta)E_\pm - \mathrm{i}\,\frac{c^2}{2\Omega n_e n_g}\nabla_\perp^2 E_\pm + P_\pm\,, && (3.60)\\
\partial_t P_\pm(x,y;t) &= -\gamma_\perp(1-\mathrm{i}\,\theta)P_\pm + \gamma_\perp a(1+\theta^2)(N - N_0 \pm n)E_\pm \\
&\quad + \sqrt{\beta(N\pm n)}\psi_\pm(x,y;t)\,, && (3.61)\\
\partial_t N(x,y;t) &= C(x,y) - \gamma_e N + \mathcal{D}\nabla_\perp^2 N \\
&\quad - \left[(E_+P_+^* + E_-P_-^*) + (c.c.)\right]\,, && (3.62)\\
\partial_t n(x,y;t) &= -\gamma_s n + \mathcal{D}\nabla_\perp^2 n - \left[(E_+P_+^* - E_-P_-^*) + (c.c.)\right]\,, && (3.63)
\end{aligned}
$$

where $P_\pm$ are the slowly varying amplitudes of the material dipole densities corresponding to the left and right circularly-polarized optical fields $E_\pm$, $N - N_0$ is the total carrier distribution referred to the transparency value N_0, and n is the difference of the carrier distributions associated with the transitions σ_+ and σ_-.
The spin-flip decay rate is now given by the parameter

$$\gamma_s = \gamma_e + 2\gamma_j \ . \tag{3.64}$$

The differential gain at the lasing frequency, a, has been defined as

$$a = \frac{|\Theta_\pm|^2}{\gamma_\perp(1+\theta^2)} \frac{\Omega\Gamma_z}{4\hbar\epsilon_o n_e n_g} \ . \tag{3.65}$$

The total injected current, I, is given by

$$I = qd \int_{-\infty}^{\infty} dx \int_{-\infty}^{\infty} dy \ C(x,y) \ , \tag{3.66}$$

where q is the electron charge and d is the thickness of the quantum-well layer, and $C(x,y)$ is the transverse density of injected carriers per unit time.

The semiclassical theory developed here ignores the quantum-mechanical nature of the electromagnetic field. Therefore, this approach neglects spontaneous emission processes although they can be included by adding Langevin noise sources, $\sqrt{\beta N_\pm}\psi_\pm(x,y;t)$, to the polarization equation, where β is the spontaneous emission factor, and $\psi_\pm(x,y;t)$ are two complex Gaussian white noise sources of zero mean value and correlation $< \psi_\pm(x,y;t)\psi^*_\pm(x',y';t') >= 2\delta(x-x')\delta(y-y')\delta(t-t')$

The model given by Eqs. (3.60)-(3.63) is the first fundamental model to explain polarization dynamics in VCSELs and was introduced by San Miguel, Feng and Moloney in 1995 [112]. Since then, the SFM model has been extensively used by many theoretical and experimental groups in the study of the polarization properties of quantum-well VCSELs [76, 77, 82, 113]-[121, 150, 155]-[157].

3.4 Limitations of the two-level Maxwell-Bloch model for semiconductor lasers

The material dipole densities $P_\pm$ are the sources for the optical fields, providing both material gain and changes in the background refraction index of the system (dispersion) through the complex susceptibility. The complex nonlinear susceptibility resulting from our nonlinear dipole polarizations can be obtained, under linearly polarized steady state conditions [10], by Fourier transform of Eq. (3.61) into the frequency domain

[10] For linearly polarized light, n=0.

$$P_{\pm}^{\nu} \;=\; \epsilon_o \chi_\nu(N) E_{\pm}^{\nu} = \frac{a(1+\theta^2)(N-N_0)}{1+(\theta-\nu/\gamma_\perp)^2}(1+\mathrm{i}\,(\theta-\nu/\gamma_\perp))E_{\pm}^{\nu}\;, \qquad (3.67)$$

The real part of the complex susceptibility yields the gain spectrum which in the two-level approach has a symmetric, lorentzian profile. The dispersion spectrum, associated with the imaginary part of the complex susceptibility, is antisymmetric. The gain peak is located at the dipole resonance frequency (ω_g), where dispersion vanishes. The ratio of the carrier-induced changes in the imaginary and the real parts of the susceptibility, which would correspond to Henry's α-factor in semiconductor lasers [101], is given by

$$\alpha = \frac{\partial_N \; Im(\chi_\nu)}{\partial_N \; Re(\chi_\nu)} = \theta - \frac{\nu}{\gamma_\perp}\;. \qquad (3.68)$$

where ν is the emission frequency referred to the carrier frequency ($\nu \ll \Omega$). Hence, the detuning in the two-level model plays the role of the α-parameter in semiconductor lasers [95]. The main effects of the detuning, θ, in the two level model are: (*i*) it provides phase-amplitude (AM-FM) coupling of the optical field; and (*ii*) its sign determines the change in refraction index induced by the carrier density: positive (negative) detuning leads to carrier-induced index anti-guiding (guiding). Typical values of the detuning in real two-level lasers are $-0.25 < \theta < 0.25$ while $\alpha \sim 2-6$ for semiconductor lasers. Hence, in order to match the typical measured values of the α-factor in semiconductors with a detuning in two-level models, lasing away from resonance must be artificially enforced.

Another important limitation of the Maxwell-Bloch two level model to describe semiconductor laser dynamics comes when transverse effects are considered. Since higher order modes have always higher frequencies than the fundamental one, the sign of the detuning also affects the stability of the fundamental mode: for negative detuning (focusing), the gain of the fundamental mode is always the highest, while for positive detuning (defocusing) there might be a higher transverse mode with higher gain than the fundamental mode [158].

From the above discussion, we see that the two-level model does not take into account some features of the semiconductor medium, which is characterized by: *i*) a strongly asymmetric gain spectrum, *ii*) an operation wavelength close to the gain peak, *iii*) a strong amplitude-phase coupling in the vicinity of the gain peak, and *iv*) carrier-induced antiguiding. Having spelled out clearly the limitations of modeling the nonlinear dynamics of semiconductor gain-guided VCSELs with two-level models, we proceed in the next Chapters as follows.

In Chaps. 4-6 we analyze the polarization behavior of VCSELs within the fundamental mode regime. The single longitudinal and transverse mode operation allows us both to dismiss the spatial terms — optical diffraction and carrier diffusion — and to adiabatically eliminate the material polarization in the general model given by Eqs. (3.60)-(3.63)). The resulting rate equation model accounts for the general features of the four-level scheme and, more important, will have a proper description of the effects of the α-factor. The studies performed in these Chapters will be independent of the guiding mechanism of the VCSEL.

However, the description of the polarization dynamics in multi-transverse mode gain-guided VCSELs, carried out in Chap. 7, requires the use of the general model in order to provide the laser medium of a gain spectrum. The reason is that transverse modes in common VCSELs are separated, typically, 100-150 GHz in frequency, so gain differences between transverse modes might be important. In addition, in order to preserve the commonly observed property that higher order transverse modes have lower gain (higher threshold) that the fundamental one, we will force VCSELs operation in the negative detuning (negative α-factor) side of the gain curve [11].

[11] Results from previous studies in gain-guided edge-emitting lasers [159, 160] illustrate that the two-level Maxwell-Bloch model can provide a proper description of the spatio-temporal dynamics when the lasers are operated in the negative detuning side of the gain peak, which seems to indicate that gain-guided semiconductor lasers are strongly dominated by transverse mechanisms as the modal gain, the carrier diffusion and optical field diffraction.

Chapter 4

Polarization properties in the fundamental transverse mode of VCSELs

Abstract [1]

Polarization state selection, polarization state dynamics, and polarization switching of a quantum-well Vertical Cavity Surface Emitting Laser for the lowest order transverse spatial mode of the laser is explored using a recently developed model that incorporates material birefringence, the saturable dispersion characteristic of semiconductor physics, and the sensitivity of the transitions in the material to the vector character of the electric field amplitude. Three features contribute to the observed linearly polarized states of emission: linear birefringence, linear gain or loss anisotropies, and an intermediate relaxation rate for imbalances in the populations of the magnetic sublevels. In the absence of either birefringence or saturable dispersion, the gain or loss anisotropies dictate stability for the stronger linearly polarized mode and switching is only possible if the relative strength of the gain for the two modes is reversed. When birefringence and saturable dispersion are both present there are possibilities of bistability, monostability, and dynamical instability, including switching by destabilization of the mode with the higher gain to loss ratio in favor of the weaker mode. We compare our analytical and numerical results with recent experimental results on bistability and switchings caused by changes in the injection current and changes in the intensity of an injected optical signal.

[1] This chapter is based on the papers *(i) "Polarization Switching in Quantum Well Vertical Cavity Surface Emitting Lasers"*, by , J. Martín-Regalado, M. San Miguel, N. B. Abraham, and F. Prati, *Optics Lett.* **21**, 351 (1996); and *(ii) "Polarization Properties of Vertical Cavity Surface Emitting Lasers"*, by J. Martín-Regalado, M. San Miguel, N. B. Abraham, and F. Prati, *IEEE Journal of Quantum Electronics* **33**, 765 (1997).

4.1 Introduction

When the injection current is changed near the lasing threshold in a VCSEL, variations in the polarization state of the fundamental Gaussian pattern can be distinguished. In several experiments it is found that laser emission on the fundamental spatial mode with linear polarization near threshold switched to the orthogonal linear polarization as the current was increased (e.g., see Fig. 1 of [70] and Fig. 2(c) of [58] in the region of injection currents $I < 1.2I_{th}$). Polarization switching has also been biased or induced by an injected optical field of a particular polarization state [70].

We explore in this Chapter a fundamental explanation for these polarization phenomena. We first review in Sec. 4.2 a rate-equation model for polarization dynamics in VCSELs based on the general model derived in the previous Chapter. Linear anisotropy terms are added to the simpler rate-equation model in order to account for the birefringency and dichroism typical from VCSELs. Sec. 4.3 describes the polarization states predicted by the rate-equation model and their stability when the gain is the same for both linearly polarized modes. Polarization switching phenomena is anticipated by representing domains of stability of the linearly polarized modes in the parameter space of injection current and birefringence. The polarization behaviors found by numerical integration of the model equations as the injection current is increased, are discussed for particular parameter values in Sec. 4.4. The polarization state selection when there are small anisotropies in the gain or loss are considered in Sec. 4.5. Sec. 4.6 presents results for the effects of the transverse spatial variation of the fundamental mode neglected in the previous sections, showing that there are no qualitative differences in the polarization state selection and switching. Finally, Sec. 4.7 presents results from our model for polarization switching or dynamical hysteresis induced by an injected optical signal.

4.2 A rate-equation model for polarization dynamics in VCSELs

The rate-equation model that describes polarization dynamics of a single longitudinal VCSEL operating in the fundamental transverse mode can be directly derived from the schematic band structure of quantum well VCSELs depicted in Fig. 4.1 by using general rate equation arguments supplemented with the introduction of phase dynamics. A more rigorous derivation can be performed from the Maxwell-Bloch model developed in the previous Chapter after the material dipole polarization is adiabatically eliminated provided that the VCSEL operates in the single longitudinal spatial mode with the lowest order transverse field pattern (fundamental transverse mode). For single mode lasers, the transverse dependence in Eqs. (3.60)-(3.63) can be disregarded, leading to the following set of equations for the amplitudes of the circularly polarized fields coupled to the material variables which describe the laser system

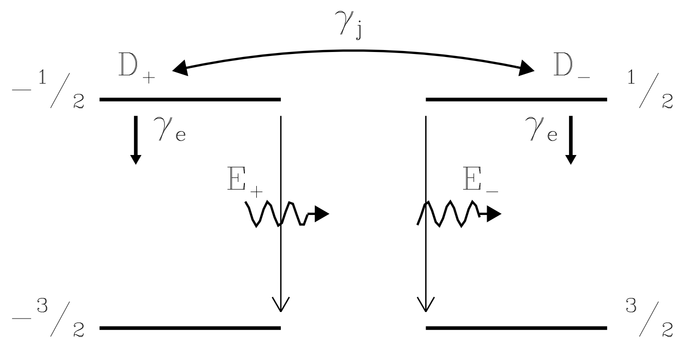

Figure 4.1: Four level model for polarization dynamics in QW-VCSEL's.

$$\begin{aligned}
\dot{E}_\pm &= -\kappa(1+\mathrm{i}\,\theta)E_\pm + P_\pm \ , && (4.1)\\
\dot{P}_\pm &= -\gamma_\perp(1-\mathrm{i}\,\theta)P_\pm + \gamma_\perp a(1+\theta^2)(N-N_0\pm n)E_\pm && (4.2)\\
\dot{N} &= C - \gamma N - [(E_+P_+^* + E_-P_-^*) + (c.c.)] \ , && (4.3)\\
\dot{n} &= -\gamma_s n - [(E_+P_+^* - E_-P_-^*) + (c.c.)] \ , && (4.4)
\end{aligned}$$

The adiabatic elimination of the material polarization variables $P_\pm$, relies of the fact that the polarization decay rate is large compared with the decay rates of the rest of the dynamical variables describing the system ($\gamma_\perp \gg \kappa > \gamma_s > \gamma$) (Class B laser [161]). Under the assumption $\gamma_\perp^{-1} \to 0$, the macroscopic polarizations "adiabatically" follow the optical field, and the approximation $\dot{P}_\pm$=0 can be considered in Eq. (4.2). The resulting material polarizations are

$$P_\pm = (1+\mathrm{i}\,\theta)a(N-N_0\pm n)E_\pm \ , \qquad (4.5)$$

Inserting Eq. (4.5) in the rest of the equations and rescaling the remaining dynamical variables as $F_\pm = \sqrt{2a/\gamma}\ E_\pm$, $D = (D_+ + D_-)/2 = a(N-N_0)/\kappa$, and $d = (D_+ - D_-)/2 = an/\kappa$ [2], the model equations, appropriate for narrow contact (single mode) VCSELs operating at constant active region temperature (constant gain), read

$$\begin{aligned}
\dot{F}_\pm &= \kappa(1+\mathrm{i}\,\alpha)(D\pm d-1)F_\pm \ , && (4.6)\\
\dot{D} &= -\gamma(D-\mu) - \gamma(D+d)|F_+|^2 - \gamma(D-d)|F_-|^2 \ , && (4.7)\\
\dot{d} &= -\gamma_s n - \gamma(D+d)|F_+|^2 + \gamma(D-d)|F_-|^2 \ . && (4.8)
\end{aligned}$$

where κ is the field decay rate, α is the linewidth enhancement factor which have been identified with the detuning θ (see Eq. (3.68)), γ is the decay rate of the total carrier population, μ is the injection current normalized to threshold, and γ_s is the decay

[2] $D_\pm$ are the carrier populations of the circularly polarized channels, as depicted in Fig. 4.1.

rate of the carrier population difference through spin-flip relaxation processes [151]. We point out that, since typically $\gamma^{-1} \approx 1$ ns, and $\kappa^{-1} \approx 1$ ps [162, 163], the spin mixing processes described by γ_s occur on an intermediate time scale between that of the field decay and that of the total carrier population difference decay. Hence, the dynamics of d cannot be in principle adiabatically eliminated.

Eqs. (4.6)-(4.8) describe polarization dynamics in a perfect isotropic VCSEL, and predicts the preference of quantum-well material for linearly polarized emission due to the finite coupling, via spin-flip relaxation processes, between the carrier populations involved in the two circularly left and right polarized transitions [112]. In the mathematical limit of very fast mixing of populations with different spins, $\gamma_s \longrightarrow \infty$, d quickly relaxes to zero. Therefore, the spin dynamics can be adiabatically eliminated so the two polarization field amplitudes $F_\pm$ are coupled to a single carrier population D, a model that is sometimes assumed phenomenologically for dual polarization semiconductor lasers [164]. When γ_s takes on its minimum value, given by the radiative lifetime of the carriers ($\gamma_s = \gamma$), the right and left circularly polarized transitions are decoupled and two sets of independent equations for (F_+, D_+) and (F_-, D_-) emerge. The physics of the conventional semiconductor laser rate equations for the intensity of a linearly polarized mode (given by $I = |F_+|^2 + |F_-|^2$) is recovered by forcing $d = 0$.

As pointed out previously, the eigenstates of the model are linearly polarized (rather than circularly or elliptically polarized) because of the cross-saturation preference exerted through the nontrivial value of γ_s. However the orientation of the linearly polarized modes is not fixed by the nonlinear field-matter interaction in this model. Therefore, any amount of linear birefringence or linear gain anisotropy resulting from material or cavity anisotropies restricts the linearly polarized solutions to one of two specific states along the linear anisotropy axes, that we call here the $\hat{x}$- and $\hat{y}$ directions. Incorporating the linear phase anisotropy and the linear amplitude anisotropy into Eq. (4.6) by considering the cavity anisotropy tensor in Appendix C [97, 103], leads to

$$\dot{d}F_\pm = \kappa(1 + \mathrm{i}\,\alpha)(D \pm d - 1)F_\pm - (\gamma_a + \mathrm{i}\,\gamma_p)F_\mp \,, \tag{4.9}$$

while the equations for D and d remain unchanged.

Eq. (4.9) can be rewritten in the matrix form.

$$\begin{aligned}\begin{pmatrix} \dot{F}_+ \\ \dot{F}_- \end{pmatrix} &= \kappa(1+\mathrm{i}\,\alpha)\left[-\begin{pmatrix} 1 & 0 \\ 0 & 1 \end{pmatrix} + D\begin{pmatrix} 1 & 0 \\ 0 & 1 \end{pmatrix} + d\begin{pmatrix} 1 & 0 \\ 0 & -1 \end{pmatrix}\right]\begin{pmatrix} F_+ \\ F_- \end{pmatrix} \\ &\quad -(\gamma_a + \mathrm{i}\,\gamma_p)\begin{pmatrix} 0 & 1 \\ 1 & 0 \end{pmatrix}\begin{pmatrix} F_+ \\ F_- \end{pmatrix}.\end{aligned} \tag{4.10}$$

Therefore, the matrices on the RHS of Eq. (4.9) represent[3], from left to right, (i) the isotropic amplitude loss, (ii) the isotropic gain (real part) and the isotropic change

[3]see Appendix C

of the emission frequency due to the pumped material (imaginary part), (*iii*) a circular anisotropy induced for non-zero values of d [4], and (*iv*) the linear anisotropies, respectively.

The parameter γ_p represents the effect of a different index of refraction — different emission frequency — for each linear polarization as a consequence of the birefringency of the crystal. In addition, the two polarization modes may have a slightly different gain-to-loss ratio that can be related to the anisotropic gain properties of the crystal [88, 165], the slightly different position of the frequencies of the modes with respect to the gain profile [79, 166], and/or different cavity geometries for the differently polarized modes [60, 87]. These effects are included in the parameter γ_a. Notice also that, for simplicity, we have assumed that the directions of linear phase and amplitude anisotropy coincide, so that both are diagonalized by the same basis states. The axis mismatch between birefringency and dichroism leads to elliptically, instead of linearly, polarized light emission [75, 129], the ellipticity depending on the angle between the linear anisotropies [129, 130]. However, reported measurements of elliptically polarized emission in VCSELs show that the ellipticity is very small [75], which indicates that the amplitude and phase anisotropy axes are nearly aligned.

The meaning and effect of the parameters γ_p and γ_a are most clearly displayed when these equations are rewritten in terms of the orthogonal linear components of the electric field:

$$F_x = \frac{F_+ + F_-}{\sqrt{2}}\,, \qquad F_y = -\mathrm{i}\,\frac{F_+ - F_-}{\sqrt{2}}\,. \tag{4.11}$$

For the $\hat{x}$– and $\hat{y}$-polarized components the complete model becomes

$$\begin{aligned}
\dot{F}_x &= -(\kappa+\gamma_a)F_x - \mathrm{i}\,(\kappa\alpha+\gamma_p)F_x + \kappa(1+\mathrm{i}\,\alpha)(DF_x + \mathrm{i}\,nF_y)\,, && (4.12)\\
\dot{F}_y &= -(\kappa-\gamma_a)F_y - \mathrm{i}\,(\kappa\alpha-\gamma_p)F_y + \kappa(1+\mathrm{i}\,\alpha)(DF_y - \mathrm{i}\,nF_x)\,, && (4.13)\\
\dot{D} &= -\gamma[D(1+|F_x|^2+|F_y|^2) - \mu + \mathrm{i}\,d(F_yF_x^* - F_xF_y^*)]\,, && (4.14)\\
\dot{d} &= -\gamma_s n - \gamma[d(|F_x|^2+|F_y|^2) + \mathrm{i}\,D(F_yF_x^* - F_xF_y^*)]\,. && (4.15)
\end{aligned}$$

It is clear here that γ_p leads to a frequency difference of $2\gamma_p$ between the $\hat{x}$– and $\hat{y}$-polarized solutions (with the $\hat{x}$-polarized solution having the lower frequency when γ_p is positive) and that γ_a leads to different thresholds for these linearly polarized solutions (with the $\hat{y}$-polarized solution having the lower threshold when γ_a is positive). The values of these parameters depend critically on VCSEL designs, which range from etched posts to buried structures. Both index-guided and gain-guided structures have been fabricated. We use a here a generic model for all devices and reasonable parameter values.

In the absence of saturable dispersion ($\alpha = 0$) or birefringence ($\gamma_p = 0$), the anisotropic gain, γ_a, fully controls the stability of these two modes: the mode with

[4] Notice that here is an important subtle effect of d on the cross saturation coupling of the right and left circularly polarized field amplitudes which might seem to interact independently with the two lasing transitions.

the higher gain-to-loss ratio (which thereby has the lower threshold current) is always stable above its lasing threshold and the orthogonally polarized mode is always unstable when the solution exists (above a higher threshold value of the current). Without external injection of optical signals to excite and enforce operation of the unstable mode and without strong noise perturbations to induce temporary switchings to the unstable mode, simple variations of the injection current will not lead to polarization state switching unless the gain anisotropy changes sign as the injection current is varied. Polarization switching will occur, without hysteresis, as the current crosses the value at which the gain anisotropy changes sign [58].

Semiconductor physics makes the saturable dispersion of the α-factor unavoidable. Since birefringence also seems to be a common feature of VCSELs, it is important that these properties be studied in conjunction with the gain anisotropy for their combined effect on polarization state selection and polarization switchings. In addition, the dynamics of the magnetic sublevel populations provides a natural mechanism for enforcing the observed preference of VCSELs for linearly polarized emission. In the remainder of this Chapter we investigate the effects of these physical phenomena and show that many of the interesting polarization switchings (elsewhere attributed to gain anisotropies) can be explained as a consequence of birefringence and saturable dispersion.

4.3 Polarization states and their stability for isotropic gain

The model presented in Sec. 4.2 contains a variety of solutions with constant population variables, constant intensity and a single optical frequency in their field spectrum. We will call them stationary solutions because of their trivial time dependence that corresponds to an optical frequency shift. In order to obtain the analytical expressions for these solutions, we write an arbitrary steady state solution as

$$F_{\pm} = Q_{\pm} e^{\mathrm{i}\,(\omega_{\pm} t \pm \psi) + i\theta} \,, \quad D = D_0 \,, \quad d = d_0 \,, \tag{4.16}$$

where θ is the global phase that can be ignored or set to zero without loss of generality, and ψ is a relative phase which indicates the direction of linear polarization in the transverse plane of the laser.

In absence of anisotropies ($\gamma_a = \gamma_p = 0$) the solutions are linearly polarized but oriented in an arbitrary direction of the quantum-well plane [112]. For these solutions, the amplitudes of the two circularly polarized components are equal and have the same frequency:

$$Q_{\pm} = \sqrt{\frac{\mu - 1}{2}} \,, \qquad \omega_{\pm} = 0 \,. \tag{4.17}$$

The relative phase ψ is arbitrary and determines the orientation of the linear

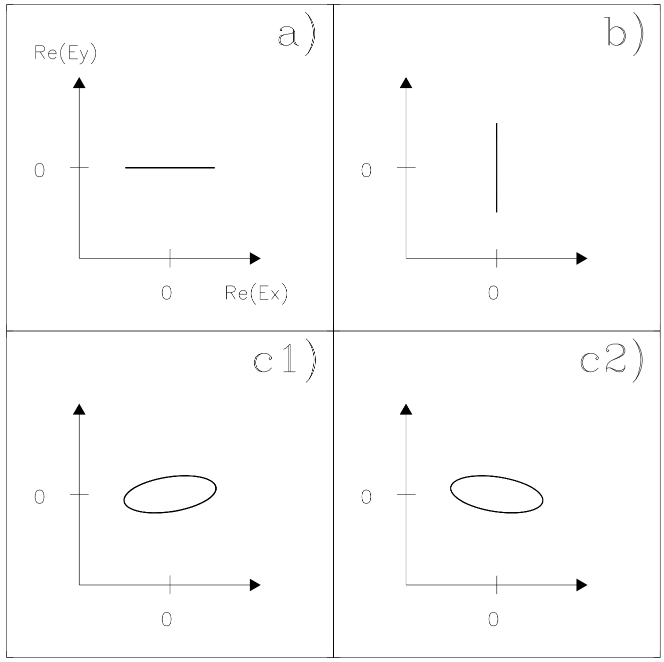

Figure 4.2: Steady state solutions of Eqs. (4.12)-(4.15): a) $\hat{x}$-polarized, b) $\hat{y}$-polarized, and c) elliptically polarized.

polarization. The projection of the linearly polarized field on the $x-y$ basis is given by:

$$F_x = \sqrt{\mu - 1}\cos\psi \;, \qquad F_y = \sqrt{\mu - 1}\sin\psi \;. \tag{4.18}$$

While this solution is susceptible to orientational diffusion due to perturbations of the phase ψ, this state is linearly stable for any finite value of the parameters with respect to amplitude perturbations. However, as $\gamma_s \to \infty$, it becomes marginally stable with respect to amplitude fluctuations [112]. This means that the finite value of γ_s for the isotropic case stabilizes the linearly polarized emission and destabilizes circularly polarized or elliptically polarized emission.

For $\gamma_p \neq 0$, and when there are no amplitude (gain or loss) anisotropies ($\gamma_a = 0$), we obtain four types of steady state solutions (see Fig. 4.2). For each of these solutions the phase anisotropy breaks the rotational invariance of the orientation of the field (polarization) vector, that is, the relative phase ψ is no longer arbitrary. Two of these types of solutions have orthogonal linear polarization. We will call these states the $\hat{x}-$ and $\hat{y}$-polarized solutions (modes).

For the linearly polarized modes the circularly polarized components have equal amplitudes and frequencies, but differ in the relative phase. The $\hat{x}$–linearly polarized solution [shown in Fig. 4.2(a)], is given by

$$Q_\pm = \sqrt{\frac{\mu - 1}{2}} \;, \qquad \omega_\pm = -\gamma_p \;, \qquad \psi = 0 \;, \tag{4.19}$$

and corresponds to

$$F_x = \sqrt{\mu - 1} e^{-\mathrm{i}\,\gamma_p t} \,, \qquad\qquad F_y = 0 \,. \tag{4.20}$$

The $\hat{y}$–linearly polarized solution [shown in Fig. 4.2(b)], is given by

$$Q_\pm = \sqrt{\frac{\mu - 1}{2}} \,, \qquad \omega_\pm = \gamma_p \,, \qquad \psi = \frac{\pi}{2} \,, \tag{4.21}$$

and corresponds to

$$F_x = 0 \,, \qquad\qquad F_y = \sqrt{\mu - 1} e^{\mathrm{i}\,\gamma_p t} \,. \tag{4.22}$$

The steady state values of the total carrier population and the population difference between the sublevels with opposite value of the spin for both linearly polarized solutions are

$$D_0 = 1 \,, \qquad\qquad d_0 = 0 \,. \tag{4.23}$$

The other two types of solutions are elliptically polarized solutions for which the circularly polarized components have equal frequencies but unequal amplitudes. These elliptically polarized solutions are given by

$$Q_\pm^2 = \frac{1}{2}(\mu - D_0)\left(1 \mp \frac{D_0 - 1}{d_0}\right) \,, \tag{4.24}$$

$$\omega_\pm = \kappa\alpha \frac{(D_0 - 1)^2 - d_0^2}{D_0 - 1} \,, \tag{4.25}$$

$$\tan(2\psi) = \frac{1}{\alpha}\frac{D_0 - 1}{d_0} \,. \tag{4.26}$$

The two elliptically polarized solutions are distinguished by the two possible values of d_0 which are given by

$$d_0 = \pm\sqrt{\frac{(\mu - D_0)(D_0 - 1)D_0}{\gamma_s/\gamma + \mu - D_0}} \,. \tag{4.27}$$

The value for D_0 is obtained from the following equation

$$\gamma_p^2 \left(\frac{\gamma_s}{\gamma} + \mu - D_0\right)^2 = \kappa^2 \left[\left(\frac{\gamma_s}{\gamma} + \mu - D_0\right) - \frac{\gamma_s}{\gamma} D_0\right] \left[\left(\frac{\gamma_s}{\gamma} + \mu - D_0\right)(D_0 - 1) + \alpha^2(\mu - D_0)D_0\right] \,. \tag{4.28}$$

Eq. (4.27) restricts the possible values to those for which D_0 is greater than 1. From Eq. (4.28), $D_0 > 1$ requires

$$\mu > 1 + \frac{\gamma_s \gamma_p}{\gamma(\kappa\alpha - \gamma_p)} \ . \tag{4.29}$$

which gives the range of currents where elliptically polarized solutions exist.

In general, for $\gamma_p \neq 0$, the relation $| \ d_0 \ | \geq D_0 - 1$ is always satisfied if Eq. (4.29) holds. The two different elliptically polarized solutions have the same optical frequency but different orientations of their polarization ellipses and different senses of rotation [see Fig. 4.2(c)]. An interesting result is obtained when $\gamma_p = 0$, for which the elliptically polarized solution becomes circularly polarized light. In this case we have

$$D_0 = \frac{\mu + \frac{\gamma_s}{\gamma}}{1 + \frac{\gamma_s}{\gamma}} \ , \qquad d_0 = \pm(D_0 - 1) \ , \tag{4.30}$$

where the positive (negative) sign yields left (right) circularly polarized light. However, these circularly polarized solutions are always unstable [112].

In order to study the linear stability of these stationary solutions we have used a standard procedure. The stability of a particular solution is studied by writing it as:

$$\begin{cases} F_\pm = (Q_\pm + a_\pm) e^{i(\omega_\pm t \pm \psi)} \ , \\ D = D_0 + \Delta \ , \\ d = d_0 + \delta \ , \end{cases} \tag{4.31}$$

where $a_\pm$ is a complex perturbation of the field amplitude, and Δ and δ are real perturbations related to the carrier variables.

After substituting the perturbed solution given by Eq. (4.31) in the equations of the model and linearizing to first order in the perturbation, one obtains the following set of linear coupled differential equations for $a_\pm$, Δ and δ

$$\begin{cases} \dot{a}_\pm = \kappa(1 + \mathrm{i}\,\alpha)(D_0 \pm d_0 - 1)a_\pm - \mathrm{i}\,\omega_\pm a_\pm \\ \qquad +\kappa(1 + \mathrm{i}\,\alpha)(\Delta \pm \delta)Q_\pm - \mathrm{i}\,\gamma_p a_\mp e^{\mp \mathrm{i}\,2\psi} \ , \\ \dot{\Delta} = -\gamma(D_0 + d_0)Q_+(a_+ + a_+^*) - \\ \qquad \gamma(D_0 - d_0)Q_-(a_- + a_-^*) - \\ \qquad \gamma(1 + Q_+^2 + Q_-^2)\Delta - \gamma(Q_+^2 - Q_-^2)\delta \ , \\ \dot{\delta} = -\gamma(D_0 + d_0)Q_+(a_+ + a_+^*) + \\ \qquad \gamma(D_0 - d_0)Q_-(a_- + a_-^*) - \\ \qquad \gamma(Q_+^2 - Q_-^2)\Delta - [\gamma_s + \gamma(Q_+^2 + Q_-^2)]\delta \ , \end{cases} \tag{4.32}$$

which can be shortenly written in the vectorial form as

$$\partial_t \vec{A} = \mathbf{M}\vec{A} \ , \tag{4.33}$$

where $\vec{A} = (a_+, a_+^*, a_-, a_-^*, \Delta, \delta)$, and $\mathbf{M}$ is a 6×6 matrix whose coefficients can be easily derived from Eq. (4.32). The eigenvalues of $\mathbf{M}$ are determined by a $6-th$ order polynomial that has to be solved. The linear stability of a steady state solution is given by the real parts of the eigenvalues which indicate if the solution is stable (when $Re(\lambda) < 0$ for all λ) or unstable (when $Re(\lambda) > 0$ for at least one λ), while the imaginary part of λ, when it exists, gives a frequency characteristic of the evolution of the perturbation.

We first consider the stability of the linearly polarized solutions, by substituting in Eq. (4.33) the steady state solution for the linearly $\hat{x}-$ and $\hat{y}$-polarized states given by Eq. (4.19) and (4.23), or Eq. (4.21) and (4.23), respectively. The set of equations given by Eq. (4.33) can be decoupled into two independent subsets if the equations are rewritten for the new perturbation variables $S = a_+ + a_-$ and $R = a_+ - a_-$ as was done in [112]. The first subset is

$$\left\{ \begin{array}{l} \dot{S} = 2\kappa(1 + \mathrm{i}\,\alpha)Q\Delta \;, \\ \dot{S}^* = 2\kappa(1 - \mathrm{i}\,\alpha)Q\Delta \;, \\ \dot{\Delta} = -\gamma\mu\Delta - \gamma QS - \gamma QS^* \;, \end{array} \right. \tag{4.34}$$

which determines the stability of a polarized solution with respect to perturbations with the same polarization. This subset of equations is independent of γ_p and γ_s. The general solution

$$\begin{pmatrix} S \\ S^* \\ \Delta \end{pmatrix} = \begin{pmatrix} S_0 \\ S_0^* \\ \Delta_0 \end{pmatrix} e^{\lambda\,\gamma\,t} \;, \tag{4.35}$$

leads always to a zero eigenvalue, associated with the arbitrary global phase θ, and two complex conjugate eigenvalues with always negative real parts. This means that each linearly polarized steady state solution is always stable with respect to perturbations with the same polarization. The complex eigenvalues are associated with ordinary relaxation oscillations characteristic of many lasers, including semiconductor lasers.

The second subset of equations reads

$$\left\{ \begin{array}{l} \dot{R} = 2\kappa(1 + \mathrm{i}\,\alpha)Q\delta \pm i2\gamma_p R \;, \\ \dot{R}^* = 2\kappa(1 - \mathrm{i}\,\alpha)Q\delta \mp i2\gamma_p R^* \;, \\ \dot{\delta} = -(\gamma_s + \gamma(\mu - 1))\delta - \gamma QR - \gamma QR^* \;, \end{array} \right. \tag{4.36}$$

where the positive (negative) sign is for the stability of the linearly $\hat{x}$- ($\hat{y}$-) polarized steady state solution. This subset determines the stability of a polarized solution with respect to perturbations of the orthogonal polarization.

For $\gamma_p = 0$ there is a zero eigenvalue associated with the arbitrariness of the polarization direction, and there are two more eigenvalues that always have negative real parts [112]. These two eigenvalues are complex for small γ_s, describing polarization relaxation oscillations. These eigenvalues become real for large γ_s and one of them approaches zero as $\gamma_s \to \infty$, corresponding to the existence of (and diffusion among) a family of elliptically polarized states with arbitrary ellipticity.

When $\gamma_p \neq 0$, the zero eigenvalue becomes nonzero, thus stabilizing or destabilizing a given steady state. To determine the eigenvalues of Eq. (4.36) we set

$$\begin{pmatrix} R \\ R^* \\ \delta \end{pmatrix} = \begin{pmatrix} R_0 \\ R_0^* \\ \delta_0 \end{pmatrix} e^{\lambda\,\gamma\,t} \,. \tag{4.37}$$

The resulting third order polynomial for λ is

$$\begin{aligned} P(\lambda) &= \lambda^3 + \left(\frac{\gamma_s}{\gamma} + \mu - 1\right)\lambda^2 + \left[2\frac{\kappa}{\gamma}(\mu-1) + 4\left(\frac{\gamma_p}{\gamma}\right)^2\right]\lambda \\ &+ 4\left(\frac{\gamma_p}{\gamma}\right)^2\left(\frac{\gamma_s}{\gamma} + \mu - 1\right) \mp 4\frac{\kappa\gamma_p}{\gamma^2}\alpha(\mu-1)\,, \end{aligned} \tag{4.38}$$

where the negative (positive) sign holds for the stability of the linearly $\hat{x}$- ($\hat{y}$-) polarized solution.

Let us consider first a situation in which there is no saturable dispersion in the field–matter interaction. In semiconductor physics language, this would be a case of no amplitude-phase modulation (no coupling between amplitude fluctuations and frequency fluctuations) in which α =0. In this case both linearly polarized solutions are always stable (the coefficients of the polynomial are all positive), so that there exists a regime of bistability for any value of μ or γ_p. Therefore, for α=0 no polarization switching occurs as the injection current is changed. However we show below that the nonvanishing value of α together with the phase anisotropy may cause polarization switching. This is the same type of behavior known for gas lasers, where for zero detuning, both linearly polarized modes are stable for any value of the birefringence parameter, but polarization switching occurs for nonzero detuning.

We determine the stability of a particular solution for a general value of α in terms of two control parameters, the injection current μ and the birefringence parameter γ_p/γ, which are commonly measured in polarization switching experiments. The lines separating stability regions in this parameter space are those for which $\lambda = 0 \pm i\omega$. For the $\hat{x}$-polarized solution the critical value of μ at which the stability of this solution changes is given by

$$\mu_x = 1 + \frac{\gamma_s\gamma_p}{\gamma(\kappa\alpha - \gamma_p)}\,, \tag{4.39}$$

with ω =0. Hence, the eigenvalue which vanishes at μ_x is real, indicating that $\hat{y}$ polarization fluctuations have pure exponential growth or decay in the vicinity of μ_x.

Similarly, for the $\hat{y}$-polarized solution we find two $\lambda = 0 \pm i\omega$ eigenvalues. The first one occurs at threshold [5],

[5] The real part of this eigenvalue is negative for any value of γ_p when the injection current is above threshold.

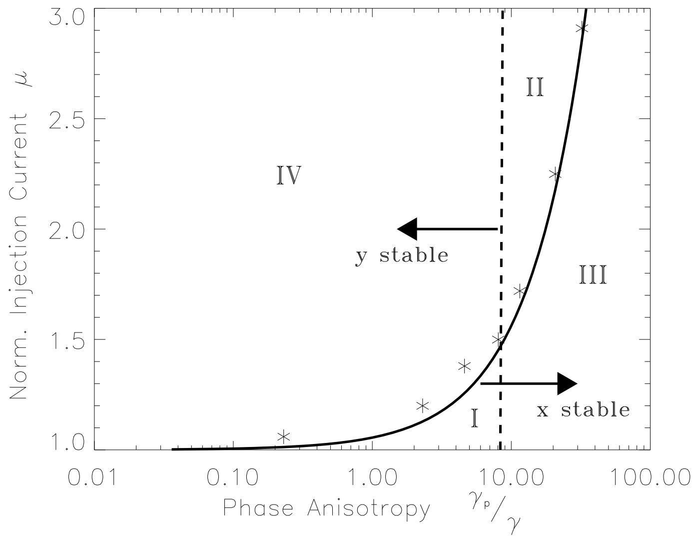

Figure 4.3: Stability diagram for the steady state solutions. The $\hat{x}$-polarized state is stable below the continuous line (μ_x), while the $\hat{y}$-polarized state is stable to the left of the dashed line (μ_y). Elliptically polarized solutions are stable within the narrow region between the solid line and the stars. The following parameters have been used: $\kappa = 300\ ns^{-1}$, $\gamma = 1\ ns^{-1}$, $\gamma_s = 50\ ns^{-1}$ and $\alpha = 3$.

$$\mu_y^{th} = 1 \ , \tag{4.40}$$

for which $\omega = 2\gamma_p$. The second zero eigenvalue occurs at

$$\mu_y = 1 - \frac{\gamma_s}{\gamma} + 2\alpha\frac{\gamma_p}{\gamma} \ , \tag{4.41}$$

with $\omega = [4{\gamma_p}^2 + 2\kappa(2\alpha\gamma_p - \gamma_s)]^{1/2}$. Therefore, $\hat{x}$ polarization fluctuations have oscillatory exponential growth or decay (polarization relaxation oscillations) in the vicinity of the instability boundaries given by Eqs. (4.40) and (4.41).

We have plotted in Fig. 4.3 the stability domains for the linearly $\hat{x}$- and $\hat{y}$-polarized solutions in the ($\gamma_p - \mu$) stability diagram. The $\hat{x}$-polarized solution is always stable for any current $\mu < \mu_x$, which occurs below the solid line. The $\hat{y}$-polarized solution is stable when $\mu > \mu_y^{th}$ and $\mu > \mu_y$, which occurs to the left of the dashed line. Therefore, the stability diagram is divided into four different regions with different stability for the linearly polarized solutions: region I, where both linearly polarized states are stable, region II where both are unstable, and regions III and IV where only $\hat{x}$-or $\hat{y}$-polarized solutions are stable, respectively. The stabilities of the $\hat{x}$– and $\hat{y}$-polarized solutions can be interchanged by changing the sign of γ_p.

Finally, the linear stability of elliptically polarized solutions has also been examined. In this case, the values of $Q_\pm, \omega_\pm, \psi$ and d_0 are given by Eqs. (4.24)–(4.27) after solving Eq. (4.28) for D_0. However, the particular values of the steady state do not allow decoupling Eq. (4.33) into the subsets for (S, S^*, Δ) and (R, R^*, δ) as was done for the linearly polarized solutions. This forces us to work directly with a 6–*th* order polynomial for the eigenvalues. To find the stability of a particular elliptically polarized solution, we numerically obtain the values of the coefficients of the polynomial and then we find their eigenvalues. The stability is determined by looking at the real part of the eigenvalues as previously described. The procedure has been applied to several values of the birefringence parameter for the range of injection current shown in the stability diagram of Fig. 4.3. We have indicated on the figure by stars, the values of μ and γ_p/γ that verify $Re(\lambda)$ =0. The elliptically polarized solution is stable in a narrow domain of parameters in which μ is close to but larger than μ_x. Note that according to Eq. (4.29), this solution only exists for $\mu > \mu_x$.

For realistic values of the parameters used in Fig. 4.3, the stability diagram is a consequence of the combined effect of saturable dispersion associated with the α-factor and spin dynamics associated with a finite value of γ_s. The existence of regions II (which is an obvious candidate for coexistence of the two polarizations) and III is a consequence of spin dynamics. This is verified by studying the steady-state solutions and their stability in the case $\gamma_s \gg \kappa, \gamma$. In this limit it is possible to adiabatically eliminated the population difference variable, which reads

$$d \approx -\frac{\gamma}{\gamma_s}(|E_+|^2 - |E_+|^2)D \; . \tag{4.42}$$

In this approximation, spin-flip dynamics is neglected. The linearly polarized states correspond exactly to those given by Eqs. (4.19)-(4.23). Their stability analysis give now two instability boundaries

$$\begin{aligned} \mu_x &= 1 + \frac{\gamma_s \gamma_p}{\gamma \kappa \alpha} \; , \qquad \omega = 0 \; , && (4.43) \\ \mu_y^{th} &= 1 \; , \qquad\qquad\;\; \omega = 2\gamma_p \; . && (4.44) \end{aligned}$$

Notice that these instability boundaries correspond to Eq. (4.39) (in the limit $\gamma_p \ll \alpha$) and Eq. (4.40), respectively, but the polarization instabilities associated with Eq. (4.41) do not occur. Hence, we conclude that regions II and III in Fig. 4.3 are a consequence of spin-dynamics.

On the other hand, only region I survives when phase-amplitude modulation is neglected by setting $\alpha = 0$. Therefore, region IV appears as a consequence of saturable dispersion which favors the $\hat{y}$-polarized mode with a small positive frequency shift induced by birefringence. This fact also becomes clear in a third order Lamb theory obtained from Eqs. (4.7)–(4.9) by adiabatic elimination of D and d in the limit $\gamma_s, \gamma \rightarrow \infty$ but $\rho = \frac{\gamma_s}{\gamma}$ finite. We find $(|E_+|^2, |E_+|^2 \ll 1)$

$$\begin{aligned} D &\approx \mu(1 - |E_+|^2 - |E_+|^2) \; , && (4.45) \\ d &\approx -\mu(|E_+|^2 - |E_+|^2)/\rho \; , && (4.46) \end{aligned}$$

and the dynamical equation for the optical field vector becomes (notice that we change α by θ in the spirit of gas laser theory, with θ being the detuning)

$$\dot{F}_{\pm} = \kappa(1+i\theta)\left(\mu+\frac{\mu}{\rho}\right)\left[\frac{\mu-1}{\mu+\frac{\mu}{\rho}} - |F_{\pm}|^2 - \delta|F_{\mp}|^2\right]F_{\pm} - i\gamma_p F_{\mp}\ , \qquad (4.47)$$

where $\delta = \left(\frac{\rho-1}{\rho+1}\right)$ is the coupling parameter [6].

The steady state solutions of Eq. (4.47) are $F^x_{\pm} = Qe^{-\mathrm{i}\,\gamma_p t}$ for the $\hat{x}$-polarized mode, and $F^y_{\pm} = Qe^{\mathrm{i}\,\gamma_p t}$ for the $\hat{y}$-polarized mode, where $Q^2 = (\mu-1)/(2\mu)$. From the linear stability analysis it is straightforward to derive an expression for the eigenvalue which causes the instability

$$\lambda = -\frac{\kappa(\mu-1)}{\rho} + \frac{1}{\rho}\sqrt{(\kappa(\mu-1))^2 - (2\rho\gamma_p)^2 \pm 4\gamma_p\kappa\theta\rho(\mu-1)}\ , \qquad (4.48)$$

where the positive (negative) sign is for the $\hat{x}$- ($\hat{y}$-) polarized mode.

Choosing the detuning as the control parameter in analogy to gas laser theory, we recover the characteristic polarization behavior of gas lasers. For a fix birefringency and pump values (*i*) the $\hat{x}$-polarized mode is unstable for $\theta_x > \rho\gamma_p/(\kappa(\mu-1))$, (*ii*) the $\hat{y}$-polarized mode is unstable for $\theta_y < -\rho\gamma_p/(\kappa(\mu-1))$, (*iii*) both polarization modes are stable (bistability) for $\theta_y < \theta < \theta_x$. What allows us to identify that regions I and IV come as consequence of saturable dispersion becomes clear when we write down the instability in terms of μ. For $\gamma_p, \theta > 0$, we find that the $\hat{x}$-polarized mode becomes unstable for

$$\mu_x \quad > \quad 1 + \frac{\rho\gamma_p}{\kappa\theta}\ , \qquad (4.49)$$

which corresponds to Eq. (4.39) in the limit ($\gamma_p \ll \theta$)

4.4 Injection current scans and polarization switching for isotropic gain

In experiments on polarization switching in VCSELs, it is common to measure the optical power of each of the linearly polarized modes as the injection current is increased. The frequency difference between the modes remains constant as the injection current is varied [49]. These experimental conditions and constraints can be reproduced in our model by varying the injection current while holding the birefringence parameter fixed, that is, by moving vertically in the parameter space of Fig. 4.3. To see the resulting dynamics and changes in the polarization state, we numerically

[6] For weak coupling ($\delta < 1$), there is a preference for linearly polarized emission, while for large coupling ($\delta > 1$), there is a preference for circular polarization. The limiting cases here are $\rho \to 1$, giving light strongly linearly polarized, and $\rho \to \infty$ (fast spin relaxation) in which there is marginal coupling ($\delta = 1$).

integrated Eqs. (4.7)–(4.9) in time with weak stochastic noise perturbations added to the optical field equation [7] [167]. The injection current was periodically increased in small abrupt steps (5% of the threshold value), beginning from a value of the injection current which started the laser below threshold. Each new value of the current was held constant for a time interval equivalent to about 40 ns, long enough in most cases to ensure that the transient evolution of the fields and carriers was almost completely finished. Fig. 4.4 shows an example of the temporally stepped injection current and the resulting evolution and changes in the intensities of each linearly polarized mode and in the carrier numbers. The final states in the time ranges #1 and #6 (indicated on the figure) correspond to linearly $\hat{x}-$ and $\hat{y}$-polarized emission, respectively. In time ranges #2 and #3 the final state is elliptically polarized. Solutions with periodic modulation of the variables corresponding to states of mixed polarization, were found in time ranges #4 and #5.

If we assume that the laser will most often settle on an available stable steady state solution, Fig. 4.3 allows us to predict polarization switching when the injection current is varied, as these variations can move the laser from a zone where one linearly polarized mode is stable to a zone where the other linearly polarized mode is stable. From Fig. 4.3 alone it is not clear how, or whether, the elliptically polarized steady states would be involved in these transitions.

We first consider a scan of the injection current in the domain where $\hat{y}$-polarized emission is always stable, that is, for small values of the birefringence parameter. "Small" in this case is determined by having frequency splittings between the linearly polarized modes that are less than the typical relaxation rate of the population differences in the magnetic sublevels (spin relaxation rate). In this case, just above threshold there is bistability of the two linearly polarized solutions. Spontaneous emission noise fluctuations as the laser is brought from below threshold to above threshold will set the initial conditions that select one of the two linearly polarized modes. However, because the two modes are not equally stable there would be a greater likelihood of finding the more stable ($\hat{y}$-polarized) mode. The time evolution as the current is increased depends on which mode is initially selected: (1) if the system begins with a $\hat{y}$-polarized solution, this polarization mode is retained as μ is raised and lowered because it is stable for the whole range of injection currents; or (2) if the system begins with $\hat{x}$-polarized emission, it will switch to $\hat{y}$-polarized emission at a value of the injection current given by $\mu = \mu_x(\gamma_p)$. Once the laser reaches $\hat{y}$-polarized emission, this new state will be retained stably if the injection current is raised further, or if it is lowered, even if it is lowered into the bistable region. This would provide an evident "one-time" hysteresis signature which would not be repeated as the injection current was raised and lowered unless the laser again, due to spontaneous emission noise or other fluctuations, switched stochastically to the $\hat{x}$-polarized mode in the bistable region or when the laser was operated below the lasing threshold.

[7] $\sqrt{\beta(D \pm d)}\Psi_{\pm}(t)$ is added to Eq. (4.9), where $\beta(=10^{-4}\ \mathrm{s}^{-1})$ is the spontaneous emission factor, and $\Psi_{\pm}(t)$ are two complex Gaussian white noise sources of zero mean value and correlation give by $< \psi_{\pm}(t)\psi^{*}_{\pm}(t') >= 2\delta(t-t')$.

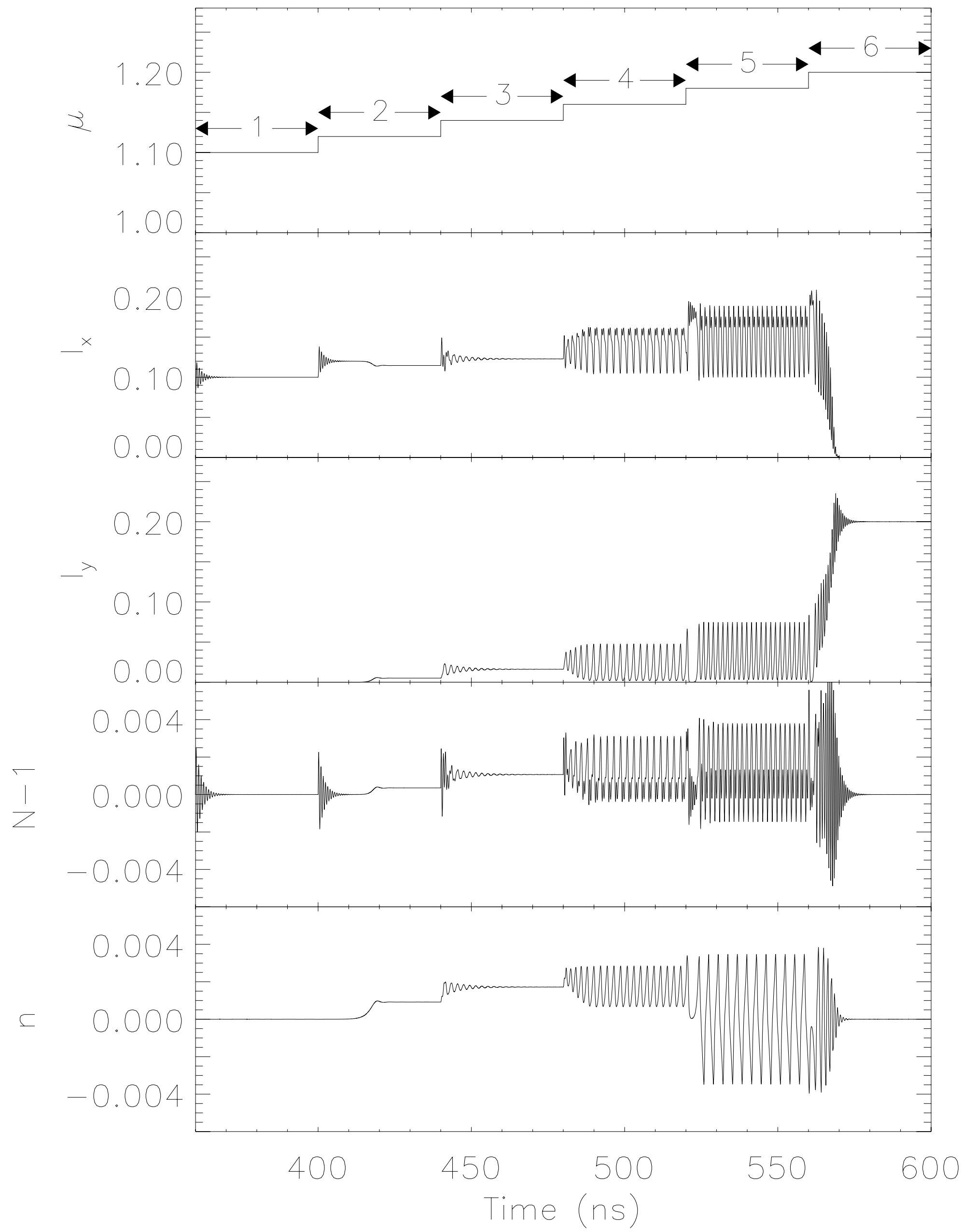

Figure 4.4: Time dependent evolution of the injection current (increased in steps), the intensities of each polarized mode ($I_x = |F_x|^2, I_y = |F_y|^2$) and the carrier variables D and d, when the injection current μ is increased. The parameters used are those of Fig. 4.3 and $\gamma_p = 2\gamma$.

Results for a scan of the injection current with a fixed value $\gamma_p = 2\gamma$, which is midway in the zone that is initially bistable, are shown in Fig. 4.5. In order to compare this result with the experimental results which are typically completed with a slow (quasi-adiabatic) scan of the injection current, the intensity was averaged during the last 20 ns (second half) of each time interval during which the injection current was held at a particular value. The averaged intensity for each linearly polarized mode is plotted versus the value of the injection current, giving a light-current characteristic for each polarized mode. This procedure was followed rather than a quasi-adiabatic scan of the current which could be fashioned from a series of many smaller steps, in order to allow transients to die out and to avoid the phenomena which result from scanning a parameter through a bifurcation point with the consequent critical slowing [96]. Of course in detailed comparisons with experiments with continuously scanned currents, such critical phenomena must be present and one would also have to include adequate noise strengths in all variables to make an accurate prediction.

As expected, two different light-current characteristics were obtained, depending on which of the two stable steady states was selected as the laser was brought above threshold. When the initial selected state was $\hat{y}$-polarized, this state was retained for any value of the injection current. As this is a relatively trivial result for presentation (even though it is slightly more common because this state is slightly more stable, and thus more frequently selected at the lasing threshold), it is not represented in Fig. 4.5. Instead, Fig. 4.5 shows the light-current characteristic for the other case, when the selected initial state is $\hat{x}$-polarized. The $\hat{x}$-polarized state is retained up to μ =1.1 where it loses its stability to elliptically polarized emission. After a further increase in the injection current the output changes to the $\hat{y}$-polarized state at μ =1.2. The switching involves intermediate states of different polarization, such as an elliptically polarized state (an example is labeled by β) and some other complex time dependent intensity solutions (an example is labeled by γ). Each emission state can be also characterized by the optical spectrum (spectrum of the optic field amplitude) which we compute for the last 20 ns of each transient for each of the labeled states. For the linearly polarized (α and δ) and the elliptically polarized state (β) the spectra have one well-defined peak. For the solution with time-varying intensities (γ) each of the spectra for the linearly polarized field amplitudes have a main peak (at the same frequency in the two cases) and many equally spaced sidebands, which is the signature of the periodic modulation of the intensity (and phase) for each component.

For a better description of these intermediate states we use three alternative characterizations of the data from the last 20 ns of each current step: first a plot of $Re(F_x)$ versus the $Re(F_y)$ for a given time interval, secondly, the Poincare sphere representation, and third, a measure of polarization given by the Fractional Polarization ($F.P.$). We have selected a particular example from each qualitatively different type of emission along the light-current characteristic curve in Fig. 4.5 (for example, α labels a condition of $\hat{x}$-polarized emission while δ labels a case with $\hat{y}$-polarized emission). The $Re(F_x)$ versus the $Re(F_y)$ plots are shown beside the light-current characteristics for the labeled states and clearly identify the different types of polarization; a curve or line is obtained because the solutions have a non-zero optical frequency relative to the rotating reference frame selected for the slowly varying amplitudes of the model. This kind of plot represents the projection of our six dimensional space of dynamical variables onto a two-dimensional space, and some information is necessarily lost or obscured.

An alternative two-dimensional plot is that of one carrier variable (**D**) versus the other one (**d**) . For the steady states (constant intensity solutions, both linearly and elliptically polarized) both carrier variables are time independent, resulting in a single point in the plot as given by Eq. (4.23) or Eqs. (4.27) and (4.28), respectively.

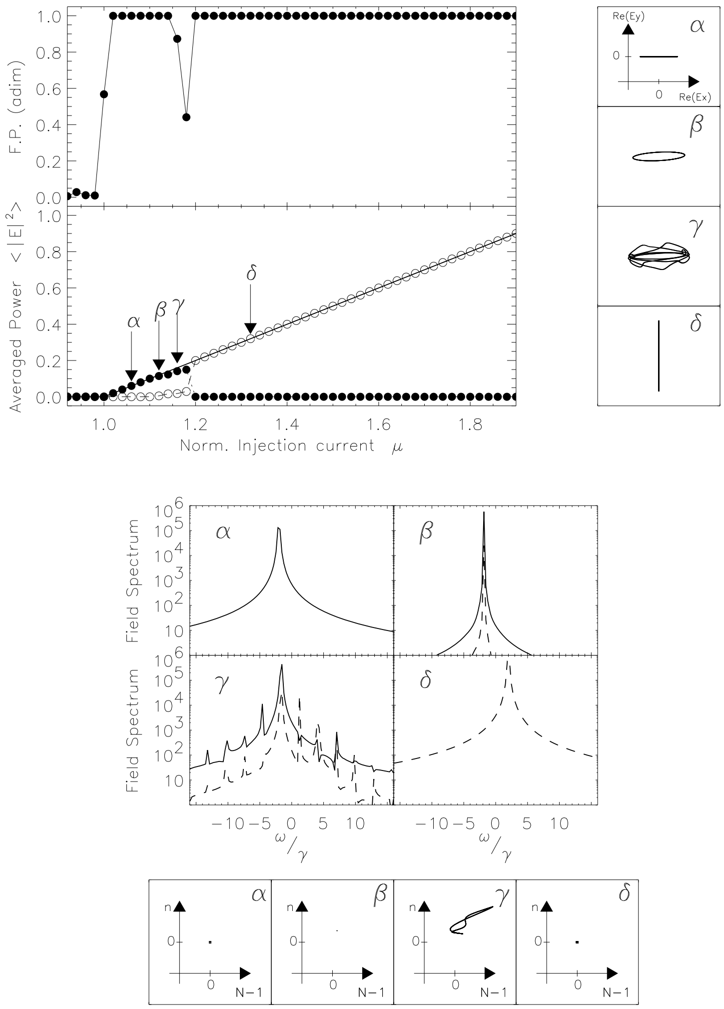

Figure 4.5: Light-current (LI) characteristic for the intensity of each linearly polarized mode and the associated fractional polarization (F.P.). $Re(F_x)$ vs. $Re(F_y)$ plots, D-1 vs. d, and optical spectra of the field amplitudes F_x (solid line) and F_y (dashed line) for the solutions labeled on the LI characteristic. The parameters are those of Fig. 4.3 and $\gamma_p = 2\gamma$.

The time-dependence of the carrier variables for the case labeled as γ reflects the lack of a well defined state of polarization. However, a closed trajectory is obtained which indicates a distinct relation between the two carrier magnitudes and an overall periodic evolution. For comparisons, the behavior labeled γ in Fig. 4.5 corresponds to the time range #4 in Fig. 4.4.

Another way to characterize the polarization of a state is the Poincare sphere plot [99], where for the given pair of field amplitudes $(F_+(t), F_-(t))$ we assign the radial value of a point on the trajectory $(\rho_0^2(t))$ to the total intensity of this state; the azimuth angle on the Poincare sphere is given by $2\varphi(t)$, where φ is the angle of the instantaneous polarization in the x-y plane; and the polar angle, $2\chi(t)$, of the point on the Poincare sphere is set by χ which is the instantaneous ellipticity of the emission. These quantities appear in the definition of the Stokes parameters:

$$\begin{cases} s_0(t) = \mid F_+(t) \mid^2 + \mid F_-(t) \mid^2 = \rho_0^2(t) \ , \\ s_1(t) = 2Re(F_+(t)F_-^*(t)) = \rho_0^2(t)\cos(2\chi(t))\cos(2\varphi(t)) \ , \\ s_2(t) = 2Im(F_+(t)F_-^*(t)) = \rho_0^2(t)\cos(2\chi(t))\sin(2\varphi(t)) \ , \\ s_3(t) = \mid F_+(t) \mid^2 - \mid F_-(t) \mid^2 = \rho_0^2(t)\sin(2\chi(t)) \ . \end{cases} \tag{4.50}$$

The Stokes parameters obey the time-dependent identity

$$s_0(t)^2 = s_1(t)^2 + s_2(t)^2 + s_3(t)^2 \ . \tag{4.51}$$

By identifying s_i/s_0, i=1,2,3, with the linear coordinates x, y and z, Eq. (4.51) can be regarded as the equation of the unit sphere. Every polarization state of the laser beam is then represented by a point on the surface of the sphere. In case of polarized light, the Stokes parameters are constant in time, since intensity, polarization and helicity are fixed. For incompletely polarized light, the Stokes parameters vary in time because the amplitudes F_+ and F_- and the relative phases vary. In this case what one can do is to measure the averages $< s_i >$ over a suitable time interval. In general Eq. (4.51) must be replaced by the inequality

$$< s_0 >^2 \geq < s_1 >^2 + < s_2 >^2 + < s_3 >^2 \ , \tag{4.52}$$

where the equals sign holds only for a state of pure polarization. A measure of the degree of polarization of a vector optical field is given by the Fractional Polarization ($F.P.$), defined as [169]

$$F.P. = \frac{< s_1 >^2 + < s_2 >^2 + < s_3 >^2}{< s_0 >^2} \ . \tag{4.53}$$

The $F.P.$ ranges from 0 (natural unpolarized light) to 1 (polarized light), taking intermediate values for incompletely polarized light. This new physical quantity can supply some of the information missing in the $Re(F_x)$ vs. $Re(F_y)$ plots when the solutions are time dependent ($0 < F.P. < 1$). The values of the $F.P.$ averaged over the last 20 ns of each current step are plotted above the light-current characteristic in Fig. 4.5. The linearly polarized and the elliptically polarized states have $F.P. = 1$, while the time-dependent states (of mixed polarization) have $F.P. < 1$.

The Poincare sphere representation of each of the four identified states (α, β, γ and δ) is shown in Fig. 4.6. When the state has $F.P. = 1$ (states α, β and δ), it is represented by a fix point on the sphere. This point lies on the equator of the sphere if the state is linearly polarized. However, when the state has $F.P. < 1$, the representative point moves on the surface of the normalized sphere. When the intensities vary periodically the representative point moves on a closed trajectory (state γ). The state γ can be understood as an elliptically polarized state whose ellipticity and azimuth change in time in a periodic way. For states with a broad

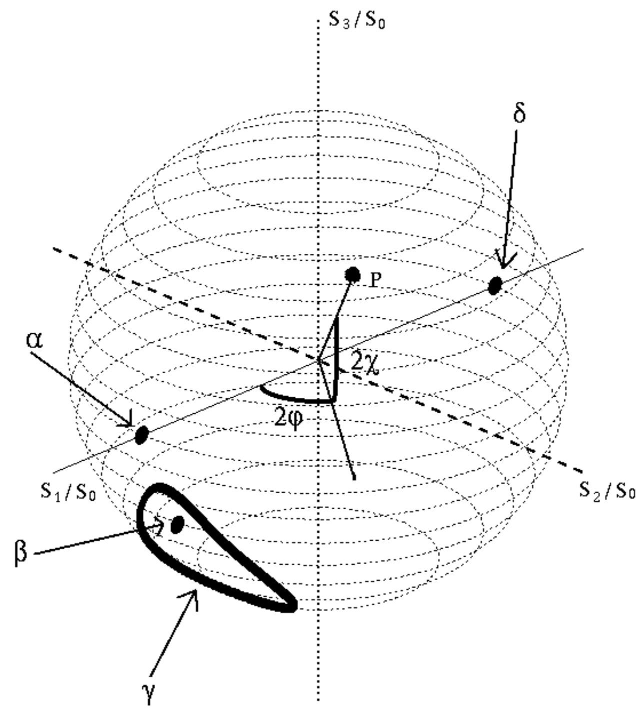

Figure 4.6: Time evolution of the labeled states of Fig. 4.5 on the normalized Poincare Sphere.

field spectrum (corresponding to quasiperiodic or chaotic variation of the intensities) the representative point would move in a complicated (not closed) trajectory on the surface of the sphere.

Elliptically polarized states are stable in a very narrow region. They can be understood as an intermediate stationary state reached in the destabilization by a steady bifurcation of a linearly polarized solution as the current is increased. At the critical value of the current at which the $\hat{x}$-polarized state loses its stability, the elliptically polarized state appears as an infinitesimal distortion of the destabilized state. There are two frequency-degenerate elliptically polarized solutions with two possible signs for the azimuth [two orientations, see Fig. 4.2(c)]. The supercritical transition from one linear polarized mode to the other can occur through either of these two states.

We next consider a scan of the injection current, at a fixed value of γ_p which is comparable to the relaxation rate of the magnetic sublevels, and, therefore, where sublevel population dynamics play a crucial role. For these values of γ_p, the $\hat{x}$-polarized state is the only stable steady state near the lasing threshold, but no linearly polarized state is stable beyond $\mu = \mu_x$. Fig. 4.7 shows typical results for $\gamma_p = 10\gamma$ presented as in Fig. 4.5. In this case, different initial conditions as the injection current first crosses the lasing threshold lead to the same qualitative behavior. The initial state of the system just above threshold is always $\hat{x}$-polarized (labels A and B). As in the previous case, if the injection current is raised enough, this state loses its stability at $\mu = \mu_x$ by way of a supercritical bifurcation to an elliptically polarized

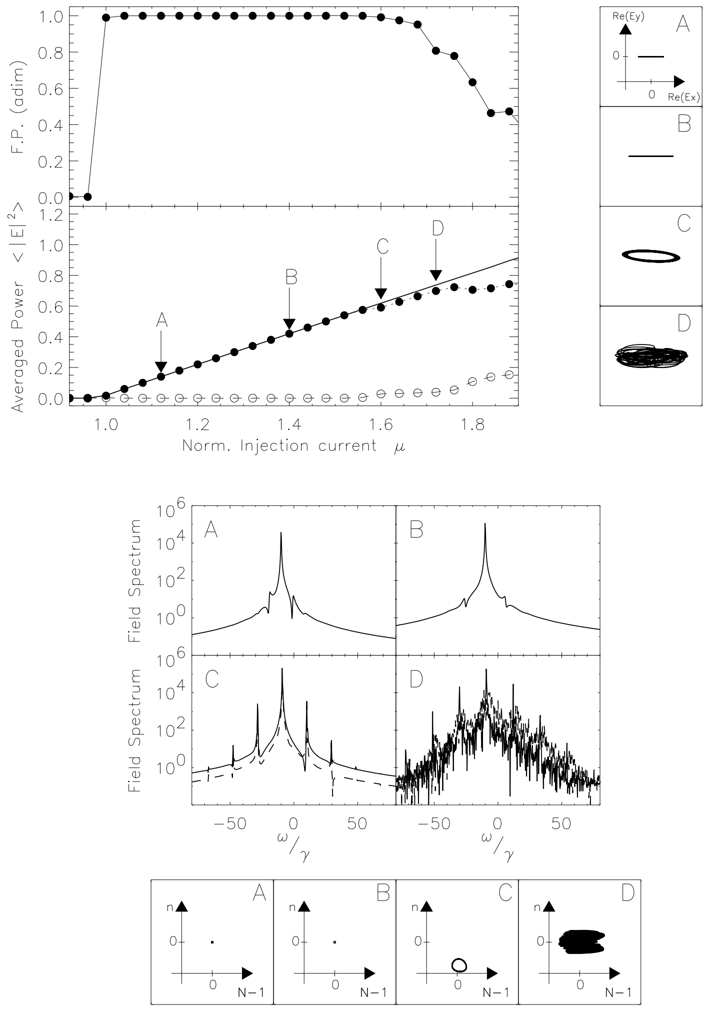

Figure 4.7: Same as Fig. 4.5, but for γ_p=10γ. The y-scale of figure C in the N-1 vs. n plot has been expanded 20 times to increase the resolution.

state as was true for the conditions of Fig. 4.5.

When the injection current is increased further, we find a state of mixed polarization (labeled as C) involving periodic modulation of the intensities of the linearly polarized components and a periodic modulation of the total intensity (evident in the equal spacing of the optical sidebands in the field spectra and in the closed curve nature of the d vs. D plot). From the various representations and spectra we infer that this is a state of nearly elliptical polarization with a dominant optical frequency close to that of the horizontally polarized state with about a 1% modulation. The intensity modulation frequency is approximately $2\gamma_p$, which would be the approximate beat frequency between $\hat{x}$-polarized and $\hat{y}$-polarized emissions. This state of time-dependent intensities has a *F.P.* value slightly smaller than one indicating that we might think of it as a strong amplitude of an elliptically polarized state at one optical frequency with the addition of two weak fields at different optical frequencies with different polarization states. It appears that this is reached through a supercritical

Hopf bifurcation from elliptically polarized steady state solutions. Thus it is likely that the additional fields (at different optical frequencies from the main peak) that are evident in the optical spectrum are those represented by the eigenvectors at the Hopf bifurcation point (with specific polarization states and optical frequencies given by positive and negative shifts of the Hopf bifurcation frequency) of the linear stability analysis for the elliptically polarized solutions. While we have only numerical evidence for the six eigenvalues that govern the stability of the elliptically polarized solution, it appears that the boundary denoted by the stars in Fig. 4.3 is always the result of such a Hopf bifurcation. It is also worth noting that the overall sequence from linear to elliptical to modulated elliptical solutions by way of supercritical steady and Hopf bifurcations, respectively, appears to be common to both the of the cases examined in Figs. 4.5 and 4.7.

For larger injection currents in the conditions of Fig. 4.7, the system loses almost all of its temporal coherence, presenting broad spectra (probably chaotic, in the sense of deterministic chaos) with a less well defined principal frequency (state D). The fractional polarization decreases significantly below one as the injection current is increased still further. The time-averaged output powers of the linearly polarized components might be interpreted as "coexistence" of the two linearly polarized modes if one were looking only at the time averaged light-current characteristics for linearly polarized components, but an optical spectral analysis would reveal several sidebands, rather than a single sideband, to the primary spectral peak. Analysis of the polarization states of the spectrally resolved peaks might be required before a decision could be made about the usefulness or validity of a possible interpretation of the result as combination of a few components of definite polarization and different optical frequencies, though the proper basis set for such a description, if it exists, is not the linearly polarized states.

The stability region of elliptically polarized emission (and of the periodically modulated elliptically polarized emission) is very narrow for these parameter values. Hence elliptically polarized states are not easy to observe in the switching from $\hat{x}$-polarization to the "coexistence" regime. If the model accurately describes the physics, this would indicate that it would also be difficult to observe elliptically polarized solutions in the polarization switching found experimentally.

We finally mention that we have found polarization states that can be characterized by the dynamical coexistence of the two linearly polarized modes with different frequencies. These "two-frequency" solutions appear in the case of very fast mixing of carrier subpopulation between the two channels (large γ_s) such that d is effectively adiabatically eliminated in the dynamical evolution. An example of these polarization states is shown in Fig. 4.8. Just above the lasing threshold, stable simultaneous emission in both $\hat{x}$- and $\hat{y}$-polarizations is observed. Two peaks are observed in the spectrum of the emitted optical field (state labeled α) with nearly equal power in the two spectral components and with the frequency difference corresponding to the birefringence induced splitting of the linearly polarized single-frequency solutions. The two-frequency state is unstable at currents above $\mu \sim 1.15$. Beyond this current value, only the $\hat{x}$-polarized survives as can be inferred from the field spectrum (state labeled β). The power versus current (L-I) characteristic curve shown in this figure has been

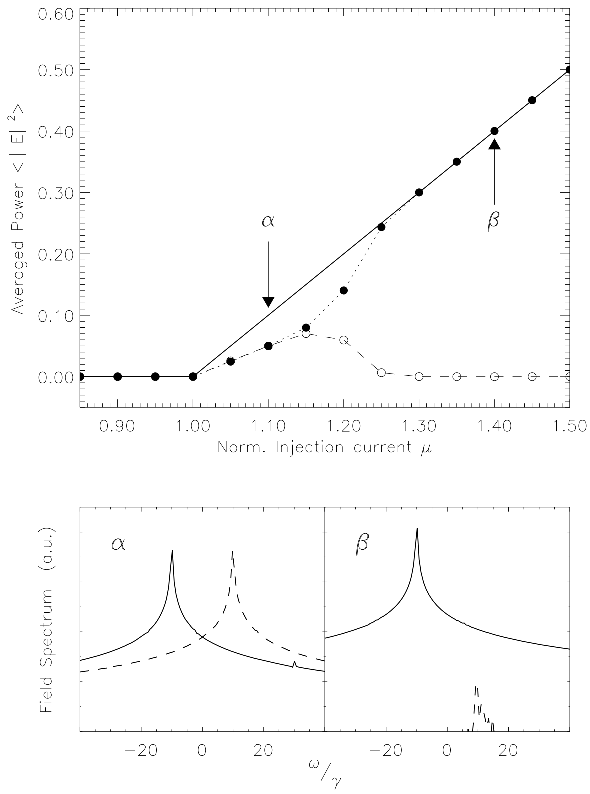

Figure 4.8: Two frequency solutions: L-I characteristic and optical spectra of the field amplitudes F_x (solid line) and F_y (dashed line) for fast spin-flip relaxation. The parameters used are $\gamma = 1$ ns^{-1}, $\kappa/\gamma = 300$, $\gamma_s/\gamma = 1000$, $\alpha = 3$, $\gamma_p/\gamma = 10.0$.

observed for many circular lasers emitting at room temperature [58, 60]. Qualitatively similar polarization and spectral behavior has been observed for γ_p values in the range $0.5 \leq \gamma_p \leq 20$. All these birefringence values are within the bistability region (region I of Fig. 4.3) which, for the set of parameters used here(see figure caption), extends up to $\gamma_p/\gamma = 150$. The range of currents for which the two-frequency solutions remain stable is enlarged as the value of spin-flip relaxation rate becomes larger. In the limit of very fast spin-flip mixing ($\gamma_s \longrightarrow \infty$), the population difference d is zero, and two-frequency states are stable for any value of the injection current.

4.5 Anisotropies in both amplitude and phase

In this section, we obtain the steady state solutions and their stability in the presence of amplitude anisotropy $\gamma_a \neq 0$. In this case the $\hat{x}-$ and $\hat{y}$-polarized modes have different thresholds. This is a typical experimental situation in which small amplitude anisotropies are unavoidable. We proceed here from the knowledge gained in the simpler case of Sec. 4.3 and follow the same methodology. Assuming a general steady state of the form of Eq. (4.16), we obtain that the $\hat{x}$-polarized solution is given by

$$\begin{cases} Q_{\pm}^2 = \frac{1}{2}\frac{\mu - D_0}{D_0} \;, & \psi = 0 \;, \\ \omega_{\pm} = -\gamma_p + \gamma_a \alpha \;, & \\ D_0 = 1 + \frac{\gamma_a}{\kappa} \;, & d_0 = 0 \;, \end{cases} \tag{4.54}$$

while the $\hat{y}$-polarized solution is given by

$$\begin{cases} Q_{\pm}^2 = \frac{1}{2}\frac{\mu - D_0}{D_0} \;, & \psi = \frac{\pi}{2} \;, \\ \omega_{\pm} = \gamma_p - \gamma_a \alpha \;, & \\ D_0 = 1 - \frac{\gamma_a}{\kappa} \;, & d_0 = 0 \;. \end{cases} \tag{4.55}$$

These orthogonal linearly polarized solutions have different steady state amplitudes and different (symmetrically detuned) optical frequencies, though the value of γ_a shifts the frequency splitting from that caused by the birefringence alone ($2\gamma_p$). γ_a (together with α) even creates a splitting of the optical frequencies in the absence of true birefringence, a complication in interpreting experimental lasing spectra for the value of the birefringence.

The stability of these linearly polarized solutions is modified by the amplitude anisotropy. Linear stability analysis of Eq. (4.31) for the perturbed solution gives a system of equations for the perturbations which can be decoupled (as for the amplitude isotropic case) into two subsystems for $S = a_+ + a_-$ and $R = a_+ - a_-$. The set of equations for S and Δ is independent of γ_a so, as in Sec. 4.3, a given linearly polarized state is stable with respect to perturbations of the field amplitude having the same polarization.

For the stability of a linearly polarized state with respect to perturbations of the field amplitude having the orthogonal polarization, we find

$$\begin{cases} \dot{R} = 2\kappa(1 + \mathrm{i}\,\alpha)Q\delta \pm 2(\gamma_a + \mathrm{i}\,\gamma_p)R \;, \\ \dot{R}^* = 2\kappa(1 - \mathrm{i}\,\alpha)Q\delta \pm 2(\gamma_a - \mathrm{i}\,\gamma_p)R^* \;, \\ \dot{\delta} = -\gamma D_0 Q R - \gamma D_0 Q R^* - (\gamma_s + 2\gamma Q^2)\delta \;, \end{cases} \tag{4.56}$$

where the positive (negative) sign is for the stability of the linearly $\hat{x}$- ($\hat{y}$-) polarized steady state solution. The characteristic polynomial for the eigenvalues λ is

$$\begin{aligned} P(\lambda) \;\; = \;\; & \lambda^3 + \left(\frac{\gamma_s}{\gamma} + 2Q^2 \mp 4\frac{\gamma_a}{\gamma}\right)\lambda^2 \\ & +4\left[\left(\frac{\gamma_p}{\gamma}\right)^2 + \left(\frac{\gamma_a}{\gamma}\right)^2 + \frac{\kappa}{\gamma}Q^2 D_0 \mp \frac{\gamma_a}{\gamma}\left(\frac{\gamma_s}{\gamma} + 2Q^2\right)\right]\lambda \\ & +4\left[\left(\frac{\gamma_p}{\gamma}\right)^2 + \left(\frac{\gamma_a}{\gamma}\right)^2\right]\left(\frac{\gamma_s}{\gamma} + 2Q^2\right) \mp 8\frac{\kappa}{\gamma}Q^2 D_0\left(\frac{\gamma_a}{\gamma} + \alpha\frac{\gamma_p}{\gamma}\right) \;. \end{aligned} \tag{4.57}$$

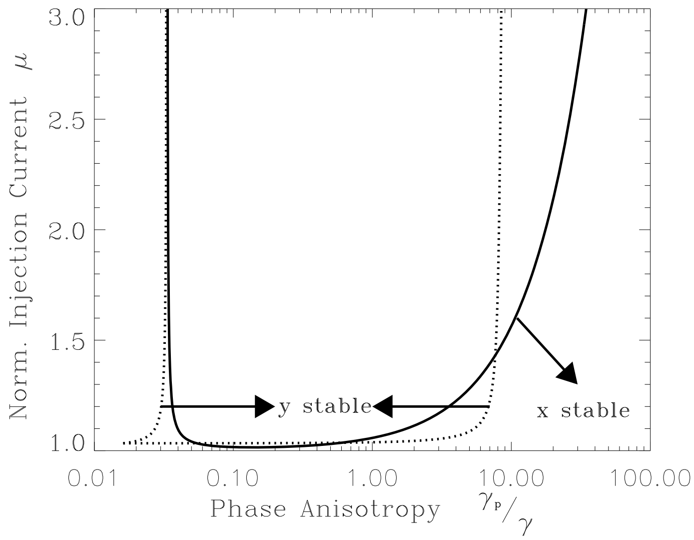

Figure 4.9: Stability diagram for γ_a =-0.1γ; other parameters as in Fig. 4.3. The $\hat{x}$-polarized mode has the lowest threshold.

The plus and minus signs correspond to the stability of the $\hat{y}$-polarized and $\hat{x}$-polarized steady state solutions, respectively, under perturbations of the orthogonal polarization, while D_0 is the steady state value for the solution (either Eq. 4.54 or Eq. 4.55) being analyzed for its stability.

The amplitude anisotropy breaks the previous symmetry between $\hat{x}$ and $\hat{y}$ polarizations when the sign of the phase anisotropy is changed, as can be inferred from Eq. (4.56). Now in order to have equivalent stability of the states by interchanging $\hat{x}$ and $\hat{y}$, one has to change both the sign of γ_a and the sign of γ_p. This is consistent with the idea that if we change which polarization state corresponds to a particular optical frequency (which is done by changing the sign of γ_p), we should change the sign of the amplitude anisotropy parameter that prefers one state over the other, if we want to have the modes interchange all of their properties and relative stabilities. For a fixed sign of γ_a, different signs of γ_p correspond now to different physical situations because of the fixed sign of the saturable dispersion governed by α.

Proceeding as we did in the case for $\gamma_a = 0$, we can determine the new instability boundaries for the linearly polarized solutions. We have considered two cases in which a small amplitude anisotropy is introduced in the system. The first case is when γ_a is negative (Fig. 4.9), in which $\hat{x}$-polarized emission is "favored" because its lasing threshold (threshold value of the injection current) is lower than the threshold for existence of the $\hat{y}$-polarized emission. The other situation is when γ_a is positive (fig. 4.10), in which the $\hat{y}$-polarization is "favored" because its lasing threshold is lower than that of the $\hat{x}$-polarized state.

In the stability diagram for $\gamma_a = -0.1\gamma$ (shown in Fig. 4.9), the $\hat{x}$-polarized solution is stable below the solid line, while the $\hat{y}$-polarized solution is stable inside the zone bounded by the dashed curves. There are zones in which only one mode is stable, zones of bistability and zones in which neither linearly polarized mode is stable.

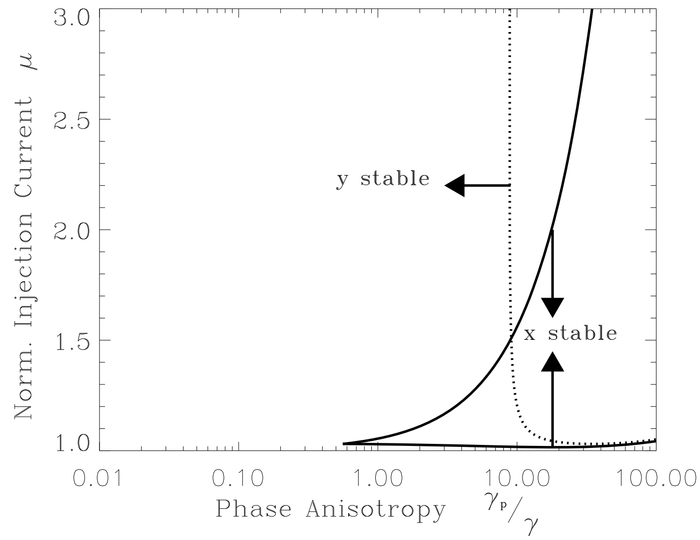

Figure 4.10: Stability diagram for γ_a =0.1γ; other parameters as in Fig. 4.3. $\hat{y}$-polarized mode has the lowest threshold.

As the birefringence (γ_p) goes to zero, only the $\hat{x}$-polarized solution is stable. In a large domain given roughly by $\mu > 1.1$ and $0.03 < \gamma_p/\gamma < 8.0$ only the $\hat{y}$-polarized mode is stable, indicating that despite the favoring by the gain anisotropy for the $\hat{x}$-polarized solution, the emission will switch to $\hat{y}$-polarized emission as the current is increased near threshold, an effect of the combination of saturable dispersion and birefringence similar to that which appeared in Fig. 4.3. For those values of γ_p for which as the current is increased the dashed curve is crossed before the solid curve is crossed, there will be hysteresis in the switching points as the injection current is raised from its threshold value where $\hat{x}$-polarized emission is found (switching at the solid line) or lowered from a value high enough that $\hat{y}$-polarized emission is found initially (switching at the dashed line). The $\hat{x} \longrightarrow \hat{y}$ switching current is given by

$$\mu = 1 + \frac{(\gamma_p^2 + \gamma_a^2)}{\kappa(\gamma_a + \alpha\gamma_p) - \gamma_p^2}\frac{\gamma_s}{\gamma_e} \ , \tag{4.58}$$

This switching is not abrupt. Rather it occurs through one of two frequency-degenerate (orthogonal orientations) stable elliptically polarized states. Consequently, elliptically polarized light can be understood as intermediate states reached in the destabilization by a steady bifurcation of the linearly polarized solution as the current is increased.

In the stability diagram for $\gamma_a = 0.1\gamma$ (shown in Fig. 4.10), the $\hat{x}$-polarized solution is stable in the region between the solid curves, while the $\hat{y}$-polarized solution is stable to the left and below the dashed curve. As in Fig 4.9 there are also zones where either one, both or none of the linearly polarized states are stable. As the birefringence (γ_p) goes to zero, only the $\hat{y}$-polarized (lower threshold) solution is stable. For $\gamma_p > 10.0\gamma$ and as the current is increased, there is a switching of stability from the $\hat{y}$-polarized mode to the $\hat{x}$-polarized mode — destabilization of the mode with higher gain-to-loss ratio in favor of the weaker mode—.

The main difference in the new values of the parameters from the case of isotropic gain shown in Fig. 4.3 is that the thresholds for the existence of the two modes differ. For the parameters we have chose these differences are small (the threshold current for the favored mode is lowered to 1 - 1/3000 and the threshold current for the existence of the other mode is raised to 1 + 1/3000). The somewhat unexpected consequence is that when the injection current is increased, the weaker mode does not always gain stability where the solution exists. Most strikingly the weak mode does not gain stability for any value of the current when the birefringence is small. These two effects are those which indicate the importance of the gain anisotropy, giving stability only to the mode with the higher gain-to-loss ratio. However, important zones remain near threshold, accessible for typical values of many VCSELs, in which the saturable dispersion and the birefringence combine to induce switching to the mode with the lower gain-to-loss ratio.

Now, we compare the polarization state switchings observed in these cases with those found in Sec.4.4. If the amplitude anisotropy favors $\hat{y}$-polarized emission as in Fig. 4.10, the state close to threshold will be always $\hat{y}$-polarized. For $\gamma_p = 2\gamma$ (barring strong noise-induced switching in the bistable region) this polarization state will be retained as the injection current is raised and lowered. However, if the amplitude anisotropy favors $\hat{x}$ polarization as in Fig. 4.9, the polarized state selected close to threshold will be $\hat{x}$-polarized. In this case, when $\gamma_p = 2\gamma$, we find the same type of switching (from $\hat{x}$-polarized to $\hat{y}$-polarized) when the current is increased as shown in Fig. 4.5, (recall that what is shown there is one of two possible outcomes depending on the noise-selected initial state at the lasing threshold). Unlike the switching found in the conditions of Fig. 4.5a, with the gain anisotropy represented in Fig. 4.9 there would be a reverse switching from $\hat{y}$-polarized to $\hat{x}$ polarized emission at about $\mu = 1.05$ as the current is lowered (instead of retaining the $\hat{y}$-polarized emission all the way down to the lasing threshold).

The amplitude anisotropy can also force a polarization switching in a situation where it does not exist when $\gamma_a = 0$. As an example, Fig. 4.11 shows the time-averaged power of each polarized mode for $\gamma_p = 10\gamma$ and $\gamma_a = 0.1\gamma$, where an abrupt switching from $\hat{y}$– to $\hat{x}$-polarized emission occurs (compare with Fig. 4.7). The switching current is given by

$$\mu = 1 + \frac{2(\gamma_s^2 + 4\gamma_p^2)}{\kappa(2\alpha\gamma_p - \gamma_s)}\frac{\gamma_a}{\gamma_e} \; . \tag{4.59}$$

Notice that the switching current linearly depends on the value of the amplitude anisotropy. The larger the amplitude anisotropy, the larger the current at which switching occurs for a fixed value of the rest of the parameters [8]. Such a dependence is consistent with recent experimental results in gain-guided VCSELs operated under fast pulse current operation (see Chap. 6). Hysteresis in the switching current, as reported experimentally [81] (see Fig. 1.11 (left, below)), is also numerically observed as the injection current is raised and lowered (see Fig. 4.12).

[8] If the amplitude anisotropy is large enough, the $\hat{y}$-polarized state will be the only stable polarization state for all accessible values of the current.

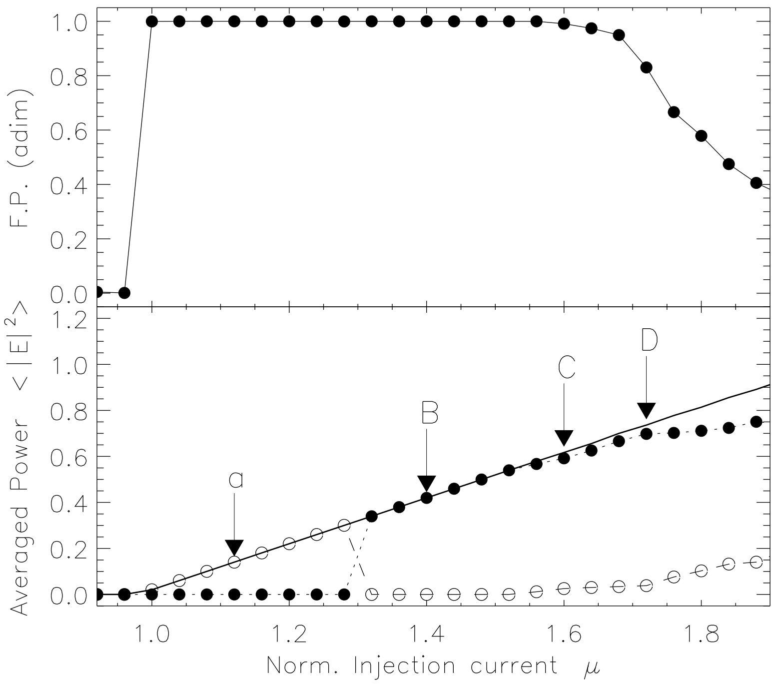

Figure 4.11: Light-current characteristic for each linearly polarized mode, and associated fractional polarization for γ_a =0.1γ. Rest of the parameters as in Fig. 4.7. Labels indicate emission in (a) $\hat{y}$ polarization, (B) $\hat{x}$ polarization, (C) periodically, and (D) chaotically modulated emission.

In summary, in this section we have demonstrated that a combination of spin-dynamics, birefringence and saturable dispersion can lead to polarization switchings, particularly to the selection (preferential stability) of the mode with higher losses. This points out that changes in the relative gain that result from self-heating of the device are not the only factor that influence the stability of linearly polarized solutions when spin-dynamics, VCSEL anisotropies and nonlinear dispersion of the semiconductor laser are considered. Which of these mechanisms, including temperature, is the primarily responsible for the experimentally observed switchings merits detailed experimental study because of the implications for specific designs and applications. Chap. 6 is devoted to this topic.

Finally, we point out that the rate-equation version of our model does not account for the appearance of higher order transverse modes as the fields and carrier numbers develop transverse spatial dependence. Hence, we have limited the studies in this and the previous Sections to values of the injection current for which the experiments indicate that it is reasonable to expect that only the fundamental transverse spatial mode would be lasing. Transitions to higher order transverse modes are observed experimentally depending on the device parameters, but they usually occur in VCSELs when the current exceeds between 1.3 and 2 times the threshold current. Then additional polarization instabilities are combined with changes in transverse mode profile [31, 47, 58]. The effects of higher-order transverse modes on the polarization state and spatial mode selection are studied in Chap. 7.

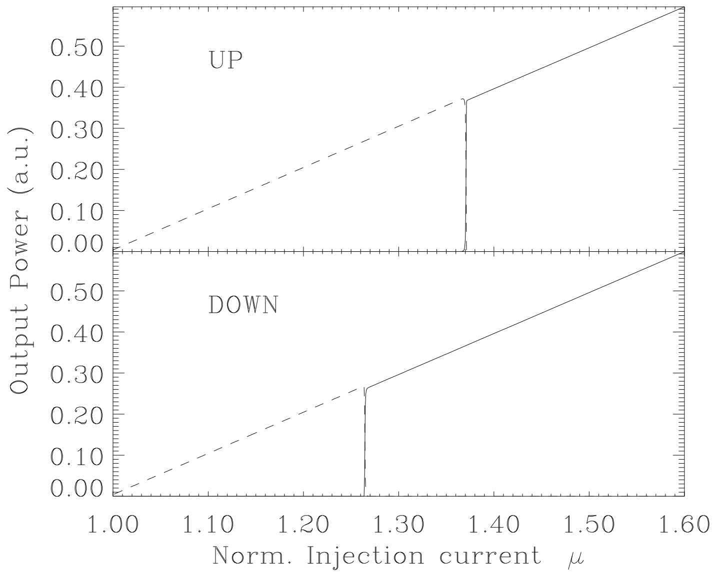

Figure 4.12: Hysteresis of the switching current when the injected current is raised (UP) and then lowered (DOWN). Solid (dashed) line stands for $\hat{x}$- ($\hat{y}$-) polarized light. The parameters used are $\gamma = 1\ ns^{-1}$, $\kappa/\gamma = 300$, $\gamma_s/\gamma = 50$, $\alpha = 3$, $\gamma_p/\gamma=60.0$, and $\gamma_a/\gamma=1.0$.

4.6 Plane wave vs. Gaussian approximation

In the previous sections we have neglected the dependence of the laser emission on the transverse coordinates. However, it is known that VCSELs close to threshold operate with the Gaussian mode TEM$_{00}$. In this section we show that the linear stability analyses for the plane wave model performed in Secs. 4.3 and 4.5 remain qualitatively valid even if one assumes that the laser beam has a Gaussian transverse profile. We write

$$F_{\pm}(r,t) = \mathrm{e}^{-(r/w_0)^2} f_{\pm}(t) \,, \tag{4.60}$$

where $f_{\pm}$ is the modal amplitude of the Gaussian mode, and w_0 is the beam waist, which can be taken constant along the very short active region in the longitudinal direction. The carrier populations D and d must then be functions of r and t, as well. The dynamical Eqs. (4.7)-(4.9) become [9]

$$\begin{aligned}
\dot{f}_{\pm} &= \kappa(1+\mathrm{i}\,\alpha)\left[\int_0^{\infty} du\ \mathrm{e}^{-u}(D\pm d)-1\right] f_{\pm} - (\gamma_a + \mathrm{i}\,\gamma_p) f_{\mp} \,, &(4.61)\\
\frac{\partial D}{\partial t} &= -\gamma\left[D-\mu(u)\right] - \gamma(D+d)\,\mathrm{e}^{-u}|f_+|^2 - \gamma(D-d)\,\mathrm{e}^{-u}|f_-|^2 \,, &(4.62)\\
\frac{\partial d}{\partial t} &= -\gamma_s d - \gamma(D+d)\,\mathrm{e}^{-u}|f_+|^2 + \gamma(D-d)\,\mathrm{e}^{-u}|f_-|^2 \,, &(4.63)
\end{aligned}$$

where we have introduced the new radial variable $u = 2(r/w_0)^2$. We also take the pump parameter μ to be a function of u. If the active region is a cylinder of radius

[9] We neglect the effects of carrier diffusion.

r_A, μ takes two different values for $u < 2(r_A/w_0)^2$ and $u > 2(r_A/w_0)^2$. Taking a finite value of the ratio r_A/w_0 allows to consider the effects of gain guiding. For simplicity we assume that the radius of the active region is much larger than the beam waist w_0, so that $2(r_A/w_0)^2 \to \infty$. In this approximation the pump parameter μ can be taken constant and the integration range for the variable u is $(0, \infty)$.

The linearly $\hat{x}$-polarized state is given by

$$
\begin{aligned}
f_\pm &= Q \; \mathrm{e}^{-\mathrm{i}\,(\gamma_p - \alpha\gamma_a)t} \,, && (4.64)\\
1 + \frac{\gamma_a}{\kappa} &= \mu \, \frac{\ln(1+2Q^2)}{2Q^2} \,, && (4.65)
\end{aligned}
$$

and the $\hat{y}$-polarized state by

$$
\begin{aligned}
F_\pm &= \pm\mathrm{i} \; Q \; \mathrm{e}^{\mathrm{i}\,(\gamma_p - \alpha\gamma_a)t} \,, && (4.66)\\
1 - \frac{\gamma_a}{\kappa} &= \mu \, \frac{\ln(1+2Q^2)}{2Q^2} \,. && (4.67)
\end{aligned}
$$

The amplitude Q has been taken real without loss of generality. A comparison with Eqs. (4.54) and (4.55) shows that the thresholds for the two solutions, obtained in the limit $Q \to 0$, coincide with those of the plane wave model ($\mu = 1 \pm \gamma_a/\kappa$). Linear stability analysis yields the following characteristic equation, where the upper (lower) signs hold for the $\hat{x}$- ($\hat{y}$-) polarized solution

$$
\left(\lambda + \frac{\gamma_s}{\gamma} - 1\right)\left[\lambda^2 \mp 4\frac{\gamma_a}{\gamma}\lambda + 4\left(\frac{\gamma_p}{\gamma}\right)^2 + 4\left(\frac{\gamma_a}{\gamma}\right)^2\right]
$$
$$
-2\left(\frac{\kappa}{\gamma} \pm \frac{\gamma_a}{\gamma}\right)\left[\lambda \mp 2\left(\alpha\frac{\gamma_p}{\gamma} + \frac{\gamma_a}{\gamma}\right)\right] + 2\left(\lambda + \frac{\gamma_s}{\gamma}\right)\left(\frac{\kappa}{\gamma} \pm \frac{\gamma_a}{\gamma}\right)
$$
$$
\left[\lambda \mp 2\left(\frac{\gamma_a}{\gamma} + \alpha\frac{\gamma_p}{\gamma}\right)\right] \frac{\ln\left[1 + 2Q^2/(\lambda + \gamma_s/\gamma)\right]}{\ln(1+2Q^2)} = 0 \,. \qquad (4.68)
$$

Eq. (4.68) is implicit in λ because λ is contained in the argument of a logarithm. However, we are interested just in finding the stability boundaries, where, by definition, $Re(\lambda) = 0$. Therefore, we can study Eq. (4.68) in the limit $Re(\lambda) \ll \gamma_s/\gamma$. Since $\gamma_s \gg \gamma$ and Q^2 is typically of order 1 or less, we can make the following approximation

$$
\ln\left(1 + \frac{2Q^2}{\lambda + \gamma_s/\gamma}\right) \simeq \frac{2Q^2}{\lambda + \gamma_s/\gamma} = \frac{\mu\kappa}{\kappa \pm \gamma_a} \frac{\ln(1+2Q^2)}{\lambda + \gamma_s/\gamma} \,. \qquad (4.69)
$$

Inserting Eq. (4.69) into Eq. (4.68) we obtain a cubic equation in λ of the form $P(\lambda) = 0$, as in the plane wave case. The characteristic polynomial is

$$P(\lambda) = \lambda^3 + \left(\frac{\gamma_s}{\gamma} - 1 \mp 4\frac{\gamma_a}{\gamma}\right)\lambda^2$$

$$+4\left[\left(\frac{\gamma_p}{\gamma}\right)^2 + \left(\frac{\gamma_a}{\gamma}\right)^2 + \frac{\kappa}{\gamma}\frac{\mu - 1}{2} \mp \frac{\gamma_a}{\gamma}\left(\frac{\gamma_s}{\gamma} - \frac{1}{2}\right)\right]\lambda$$

$$+4\left[\left(\frac{\gamma_p}{\gamma}\right)^2 + \left(\frac{\gamma_a}{\gamma}\right)^2\right]\left(\frac{\gamma_s}{\gamma} - 1\right) \mp 4\frac{\kappa}{\gamma}\left(\mu - 1 \mp \frac{\gamma_a}{\kappa}\right)\left(\frac{\gamma_a}{\gamma} + \alpha\frac{\gamma_p}{\gamma}\right) , \qquad (4.70)$$

which is very similar to Eq. (4.57). In the limit $\gamma_s \gg \gamma$ and $Q^2 \simeq 1$ the two polynomials coincide. For $\gamma_s = 50\gamma$ the stability boundaries defined by Eq. (4.70) are almost indistinguishable from those given by Eq. (4.57) and represented in Fig. 4.3. We have also checked that the averaged light power vs. injected current curve for each polarization state obtained by numerical integration of Eqs. (4.61–4.63) coincides with that of Fig. 4.5 if the same parameters values are used (except for a different scaling of average power). As a consequence the polarization behavior of the laser is essentially the same if the modal profiles of the fundamental mode are taken into account.

4.7 Polarization switching induced by optical injection

In Secs. 4.4 and 4.5 we have shown several examples of polarization switching obtained by varying one of the VCSELs parameters, namely the pump intensity μ. However, polarization switching can be also obtained by fixing the parameters of the VCSEL and by injecting into the laser an optical signal whose polarization is orthogonal to that emitted by the laser [70, 81]. Two different situations should be considered depending on the stability of both linearly polarized states. If the system is bistable, with a sufficiently strong or sufficiently long injected signal to cause switching, the laser will remain on the new state. If the system is monostable the laser will go back to the initial state soon after the injected signal is removed.

We have analyzed both cases, considering the Gaussian model presented in the previous section. The term describing the external field can be easily inserted in the equations. For instance, if one considers injection of a $\hat{y}$-polarized beam, the equations for the field amplitudes are

$$\begin{aligned} \frac{df_x}{dt} &= \kappa\,(1+\mathrm{i}\,\alpha)\left[\int_0^\infty du\;\; \mathrm{e}^{-u}\,(D\;f_x + \mathrm{i}\;\;d\;f_y) - f_x\right] \\ &\quad -\mathrm{i}\;\,(\gamma_p + \Delta\omega)\;f_x - \gamma_a\;f_x\;, &(4.71)\\ \frac{df_y}{dt} &= \kappa\,(1+\mathrm{i}\,\alpha)\left[\int_0^\infty du\;\; \mathrm{e}^{-u}\,(D\;f_y - \mathrm{i}\;\;d\;f_x) - f_y\right] \\ &\quad +\mathrm{i}\,(\gamma_p - \Delta\omega)\;f_y + \gamma_a\;f_y + \kappa_{inj}\;f_{inj}\;, &(4.72)\end{aligned}$$

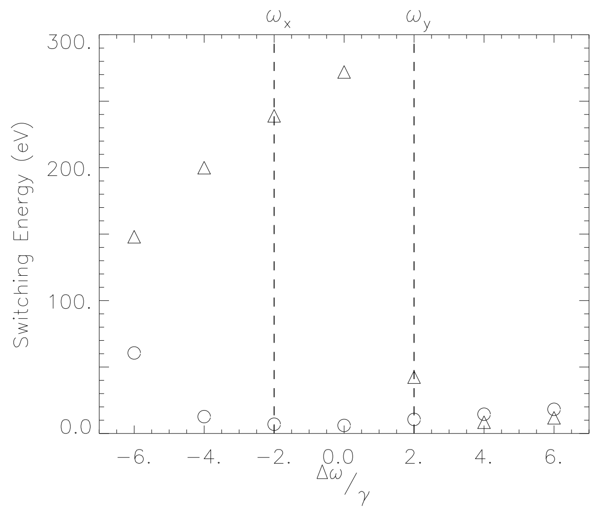

Figure 4.13: Switching by injection of 1 ns long pulses in a bistable situation given by $\mu = 1.1$ from the conditions of Fig. 4.5 and γ_a=0.5 γ. Switching energy for the transition $\hat{y} \to \hat{x}$ (triangles) and for the opposite transition (circles) as a function of the scaled frequency detuning $\Delta\omega/\gamma$.

where κ_{inj} is the coupling coefficient, which coincides with the inverse photon lifetime κ for an ideal case of effectively mode-matched injected input beam — the injected beam has the same waist than the input beam, and does not present misalignment —. The amplitude of the injected field is f_{inj} and its frequency ω_{inj} is now taken as the reference frequency. The frequency detuning $\Delta\omega$ is defined as the difference between ω_{inj} and the frequency intermediate between those of the $\hat{x}$-polarized ($\omega_x = -\gamma_p$) and $\hat{y}$-polarized ($\omega_y = \gamma_p$) solutions. Therefore $\Delta\omega = -\gamma_p$ ($\Delta\omega = \gamma_p$) means that the injected field is resonant with the $\hat{x}$ ($\hat{y}$) polarization of the VCSEL. We have studied the response of the laser to optical injection for different values of the injected power $|f_{inj}|^2$ and of the frequency detuning $\Delta\omega$, in both the bistable and the monostable cases.

Fig. 4.13 presents results for a bistable case corresponding to the parameters of Fig. 4.3 and $\gamma_p = 2\gamma$, $\mu = 1.1$, and $\kappa_{inj} = \kappa$. The frequency detuning $\Delta\omega$ varies from -6γ to 6γ. For this bistable situation, the injected signal is a rectangular pulse of normalized duration Δt_{inj}. We estimated the injected energy in the following way: the injected power P and the power emitted by the VCSEL P_0 are proportional, respectively, to $|f_{inj}|^2$ and $2Q^2$, where Q is the stationary amplitude given by Eqs. (4.65) and (4.67). Then, the injected energy is

$$F_{inj} = P\,\Delta t_{inj} = \frac{P}{P_0}\,P_0\,\Delta t_{inj} = \frac{|f_{inj}|^2}{2Q^2}\,P_0\,\Delta t_{inj}\ . \tag{4.73}$$

We have fixed $\Delta t_{inj} = 1$ ns in all simulations, and the power P_0 emitted by the VCSEL close to threshold can be assumed to be about 0.1 mW. The switching energy is then obtained by inserting in Eq. (4.73) the minimum value of f_{inj} for which switching occurs.

In Fig. 4.13 the triangles indicate the switching $\hat{y} \to \hat{x}$ by injecting a $\hat{x}$-polarized pulse in a state initially $\hat{y}$-polarized. The circles are for the inverse switching $\hat{x} \to \hat{y}$

caused by injection of a $\hat{y}$-polarized pulse. The dashed lines indicate resonance of the injected signal with the eventually reached $\hat{x}$– or $\hat{y}$-polarized state. The behavior of the laser is very different for two possible directions of switching. In general, the switching energy is much higher for the first case (switching to the less stable state). It is evident that the most efficient (least energy demanding) switch is accomplished by setting the frequency of the injected signal to a value different from the frequency of the desired final state. This is a reminder that the actual switching transient may be a complicated trajectory in the 6-dimensional phase space. For $\Delta\omega/\gamma = 4$ and $\Delta\omega/\gamma = 6$ the switching energies are comparable and very small, on the order of 10 eV. Taking into account that the energy of 1 photon of wavelength 850 nm is about 1.5 eV, the arrival of 10 photons in 1 ns is enough to make the laser to switch in the situation of effectively mode matched injection considered here.

We next consider a different situation of switching by injection as it occurs in a parameter region in which there is no bistability. This is the experimental situation described in [70] and we have tried to keep our simulations as close as possible to those experiments. The reported frequency difference between orthogonal linearly polarized emissions is 9 GHz. Taking into account that in our model this frequency difference is given by $2\gamma_p/(2\pi)$, we took γ_p=30 rad ns^{-1}. The amplitude anisotropy parameter γ_a was chosen in such a way that in a scan of the injected current as in Fig. 4.11, the laser switches from the $\hat{y}$-polarized to the $\hat{x}$-polarized state at about $\mu = 1.2$, in agreement with Figure 1 of [70] (see Fig. 1.11 (right,above)). For the other parameters we used the same values as those used for Fig. 4.3 and $\kappa_{inj} = \kappa$. We fixed $\mu = 1.5$, above the current at which the polarization switching occurred, where only the $\hat{x}$-polarized state is stable, and we simulated an injected signal of a beam of orthogonally polarized light. Following the experimental procedure, the injected optical power was increased linearly in time until switching occurred, and then the injected power was decreased to zero. In agreement with the experimental results, we found polarization bistability in laser emission, as shown in Fig. 4.14(left). Adiabatically sweeping the injected power P from 0 to 0.7% of the emitted power P_0 and back, we found an hysteresis cycle for both polarization components. Sometimes the switching is not so clean (abrupt) as in Fig. 4.14(left), and we have found more gradual transitions from one polarized mode to the other. This feature appears frequently in experimental results. Moreover, in our dynamical simulations very often the intensities of both modes oscillated, though at high frequencies corresponding to the intermode beat note frequency ($2\gamma_p$) and higher harmonics.

The values of power P for which the $\hat{x}$-polarized component of the emitted field switches off and on for different detunings $\Delta\omega$ are shown in Fig. 4.14(right). The triangles indicate switch–off power and the circles switch–on power. This figure presents many similarities with Figure 4 of [70]. In both cases the minimum switch–off power is attained when the frequency of the injected field coincides with that of the VCSELs state with the same polarization (in our case ω_y, in the case of [70] $\omega_\perp$). Moreover the hysteresis cycle is larger on the small frequency (large wavelength) side, while there is a gradual transition from one polarization to the other in the opposite side.

However, the value of the switching power compared to the power emitted by the VCSEL is about three orders of magnitude smaller than in the experiment, although

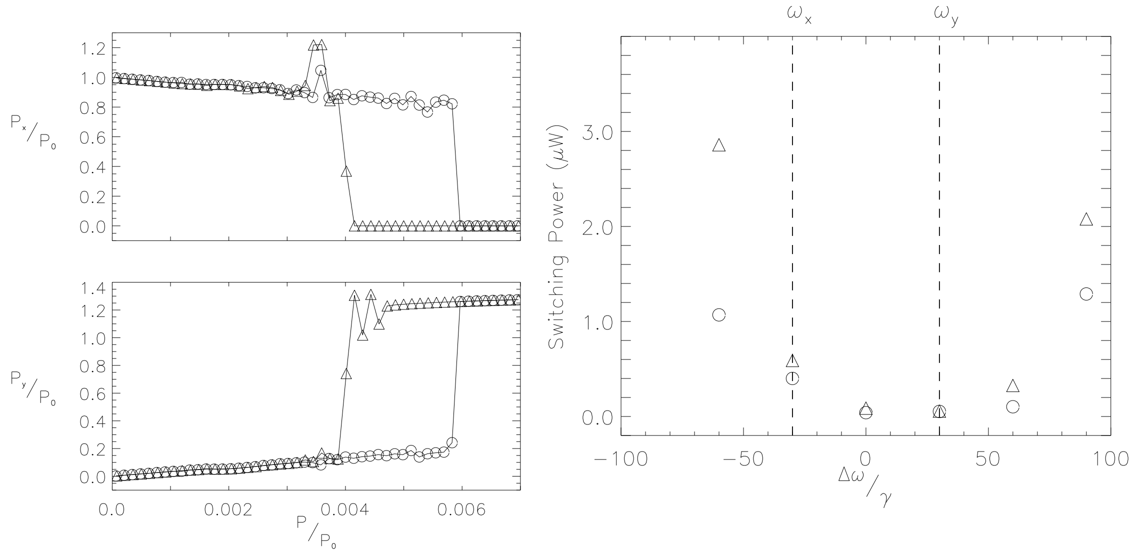

Figure 4.14: (left) Switching occurring upon injection of signal with first linearly increasing and then linearly decreasing intensity in a monostable situation. Hysteresis cycles for the power of the $\hat{x}$-polarized and $\hat{y}$-polarized components of the light emitted by the VCSEL versus the normalized injected power. The symbols represent average emitted power over a time interval of 80 ns. The circles refer to the scan with increasing injected power and the triangles to the scan with decreasing injected power. The frequency detuning is $\Delta\omega = -30\gamma$, and γ_a=0.5 γ; and (right) Switching points found by injection in a monostable situation as in Fig. 4.13. Switch–off (triangles) power level for increasing injected power and switch–on (circles) power level for decreasing injected power for different values of the scaled frequency detuning $\Delta\omega/\gamma$.

one has to take into account that such a ratio depends critically on the value of the coupling parameter κ_{inj} (in our analysis we consider $\kappa_{inj} = \kappa$). In the real experiment most of the injected power is lost because it is very difficult to match perfectly the injected beam and the beam inside the resonator. Hence, differences in the beam waist of the input beam relative to the fundamental mode waist of the VCSEL and/or displacement or misalignment of the injected beam relative to the VCSEL axis will lead to a value of κ_{inj} considerably smaller than κ which results in a much larger experimental value of the switching power. In addition, discrepancies of our results with experiments can also be due to the intensity induced changes in the frequency difference between the two polarization modes which are not included in our model.

Chapter 5

Polarization dynamics in the fundamental transverse mode of a VCSEL with an axial magnetic field

Abstract [1].

We study the effects of an axial magnetic field on the polarization characteristics of Vertical-Cavity Surface-Emitting Lasers. We observe that a weak magnetic field induces emission of elliptically polarized light. Hence, the characteristic switching between orthogonal linearly polarized states with zero magnetic field becomes a switching between elliptically polarized states with low ellipticity. Larger magnetic fields induce time-dependent solutions with two main peaks in the optical spectrum and orthogonal elliptically polarized basis states. Strong magnetic fields induce rotating elliptically polarized emission, a state which closely resembles rotating linearly polarized light but with small residual modulation of the ellipticity because of linear birefringence. Based on the latter result, we explore the possibility of generating low-chirped, fast optical, linearly polarized pulses in closely isotropic VCSELs.

[1]This chapter is based on the papers *(i) "Polarization dynamics in a vertical cavity laser with an axial magnetic field"*, by C. Serrat, N. B. Abraham, M. San Miguel, R. Vilaseca, and J. Martín-Regalado, *Physical Review A (Rapid Comm.)*, **53**, 3731 (1996); and *(ii)"High-Bit-Rate Generation of Low-Chirped Pulses from Vertical-Cavity Surface-Emitting Lasers via External Axial Magnetic Field"*, by Han van der Lem, J. Martín-Regalado, S. Balle, and Claudio R. Mirasso, accepted in *Photon. Tech. Lett.*

5.1 Introduction

VCSELs most often emit linearly polarized light preferentially oriented along one of two perpendicular directions associated with the crystal axes. Misalignment of linear birefringency and dichroism axes may cause elliptically polarized emission with small remnant ellipticity [130]. Elliptically polarized emission has also been observed experimentally for VCSELs under the influence of an axial magnetic field, with greater ellipticity for increasing injection current and/or magnetic field strength [82].

From the point of view of the four-level model described in Chap. 4 one would expect an applied magnetic field to enhance the dynamical role of the magnetic sublevels by breaking the degeneracy of the resonant frequencies for left and right circularly polarized fields as a consequence of Zeeman splitting. When combined with the intrinsic linear birefringence of the VCSEL, the magnetically-induced circular birefringency would then naturally transform the preferred basis states of the system from linearly polarized to elliptically polarized. An extreme case of magnetically coupled radiation channels for circularly polarized fields might lead to simultaneous emission on both transitions, with the frequency difference resulting in a state of almost rotating linear polarization. This leads us to expect that a magnetic field of intermediate strength might stabilize two-frequency solutions with simultaneous emission of two elliptically polarized states. Motivated by these expectations we analyze in this Chapter the predictions of the rate-equation four-level model for single transverse mode VCSELs in an axial magnetic field.

5.2 Model and analytical results

The starting point is the simplified four-level model describing the allowed optical transitions in the VCSEL quantum-well medium. An axial magnetic field, $B = B_z\vec{z}$, will induce Zeeman splitting [2] on the magnetic sublevels involved in the lasing process as [97]

$$E^i = E_0^i - \mu_B g \vec{B} \cdot \vec{J} = E_0^i - \mu_B g B_z J_z^i \tag{5.1}$$

where E_0^i is the zero field energy of level i, μ_B is the Bohr magneton, g is the Lande factor, and J_z is the third component of the total angular momentum. The resulting four-level model is depicted in Fig. 5.1.

Therefore, as a consequence of the magnetic field the frequencies of the circularly polarized fields with opposite helicities will be split proportionally to the strength of the applied magnetic field. This effect can be included in the equations governing the laser dynamics by means of a circular phase anisotropy (see Appendix C). Eqs. (4.7)-(4.9) now read

[2] Zeeman splitting has been observed in GaAs/AlGaAs quantum-well samples in magnetic fields up to 4T [149]. In this study, it is found that the magnetic field has small influence on the spin-flip relaxation time.

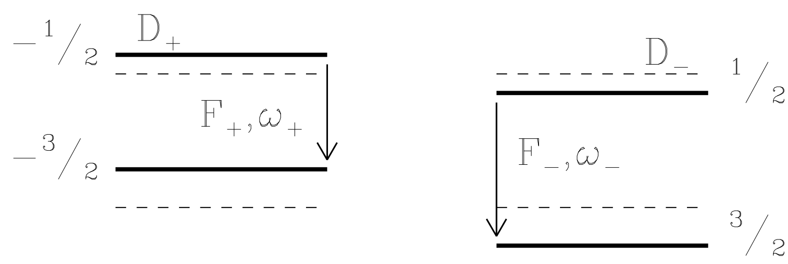

Figure 5.1: Four level model for polarization dynamics in QW-VCSEL's (dashed levels) modified by an axial magnetic field (solid levels).

$$
\begin{aligned}
\dot{F}_{\pm} &= \kappa(1+\mathrm{i}\,\alpha)(D \pm d - 1)F_{\pm} - (\gamma_a + \mathrm{i}\,\gamma_p)F_{\mp} \pm \mathrm{i}\,\gamma_z(B)F_{\pm}\ , &(5.2)\\
\dot{D} &= -\gamma(D-\mu) - \gamma(D+d)|F_+|^2 - \gamma(D-d)|F_-|^2\ , &(5.3)\\
\dot{d} &= -\gamma_s d - \gamma(D+d)|F_+|^2 + \gamma(D-d)|F_-|^2\ , &(5.4)
\end{aligned}
$$

where $\gamma_z(B)$ represents the magnetically-induced frequency splitting of the circularly polarized modes — circular birefringency — which depends linearly on the magnetic field strength, B, as [82]

$$d\gamma_z/dB = 8.3 \text{ rad } GHz\, T^{-1}\ . \tag{5.5}$$

For a perfect isotropic VCSEL, γ_p=γ_a=0, Eqs. (5.2)-(5.4) allows three different steady-state solutions. Considering the general solution

$$F_{\pm} = Q_{\pm} e^{\mathrm{i}\,(\omega_{\pm} t \pm \psi)}\ , \quad D = D_0\ , \quad d = d_0\ ,$$

the first two solutions are a pair of unstable, orthogonal, circularly polarized states, given by

$$\left\{ \begin{array}{ll} Q_+^2 = \frac{1}{2}\left(\mu - D_0 - d_0\gamma_s/\gamma\right)\ , & Q_- = 0\ , \\ \omega_+ = +\gamma_z\ , & \psi \text{ is arbitrary}\ , \\ d_0 = -(\mu-1)/(\gamma_s/\gamma+1)\ , & D_0 = 1 - d_0\ , \end{array} \right. \tag{5.6}$$

and

$$\left\{ \begin{array}{ll} Q_-^2 = \frac{1}{2}\left(\mu - D_0 + d_0\gamma_s/\gamma\right)\ , & Q_+ = 0\ , \\ \omega_- = -\gamma_z\ , & \psi \text{ is arbitrary}\ , \\ d_0 = +(\mu-1)/(\gamma_s/\gamma+1)\ , & D_0 = 1 + d_0\ , \end{array} \right. \tag{5.7}$$

The only stable state is a rotating linearly polarized solution, which reads

$$F_{\pm} = \sqrt{\frac{\mu - 1}{2}} e^{\pm \mathrm{i}\,(\gamma_z t + \psi)} \,, \quad D = 1 \,, \quad d = 0 \,, \tag{5.8}$$

corresponding to the vector optical field

$$\vec{F} = \sqrt{\mu - 1}[e^{\mathrm{i}\,(\gamma_z t + \psi)} \vec{a}_+ + e^{-\mathrm{i}\,(\gamma_z t + \psi)}) \vec{a}_-] \,, \tag{5.9}$$

or, equivalently

$$\vec{F} = \sqrt{\mu - 1}[cos(\gamma_z t + \psi)\vec{a}_x + sin(\gamma_z t + \psi)\vec{a}_y] \,, \tag{5.10}$$

with ψ being an arbitrary angle set to zero for convenience. Hence, the emitted power in each linearly polarized component is given by

$$P_{\substack{x \\ y}} = |F_{\substack{x \\ y}}|^2 \;\; = \;\; \frac{\mu - 1}{2}[1 \pm cos(2\gamma_z t)] \,. \tag{5.11}$$

Therefore, a perfectly isotropic VCSEL in an axial magnetic field can only emit in a rotating linearly polarized state, where the polarization of the output light is linear but its azimuth (orientation) periodically oscillates in time with a frequency $(2\gamma_z)$ that depends on the strength of the magnetic field.

In the next section, we will numerically study the polarization state of the VCSEL output under the influence of an axial magnetic field in the case of an anisotropic VCSEL.

5.3 Numerical analysis

In absence of external magnetic field ($\gamma_z = 0$), Eqs. (4.7)-(4.9) predict different domains of stability for the $\hat{x}$- and $\hat{y}$-polarized steady — constant intensity — states (see, Fig. 4.3)) which have different optical frequencies given by $-\gamma_p$ and $+\gamma_p$, respectively. Depending on the values of the birefringence parameter γ_p and the injection current μ either one, both or none of the two linearly polarized states are stable. As an illustration we restrict this Section to a situation of low birefringence in which increasing μ changes the system from a domain of bistability to a domain in which only the $\hat{y}$-polarized emission is stable. Let us consider also that $\gamma_a < 0$, such that the $\hat{x}$-polarized mode is favored close to threshold and for increasing current there is a $\hat{x} \longrightarrow \hat{y}$ polarization switching at $\mu = 1.15$ ($\gamma_p = 2\gamma, \gamma_a = -0.1\gamma$).

For non-zero but weak magnetic field the linearly $\hat{x}$ and $\hat{y}$-polarized steady states become elliptically polarized with small ellipticity and major axis oriented towards the $\hat{x}$ and $\hat{y}$ axes. We will denote these states as ϵ_x and ϵ_y, respectively. These elliptically polarized states are characterized by the ellipticity parameter, defined as

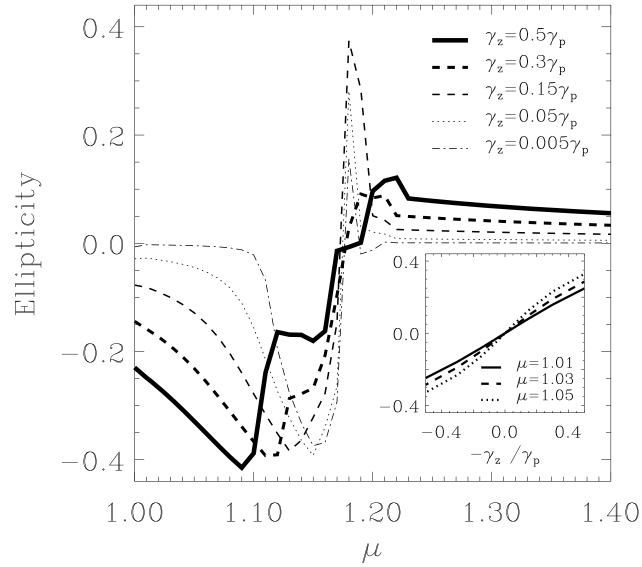

Figure 5.2: Ellipticity (χ) vs. injection current (μ) for indicated values of the magnetic field strength (γ_z). Inset: χ vs. γ_z for small values of μ. The parameter values are: $\kappa = 300ns^{-1}$, $\gamma = 1ns^{-1}$, $\gamma_s = 50ns^{-1}$, $\alpha = 3$, $\gamma_p = 2\gamma$, and $\gamma_a = -0.1\gamma$.

$$\chi(t) = \frac{1}{2} \arcsin\left(\frac{|E_+(t)|^2 - |E_-(t)|^2}{|E_+(t)|^2 + |E_-(t)|^2}\right) \tag{5.12}$$

Fig. 5.2 shows the ellipticity for the solutions found as the current was increased in small steps and for several circular birefringences (several magnetic field strengths). At threshold, the solutions are ϵ_x-type. Its ellipticity increases in absolute value for increasing current up to $\mu \approx 1.1$. The inset of the figure shows the dependence of the ellipticity on γ_z for fix current values close to threshold. The ellipticity linearly depends on the circular birefringence in the range of very weak magnetic fields and saturates for larger values. Both features are in good agreement with the experimental observations in [82]. For current values above the switching current, the solutions are ϵ_y-type, with the ellipticity decreasing with increasing current, but very smoothly.

Time-dependent states are found as intermediate states in the switching from ϵ_x to ϵ_y. These time-dependent solutions are more prevalent with increasing magnetic field, and some samples are shown in Fig. 5.3. We denote them as "M"-states (elliptical polarization with Modulated ellipticity and modulated azimuth about nonzero mean values), "R"-states (states with periodically modulated ellipticity around a zero mean and with a Rotating azimuth), and "R_E"-states (states which resemble rotating linearly polarized light but having a small residual modulation of the ellipticity as a consequence of the non-vanishing linear anisotropies.). Their characterization in Fig. 5.3 is given in terms of their total optical spectrum (sum of the optical spectra of the circular field components, E_+ and E_-) and their representation in the Poincare sphere [99].

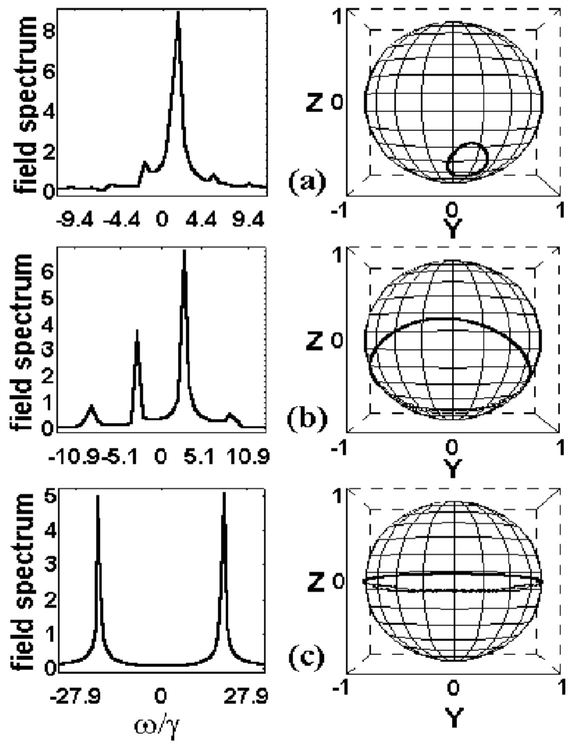

Figure 5.3: Optical power spectrum and Poincare sphere representation of time-dependent solutions termed (a) M, (b) R, and (c) R_E as discussed in the text. The parameter values are those in Fig. 5.2 and (a) $\mu = 1.16$, $\gamma_z = 0.01\gamma_p$; (b) $\mu = 1.1$, $\gamma_z = \gamma_p$; (c) $\mu = 1.1$, $\gamma_z = 10\gamma_p$.

All three states have two predominant peaks in their optical spectra. The state we call "M" has unequal strengths in its spectral components, elliptical polarization for each spectral component, and a small closed trajectory on the Poincare sphere. The stronger spectral component has the elliptical polarization state given by the center of the trajectory. The state we call "R" has two nearly equally strong spectral components, and is thus represented by what is nearly a great circle on the Poincare sphere. The elliptically polarized states of the spectral components are given by the intersections of the surface of the Poincare sphere with the diameter which is perpendicular to the plane of the circular trajectory. The state "R_E" is a limiting case of "R" in which the basis states of the spectral components are almost circularly polarized, a condition reached only asymptotically for very large magnetic fields for the parameters we have chosen (or weak magnetic fields in isotropic VCSELs).

Fig. 5.4(a) is the phase diagram showing the dominant polarization states of the VCSEL in an axial magnetic field as a function of μ and γ_z for the parameters of Fig. 5.2 [3]. For simplicity we use the symbol M in this figure to denote not only the time-dependent states of modulated ellipticity such as that shown in Fig. 5.3(a) (which appears after a Hopf bifurcation destabilizes the ϵ_x solution) but also more

[3]It is obtained by adiabatically increasing the injection current for a fixed magnetic field strength

γ_z	$100\gamma_p$	R_E	R_E	R_E	R_E	R_E	R_E	R_E	$\cdots$	R_E
	$10\gamma_p$	R_E	R_E	R_E	R_E	R_E	R_E	R_E	$\cdots$	R_E
	γ_p	ε_x	R	R	R	R	R	ε_y	$\cdots$	ε_y
	$0.7\gamma_p$	ε_x	M	R	R	R	ε_y	ε_y	$\cdots$	ε_y
	$0.1\gamma_p$	ε_x	ε_x	ε_x	M	R	ε_y	ε_y	$\cdots$	ε_y
	$0.01\gamma_p$	ε_x	ε_x	ε_x	ε_x	R	ε_y	ε_y	$\cdots$	ε_y
	0	L_x	L_x	L_x	ε_x	R	L_y	L_y	$\cdots$	L_y
(a)	μ	1.0	1.05	1.10	1.15	1.20	1.25	1.30	$\cdots$	2.0

γ_z	$100\gamma_p$	R_E	R_E	R_E	R_E	R_E	R_E	R_E	$\cdots$	R_E
	$10\gamma_p$	R_E	R_E	R_E	R_E	R_E	R_E	R_E	$\cdots$	R_E
	γ_p	ε_x	R	R	R	ε_y	ε_y	ε_y	$\cdots$	ε_y
	$0.7\gamma_p$	ε_x	M	R	ε_y	ε_y	ε_y	ε_y	$\cdots$	ε_y
	$0.1\gamma_p$	ε_x	ε_y	ε_y	ε_y	ε_y	ε_y	ε_y	$\cdots$	ε_y
	$0.01\gamma_p$	ε_x	ε_y	ε_y	ε_y	ε_y	ε_y	ε_y	$\cdots$	ε_y
	0	L_x	L_y	L_y	L_y	L_y	L_y	L_y	$\cdots$	L_y
(b)	μ	1.0	1.05	1.10	1.15	1.20	1.25	1.30	$\cdots$	2.0

Figure 5.4: Sequence of states (L–linearly polarized, others as identified in Fig. 5.3 and the text) observed with adiabatically (a) increased and (b) decreased injection current for indicated γ_z values. M states always appeared with increasing μ between ϵ_x and R states, but they are not indicated unless they appeared for the specific values of μ chosen for these tables. The parameter values are those in Fig. 5.2.

complicated states of modulated ellipticity including figure-8's on the Poincare sphere. The results for no magnetic field include states labeled "L_x" and "L_y" for x and y-polarized states, respectively.

We find three different scenarios in this switching process depending on the strength of the magnetic field (γ_z). (1) For a weak magnetic field ($\gamma_z << \gamma_p$) the switching from ϵ_x to ϵ_y occurs through narrow regions of intermediate M and R states. This is a small modification of what happens for zero magnetic field where the switch from L_x to L_y occurs through intermediate ϵ_x and M states. (2) When $\gamma_z \sim \gamma_p$, the switching occurs through broader regions of intermediate M and R states. (3) For very large magnetic fields, emission occurs in rotating elliptically polarized states, R_E. In addition, the system is bistable for low injection currents and there is hysteresis of the switching current, when μ is first raised and then lowered. State sequences with decreasing injection current showing such a behavior are shown in Fig. 5.4(b).

Therefore, the results indicate that substantial zones of polarization switching which may be useful for signal applications remain for low magnetic fields, with the switching occurring between distinguishable states of different azimuth and low ellipticity. The dynamically significant strength of magnetic fields for qualitative changes in behavior is set by $\gamma_z \sim \gamma_p$.

5.4 Generation of fast optical pulses from VCSELs via External Axial Magnetic Field

Transmissions at 10 Gb/s for 980 nm [83] and 2.5 Gb/s for 1.54 μm VCSELs [173] have been recently obtained by direct modulation of the injection current in VCSELs. However, these systems do not take advantage of their polarization properties which may lead to, e.g., chirp reduction, improvement of the Signal-to-Noise Ratio (SNR), duplication of the transmission capability, etc.

Optical pulses with alternating polarization have been obtained in VCSELs by modulating the injection current around the switching point, but a maximum modulation rate of 50 MHz has been achieved [174]. This limitation in the maximum frequency could be due to either the thermal response of the device [174], or to spatial-hole burning [93]. Polarization self-modulation at GHz rates has been also observed by means of external optical feedback-induced polarization locking [71].

Motivated by the results in Eq. (5.2), we explore now the possibility of generating fast optical pulses by applying an axial magnetic field. We have already seen that, for closely isotropic VCSELs such that $\gamma_z \gg \gamma_p, \gamma_a$, the rotating linearly polarized state becomes rotating elliptically polarized, but with a very small remnant ellipticity.

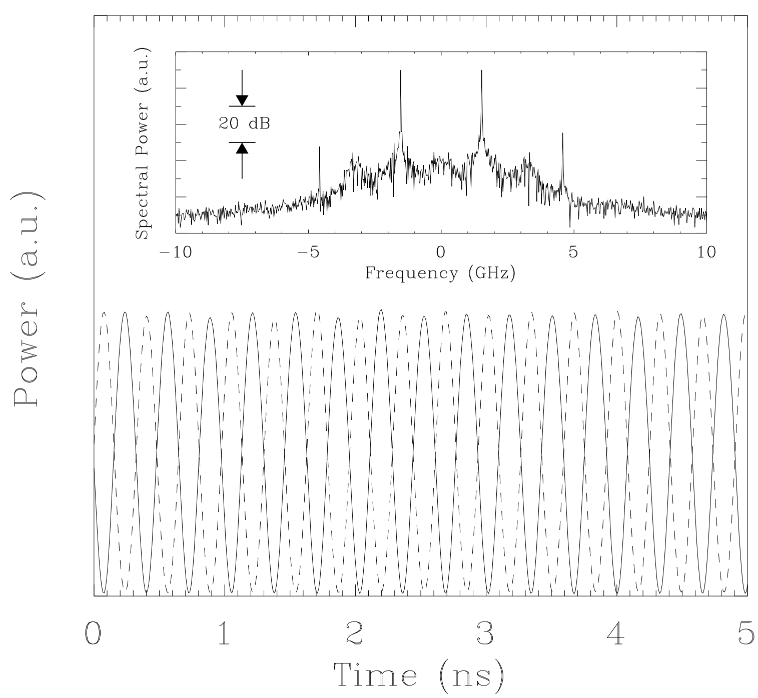

Figure 5.5: Output power for the $\hat{x}$- (solid) and $\hat{y}$- (dashed) linearly polarized components corresponding to a rotating elliptically polarized state at 1.2 μ_{th}. The inset shows the optical spectrum of this polarization state. Parameters: γ = 1 ns^{-1}, κ/γ = 300, γ_s/γ = 100, α = 4, γ_p/γ= 2, γ_a/γ=0.1, and γ_z/γ=9.42.

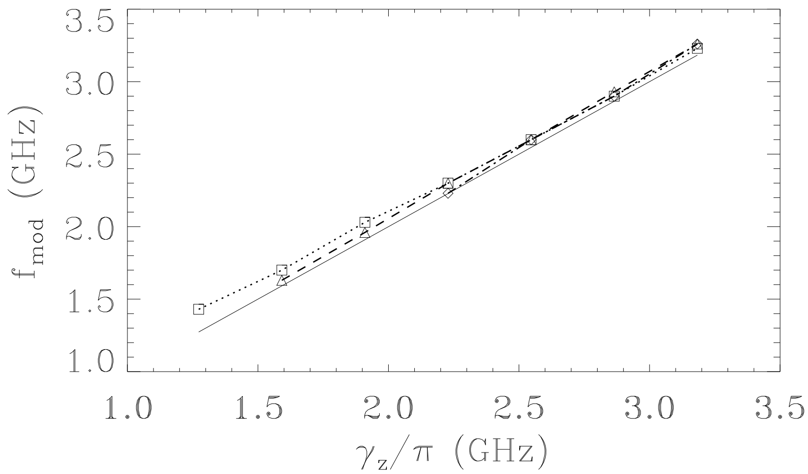

Figure 5.6: Dependence of the pulse frequency (f_p) on the magnetically-induced circular birefringency (γ_z) for different values of the applied current: 1.2 (squares), 1.5 (triangles),and 1.8 μ_{th} (diamonds). Same parameters as in Fig. 5.5. The corresponding magnetic field strengths can be roughly estimated, using Eq. (5.5), to vary between 0.4 and 1.3 T.

Nevertheless, modulation of the polarized output still occurs as inferred from Fig. 5.5, where we plot the output power for both linear polarizations as a function of time, solid (dashed) line stand for $\hat{x}$ ($\hat{y}$) polarization. Very clear optical pulses are obtained at a rate of $\sim$ 3.1 GHz for each linear polarization. This periodically modulated output can be used, e.g., for optical clock generation without requiring high speed electronics. An additional advantage of this laser system is that each polarization can be encoded independently by an external electro-optical modulator, so the amount of information can be duplicated.

The inset in Fig. 5.5 shows the optical spectrum of the rotating elliptically polarized state, after including Langevin noise terms to Eqs. (5.2)-(5.4). The two main peaks, at frequencies at -1.5 and 1.5 GHz, correspond to the emission frequencies of the left and right circularly polarized states, respectively, which form the rotating linearly polarized solution (see Eq. (5.9)). The additional side bands come as a consequence of the residual linear anisotropies. It is worth noting that, since the rotating elliptically polarized solution is a steady state of the system for a fixed value of the injection current, and consequently the carriers are clamped to the threshold, the pulses so obtained have no (or very small) transient chirp. When comparing with, for example, gain-switched pulses (with a transient chirp of $\sim 20-50$ GHz or more), it is clear that our proposed scheme looks specially attractive for optical communication systems.

The rate at which pulses are generated mainly depends on the strength of the magnetic field. Fig. 5.6 shows the frequency of the pulsations, f_{mod}, versus the circular birefringence for three different bias currents: 1.2 (squares), 1.5 (triangles),and 1.8 μ_{th} (diamonds), where μ_{th} stands for the threshold current. The solid line stands

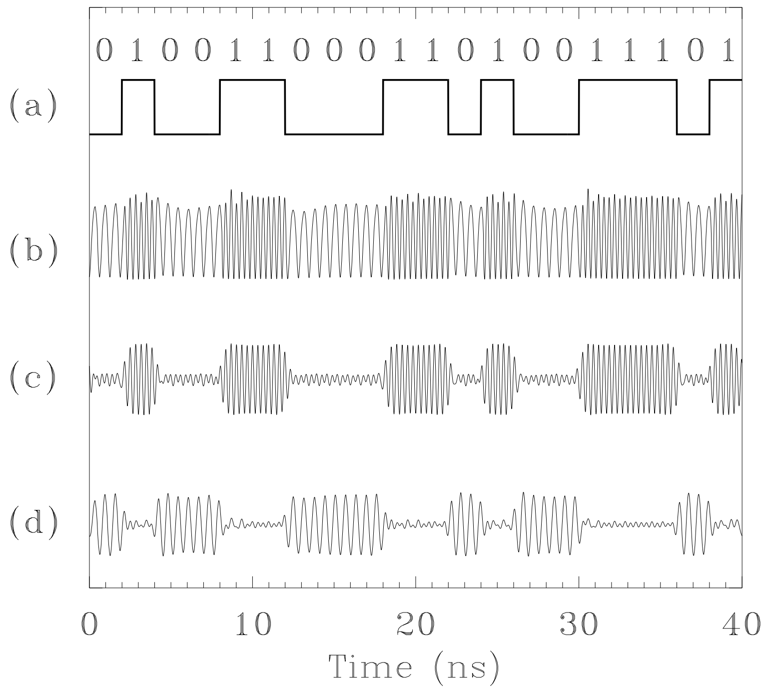

Figure 5.7: Digital frequency modulation. (a) bit sequence, (b) optical power emitted in the $\hat{x}$ polarization, (c) signal recovered with a second order Butterworth filter with 1.5 GHz band-pass centered at 3.1 GHz, (d) same as (c) but centered at 1.6 GHz. Same parameters as in Fig. 5.5.

for perfect isotropic VCSELs for which $f_{mod}=2\gamma_z/(2\pi)$. The frequency at which the VCSEL starts to pulse depends on the injection current in such a way that the higher the bias current, the larger the γ_z to observe pulses. In addition, the presence of small linear anisotropies slightly modifies the linear behavior. However, these features strongly depend on the ratio between linear and circular anisotropies in the system.

The linear dependence of the rotation frequency of the rotating elliptically polarized state on the magnetic field strength opens the possibility of information transmission with chirpless pulses by modulation of the magnetic field. Although nowadays fast modulation of strong magnetic fields is not achievable, it is interesting to speculate with this possibility.

The scheme is conceptually similar to frequency modulation, but instead of modulating the carrier frequency of the optical field here the rotating frequency of the polarization orientation is modulated. As an example, in Fig. 5.7 we show the results for such a transmission scheme for a 500Mb/s pseudo-random NRZ bit stream, where the magnetic-induced circular birefringence is digitally modulated between 4.7 ns^{-1} for "0" bits and 9.4 ns^{-1} for "1" bits, leading to pulsation frequencies $f_0 \approx 1.5$ GHz for "0" bits and $f_1 \approx 3$ GHz for "1" bits. A portion of the bit stream is shown in trace (a), and the power emitted in the $\hat{x}$ polarization is shown in trace (b). The different pulse repetition rates for the different bits can be clearly seen, which allows for easy recovery of the information just by filtering the signal received from a moderately fast photodetector which monitors the power on one polarization. Trace (c) shows the output obtained by filtering with a second-order Butterworth electrical band-pass filter centered at f_1. Alternatively, if the central frequency is f_0, the resulting signal is the negation of the transmitted signal, as shown in trace (d). The SNR can be improved increasing the ratio f_1/f_0 for constant filter order and filter bandwidth, which must be larger than twice the bit modulation in order to properly detect the signal. Notice also that a similar time trace will be obtained in the $\hat{y}$-polarized beam but shifted half a period. Thus, four copies of the transmitted message can be decoded, which may allow to decrease the bit error rate (BER) in the detector.

In conclusion, we have shown the possibility of generating low-chirp linearly polarized periodic pulses by applying an axial magnetic field to a almost isotropic VCSEL. Gigahertz pulse rates can be achieved for nearly isotropic devices with applications in clock generation, optical communications, optical interconnects, etc. An interesting property of such a laser system is that the pulse frequency mainly depends on the strength of the magnetic field. Based on this dependence, we propose a digital frequency modulation scheme such that information can be easily encoded and decoded. The practicality of such scheme is restricted by the capability of fast modulation of strong magnetic fields.

Chapter 6

Experiments of polarization switching in VCSELs at constant active region temperature

Abstract [1]

The influence of thermal effects on the polarization state of the light emitted by gain-guided Vertical-Cavity Surface-Emitting Lasers is experimentally studied. We demonstrate that polarization switching still occurs when the active region temperature is kept constant during fast pulse low duty cycle operation. This temperature-independent polarization switching phenomenon is explained in terms of the rate-equation analysis developed in Chap. 4. A comparison of the experimental results with the predictions of the model allows us to estimate the values of the spin-flip relaxation rate and the intrinsic dichroism of the VCSEL.

[1] This chapter is based on the paper *"Polarization switching in vertical-cavity surface emitting lasers observed at constant active region temperature"*, by J. Martín-Regalado, J. L. A. Chilla, J. J. Rocca, and P. Brusenbach, *Appl. Phys. Lett.* **70**, 3350 (1997).

6.1 Introduction

An explanation offered to polarization state selection in VCSELs operating in the fundamental transverse mode is based on the change in the material gain difference between the linearly polarized modes due to current-induced self-heating [79]. Since crystal birefringence splits the emission frequencies of the two linearly polarized modes, they experience slightly different material gains. At threshold, the polarized mode closer to the gain peak dominates suppressing the orthogonal one. For increasing current, self-heating of the device induces a faster red-shift of the gain peak frequency relative to the cavity resonances which modifies the material gain difference and leads to a change of the stability when the modes are aligned with the peak gain.

An additional mechanism for polarization state selection arises from the combined effect of saturable dispersion, VCSEL anisotropies and the difference in the population of the magnetic sublevels of the conduction and heavy-hole valence bands in quantum well VCSELs (Chap. 4). This population difference is annihilated by spin-flip relaxation processes in a time scale of tens of picoseconds [145], which is comparable to the photon lifetime and thus slow enough [2] to have an important effect on the dynamics. Within the framework of the SFM model, polarization switching occurs as the injection current is scanned above the lasing threshold even though the gain difference between the linearly polarized modes, γ_a, is kept constant.

In this Chapter we report a systematic study of the temperature dependence of the polarization switching behavior observed during fundamental mode operation in gain-guided VCSELs. First, we present polarization switching measurements carried out using a current ramp of a few seconds long, such that active region temperature adiabatically increases with dissipated power (and therefore γ_a changes with current). We next show polarized LI characteristics performed with a shorter current ramp — much shorter than the thermal response time of the VCSEL (see Sec. 2.2) — in order to keep the active region temperature constant during the current scan (γ_a constant). Both measurements will allow us to discriminate between the effects produced on the polarization state by changes in the injection current (and the associated changes in the nonlinear coupling of fields and carriers though spin dynamics, gain and dispersion) and those produced by the current-induced self-heating alone.

6.2 Measurements with varying active region temperature

The lasers used in this study are from a linear array [122], already described in Chap. 2, with VCSELs having an active region diameter of 15 μm. The array was mounted on a thermo-electric cooler and polarized LIV measurements were performed using a HP-4145A Semiconductor Parameter Analyzer (see setup in Fig. 2.8(left,below)) for different substrate temperatures. From the set of 8 VCSELs measured, three of them (VCSELs A, B, C) showed polarization switching at some substrate tempera-

[2] so it cannot be adiabatically eliminated.

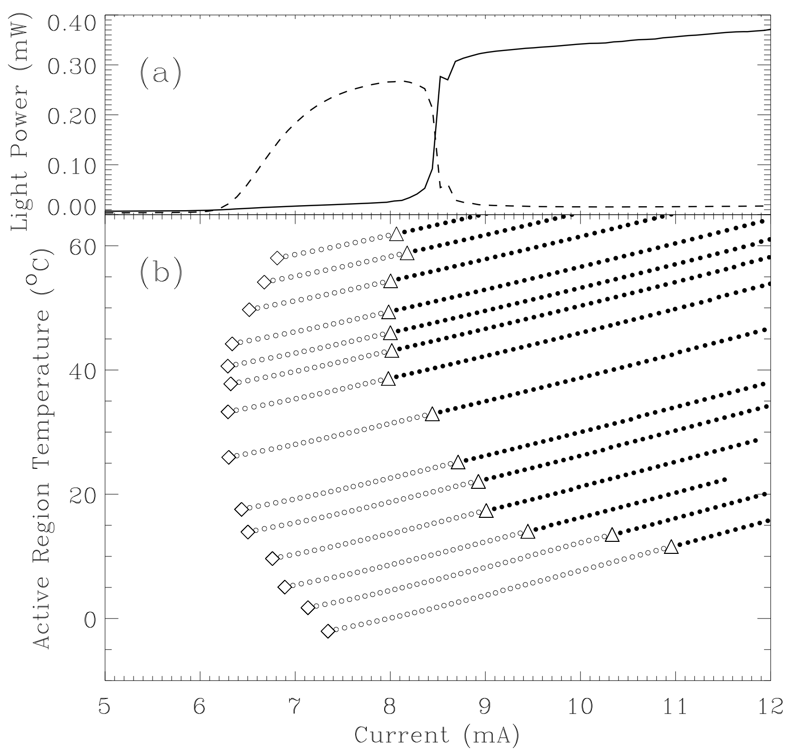

Figure 6.1: (a) Polarized Light-Current characteristics at 8^{o}C substrate temperature (T$^{th}_{act}$ ≈25 ^{o}C) under CW conditions. (b) Active region temperature vs. Injected current diagram for CW operation. Threshold currents are indicated by squares, and switching currents by triangles. The open (solid) circles corresponds to the shorter (longer) wavelength linearly polarized mode.

tures while the other devices had always stable linear polarization emission during fundamental mode operation.

From here on we focus on the study of VCSEL A since it showed polarization switching in the whole range of temperatures analyzed[3] (-30 <T$_{sub}$(^{o}C)< 50). The frequency splitting between the linearly polarized modes for this laser, measured as indicated in Sec. 2.3, is 20 GHz. In addition, its thermal characterization, carried out by monitoring the dissipated power dependence of the emission wavelength at different substrate temperatures (Sec. 2.2), gives a thermal resistance value R_{th}=1.50 ^{o}C/mW, which is used to estimate the active region temperature, T$_{act}$, through Eq. (2.1).

Fig. 6.1(a) shows the polarized LI characteristics taken at 8^{o}C substrate temperature for VCSEL A during fundamental mode operation. The threshold is at 6.2 mA. For increasing current, the shorter wavelength polarized mode is dominant up to 8.5 mA, where an abrupt polarization switching occurs. Beyond the switching current, stable emission in the orthogonal polarization is observed.

Results for different substrate temperatures are mapped out in Fig. 6.1(b), where we show the regions of polarization dominance as a function of the injected current and the associated active region temperature raise. The figure presents the general features already reported in Ref. [79], namely *i)* the threshold current (squares) de-

[3]VCSELs B and C had a similar behavior but in narrower temperature ranges.

pends quadratically on the active region temperature, with the minimum threshold at roughly 25 ^oC; and *ii)* the polarization switches from the polarized mode with shorter wavelength to the polarized mode with longer wavelength as the current is increased[4]. Both features indicate that the VCSEL has been designed with the linearly polarized cavity resonances red-shifted from the gain-peak wavelength for temperatures lower than room temperature, so switchings can be *a priori* attributed to VCSEL self-heating (thermally-induced polarization switching) [79] .

However, there are two results which are worth to point out. On the one hand, the short wavelength polarization mode still dominates at threshold for temperatures where the material gain should favor the orthogonal polarization mode — temperatures larger than the minimum threshold temperature —. On the other hand, the switching current for each measurement (triangles) increases with decreasing active region temperature but one would expect the thermally-induced switchings to occur at constant active region temperature. While the former can be attributed to the existence of an intrinsic dichroism favoring the shorter wavelength mode, the latter may indicate the existence of additional mechanisms that complement the relative spectral alignment of the cavity resonances and the material gain in determining the polarization characteristics of VCSELs.

6.3 Measurements at constant active region temperature

The effects of the temperature on the polarization dynamics of VCSELs can be minimized performing LIV measurements with short current ramps at low duty cycle. After determining the thermal response time to be roughly 1 μs (see Sec. 2.2), the duration of the ramps is chosen to be 100 ns. Notice that, as the characteristic time in carrier-field interaction (relaxation oscillations) is roughly 1 ns, this ramp duration is slow enough to ensure that the measurements are taken in a quasi-steady situation while being fast enough to avoid the effects of self-heating.

Fig. 6.2 shows schematically the setup for this type of measurements. The current source consists of a DC pre-bias and a fast (100 ns ramp, 20 kHz repetition rate) current ramp generator connected to the VCSEL through a bias-tee network. The injected current and voltage drop in the VCSEL are measured using a 50 Ω load resistance. The light power is measured independently for both polarizations using a fast ($\sim$ 1 ns) photodiode located after a polarizer. All the signals are monitored using a digital scope (100 Ms, 100 MHz bandwidth), stored in a computer, and then processed taking into account the different delays in the transmission lines.

In this measurements the active region temperature does not change significantly during the current ramp. This feature is verified by time-resolved spectrum measurements which show a small blue-shift ($\sim$ -0.5 $\mathring{A}$) of the VCSEL emission wavelength during the pulse duration [5]. Such a blue-shift can be attributed to a relatively small

[4]These polarization switchings correspond to the $\hat{y} \longrightarrow \hat{x}$ switching in the notation of Chap. 4.
[5]A red-shift is expected from thermal effects

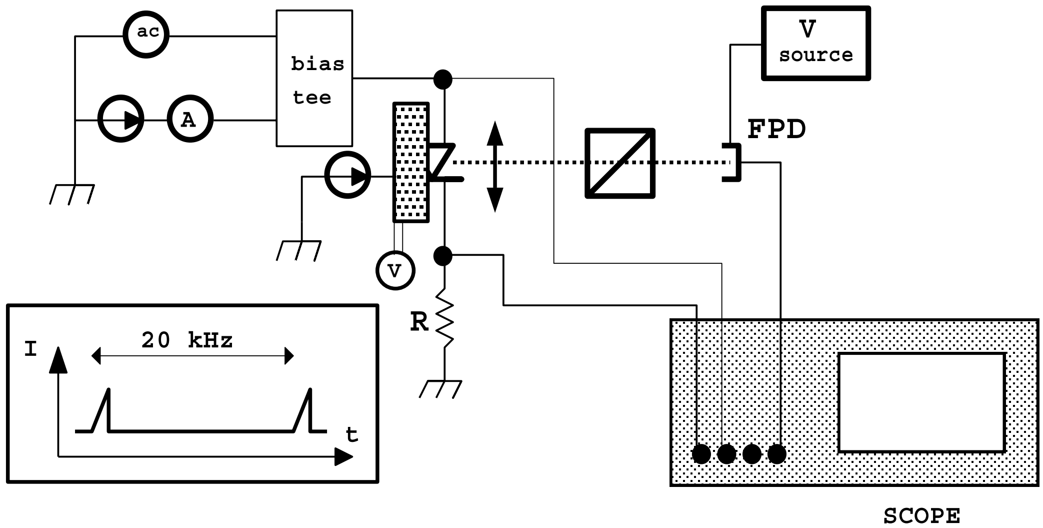

Figure 6.2: Setup for LIV measurements at constant active region temperature.

carrier-induced change of the refractive index ($\Delta n = n/\lambda_0\ \Delta\lambda \approx$-2·$10^{-4}$) [56], so it is consistent with the quasi-steady state conditions assumed for the measurements.

The polarized LI characteristics obtained during fast current ramp excitation with a pre-bias current of 3 mA and a substrate temperature of 8 ^{o}C is depicted in Fig. 6.3(a) (T^{th}_{act} ≈15 ^{o}C). The figure shows polarization switching from the lower

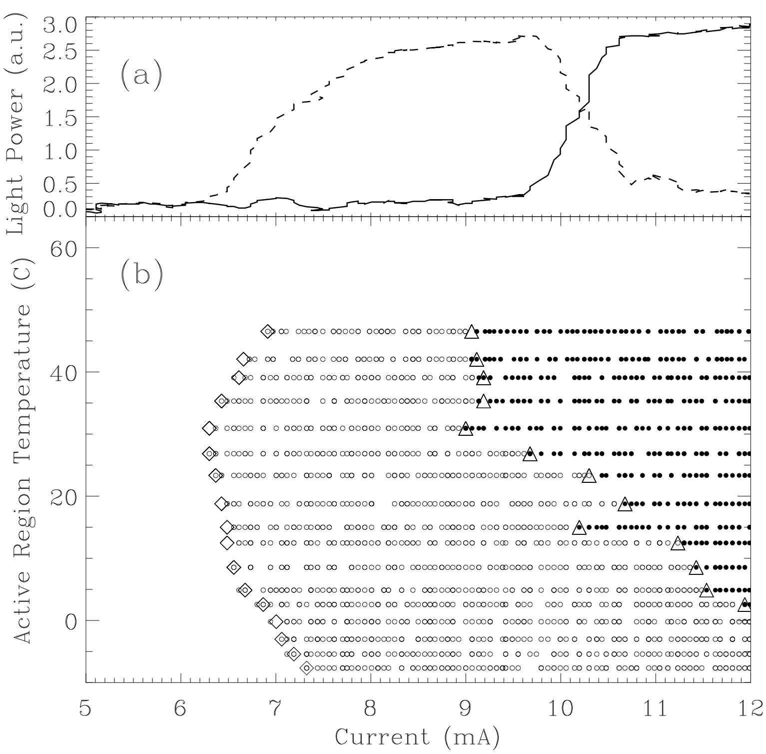

Figure 6.3: Same as Fig. 6.1 for fast current ramp operation.

to the higher wavelength polarized modes at roughly 10 mA. Notice that, since the measurement is performed at constant active region temperature (constant material gain difference), this result becomes the first clear experimental evidence for the polarization state selection mechanisms explored in Chap. 4.

In order to characterize the polarization switching behavior under fast current excitation, LIV characteristics were carried out at different substrate temperatures. Results are mapped out in Fig. 6.3(b) considering that the active region temperature, which depends on the pre-bias current (I_b) and voltage (V_b) values through $T_{act} = T_{sub} + R_{th} \cdot I_b \cdot V_b$, is constant during the scan. Notice that the dependence of the threshold current on the active region temperature follows that of Fig. 6.1(b) since the threshold current mainly depends on the mismatch of the cavity resonances and the gain peak. In addition, the regions of dominance of each polarization in Fig. 6.3(b) are similar to those obtained in the CW experiments, although not the same, providing further evidence of the action of a switching mechanism different that the thermal one in Ref. [79].

6.4 Comparison of experimental and theoretical results

We now provide a possible explanation for the observed non-thermal polarization switching in terms of the results of Chap. 4. The theoretical model allows for two different classes of polarization switching: *i)* a switching from the lower (higher) to the higher (lower) frequency (wavelength) states, $\hat{x} \to \hat{y}$, which occurs at low birefringence values and is related to saturable dispersion and linear dichroism; and *ii)* a switching from the higher (lower) to the lower (higher) frequency (wavelength) states, $\hat{y} \to \hat{x}$, which occurs at high birefringence values and arises because of saturable dispersion, linear dichroism and spin dynamics.

The switchings we observe in our experiments correspond to the $\hat{y} \to \hat{x}$ type, and for them the model predicts a linear dependence of the switching current normalized to threshold (μ_{sw}/μ_{th}) on the gain difference between the linearly polarized modes (γ_a) as (see Eq. (4.59))

$$\frac{\mu_{sw}}{\mu_{th}} = 1 + \frac{2(\gamma_s^2 + 4\gamma_p^2)}{\kappa(2\alpha\gamma_p - \gamma_s)\gamma}\gamma_a \ ,$$

where κ is the field decay rate, γ is the total carrier decay rate, γ_s is the spin-flip relaxation rate, α is the linewidth enhancement factor, and $\gamma_p = \pi\Delta\nu$ is the VCSEL birefringence.

In Fig. 6.4 we have plotted the switching current normalized to threshold (triangles) as a function of the the active region temperature for the data in Fig. 6.3. In order to compare the experimental results with the predictions of the model, we have to find a relationship between γ_a and the active region temperature, T. This can be accomplished by assuming a parabolic modal gain profile near the gain peak wavelength, λ_p, as [68]

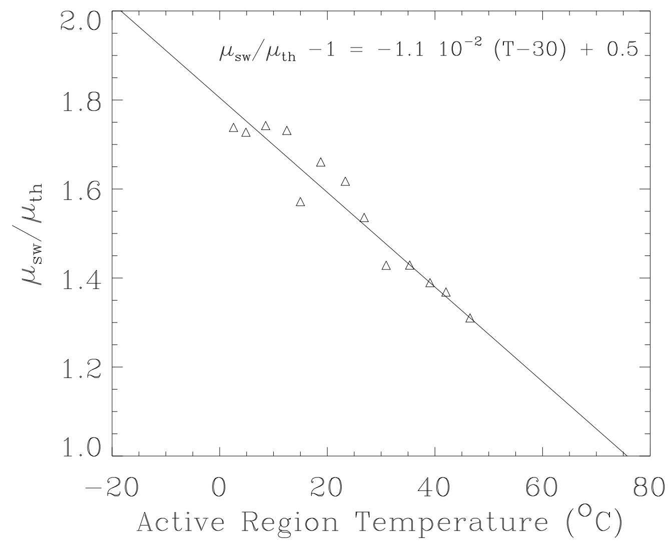

Figure 6.4: Dependence of the switching current normalized to the threshold current vs. the active region temperature. The triangles are the measured data. The solid line is the calculated result for γ_s= 70 ns^{-1}.

$$g(\lambda, T, N_{th}) = \Gamma G(N_{th}, T)\left(1 - 2\left(\frac{\lambda - \lambda_p}{\lambda_F}\right)^2\right) \qquad (\text{in cm}^{-1}) , \tag{6.1}$$

where Γ is the gain confinement factor, $G(N_{th}, T_{act}) = a(T)(N_{th} - N_0)$ is the peak modal gain at threshold, $a(T) = a_0 + b(T - T_0)$ is the differential gain, $N_{th}(T)$ and N_0 are the threshold and transparency carrier densities, respectively, T_0 is the minimum threshold active region temperature, and λ_F is the full-width half-maximum of the gain spectrum.

For two linearly polarized modes with birefringence-induce frequency splitting $\Delta\nu$, their emission wavelengths can be written as $\lambda_{\frac{x}{y}} = \lambda_c \pm \Delta\lambda/2$, where λ_c is the central wavelength of the modes, $\Delta\lambda = |\Delta\nu|\lambda_0^2 n_g/c$, c is the speed of the light, n_g is the group index, and λ_0 is the lasing wavelength. The material gain difference between these linearly polarized modes when they are red-shifted from the gain peak ($\lambda_p < \lambda_c$) is (see Fig. 6.5)

$$\Delta g = g(\lambda_y) - g(\lambda_x) = -4\Gamma G\frac{n_g}{c}\Delta\nu\left(\frac{\lambda_o}{\lambda_F}\right)^2(\lambda_p - \lambda_c) > 0 \qquad (\text{in cm}^{-1}) , \tag{6.2}$$

or equivalently, we define

$$\gamma_a^{mat} = \frac{c}{n_g}\frac{\Delta g}{2} = -2\Gamma G\Delta\nu\left(\frac{\lambda_o}{\lambda_F}\right)^2\left(\frac{d\lambda_p}{dT} - \frac{d\lambda_c}{dT}\right)(T - T_0) \qquad (\text{in ns}^{-1}) , \tag{6.3}$$

were we have considered explicitly the temperature dependence of λ_p and λ_c as [40]

$$\lambda_p = \lambda_m + \frac{d\lambda_p}{dT}(T - T_0) , \qquad \lambda_c = \lambda_m + \frac{d\lambda_c}{dT}(T - T_0) , \tag{6.4}$$

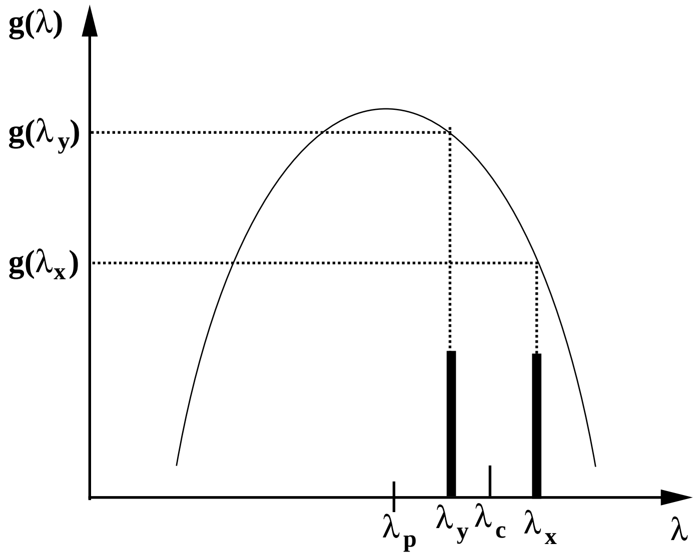

Figure 6.5: Parabolic gain approximation. ω_p and ω_0 are the gain peak frequency and the central frequency of the linearly polarized modes, respectively.

The total linear dichroism in the VCSEL has two contributions, the material gain difference, γ_a^{mat}, and the intrinsic dichroism which may arise from stress, strain, etc., γ_a^{int}, $\gamma_a = \gamma_a^{mat} + \gamma_a^{int}$. Therefore, the switching current normalize to threshold can be rewritten as

$$\frac{\mu_{sw}}{\mu_{th}} - 1 = -\frac{8(\gamma_s^2 + 4\gamma_p^2)}{(2\alpha\gamma_p - \gamma_s)\gamma}\frac{\gamma_p}{\pi}\frac{n_g}{c}\left(\frac{\lambda_o}{\lambda_F}\right)^2\left(\frac{d\lambda_p}{dT} - \frac{d\lambda_c}{dT}\right)(T - T_0) + \frac{2(\gamma_s^2 + 4\gamma_p^2)}{\kappa(2\alpha\gamma_p - \gamma_s)\gamma}\gamma_a^{int} \quad (6.5)$$

where we have considered that the main thermal contribution to the material gain difference in the range of temperatures analyzed comes from the thermal wavelength red-shifts of λ_p and λ_c, so we have taken a temperature independent modal gain peak whose value corresponds to the modal threshold gain: $\Gamma G \approx \Gamma g_{th} = 2\kappa\frac{n_g}{c}$.

The solid line in Fig. 6.4 corresponds to the fitting of the experimental data with typical parameters values: κ= 300 ns^{-1}, n_g = 3.8 (Γg_{th}=76 cm^{-1}), α=4, γ^{-1}= 1 ns, $d\lambda_p/dT$=3.3 $\overset{o}{A}/^o$C, our measured values λ_0=850 nm, T$_0$=30 ^{o}C, γ_p = 60 ns^{-1} ($\Delta\nu \approx$ 20 GHz), $d\lambda_c/dT$= 0.69 $\overset{o}{A}/^o$C, and using the spin-flip relaxation rate as a fitting parameter.

The best fitting results for γ_s=70 ns^{-1}, which is similar to the estimate in [82]. In addition, the intrinsic amplitude anisotropy is $\gamma_a^{int} \approx 1.7\ ns^{-1} \sim 0.2\ cm^{-1}$, in good agreement with other reported values [75, 164, 175]. Howevcer, despite the good agreement between the experimental data and the analytical result, notice that the values for the spin-flip relaxation rate and the intrinsic amplitude anisotropy should be considered only as approximate or mean values of the real ones due to the temperature-independent assumtions taken for many of the fitting parameters within the range of temperatures analyzed (-10 < T_{act}(^{o}C)<50).

Chapter 7

Polarization and transverse mode dynamics of gain-guided VCSELs

Abstract [1]
We discuss a Maxwell-Bloch Two-Level model to describe polarization and transverse mode selection in wide-area gain-guided Vertical-Cavity Surface-Emitting Lasers. The model incorporates the vector nature of the laser field, saturable dispersion, different carrier populations associated with different magnetic sublevels of the conduction and heavy-hole valence bands in quantum-well media, spin-flip relaxation mechanisms, cavity birefringence and dichroism, field diffraction, carrier diffusion and frequency-dependent gain and dispersion. We study polarization dynamics and transverse mode competition in conditions in which VCSEL self-heating is avoided. Polarization stability and polarization switching behaviors are found during fundamental mode operation for different sets of cavity anisotropy values. In addition, we find that the first-order transverse mode starts lasing orthogonally polarized to the fundamental one. At larger currents, polarization coexistence with several active transverse modes occur. Our results are shown to be sensitive to the carrier spin-flip relaxation rate.

[1]This chapter is based on the papers *(i) "Polarization and Transverse Mode Dynamics of Gain-Guided Vertical-Cavity Surface-Emitting Lasers"*, by , J. Martín-Regalado, S. Balle, M. San Miguel, *Optics Lett.* **22**(7), 460 (1997), *(ii) "Polarization and Transverse Mode Selection in Quantum Well Vertical-Cavity Surface-Emitting Lasers: Index- and Gain-guided Devices"*, by J. Martín-Regalado, S. Balle, M. San Miguel, A. Valle and L. Pesquera, *Quantum and Semiclass. Opt.*, **9**, 1 (1997); and *(iii)* the post-deadline paper EPD2.3 + video presentation "Polarization and transverse mode dynamics of gain-guided vertical-cavity surface-emitting lasers", by , J. Martín-Regalado, S. Balle, M. San Miguel, in *CLEO /EUROPE -EQEC'96, Hamburg, Germany. 8-13 September, 1996.*

7.1 Introduction

A practical limitation of many VCSELs is the polarization and transverse mode instabilities which appear as the injected current is increased beyond the threshold value [31, 47]. Narrow contact VCSELs always operate in the fundamental Gaussian TEM_{00} mode. Although some of these devices have stable polarization emission [69], VCSELs where the polarization state of the TEM_{00} mode changes with the injection current — polarization switching — are also reported [70]. In wider contact VCSELs, fundamental transverse mode operation is restricted to a current range close above the lasing threshold. In this regime, stable polarization emission [56, 79, 80] as well as polarization switching [58, 80, 83] behaviors have been reported. In the multi-transverse mode regime, a commonly observed feature is that the first-order transverse mode starts lasing orthogonally polarized to the fundamental one [56, 58, 79, 80, 83]. Coexistence of several transverse modes in both polarizations occurs at high currents. These experimental features raise the question about which are the mechanisms responsible for the selection of a particular polarization state in VCSELs mediated by the transverse mode dynamics.

7.2 Model and numerical method

In order to describe polarization and transverse mode dynamics in gain-guided quantum-well VCSELs we use the general model derived in Chap. 3. The equations, including the characteristic VCSEL anisotropies, read (from Eqs. (3.60)-(3.63))

$$\partial_t E_\pm = -\kappa(1+\mathrm{i}\,\theta)E_\pm + P_\pm - \mathrm{i}\,\frac{c^2}{2\Omega n_e n_g}\nabla^2 E_\pm - (\eta_a - \mathrm{i}\,\eta_p)E_\mp \ , \tag{7.1}$$

$$\begin{aligned}\partial_t P_\pm &= -\gamma_\perp(1-\mathrm{i}\,\theta)P_\pm + \gamma_\perp a(1+\theta^2)(N-N_0\pm n)E_\pm \\ &+ \sqrt{\beta(N\pm n)}\psi_\pm \ ,\end{aligned} \tag{7.2}$$

$$\partial_t N = j(t)C(x,y) - \gamma_e N + \mathcal{D}\nabla^2 N - [(E_+P_+^* + E_-P_-^*) + (c.c.)], \tag{7.3}$$

$$\partial_t n = -\gamma_s n + \mathcal{D}\nabla^2 n - [(E_+P_+^* - E_-P_-^*) + (c.c.)] \ , \tag{7.4}$$

where the parameters η_a and η_p are related to the linear dichroism and birefringence of the VCSEL, respectively. The total injected current, I, is assumed to be uniformly distributed within a circular region of diameter ϕ (VCSEL contact) and zero outside, defining a step-like[2] current density distribution, $C(x,y)$, which is characteristic of proton-implanted gain-guided VCSELs. In addition, the prefactor $j(t)$ allows for the generation of current ramps. The rest of the parameters involved in the equations have already been defined in Chap. 3.

The polarization and transverse mode dynamics of gain-guided VCSELs is studied by numerical integration of Eqs. (7.1)-(7.4). The laser variables are discretized in space using a square grid. Then, for each integration step the integration scheme

[2]We use a super-Gaussian distribution: $C(r) = C_0\cdot \exp[-(2r/\phi)^{2n}]$, $r^2 = x^2+y^2$, $n=3$.

we follow has four steps: (*i*) diffraction and diffusion terms are calculated via Fast-Fourier-Transform of the fields and carrier density distributions, respectively, from the previous integration step (initially from noise conditions); (*ii*) complex distributions of random Gaussian numbers, $\psi_{\pm}(x, y)$, are generated; (*iii*) the optical fields $E_{\pm}$, carrier densities N and n, and material polarizations $P_{\pm}$ variables at each point of the trasverse plane are updated via the Euler method for the integration of stochastic differential equations [176]; and (*iv*) to obtain the light-current (LI) characteristics, the current density distribution is updated by increasing $j(t)$ in a small amount.

Several things are worth noticing from the numerical scheme: (*i*) the calculation of the Laplacian terms by the FFT method requires the use of periodic boundary conditions for the dynamical variables. Hence, in order to avoid not-realistic spurious reentering waves, we consider a transverse integration region much wider than the pumped area (given by $C(x, y)$), such that the dynamical variables decay to values of the order of the noise level at the integration boundaries; (*ii*) since the carrier-field interaction is roughly 1 ns, the use of short current ramps (40 ns) to generate the light-current characteristics ensures that the measurements are taken in a quasi-steady situation [3]; (*iii*) a linear stability analysis reveals that the integration time-step is strongly related to the optical diffraction coefficient, which depends on the spatial discretization. In order to achieve a compromise between spatial resolution, equation stability and computation time, we use 32x32 grid points for a transverse width of 40x40 μm^2 and an integration time-step of $10^{-4} ps$.

The equations of the model are properly rescaled so that $|E_i(x_o, y_o)|^2$ represents a magnitude proportional to the photon number i=x,y polarized going out from the VCSEL at the point (x_o, y_o) of the transverse plane. The total emitted power is calculated by integrating the optical intensity transverse distribution for each polarization and assuming a quantum efficiency of 100 % and a 1.5 μm effective cavity length. The rest of the physical parameter values involved in the equations are [82, 160, 162, 177]: $\kappa = 300\ ns^{-1}$, $\gamma_\perp = 20\ ps^{-1}$, $\gamma_e = 1\ ns^{-1}$, $\gamma_s = 50\ ns^{-1}$, $N_0 = 1.3\ 10^6 \mu m^{-3}$, $\lambda = 750\ nm$, n_e=3.55, n_g=3.8, $a = 10^{-6} \mu m^3 ps^{-1}$, $\mathcal{D} = 3\ cm^2/s$, and θ=-3.

Notice that with θ=-3 we choose to operate the VCSEL on the negative detuning side of the gain spectrum in order to preserve the commonly observed property that higher-order transverse modes experience lower material gain (have a higher threshold) than the fundamental one. Such a negative value of the detuning — which leads to carrier-induced guiding instead of antiguiding — can be "justified" in our model by associating it to a thermally-induced index-guiding effect. In real VCSELs, the index profile depends on both the carrier distribution and the temperature profile reached in the active layer where the current is injected. The former leads to a carrier-induced index antiguiding effect through the α-factor. In the latter, the temperature profile associated with the dissipated power is maximum on the symmetry axis of the pumped area, and provides a thermally-induced index-guiding mechanism in the resonator. Hence, both effects act in opposite directions, so the carrier-induced index antiguiding can be compensated or even avoided by the thermally-induced index-

[3] This is verified by performing new simulations at constant current and using as initial conditions the values from the LI characteristics at that current.

guiding. Typical values for these mechanisms are dn/dN=-1.2 × 10 $^{-8}\mu m^3$ [178] and dn/dT=3 × 10 $^{-4}K^{-1}$ [179]. However, from measurements of the wavefront curvature in gain-guided VCSELs it turns out that the thermally-induced guiding effect is stronger than the carrier-induced antiguiding effect [56].

Finally, it is important to review the mechanisms that can lead to gain/loss anisotropies for the linearly polarized modes in the present model. These are the external gain/loss anisotropies, the modal gain anisotropy, and material gain anisotropy. External anisotropies can have different origins; they can be either deliberate — e.g., introduced in either the cavity geometry [60, 87, 174] or in the gain medium [88] — or unintentional — e.g., due to the imperfections in the fabrication process [75] —. The modal gain anisotropy is due to the different overlap of the optical mode profiles (which are slightly different for the $\hat{x}$- and $\hat{y}$-polarized modes due to birefringency) with the threshold carrier distribution. Finally, the material gain anisotropy is related to both birefringence and the material gain spectrum (see Appendix D): since the two linearly polarized modes are frequency split, they have also slightly different material gain coefficients. Notice that both modal and material gain anisotropies are intrinsicly included in the model, so the parameter η_a in Eq. (7.1) will only describe external gain/loss anisotropies.

7.3 Numerical results

The devices we study are circular contact VCSELs with different diameters, a fixed value of η_p, and different η_a values. The first device we consider, VCSEL A, has a diameter ϕ =12.5 μm, and we chose η_p= 3 γ_e, and η_a=0. For these parameters (see the inset in Fig. 7.1), $\omega_y < \omega_x$ with $\Delta\nu \approx 0.95$ GHz. In addition, the material gain difference ($\Delta g \approx$0.05 ns^{-1})[4] favors the $\hat{y}$-polarized mode at threshold since it is closer to the gain peak.

We first study the polarization dynamics during the laser turn-on. Fig. 7.1 shows the time evolution of the total emitted power for each linear polarization when a 10 ns square current pulse with pre-bias and bias currents of 0.98 I_{th} and 1.05 I_{th}, respectively, is applied to the VCSEL at t=0 ($I_{th} \sim 5$ mA). Initially, the laser suffers a delay of 0.5 ns in the switch-on time since the pre-bias current is below threshold. After the switch-on, the intensity in both polarizations show the typical relaxation oscillations, the power in the $\hat{y}$ polarization being larger than in the $\hat{x}$ polarization. The reason is that, during the switch-on, the total carrier density overcomes the threshold carrier density for both linearly polarized modes, and therefore, their modal gains overcome their threshold values. However, 2 ns after the switch-on, the output power in the $\hat{x}$-TEM$_{00}$ mode goes to zero since the total carrier density reaches the threshold carrier density for the mode closer to the gain peak, $N_y^{th}(x,y)$. As a consequence, the $\hat{x}$-polarized mode switches-off for the rest of the pulse and the $\hat{y}$-polarized mode reaches its steady-state. A similar behavior has been experimentally found in Ref. [164] but there the relaxation oscillations are more damped because of the pumping conditions (pre-bias current of I_{th} and biased to 2 I_{th}). Nevertheless, the

[4] See Appendix D for details.

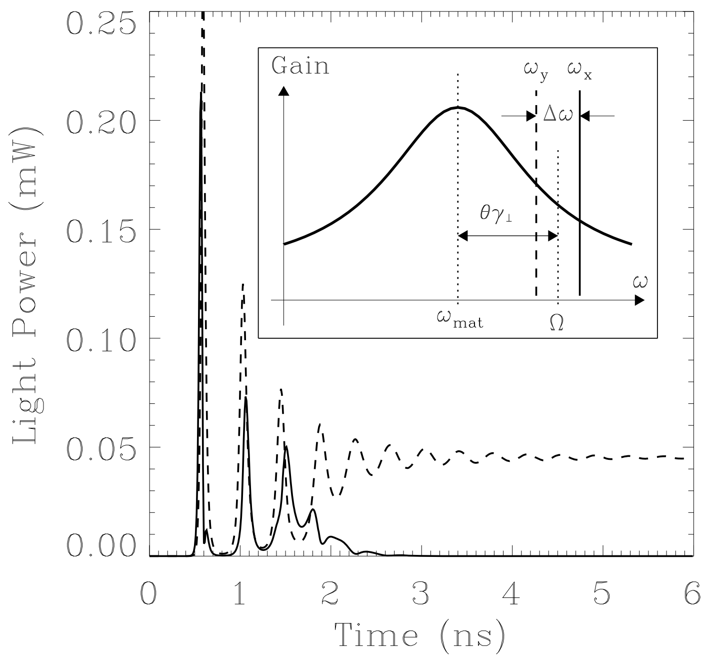

Figure 7.1: Turn-on event for VCSEL A. The inset shows the Maxwell-Bloch two-level gain spectrum and the location of the linearly polarized TEM_{00} modes for the set of parameters chosen.

characteristic time for the selection of the polarization state obtained experimentally in Ref. [164] ($\sim$ 2 ns) is in good agreement with the one found numerically in Fig. 7.1.

Fig. 7.2 shows the polarized L-I characteristics for VCSEL A obtained by linearly increasing the applied current from $I = 1.05I_{th}$ to $I = 2.16I_{th}$ in 40 ns. Fundamental mode emission is observed up to $I \sim 1.50I_{th}$. In this regime, the total output power emitted by the VCSEL increases linearly with the current, while the polarization of the output light ($\hat{y}$) is very stable. For current values larger than $1.50I_{th}$ higher-order modes start to lase. Here we first observe a basic feature of the polarization instabilities oftenly observed in gain-guided VCSELs, namely the first order transverse mode starts lasing orthogonally polarized to the fundamental mode. For increasing current, coexistence of both polarizations occurs. Such L-I characteristic corresponds to the scenario observed in some VCSELs [56, 79, 80].

The insets in Fig. 7.2 show the instantaneous transverse near-field profiles at the indicated currents (the plotted area corresponds to a square of $10 \times 10 \mu m^2$). During fundamental mode operation, the off-polarization mode only emits amplified spontaneous emission from the entire VCSEL contact. The width of the $\hat{y}$-polarized Gaussian mode is about 60% of the current contact, and slightly increases with current. This feature has never been observed experimentally in gain-guided VCSELs[5] and here occurs because the carrier-induced index-guiding associated with the spatial-hole burnt in the carrier profile by the Gaussian mode favors the spreading of the mode profile. In the multitransverse mode regime, the insets in Fig. 7.2 show that,

[5]In gain-guided VCSELs, the fundamental mode typically shrinks as the applied current increases due to the combined effect of thermal lensing and carrier-induced index anti-guiding [180].

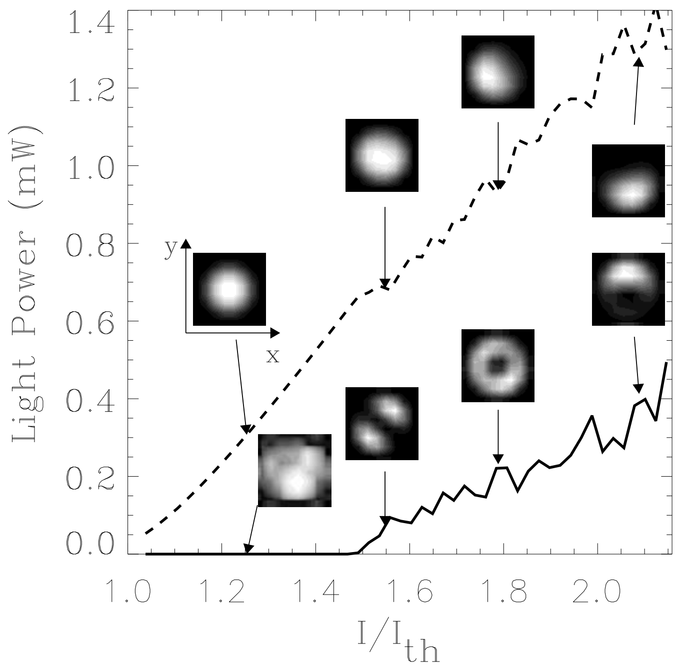

Figure 7.2: VCSEL A. L-I characteristic for the linearly $\hat{x}$ (solid) and $\hat{y}$ (dashed) polarizations.

while the $\hat{y}$-polarized beam consists on a single lobe with the peak moving around the VCSEL axis as current increases, the $\hat{x}$-polarized beam can adopts different profiles: (i) two lobes oscillating in time around the center of the VCSEL at $I \sim 1.55I_{th}$, (ii) a doughnut-shape at $I \sim 1.79I_{th}$, and (iii) an off-centered lobe distribution at $I \sim 2.08I_{th}$.

In order to force $\hat{x}$-polarized emission at threshold we have to introduce an external gain/loss anisotropy ($\eta_a < 0$) to overcome the material gain anisotropy. In addition, to increase the current range where fundamental mode operation occurs, we have to decrease the diameter of the pump region. For these reasons, we consider now a new device (VCSEL B) with a contact diameter of 10 μm and the anisotropy parameters values $\eta_p = 3.0\gamma_e$ and $\eta_a = -5.0\gamma_e$. For these parameters, we numerically found a threshold current of $I_{th} = 3.25\ mA$.

Fig. 7.3 shows the L-I characteristics for VCSEL B. The device switches-on in the $\hat{x}$-polarized fundamental mode because of the effect of the external amplitude anisotropy. For increasing current, an abrupt $\hat{x} \to \hat{y}$ polarization switching within the fundamental transverse mode is observed at $I \sim 1.45I_{th}$ (the switching current depends on the η_a value, e.g., for $\eta_a = -2.5\gamma_e$ the PS occurs at $I \sim 1.30I_{th}$). As a consequence of the smaller active region size, the fundamental mode regime extends to 1.85 I_{th}, a value slightly larger than for VCSEL A. Above 1.85 I_{th} the first-order transverse mode starts lasing orthogonally polarized to the fundamental mode. During the multi-transverse mode regime, the $\hat{x}$-polarized total power increases almost linearly with the injected current while $\hat{y}$-polarized total power almost saturates. Such general behavior corresponds to the scenario found in [58, 80, 83].

The modal behavior of the VCSEL emission can be obtained by integrating

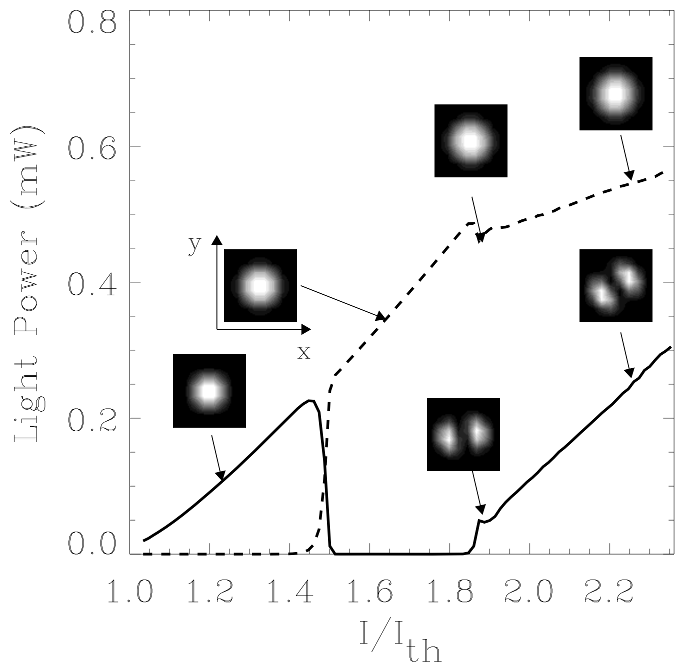

Figure 7.3: Same as in Fig. 7.3 but for VCSEL B.

Eqs. (7.1)-(7.4) at a fixed current value instead of using a current ramp. Fig. 7.4 shows the optical spectra and the transverse mode profiles obtained at four different injection current values for VCSEL B. These spectra are equivalent to those obtained by a Fabry-Perot interferometer with a free spectral range of 1000 GHz and a frequency resolution of 2 GHz. At $I \sim 1.29 I_{th}$, the polarized spectrum in Fig. 7.4(a) shows that the laser mainly emits in the $\hat{x}$-TEM$_{00}$ mode. However, the orthogonal polarization shows a strongly suppressed peak ($\sim$-40 dB) while the frequency difference between the two peaks is not resolved. Beyond the switching current, at $I \sim 1.67 I_{th}$, laser emission occurs in the $\hat{y}$-polarized Gaussian mode (Fig. 7.4(b)). For increasing current, $I \sim 1.87 I_{th}$, two transverse modes, the TEM$_{00}$ (α) and the TEM$_{10}$ (β), coexist but with orthogonal polarizations (Fig. 7.4(c)). The onset of the TEM$_{10}$ can be explained through the change in its modal gain due to the competition between spatial hole burning and carrier diffusion [55, 65, 66, 67], but the reason why it is orthogonally polarized to the fundamental mode is unclear. Also notice that, as a consequence of the negative detuning, there is a small red shift of the modal frequencies for increasing current, whereas a blue shift is expected for semiconductor lasers.

Fig. 7.4(d) shows the spectrum at $I \sim 2.26 I_{th}$. Several transverse modes are active at this current value, and their frequency difference — $\nu_{01} - \nu_{00} \sim 90$ GHz, $\nu_{10} - \nu_{01} \sim 10$ GHz, and $\nu_{11} - \nu_{00} \sim 200$ GHz — is in good agreement with the experimental data shown in Sec. 2.1 and other reported values [49, 50]. Regarding the polarization characteristics, it is worth noting that the two linear polarizations choose to operate in modes of different parity. Even-order modes are $\hat{y}$-polarized (a dominant TEM$_{00}$ mode (α), and some strongly suppressed second-order modes (δ

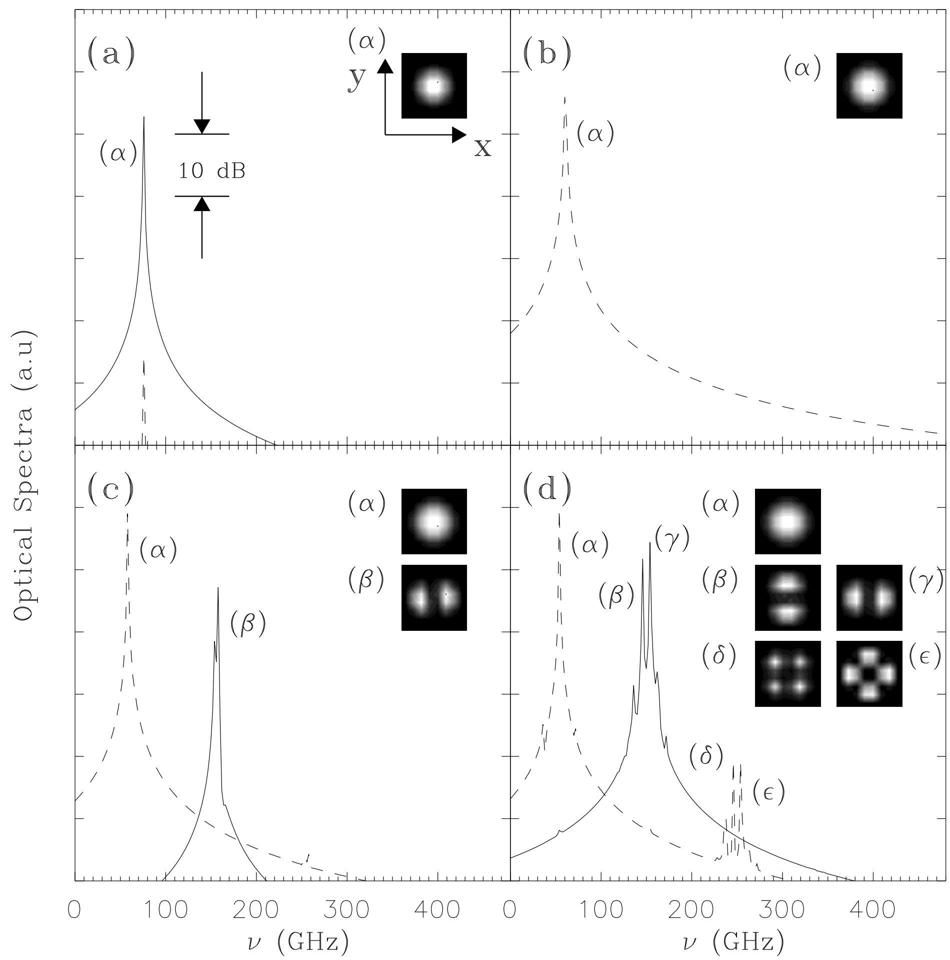

Figure 7.4: VCSEL B. Optical spectra of the linearly polarized field components E_x (solid) and E_y (dashed) for fixed current values indicated in Fig. 7.3 by arrows: (a) $I = 1.29I_{th}$, (b) $I = 1.67I_{th}$, (c) $I = 1.87I_{th}$, (d) $I = 2.26I_{th}$. The insets in the spectra correspond to the transverse mode profiles associated to the corresponding labeled peaks.

and ϵ)), while $\hat{x}$-polarized modes have odd-order profiles (TEM$_{10}$ (β) and TEM$_{01}$ (γ) modes). In opposition to the cases shown in Fig. 7.4(a)-(c), where the total power emitted in each linear polarization is constant in time, at $2.26I_{th}$ it oscillates: the total $\hat{x}$-polarized power is modulated at twice the beat note between the $\hat{x}$-polarized first-order transverse modes ($\nu_{01} - \nu_{10} \approx 9\ GHz$); a very weak modulation at twice this beat frequency is also observed in the total $\hat{y}$-polarized power but, in this case, induced by the nonlinear coupling between the two linearly polarized field components through the total carrier population (α-factor).

For even larger current values, $I \sim 2.55I_{th}$, coexistence of several transverse modes in both linear polarizations is observed in the optical spectrum (Fig. 7.5(b)). The time evolution of the total $\hat{x}$- and $\hat{y}$-polarized light intensities, shown in Fig. 7.5(a), is as previously described for $I \sim 2.26I_{th}$, but an additional modulation (fast ripples) at twice the beat notes between the fundamental mode and the frequency non-degenerated first order modes ($\nu_{01} - \nu_{00} \approx 90\ GHz$ and $\nu_{10} - \nu_{00} \approx 100\ GHz$, respec-

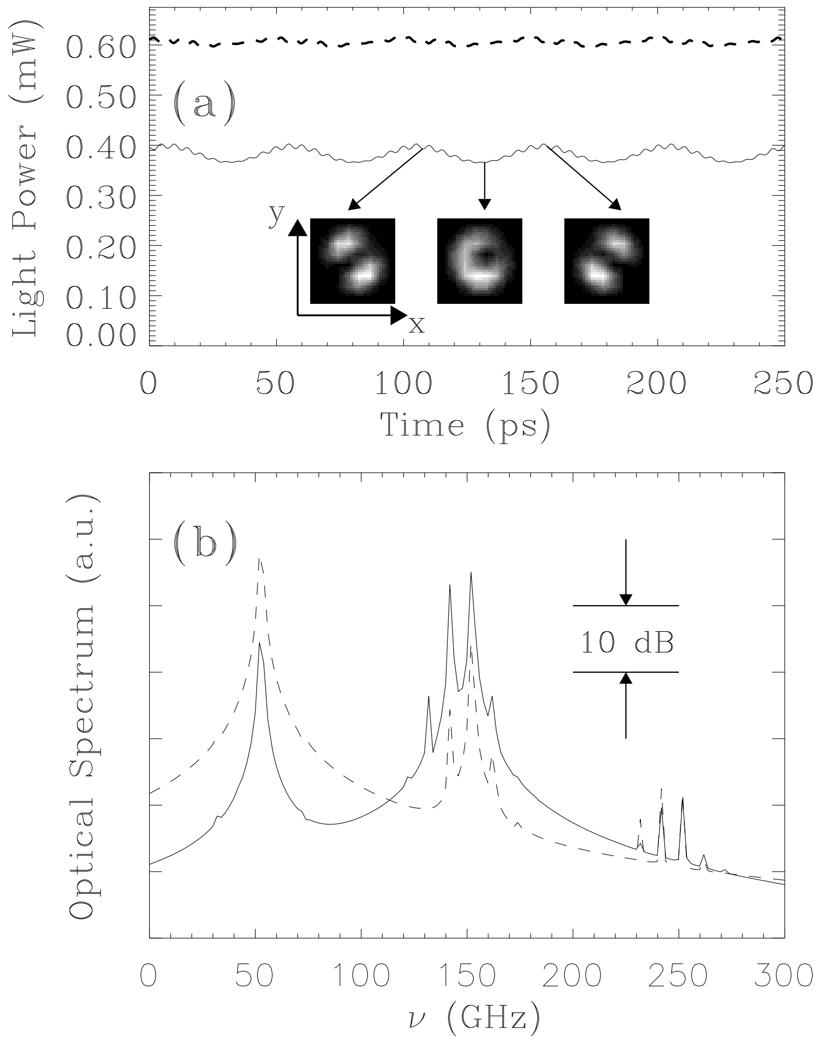

Figure 7.5: VCSEL B. (a) Time evolution of the total emitted power, and (b) optical spectrum at $I = 2.55I_{th}$. Solid (dashed) line stands for the $\hat{x}$ ($\hat{y}$) polarized field component.

tively) is observed in the intensity of the $\hat{x}$ polarization and evidenced in its intensity spectrum (not shown). At this current, the spatio-temporal dynamics of the beam is different depending on the polarization. The $\hat{y}$-polarized beam keeps a single-lobe distribution (almost Gaussian) with the peak slightly moving around the center of the VCSEL axis. In the orthogonal polarization, the beam profile oscillates periodically (it does not twist) between two positions where the beam consists on two-lobes oriented along the diagonals of the $x - y$ plane (see the insets in Fig. 7.5) and the emitted power is maximum. Between these two positions, we observe doughnut-like emission corresponding to the minimum emitted power.

We have finally studied the relevance of the coupling mechanism between the circularly polarized emission channels in the transverse and polarization properties of gain-guided VCSELs. Fig. 7.6 shows the L-I characteristics for VCSEL B assuming a larger spin-flip relaxation rate ($\gamma_s = 500\gamma_e$). For these conditions, there is very

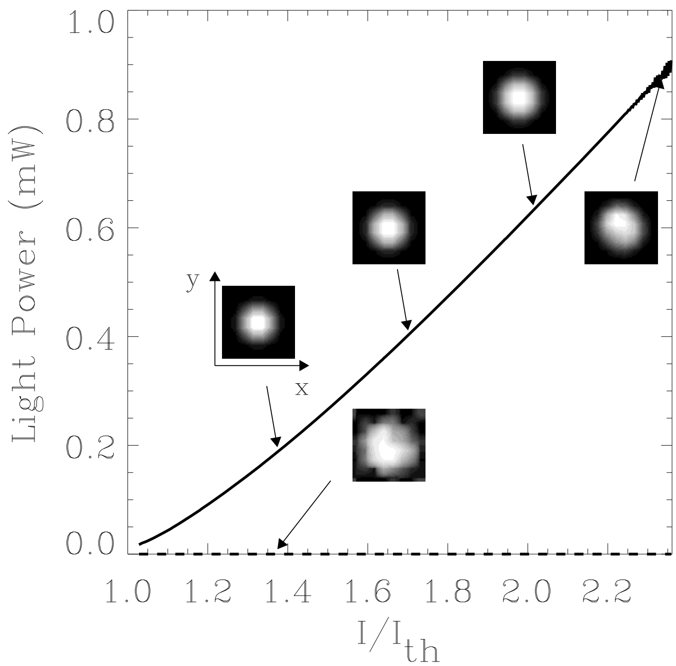

Figure 7.6: Fast spin-flip relaxation rate. Same as in Fig. 7.3 but for ϕ=10 μm, η_p=3γ_e, η_a=-5γ_e, and γ_s=500 γ_e.

fast mixing of the carrier population between the two circularly polarized emission channels, so that n quickly relaxes to zero and the two linearly polarized fields are coupled to a single carrier population N. The most relevant difference with respect to previous cases is that now the dynamics is not sensitive to the polarization: *i)* polarization switching is not observed in the fundamental mode regime; and *ii)* the first-order transverse mode starts lasing in the same polarization than the fundamental mode. Both features point out the relevance of spin-flip relaxation processes in the polarization and transverse mode instabilities commonly observed in VCSELs.

An additional relevant feature is that the fundamental mode regime extends up to $I \sim 2.25 I_{th}$. This result may indicate that the onset of higher-order modes does not only depend on the modal gain, as one could think *a priori* but additional mechanisms, such as spin-flip dynamics, may influence the threshold condition for the high-order transverse modes.

Chapter 8

Summary and conclusions

This work has been devoted to the study of the polarization and transverse mode characteristics of Vertical Cavity Surface Emitting Lasers. Theoretical analysis, numerical simulations and experiments have been combined to investigate the role of physical mechanisms — such as the saturable dispersion (or α-factor), the VCSEL anisotropies, the spin-flip relaxation processes, and the temperature — on the polarization and the transverse mode properties of unstrained quantum-well VCSELs.

After a brief introduction to semiconductor lasers in Chap. 1, Chap. 2 reports experimental measurements of the electrical, optical and thermal properties of VCSELs. We studied the dependence of the LIV characteristics on the substrate temperature. We also measured the thermal resistance and the characteristic thermal time of the devices. Regarding the polarization properties, we found the commonly observed feature that VCSELs typically emit linearly polarized light preferentially oriented along two orthogonal directions of the transverse plane. The polarization state during fundamental mode operation was found to depend on the injected current and the active layer temperature. Polarization instabilities were also observed during multi-transverse mode operation at high injection currents. The basic polarization properties measured in the experiments, together with the range of parameters determined, gave a first-hand basis to the theoretical modeling and results of the remaining Chapters.

In Chap. 3 we presented a derivation of the San Miguel-Feng-Moloney (SFM) model [112]. Starting from the Maxwell equations and taking into account the boundary conditions of the VCSEL cavity, we obtained dynamical equations for the slowly-varying circularly polarized components of the vector optical field, interacting with the medium through the macroscopic dipole vector. Dynamical equations for the material variables were derived from a four-level approximation to the band structure of quantum-well media in VCSELs — the simplest energy level picture that accounts for the quantum nature of the polarization in VCSELs — using a density-matrix formalism. The SFM model was finally written down in terms of two sets of two-level Maxwell-Bloch equations coupled through spin-flip relaxation processes and including spatial effects through optical diffraction and carrier diffusion. We also discussed the limitations of Two-Level Maxwell-Bloch type of approach in the description of semiconductor dynamics.

In Chap. 4 we presented a rate–equation model, derived from the original SFM model, useful to describe polarization state selection in VCSELs operating in the fundamental transverse mode [113, 114, 115, 116]. In order to understand the consequences of the physical mechanisms included in the model — VCSEL anisotropies, saturable dispersion and the dynamics of the magnetic sublevel populations — on the polarization state selection of VCSELs we first discussed in detail the idealized situation of isotropic gain. We then considered more realistic situations in which the effect of saturable dispersion and small gain anisotropies were combined. We demonstrated polarization switchings as the current is increased which are the result of the combined effect of saturable dispersion, spin dynamics, and cavity anisotropies. We also found elliptically polarized states in absence of magnetic field and the type of two-frequency solutions sometimes observed close to threshold. We provided a variety of representations (time series, power spectra, polarization state resolved spectra, Poincare sphere, fractional polarization, etc.) for the interpretation of the observed phenomena. We finally demonstrated polarization switchings induced by injected optical fields, including hysteresis. All the results mentioned previously reproduce the general scenarios observed experimentally.

In Chap. 5 we studied the influence of an axial magnetic field on the polarization properties of VCSELs [117]. For weak magnetic fields we found that the magnetically-induced circular birefringence combined with the intrinsic linear birefringence of the VCSEL transforms the preferred basis states of the system from linearly polarized to elliptically polarized. We observed that the characteristic switching between orthogonal linearly polarized states with no magnetic field ($\hat{x} \longrightarrow \hat{y}$) became a switching between elliptically polarized states, and we studied the dependence of the ellipticity of the emitted light as a function of the injected current and the magnetic field, obtaining a good agreement with the experimental reports. Time-dependent polarization states found in the switching process and/or at intermediate magnetic fields were also characterized using the optical spectrum and the Poincare sphere. For large magnetic fields we showed that emission was in an almost rotating linearly polarized state where the intensity in each linear polarized component was modulated in time. This feature allowed us to propose an alternative way of generating low-chirp linearly polarized periodic pulses, namely to apply an axial magnetic field to an almost isotropic VCSEL, showing that gigahertz pulse rates can be achieved for nearly isotropic devices with several technological applications [118].

In Chap. 6 we carried out polarization switching experiments minimizing the effects of temperature on the device in order to discriminate between the effects produced by the mechanisms included in the SFM model and those produced by the current-induced self-heating on the polarization state of the light emitted by VCSELs operating in the fundamental transverse mode [119]. We demonstrated for the first time to our knowledge that polarization switching phenomena can still be observed when the active region temperature is keep constant, in opposition to the common thermal explanation. Such a result pointed out that the physical mechanisms unrelated to temperature changes, namely saturable dispersion, birefringence and spin-flip dynamics, are involved in the selection of the polarization state under isothermal conditions. We also performed a quantitative comparison of the experimental data and the model predictions by studying the dependence of the switching current on the active layer temperature, which allowed us to estimate the spin-flip relaxation rate and the intrinsic dichroism of the VCSEL.

In Chap. 7 we studied the spatio-temporal and polarization properties of gain-guided VCSELs using the model derived in Chap. 3 [120, 121]. We first studied the turn-on dynamics of the VCSEL and showed that the time necessary for the selection of the polarization state is of the order of few ns. We next showed that the commonly observed scenarios of transverse mode competition and polarization state selection in gain-guided VCSELs can be accounted for within the general model, namely *i*) the fundamental transverse mode with the higher gain-to-loss ratio is always selected at threshold; *ii*) polarization stability and polarization switching behaviors can occur during fundamental mode operation of the device; *iii*) for higher injection currents, the first order transverse mode appears orthogonally polarized to the fundamental one; and *vi*) for even higher currents, there is polarization coexistence with several active transverse modes. We finally studied the case of very fast spin-flip relaxation and found that, in this case, the transverse dynamics is not sensitive to polarization.

In conclusion, within the limitations of the SFM model for a complete description of quantum-well VCSELs, we have shown that it properly describes the polarization and transverse mode behavior commonly observed in these devices in a variety of situations: as the injection current is changed, with optical injection, in axial magnetic fields, etc. In addition, supported on the experimental results of Chap. 6 we conclude that the physical mechanisms included in the model, namely saturable dispersion (or α-factor), VCSEL anisotropies, and spin-flip relaxation processes, are responsible for the selection of the polarization state in these devices when thermal effects are avoided (e.g., in LI characteristics performed under fast current ramp excitation, measurements at constant current with optical injection or in axial magnetic fields, etc.). Based on the results of Chap. 4 we claim that the particular role of each of these mechanisms on the polarization state should depend on the VCSEL characteristics. For devices where dichroism is large, the mode favored by the amplitude anisotropy must dominate at any current — this is well known for VCSEL designers —. For more isotropic VCSELs (small dichroism), the polarization behavior should depend on the value of birefringence. Low birefringence devices (low as compared with the spin-flip rate) with dichroism favoring the lower wavelength polarization mode ($\hat{y}$) should also show polarization stability. However, if the favored mode is the orthogonal one (higher wavelength or $\hat{x}$), polarization switching as a consequence of saturable dispersion must be observed. For high birefringency VCSELs and gain anisotropy favoring the higher wavelength mode ($\hat{x}$), the VCSEL should emit with stable polarization at any current. For dichroism favoring the orthogonal mode, VCSEL emission has to have a polarization switching due to the combined effect of saturable dispersion and spin-dynamics. Notice, however, that these mechanisms are influenced by thermal effects in experiments where the active region temperature cannot be not controlled. For these cases, it should be difficult to isolate the mechanisms affecting the polarization state. Nevertheless, the SFM model can be applied to gain some insight on the problem, but then it needs to be complemented to account for some of these effects. As an example, the self-heating induce change in the material gain difference between the linearly polarized modes can be roughly taken into account through a linear dependence of the parameter γ_a on the temperature, as given in Chap. 6.

Appendixes

Appendix A : Transverse cavity modes

As a plane parallel resonator, gain-guided VCSELs have not well defined transverse cavity modes, so additional guiding of the optical field is required to accomplished stable operation. The guiding mechanisms in these devices have been briefly discused in Sec. 7.2, namely the nonlinear susceptibility associated with the carrier density in the medium, which provides both gain-guiding an index anti-guiding, and the thermal-lensing (thermal guiding) effect caused by Joule heating. The interplay between these mechanism is very complex and, typically, the transverse modes of gain-guided VCSELs have to be obtained by numerical simulations, as shown in Chap. 7.

Nevertheless, considerable insight about the transverse modes shapes of the circular gain-guided VCSEL resonator can be obtained by assuming that the resulting refractive index distribution, if dominated by the thermally-induced index-guiding profile, is approximately parabolic [54, 56]. Under these assumptions, one can make reference to the results relative to graded-index fibres, for which the fiber mode shape are very similar to the Gauss-Laguerre modes of a resonator with spherical mirrors [57, 181, 182].

Taking into account that VCSELs emit in a single longitudinal mode, the associated transverse modes can be labeled by the pair of indices (p, l) p=0, 1, 2, ..., l=0, ±1, ±2, ... The Gauss-Laguerre function associated with mode (p, l) is

$$A_{p,l}(u,\phi) = \sqrt{\frac{2}{\pi}} \left[\frac{p!}{(p+|l|)!}\right] u^{\frac{|l|}{2}} \mathcal{L}_p^{|l|}(u) e^{-\frac{u}{2}} e^{il\phi} \tag{8.1}$$

where $u = 2r$, r and ϕ are the polar coordinates, and $\mathcal{L}_p^{|l|}(u)$ are the generalized Laguerre polynomials of indices p and q which obey the differential equation

$$u\frac{d^2\mathcal{L}_p^{|l|}}{dx^2} + (|l|+1-u)\frac{d\mathcal{L}_p^{|l|}}{dx} + p\mathcal{L}_p^{|l|} \tag{8.2}$$

Some polynomials of low order are $\mathcal{L}_0^{|l|}(u)$=1, $\mathcal{L}_1^{|l|}(u)$=$|l|$+1-u, $\mathcal{L}_0^{|l|}(u)$= $(|l|+1)(|l|+2)/2-(|l|+2)u+u^2/2$.

The emission frequency of the transverse modes only depend on the index q=2p+$|l|$, in such a way that the higher the index q the higher the optical emission frequency and the higher the diffraction losses. Fig. 8.1 shows the transverse mode patterns of the lowest-order q-families of Gaussian-Laguerre modes. Each family of order q consists on q+1 independent modes (different transverse profiles). The fundamental mode, $\mathrm{A}_{0,0}$, is Gaussian and is usually termed the TEM_{00} mode. The family q=1 has two independent modes, the $\mathrm{A}_{0,1^+}$ and the $\mathrm{A}_{0,1^-}$, usually termed TEM_{10} and TEM_{01} modes, respectively, where we have use the notation $\mathrm{A}_{p,l^\pm}$ for the linear combination $\mathrm{A}_{p,+l} \pm \mathrm{A}_{p,-l}$. The combination of both modes yields two doughnut modes of opposite helicity but equal intensity distribution, $\mathrm{A}_{0,+1}$ and $\mathrm{A}_{0,-1}$ (or TEM_{01^*} modes).

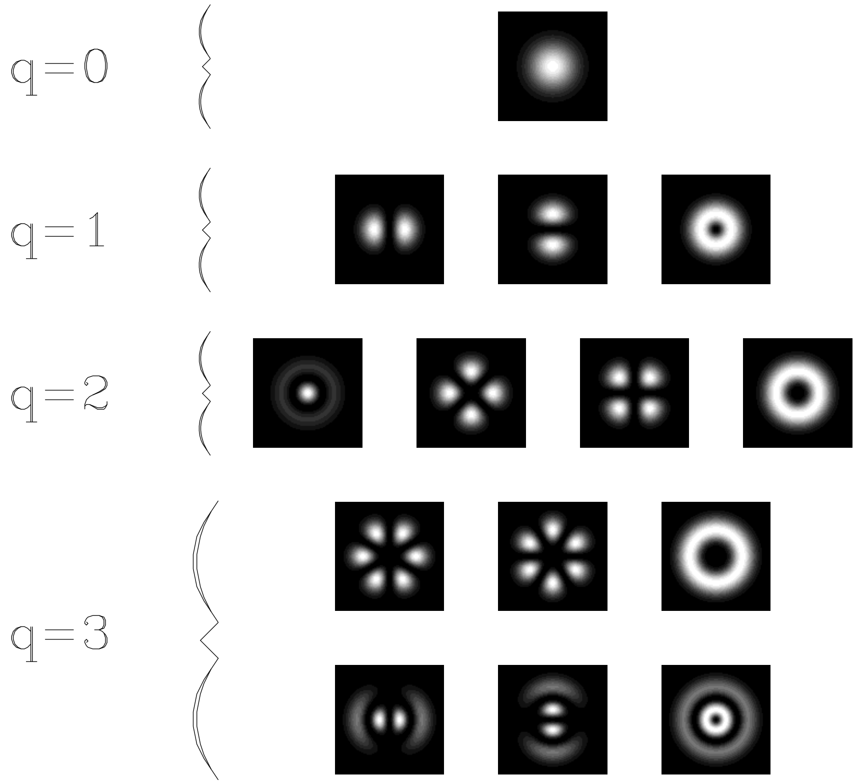

Figure 8.1: Mode patterns of the lowest-order q-families (modes of the same family are frequency degenerated) using a Gauss-Laguerre polynomials approach valid for parabolic index profile. The families are: (a) q=0, with mode $A_{0,0}$; (b) q=1, with modes $A_{0,1+}$ (left), $A_{0,1-}$ (center), and $A_{0,\pm 1}$ (right); (c) q=2, with modes $A_{1,0}$ (left), $A_{0,2+}$ (center left), $A_{0,2-}$ (center right), and $A_{0,\pm 2}$ (right); (d) q=3, with modes $A_{0,3+}$ (up left), $A_{0,3-}$ (up center), $A_{0,\pm 3}$ (up right), $A_{1,1+}$ (down left), $A_{1,1-}$ (down center), and $A_{1,\pm 1}$ (down right). Notice that the area occupied by a mode increases with the index number q, so diffraction losses increase with q.

The family q=2 has a cylindrically symmetric mode, the $A_{1,0}$, and two independent modes, the $A_{0,2+}$ (TEM_{11}) and the $A_{0,2-}$, whose combinations gives again two doughnut modes of opposite helicity and equal intensity distribution but higer diffraction losses than the doughnut modes of the q=1 family. For the family q=3, there are 4 independent transverse modes, namely $A_{0,3+}$, $A_{0,3-}$, $A_{1,1+}$, and $A_{1,1-}$.

The previous approach is rather idealized since we have not taken into account the contribution of the carrier distribution to the guiding mechanism. In addition, high-resolution spectral measurements show that transverse modes of the same q-family are frequency non-degenerated, which might be a consequence of transverse asymmetries of the VCSEL cavity [49]. Despite its simplicity, Gauss-Laguerre modes provides a good approximation to the numerical results found in Chap. 7. Similar transverse mode profiles can be obtained using Bessel functions, but using a different approach [65]-[67].

Appendix B : Generalized time evolution equation for the density-matrix elements of a N levels atom

In this section, we derive the generalized evolution equations for the density-matrix elements of a laser system with N energy levels. The Hamiltonian of such a system, H_o, determines the energy levels by the eigenvalue equation

$$H_o\psi_j = E_j\psi_j \qquad (j = 1, ..., N) \ , \tag{8.3}$$

where $\psi_j(\vec{s}\,)$ is the normalized electron wave function in the energy level j, $E_j = \hbar\omega_j$ is the electron energy at this level, and $\vec{s}$ stands for the electronic coordinate. In the presence of an optical field perturbing an atom located at the position $\vec{\mathbf{r}}_0$ of the space

$$\vec{\mathbf{E}}(\vec{\mathbf{r}}_0, t) = \vec{\mathcal{E}}(\vec{\mathbf{r}}_0, t)\ \mathrm{e}^{\mathrm{i}\,\Omega t} + \vec{\mathcal{E}}^*(\vec{\mathbf{r}}_0, t)\ \mathrm{e}^{-\mathrm{i}\,\Omega t} \ , \tag{8.4}$$

where $\vec{\mathcal{E}}(\vec{\mathbf{r}}_0, t)$ is the slowly varying amplitude of the optical field, the Hamiltonian of the system becomes time-dependent

$$H(\vec{s}\,, t) = H_0(\vec{s}\,) + V_{ext}(\vec{s}\,, t) \ , \tag{8.5}$$

where $V_{ext}(\vec{s}\,, t) = -e\vec{s}\,\vec{\mathbf{E}}(t)$, is the interaction energy in the dipole approximation [183]. The Schrödinger equation of the perturbed atom reads

$$H\psi = [H_0 - e\vec{s}\,\vec{\mathbf{E}}\,]\ \psi = -\mathrm{i}\,\hbar\,\partial_{\,t}\,\psi \ , \tag{8.6}$$

where $\psi(\vec{s}\,, t)$ is the new time-dependent electron wave function on the perturbed atom which can be written as a linear combination of the unperturbed wavefunctions $\psi_j(\vec{s}\,)$ with time-dependent coefficients

$$\psi(\vec{s}\,, t) = \sum_{j=1}^{N} a_j(t)\psi_j(\vec{s}\,) \ . \tag{8.7}$$

The macroscopic dipole polarization is defined as $\vec{\mathcal{P}} = n_a \vec{p_{at}}$, where the atomic dipole polarization is given by

$$\vec{p_{at}} = e < \vec{s}\ >= e\int d\vec{s}\ \ \psi^*\ \vec{s}\ \ \psi = \sum_{j,k=1}^{N} \rho_{j,k}\ \vec{\Theta}_{k,j} = Tr\left[\rho\ \vec{\Theta}\right] \ , \tag{8.8}$$

where ρ is the *density-matrix*, whose elements are defined as

$$\rho_{j,k} = a_j a_k^*, \qquad \text{such that} \quad \rho_{j,k} = \rho_{k,j}^* \ , \tag{8.9}$$

and $\vec{\Theta}$ is the *dipole matrix*, whose elements are defined as

$$\vec{\Theta}_{k,j} = e\int d\vec{s}\ \ \psi_k^*(\vec{s}\,)\vec{s}\,\psi_j(\vec{s}\,), \qquad \text{such that} \quad \vec{\Theta}_{k,j} = \vec{\Theta}_{j,k}^* \ . \tag{8.10}$$

Inserting Eq. (8.7) into Eq. (8.6), multiplying by ψ_k^*, and integrating over the electron coordinate ($\int d\vec{s}\ \ \psi_j\psi_k^* = \delta_{jk}$), we end up with

$$\sum_{j=1}^{N} a_j\ \hbar\omega_j\ \delta_{jk} - \vec{\mathbf{E}}\ \cdot \sum_{j=1}^{N} a_j\ \vec{\Theta}_{k,j} = -\mathrm{i}\,\hbar \sum_{j=1}^{N} \dot{a}_j\ \delta_{jk}\ , \tag{8.11}$$

from which

$$\dot{a}_k \ = \ \mathrm{i}\ \omega_k\ a_k + \frac{1}{\mathrm{i}\,\hbar}\,\vec{\mathbf{E}}\ \cdot \sum_{j=1}^{N} a_j\ \vec{\Theta}_{k,j}\ , \tag{8.12}$$

$$\dot{a}_l^* \ = \ -\mathrm{i}\ \omega_l\ a_l^* - \frac{1}{\mathrm{i}\,\hbar}\,\vec{\mathbf{E}}\ \cdot \sum_{j=1}^{N} a_j^*\ \vec{\Theta}_{l,j}^*\ . \tag{8.13}$$

Taking into account Eqs. (8.12) and (8.13) and the definition in Eq. (8.9), the time-evolution equation for the density-matrix elements can be derived from the previous equations. It reads

$$\dot{\rho}_{k,l} = +\mathrm{i}\ \ \omega_{k,l}\ \rho_{k,l} - \frac{1}{\mathrm{i}\,\hbar}\,\vec{\mathbf{E}} \cdot \sum_{j=1}^{N} \left[\rho_{k,j}\ \vec{\Theta}_{j,l} - \rho_{j,l}\ \vec{\Theta}_{k,j}\right]\ , \tag{8.14}$$

where we have defined $\omega_{k,l} = \omega_k - \omega_l$ as the frequency difference between the k and l energy levels.

Appendix C : Cavity anisotropy tensor

Apart from the isotropic amplitude and phase changes, the vector field in the VC-SEL, $\vec{F}$, is subject to cavity or gain anisotropies which might modify the polarization properties of the output light. It is possible to write a general anisotropy tensor, Γ, as [97, 103, 184]

$$\dot{\vec{F}} = \Gamma\vec{F}\ , \qquad\qquad \Gamma = \sum_{i=1}^{3} \Gamma_i\ . \tag{8.15}$$

The anisotropy tensors Γ_i can be written in the linear (l) or in the circular (c) basis independently, e.g. $\Gamma^c = \mathbf{T}\ \Gamma^l\ \mathbf{T^{-1}}$, taking into account the Jones transformation matrix, $\mathbf{T}$, given by

$$\mathbf{T} = \frac{1}{\sqrt{2}} \begin{pmatrix} 1 & \mathrm{i} \\ 1 & -\mathrm{i} \end{pmatrix}\ , \quad \mathbf{T^{-1}} = \frac{1}{\sqrt{2}} \begin{pmatrix} 1 & 1 \\ -\mathrm{i} & \mathrm{i} \end{pmatrix}\ . \tag{8.16}$$

The components of the anisotropy tensors are

- *(i=1)* The linear dichroism tensor, of magnitude (γ_a) and main axes $\theta = \theta_a$ and $\theta = \theta_a + \pi/2$ (with respect an arbitray axis of the transverse plane)

$$\Gamma_1^l = -\gamma_a \begin{pmatrix} cos(2\theta_a) & sin(2\theta_a) \\ sin(2\theta_a) & -cos(2\theta_a) \end{pmatrix} \;, \qquad \Gamma_1^c = -\gamma_a \begin{pmatrix} 0 & e^{\mathrm{i}\,2\theta_a} \\ e^{-\mathrm{i}\,2\theta_a} & 0 \end{pmatrix} . \tag{8.17}$$

- *(i=2)* The linear birefringency tensor, of magnitude (γ_p) and main axes $\theta = \theta_p$ and $\theta = \theta_p + \pi/2$

$$\Gamma_2^l = -\mathrm{i}\,\gamma_p \begin{pmatrix} cos(2\theta_p) & sin(2\theta_p) \\ sin(2\theta_p) & -cos(2\theta_p) \end{pmatrix} \;, \qquad \Gamma_2^c = -\mathrm{i}\,\gamma_p \begin{pmatrix} 0 & e^{\mathrm{i}\,2\theta_p} \\ e^{-\mathrm{i}\,2\theta_p} & 0 \end{pmatrix} . \tag{8.18}$$

- *(i=3)* The circular anisotropy tensor, including dichroism (γ_c) and birefringency (γ_z)

$$\Gamma_3^l = (\gamma_c + \mathrm{i}\,\gamma_z) \begin{pmatrix} 0 & \mathrm{i} \\ -\mathrm{i} & 0 \end{pmatrix} \;, \qquad \Gamma_3^c = (\gamma_c + \mathrm{i}\,\gamma_z) \begin{pmatrix} 1 & 0 \\ 0 & -1 \end{pmatrix} . \tag{8.19}$$

- In addition, isotropic amplitude loss, ξ_a, and phase, ξ_p, can be written down in any basis, as

$$\Gamma_{iso} = (\xi_a + \mathrm{i}\,\xi_p) \begin{pmatrix} 1 & 0 \\ 0 & 1 \end{pmatrix} . \tag{8.20}$$

For simplicity, if we consider that the directions of both linear amplitude and phase anisotropy coincide with the $\hat{x}$ axis, the anisotropy tensor can be written as

$$\Gamma^c = -(\gamma_a + \mathrm{i}\,\gamma_p) \begin{pmatrix} 0 & 1 \\ 1 & 0 \end{pmatrix} + (\gamma_c + \mathrm{i}\,\gamma_z) \begin{pmatrix} 1 & 0 \\ 0 & -1 \end{pmatrix} , \tag{8.21}$$

$$\Gamma^l = -(\gamma_a + \mathrm{i}\,\gamma_p) \begin{pmatrix} 1 & 0 \\ 0 & -1 \end{pmatrix} + (\gamma_c + \mathrm{i}\,\gamma_z) \begin{pmatrix} 0 & \mathrm{i} \\ -\mathrm{i} & 0 \end{pmatrix} , \tag{8.22}$$

Therefore, the anisotropic terms to be added to the evolution equations of the optical field in Chap. 4 are

$$\dot{F}_{\pm} = -(\gamma_a + \mathrm{i}\,\gamma_p) F_{\mp} \pm (\gamma_c + \mathrm{i}\,\gamma_z) F_{\pm} . \tag{8.23}$$

$$\dot{F}_{x(y)} = \mp(\gamma_a + \mathrm{i}\,\gamma_p) F_{x(y)} \pm \mathrm{i}\,(\gamma_c + \mathrm{i}\,\gamma_z) F_{y(x)} . \tag{8.24}$$

Appendix D : Calculation of the "material" gain anisotropy between the linearly polarized modes in the Maxwell-Bloch approximation

An estimate of the material gain difference associated with two orthogonally polarized modes of slightly different frequency, can be performed rewriting Eqs. (7.1) and (7.2) in the frequency domain, neglecting the transverse terms, and considering the steady state carrier population values for linearly polarized light (n^{ST} =0, $N^{ST} = N_i^{th}$). These equations, in the linear basis, read (η_a=0)

$$\begin{aligned} \mathrm{i}\,\omega E_i^\nu &= -\kappa(1+\mathrm{i}\,\theta)E_i^\nu + P_i^\nu \pm \mathrm{i}\,\eta_p E_i^\nu \;, && (8.25)\\ \mathrm{i}\,\omega P_i^\nu &= -\gamma_\perp(1-\mathrm{i}\,\theta)P_i^\nu + \gamma_\perp a(1+\theta^2)(N_i^{th}-N_0)E_i^\nu \;, && (8.26) \end{aligned}$$

where the positive (negative) sign stands for the $i = x(y)$ polarized TEM$_{00}$ mode. Inserting Eq. (8.26) into Eq. (8.25), the fundamental mode emission frequencies are

$$\omega_x = \frac{\eta_p}{1+\kappa/\gamma_\perp}\;, \qquad \omega_y = -\frac{\eta_p}{1+\kappa/\gamma_\perp}\;,$$

so the frequency splitting between the linearly polarized modes (birefringence) is

$$\Delta\omega = \omega_x - \omega_y = \frac{2\eta_p}{1+\kappa/\gamma_\perp}\;, \tag{8.27}$$

The carrier threshold values for each linearly polarized mode are

$$N_i^{th} - N_0 = \frac{(1+(\theta-\omega_i/\gamma_\perp)^2)}{a(1+\theta^2)}\kappa \qquad \text{i=x,y}\;, \tag{8.28}$$

Above threshold, the carrier density remains clamped to its threshold value N^{th} (smallest value of N_x^{th} and N_y^{th}), which will depend on the particular choice of the detuning. Considering the case of VCSEL A in Chap. 7, and for negative detuning ($\theta \to -|\theta|$), the carrier threshold corresponds to the $\hat{y}$-polarized mode

$$N_y^{th} - N_0 = N^{th} - N_0 = \frac{\kappa}{a}\frac{1+\left(-|\theta|+\frac{\eta_p}{\gamma_\perp+\kappa}\right)^2}{1+\theta^2}\;. \tag{8.29}$$

The material gain for this mode at threshold, given by the real part of the nonlinear susceptibility, equal losses ($g(\omega_y) = \kappa$). For the orthogonal polarization, the material gain at threshold is

$$g(\omega_x) = \kappa\frac{1+\left(-|\theta|+\frac{\eta_p}{\gamma_\perp+\kappa}\right)^2}{1+\left(-|\theta|-\frac{\eta_p}{\gamma_\perp+\kappa}\right)^2}\;. \tag{8.30}$$

so the gain difference between the linearly polarized modes, Δg, reads

$$\Delta g = g(\omega_y) - g(\omega_x) = \kappa \frac{4|\theta|\eta_p}{(1+\theta^2)(\kappa + \gamma_\perp)} \; . \tag{8.31}$$

For the parameter values given in Chap. 7 for VCSEL A, $\Delta g = 2\gamma_a \approx 0.05$ ns^{-1}.

Bibliography

[1] R. Steele, *Laser Focus World* **33**(2), 84 (1997).

[2] M. Razheghi, *Opt. & Phot. News* **6**(8), 16 (1995).

[3] A. F. J. Levi, *Physics World* **6**(10), 32 (1993).

[4] For a review in this topic see T.E. Sale, *Vertical Cavity Surface Emitting Lasers*, (Wiley, New York, 1995).

[5] For a review in this topic see C. J. Chang-Hasnain, "Vertical-Cavity Surface-Emitting Lasers", in *Semiconductor Lasers: past, present, and future*, Ed. G. P. Agrawal, (AIP Press, New York, 1995), Chap. 5.

[6] H. Soda, K. Iga, C. Kitahara, and Y. Suematsu, *Jpn. J. Appl. Phys.* **18**, 2329 (1979).

[7] J. Jewell, and G. Olbright, *Laser Focus World* **28**(5), 217 (1992).

[8] J. Jewell, and G. Olbright, *Opt. & Phot. News* **5**(3), 8 (1994).

[9] E. G. Paek, *Opt. & Phot. News* **4**(5), 16 (1993).

[10] A. Mooradian, K. Wall, and J. Keszenheimer, *Opt. & Phot. News* **6**(11), 17 (1995).

[11] I. Hayashi, M. B. Panish, P. W. Foy, and S. Sumski, *Appl. Phys. Lett.* **17**, 109 (1970); Zh. I. Alferov, V. M. Andreev, D. Z. Garbuzov, Yu. V. Zhilyaev, E. P. Mozorov, E. L. Portnoi, and V. G. Trofim, *Sov. Phys. Semicond.* **4**, 1573 (1971).

[12] For a review in this topic see J. J. Coleman, "Quantum-Well heterostructure lasers", in *Semiconductor Lasers: past, present, and future*, Ed. G. P. Agrawal, (AIP Press, New York, 1995), Chap. 1.

[13] H. Kogelnik, and C. V. Shank, *J. Appl. Phys.* **43**, 2327 (1972); W. Streifer, R. D. Burnham, and D. R. Scifres, *IEEE J. Quantum Electron.* **11**, 154 (1975).

[14] K. Utaka, S. Akkiba, and Y. Matsushima, *IEEE J. Quantum Electron.* **22**, 1042 (1986).

[15] Y. Tohmori, H. Oohashi, T. Kato, S. Arai, K. Komori, and Y. Suematzu, *Electron. Lett.* **22**, 138 (1986).

[16] Z. L. Liau, and J. N. Walpole, *Appl. Phys. Lett.* **50**, 528 (1987).

[17] N. W. Carlson, G. A. Evans, D. P. Bour, and S. K. Liew, *Appl. Phys. Lett.* **56**, 16 (1990).

[18] J. Hetch, *Laser Focus World* **29**(4), 199 (1993).

[19] J. Hetch, *Laser Focus World* **28**(5), 127 (1992).

[20] S. E. H. Turley, G. D. Henshall, P. D. Greene, V. P. Knight, D. M. Moule, and S. A. Wheeler, *Electron. Lett.* **17**, 868 (1981); H. Kawaguchi, and T. Kawakami, *IEEE J. Quantum Electron.* **13**, 566 (1977).

[21] M. Hirao, S. Tsuji, K. Mizushi, A. Doi, and M. Nakamura, *Opt. Commun.* **1**, 10 (1980).

[22] P. A. Kirkby, A. R. Goodwin, G. H. B. Thompson, and P. R. Selway, *IEEE J. Quantum Electron.* **13**, 705 (1977).

[23] N. Chinone, R. Ito, and O. Nakada, *J. Appl. Phys.* **47**, 785 (1976).

[24] D. R. Scifres, C. Lindstrom, R. D. Burnham, W. Streifer, and T. L. Paoli, *Electron. Lett.* **19**, 169 (1983).

[25] D. E. Ackley, *Appl. Phys. Lett.* **42**, 152 (1983).

[26] D. Botez, M. Jansen, L. J. Mawst, G. Peterson, and T. L. Roth, *Appl. Phys. Lett.* **58**, 2070 (1991).

[27] K. Iga, F. Koyama, and S. Kinoshita, *IEEE J. Quantum Electron.* **24**, 1845 (1988).

[28] S. W. Corzine, R. S. Geels, J. W. Scott, R. H. Yan, and L. A. Coldren *IEEE J. Quantum Electron.* **25**, 1514 (1989).

[29] J. L. Jewell, J. P. Harbison, A. Scherer, Y. H. Lee, and L. T. Florez, *IEEE J. Quantum Electron* **27**, 1332 (1991).

[30] Ref [4], Chap. 4

[31] C. J. Chang-Hasnain, J. P. Harbison, G. Hasnain, A. C. Von Lehmen, L. T. Florez, and N. G. Stoffel, *IEEE J. Quantum Electron.* **27**, 1402 (1991).

[32] C. J. Chang-Hasnain, M. Orenstein, A. C. Von Lehmen, L. T. Florez, J. P. Harbison, and N. G. Stoffel, *Appl. Phys. Lett.* **57**, 218 (1990).

[33] C. J. Chang-Hasnain, J. P. Harbison, L. T. Florez, and N. G. Stoffel, *Electron. Lett.* **27**, 163 (1991).

[34] K. D. Choquette, G. Hasnain, Y. H. Wang, J. D. Wynn, R. S. Freund, A. Y. Cho, and R. E. Leibenguth, *IEEE Photon. Technol. Lett.* **3**, 859 (1991).

[35] M. Ogura, S. Fujii, T. Okada, M. Mori, T. Asaka, and H. Iwano, *Jap. J. of Appl. Phys.* **30**, 3879 (1991).

[36] C. J. Chang-Hasnain, Y. A. Wu, G. S. Li, G.Hasnain, and K. D. Choquette, *Appl. Phys. Lett.* **63**, 1307 (1993).

[37] D. L. Huffaker, D. G. Deppe, and T. J. Rogers, *Appl. Phys. Lett.* **65**, 1611 (1994).

[38] B. Tell, K. F. Brown-Goebeler, R. E. Leibenguth, F. M. Baez, and Y. H. Lee, *Appl. Phys. Lett.* **60**, 683 (1992).

[39] G. Hasnain, K. Tai, L. Yang, Y. H. Wang, R. J. Fischer, J. D. Wynn, B. Weir, N. K. Dutta, and A. Y. Cho, *IEEE J. Quantum Electron* **27**, 1377 (1991).

[40] D. B. Young, J. W. Scott, F. H. Peters, M. G. Peters, M. L. Majewski, B. F. Thibeault, S. W. Corzine, L. A. Coldren, *IEEE J. Quantum Electron.* **29**, 2013 (1993).

[41] H. C. Casey Jr., and M. B. Panish, in "Heterostructure lasers", (Academic Press, New York, 1978).

[42] J. W. Scott, D. B. Young, B. F. Thibeault, M. G. Peters, and L. A. Coldren, *IEEE J. Select. Topics Quantum Electron.* **1**, 638 (1995).

[43] R. S. Geels, S. W. Corzine, J. W. Scott, D. B. Young, and L. A. Coldren, *IEEE Photon. Technol. Lett.* **2**, 234 (1990).

[44] E. F. Schubert, L. W. Tu, G. J. Zidzik, R. F. Kopf, A. Benvenutim, and M. R. Pinto, *Appl. Phys. Lett.* **60**, 466 (1992).

[45] K. Kojima, R. A. Morgan, T. Mullally, G. D. Guth, M. W. Focht, R. E. Leibenguth, and M. T. Asom, *Electron. Lett.* **29**, 1771 (1993).

[46] A. Scherer, J.L. Jewell, M. Walther, J.P. Harbison, and L.T. Florez, *Electron. Lett.* **28**, 1224 (1992).

[47] H. Li, T. L. Lucas, J. G. McInerney and R. A. Morgan, *Chaos, Solitons and Fractals* **4**, 1619 (1994).

[48] G. S. Li, S. F. Lim, W. Yuen, and C. J. Chang-Hasnain, *Electron. Lett.* **31**, 2014 (1995).

[49] A. K. Jansen van Doorn, M. P. van Exter and J. P. Woerdman, *Electron. Lett.* **30**, 1941 (1994).

[50] J. E. Epler, G. Gehsitz, K. H. Gulden, M. Moser, H. C. Sigg, and H. W. Lehmann, *Appl. Phys. Lett.* **69**, 722 (1996).

[51] K. Tai, Y. Lai, K. F. Huang, T. C. Lee, C. C. Wu, *Appl. Phys. Lett.* **63**, 2624 (1993).

[52] F. Brown de Colstoun, G. Khitrova, A. V. Fedorov, T. R. Nelson, and C. Lowry, *Chaos, Solitons and Fractals* **4**, 1575 (1994).

[53] R. A. Morgan, G. D. Guth, M. W. Focht, M. T. Asom, K. Kojima, L. E. Rogers, and S. E. Callis, *IEEE Phot. Tech. Lett.* **4**, 374 (1993).

[54] G. C. Wilson, D. M. Kuchta, J. D. Walker, and J. S. Smith, *Appl. Phys. Lett.* **64**, 542 (1994).

[55] D. Vakhshoori, J. D. Wynn, G. J. Zydzik, R. E. Leibenguth, M. T. Asom, K. Kojima, and R. A. Morgan, *Appl. Phys. Lett.* **62**, 1448 (1993).

[56] M. P. van Exter, A. K. Jansen van Doorn, and J. P. Woerdman, in *Physics and Simulation of Optoelectronic Devices IV*, SPIE Vol. **2693**, 202 (1996).

[57] E. Zeeb, B. Möller, G. Reiner, M. Ries, T. Hackbarth, and K. J. Ebeling, *IEEE J. Select. Topics Quantum Electron.* **1**, 616 (1995).

[58] K. D. Choquette, D. A. Richie, and R. E. Leibenguth, *Appl. Phys. Lett.* **64**, 2062 (1994).

[59] K. D. Choquette, R. P. Schneider, Jr., and J. A. Lott, *Opt. Lett.* **19**, 969 (1994).

[60] K. D. Choquette and R. E. Leibenguth, *IEEE Photon. Technol. Lett.* **6**, 40 (1994).

[61] St. Schröder, H. Grothe, and W. Harth, *Electron. Lett.* **32**, 348 (1996).

[62] B. Weigl, M. Grabherr, R. Michalzik, G. Reiner, and K. J. Ebeling, *IEEE Photon. Technol. Lett.* **8**, 999 (1996).

[63] K. Tai, Y. Lai, K. F. Huang, T. C. Lee, C. C. Wu, *IEEE Photon. Technol. Lett.* **7**, 2338 (1995).

[64] R. Michalzik, and K. J. Ebeling, *IEEE J. Quantum Electron.* **31**, 1371 (1995).

[65] C. H. Chong, and J. Sarma, *IEEE Phot. Tech. Lett.* **5**, 761 (1993).

[66] A. Valle, J. Sarma, and K. A. Shore, *IEEE J. Quantum Electron.* **31**, 1423 (1995).

[67] A. Valle, J. Sarma, and K. A. Shore, *Opt. Commun.* **115**, 297 (1995).

[68] J. P. Zhang, and K. Petermann, *IEE Proc. Optoelectron.* **142**, 29 (1995); *IEEE J. Quantum Electron.* **31**, 1423 (1995).

[69] F. Koyama, K. Morito, and K. Iga, *IEEE J. Quantum Electron.* **27**, 1410 (1991).

[70] Z.G. Pan, S. Jiang and M. Dagenais, R.A. Morgan, K. Kojima, M.T. Asom, R.E. Leibenguth, G.D. Guth, and M.W. Focht, *Appl. Phys. Lett.* **63**, 2999 (1993).

[71] S. Jiang, Z. Pan, M. Dagenais, R. A. Morgan and K. Kojima, *Appl. Phys. Lett.* **63**, 3545 (1993).

[72] M. P. van Exter, A. K. Jansen van Doorn, and J. P. Woerdman, *Phys. Rev. A* **56**, 845 (1997).

[73] A. K. Jansen van Doorn, M. P. van Exter, and J. P. Woerdman, *Appl. Phys. Lett.* **69**, 1041 (1996).

[74] A.K. Jansen van Doorn, M.P. van Exter, and J.P. Woerdman, *Appl. Phys. Lett.* **69**, 3635 (1996).

[75] A. K. Jansen van Doorn, M. P. van Exter, A. M. van der Lee, and J. P. Woerdman, *Phys. Rev. A* **55**, 1473 (1997).

[76] H. van der Lem, and D. Lenstra, "Saturation-induced frequency shift in the noise spectrum of a birefringent Vertical-Cavity Surface-Emitting Laser", to appear in *Optics Lett.*.

[77] M. P. van Exter, R. F. M. Hendriks, and J. P. Woerdman, "Physical insight into the VCSEL polarization rate equations", *Submitted*.

[78] An extensive list of references is given in Chaps. 4 and 7.

[79] K. D. Choquette, R. P. Schneider, Jr., K. L. Lear, and R. E. Leibenguth, *IEEE J. Select. Topics Quantum Electron.* **1**, 661 (1995).

[80] J. H. Ser, Y. G. Ju, J. H. Shin, and Y. H. Lee, *Appl. Phys. Lett.* **66**, 2769 (1995).

[81] H. Kawaguchi, I. S. Hidayat, Y. Takahashi, and Y. Yamayoshi, *Electron. Lett.* **31**, 109 (1995).

[82] M. Travagnin, M. P. van Exter, A. K. Jansen van Doorn and J.P. Woerdman, Phys. Rev. A **54**, 1647 (1996); *Opt. Commun.* **133**, 252 (1997).

[83] U. Fiedler, G. Reiner, P. Schnitzer, and K. J. Ebeling, *IEEE Photon. Technol. Lett.* **8**, 746 (1996).

[84] T. Mukaihara, N. Hayashi, N. Hatori, F. Koyama, and K. Iga, *IEEE Phot. Tech. Lett.* **7**, 1113 (1995).

[85] D. V. Kuksenkov, and H. Temkin *IEEE J. Select. Topics Quantum Electron.* **3**, 390 (1997).

[86] T. Mukaihara, N. Ohnoki, Y. Hayashi, N. Hatori, F. Koyama, and K. Iga, *IEEE J. Select. Topics Quantum Electron.* **1**, 667 (1995).

[87] T. Mukaihara, F. Koyama, and K. Iga, *IEEE Phot. Tech. Lett.* **5**, 133 (1993).

[88] A. Chavez-Pirson, H. Ando, H. Saito and H. Kanbe, *Appl. Phys. Lett.* **62**, 3082 (1993).

[89] T. Numai, K. Kurihara, K. Kühn, H. Kosada, I. Ogura, M. Kajita, and K. Kasahara, *IEEE J. Quant. Electron.* **31**, 636 (1995).

[90] Y. G. Ju, Y. H. Lee, H. K. Shin, and I. Kim, *Appl. Phys. Lett.* **71**, 741 (1997).

[91] A. Valle, K. A. Shore, and L. Pesquera, *IEEE J. of Lightwave Tech.* **14**, 2062 (1996).

[92] A. Valle, L. Pesquera, and K. A. Shore *IEEE Photon. Technol. Lett.* **9**, 557 (1997).

[93] A. Valle, L. Pesquera, and K. A. Shore "Polarization modulation dynamics of birefringent vertical-cavity surface-emitting lasers" *Submitted.*

[94] R. Mueller, A.Khler, A. Valle, J. Sarma, and K. A. Shore, Semiconductor Science and Technology **11**, 587 (1996).

[95] M. Etrich, P. Mandel, N. B. Abraham and H. Zeghlache, *IEEE J. Quantum Electron.* **28**, 811 (1992).

[96] P. Mandel, *IEEE J. Quantum Electron.* **29**, 836 (1993).

[97] W. van Haeringen, *Phys. Rev.* **158**, 256 (1967).

[98] W. J. Tomlinson and R. L. Fork, *Phys. Rev.* **164**, 466 (1967).

[99] H. de Lang, D. Polder, and W. van Haeringen, *Phillips tech. Rev.* **32**, 190 (1971).

[100] H. Haug, and H. Haken, *Z. Phys.* **204**, 262 (1967).

[101] C. H. Henry, *IEEE J. Quant. Electron.* **18**, 259 (1982).

[102] M. Osinski and J. Buus, *IEEE J. Quant. Electron.* **23**, 9 (1987).

[103] D. Lenstra, *Phys. Repts.* **59**, 299 (1980).

[104] D. Polder and W. van Haeringen, *Phys. Lett.* **25A**, 337 (1967).

[105] G. Bowhuis, *Phys. Lett.* **27A**, 693 (1968).

[106] W. van Haeringen and H. de Lang, *Phys. Rev.* **180**, 624 (1969).

[107] R. L. Fork and M. Sargent III, *Phys. Rev.* **139**, 617 (1965).

[108] M. Sargent III, W. E. Lamb Jr., and R. L. Fork, *Phys. Rev.* **164**, 436 (1967).

[109] A rather complete list of references is given in M. Matlin, R. Gioggia, N. B. Abraham, P. Glorieux and T. Crawford, *Opt. Commun.* **120**, 204 (1995).

[110] N. B. Abraham, E. Arimondo, M. San Miguel, *Opt. Commun.* **117**, 344 (1995); erratum: *Opt. Commun.* **121**, 168 (1995).

[111] Salvador Balle. Private communication.

[112] M. San Miguel, Q. Feng, J. V. Moloney, *Phys. Rev. A* **52**, 1728 (1995).

[113] J. Martín-Regalado, M. San Miguel, N. B. Abraham, F. Prati, *Opt. Lett.* **21**, 351 (1996).

[114] J. Martín-Regalado, M. San Miguel, N. B. Abraham, and F. Prati, in *Physics and Simulation of Optoelectronic Devices IV*, SPIE Vol. **2693**, 213 (1996).

[115] J. Martín-Regalado, M. San Miguel, N. B. Abraham, and F. Prati, in *Nonlinear Dynamics in Optical Systems*, SPIE Vol. **2792**, 136 (1996).

[116] J. Martín-Regalado, M. San Miguel, N.B. Abraham, and F. Prati, *IEEE J. Quantum Electron.*, **33**, 765 (1997).

[117] C. Serrat, N. B. Abraham, M. San Miguel, R. Vilaseca, and J. Martín-Regalado, *Phys. Rev. A (Rapid Comm.)* **53**, R3731 (1996).

[118] H. van der Lem, J. Martín-Regalado, S. Balle, and C. Mirasso, "High Bit Rate Generation of Low Chirped Pulses from Vertical-Cavity Surface-Emitting Lasers via External Axial Magnetic Field", accepted in *IEEE Photon. Tech. Lett.*

[119] J. Martín-Regalado, J. L. A. Chilla, J. J. Rocca, and P. Brusenbach, *Appl. Phys. Lett.* **70**, 3350 (1997).

[120] J. Martín-Regalado, S. Balle, and M. San Miguel, *Opt. Lett.* **22**, 460 (1997).

[121] J. Martín-Regalado, S. Balle, M. San Miguel, A. Valle and L. Pesquera, *Quantum and Semiclass. Opt.* **9**, 1 (1997).

[122] Vixel Corporation, 325 Interlocken Parkway, Broomfield, CO 80021, U.S.A.

[123] Y. H. Wang, G. Hasnain, K. Tai, J. D. Wynn, B. E. Weir, K. D. Choquette, and A. Y. Cho, *Japan. J. of Appl. Phys.* **30**, 3883 (1991).

[124] G. W. Taylor, and P. A. Evaldsson, *IEEE J. Quantum Electron.* **30**, 2262 (1994).

[125] B. Weigl, M. Grabherr, C. Jung, R. Jäger, G. Reiner, R. Michalzik, D. Sowada, and K. J. Ebeling, *IEEE J. Select. Topics Quantum Electron.* **3**, 409 (1997).

[126] W. Natwaski, and M. Osinski, *Electron. Lett.* **28**, 572 (1992).

[127] Y. G. Zhao, and J. G. McInerney, *IEEE J. Quantum Electron.* **31**, 1668 (1995).

[128] G. Gibbons, *Solid State Electron.* **13**, 799 (1970).

[129] H. van der Lem, "Polarization effects in a vertical cavity surface emitting laser", *Master's Thesis*, Vrije Universiteit (Amsterdam, 1997).

[130] M. Travagnin, "Linear anisotropies and polarization properties of Vertical-Cavity Surface-Emiting semiconductor Lasers", to be published in *Phys. Rev. A*.

[131] H. Haken, and H. Sauermann, *Z. Phys* **173**, 261 (1963); *Z. Phys* **176**, 47 (1963).

[132] W. E. Lamb Jr., *Phys. Rev. A* **134**, 1429 (1964).

[133] H. Haken, *Light Vol. 2*, (North-Holland, Amsterdam, 1985).

[134] H. Haug, and S. W. Koch, *Quantum theory of the optical and electronic properties of semiconductors*, (World-Scientific, Singapore, 1993).

[135] W. W. Chow, S. W. Koch, M. Sargent III, *Semiconductor-Laser Physics*, (Springer-Verlag, Berlin, 1994), Chap. 6.

[136] H. Haug, and S. W. Koch, *Phys. Rev. A* **39**, 1887 (1989).

[137] S. Balle, *Optics Comm.* **119**, 227 (1995).

[138] J. Yao, G. P. Agrawal, P. Gallion, and C. M. Bowden, *Optics Comm.* **119**, 246 (1995).

[139] J. D. Jackson, *Classical Electrodynamics*, (Wiley, New York,1975).

[140] D. I. Bavic, and S. W. Corzine, *IEEE J. Quantum Electron.* **28**, 512 (1992).

[141] L. J. Sham, *J. Phys. Condens. Matter* **5**, A51 (1993).

[142] Y. Z. Hu, R. Binder, and S. W. Koch, *Phys. Rev. B* **47**, 15679 (1993).

[143] Y. Z. Hu, R. Binder, S. W. Koch, S. T. Cundiff, H. Wang, and D. G. Steel, *Phys. Rev. B* **49**, 14382 (1994).

[144] M. Lindberg, R. Binder, Y. Z. Hu, and S. W. Koch, *Phys. Rev. B* **49**, 16942 (1994).

[145] T. C. Damen, L. Vina, J. E. Cunningham, J. Shah and L. J. Sham, *Phys. Rev. Lett* **67**, 3432 (1991).

[146] I. Muñoz, E. Pérez, V. Bellani, S. Zimmermann, L. Viña, K. Ploog, E. S. Koteles, and K. M. Lau, *J. Opt. Soc. Am. B* **13**, 994 (1996).

[147] V. Srinivas, Y. J. Chen, and C. E. C. Wood, *J. Opt. Soc. Am. B* **13**, 989 (1996).

[148] D. Robart, T. Amand, X. Marie, M. Brousseau, J. Barrau, and G. Bacquet, *J. Opt. Soc. Am. B* **13**, 1000 (1996).

[149] S. Bar-Ad and I. Bar-Joseph, *Phys. Rev. Lett.* **68**, 349 (1992).

[150] L. Fratta, F. Prati, and M. Travagnin "Band model for light polarization in QW-VCSELs", submitted.

[151] *Optical orientation*, edited by F. Meier and B. P. Zachachrenya, (North Holland, Amsterdam, 1984).

[152] R. Ferreira and G. Bastard, *Phys. Rev B* **43**, 9687 (1991).

[153] M. Z. Maialle , E. A de Andrada e Silva, and L. J. Sham, *Phys. Rev. B* **47**, 15776 (1993).

[154] D. C. Kilper, D. G. Steel, R. Craig and D. R. Scifre, *Opt. Lett.* **21**, 1283 (1996).

[155] H. F. Hofmann, and O. Hess, *Phys. Rev. A* **56**, 868 (1997).

[156] M. Travagnin, M. P. van Exter, and J. P. Woerdman, *Phys. Rev. A* **56**, 1497 (1997);

[157] A. Gahl, S. Balle, and M. San Miguel, "Polarization properties of optically-pumped VCSELs in a transverse magnetic field", *submitted.*

[158] P. K. Jakobsen, J. V. Moloney, A. C. Newell, and R. A. Indik, *Phys. Rev. A.* **45**, 8129 (1992).

[159] J. Martin-Regalado, S. Balle, and N. B. Abraham, *IEEE J. Quantum Electron.* **32**, 257 (1996); *IEE Proc. Optoelectron.* **143**, 17 (1996).

[160] J. Martín-Regalado, G. H. M. van Tartwijk, S. Balle, and M. San Miguel, *Phys. Rev. A* **54**, 5386 (1996).

[161] J. R. Tredicce, F. T. Arecchi, G. L. Lippi, and G. P. Puccioni, *J. Opt. Soc. Am. B* **2**, 173 (1985).

[162] J. W. Scott, B. J. Thibeault, C. J. Mahon, L. A. Coldren, and F. H. Petters, *Appl. Phys. Lett.* **65**, 1483 (1994).

[163] D. Tauber, G. Wang, R. S. Geels, J. C. Bowers, and L. A. Coldren, *Appl. Phys. Lett.* **62**, 325 (1993).

[164] D.V. Kuksenkov, H. Temkin, S. Swirhun, *Appl. Phys. Lett.* **67**, 2141 (1995).

[165] T. Ohtoshi, T. Kuroda, A. Niwa, and S. Tsuji, *Appl. Phys. Lett.* **65**, 1886 (1994).

[166] J. P. Zhang, *IEEE J. Quantum Electron.* **31**, 2127 (1995).

[167] T. B. Simpson, J. M. Liu, *Opt. Commun.* **112**, 43 (1994).

[168] P. Mandel, and T. Erneux, *Phys. Rev. Lett.* **53**,1818 (1984); see also P. Mandel, "Dynamic versus static stability" in *Frontiers in Quantum Optics*, E. R. Pike and S. Sarkar, eds., (Adam Hilger, Bristol and Boston, 1986); and P. Mandel, in *Instabilities and Chaos in Quantum Optics II*, p. 321, N. B. Abraham, F. T. Arecchi and L. A. Lugiato, eds., (Plenum, New York, 1988).

[169] J. M. Stone, *Radiation and Optics*, (New York, McGraw-Hill, 1963).

[170] G. R. Hadley, K. L. Lear, M. E. Warren, K. D. Choquette, J. W. Scott, and S. W. Corzine, *IEEE J. Quantum Electron.* **32**, 607 (1996).

[171] B. E. A. Saleh, and M. C. Teich, *Fundamentals of Photonics*, (New York, Wiley, 1991).

[172] A. D. May, P. Paddon, E. Sjerve, and G. Stephan, *Phys. Rev. A* **53**, 2829 (1996).

[173] S. Z. Zhang, N. M. Margalit, T. E. Reynolds and J. E. Bowers, *IEEE Phot. Tech. Lett.* **9**, 374 (1997).

[174] K. D. Choquette, K. L. Lear, R. E. Leibenguth, and M. T. Asom, *Appl. Phys. Lett.* **64**, 2767 (1994).

[175] Y. G. Ju, Y. H. Lee, H. K. Shin, and I. Kim, *Appl. Phys. Lett.* **71**, 741 (1997).

[176] M. San Miguel, and R. Toral, "Stochastic effects in physical systems" in *Instabilities and nonequilibrium structures VI*, E. Titapegui and W. Zelle, eds., (Kluewer, 1997).

[177] J. H. Shin, H. E. Shin, and Y. H. Lee, *Appl. Phys. Lett.* **70**, 2652 (1997).

[178] J. Manning, R. Olshansky, and C. B. Su, *IEEE J. Quant. Electron.* **19**, 1525 (1983).

[179] J. S. Blakemore, *J. Appl. Phys.* **53**, R123 (1982).

[180] Y.A. Wu, G. S. Li, R. F. Nabiev, K. D. Choquette, C. Canneau, and C.J. Chang-Hasnain, *IEEE J. Select. Topics Quantum Electron.* **1**, 629 (1995).

[181] F. Prati, A. Tesei, L. A. Lugiato, and R. J. Horowicz, *Chaos, Solitons and Fractals* **4**, 1637 (1994).

[182] F. Prati, L. Zucchetti, and G. Molteni, *Phys. Rev. A* **51**, 4093 (1995).

[183] P. W. Miloni, and J. H. Eberly, *Lasers*, (New York, John Wiley & Sons, 1988)

[184] P. Paddon, E. Sjerve, D. May, M. Bourouis, and G. Stephan, *J. Opt. Soc. Am. B* **9**, 575 (1992).

CURRICULUM VITAE
José María Martín Regalado

DATOS PERSONALES
Nombre:José María Martín Regalado
DNI: 38.449.582. Expedido en Palma de Mallorca, 8 de Mayo de 1995.
Fecha y Lugar de Nacimiento: Barcelona, 12 de Mayo de 1970.
Estado Civil: Soltero

DIRECCION ACTUAL:
Pje. Dante, 18, 3o. 1a.
07007 Palma de Mallorca
Tfno. **(971) 17 25 37/27 08 03**
e-mail: josep@hp1.uib.es

DIRECCION PERMANENTE:
Avda. Europa, 135, 3o. 2a.
08907 L'Hospitalet de Llob. (Barcelona)
Tfno. **(93) 335 26 24**
http://www.imedea.uib.es/∼josep

TITULACION

- Licenciado en Ciencias Físicas. Especialidad: Física Aplicada y Electrónica. Universidad de Barcelona, 1988-1993.
- Memoria de Investigación: *Dynamics of Gain-Guided Semiconductor lasers.* Universidad de las Islas Baleares, 19 Julio, 1996. Director: Dr. Salvador Balle.

CURSOS DE DOCTORADO

- *Universitat de les Illes Balears, cursos 93/94*: Métodos de simulación numérica en física (3 créditos); Física del láser (2 créditos); Dispositivos electrónicos VLSI (4 créditos); Aproximaciones semiclásicas: aplicaciones a física atómica y nuclear (2 créditos); Solitones en comunicaciones ópticas (2 créditos);
- *Universitat de les Illes Balears, curso 94/95*: Mecánica estadística: transiciones de fase (3 créditos); Sistemas dinámicos (3 créditos); Análisis de series temporales y espaciales (3 créditos); Sistemas de comunicaciones ópticas por fibra (2 créditos).

BECAS

- Programa Interuniversitario de Coperación ERASMUS "Instrumentación y Medidas". Univ. Catholique de Louvaine, Bélgica, Julio – Septiembre, 1992.
- Beca predoctoral del Programa de Formación de Personal Investigador (CICYT). Enero, 1994 – Septiembre, 1997.

EXPERIENCIA DOCENTE

- Colaboración en el diseño y la docencia de las prácticas correspondientes a la asignatura *Optoelectrónica* de segundo ciclo de Ciencias Físicas, y de las asignaturas *Optoelectrónica* y *Comunicaciones Opticas* de los estudios de Ingeniería Técnica Telemática. Universitat de les Illes Balears, cursos 94/95, 95/96 y 96/97. Profesores responsables: Maxi San Miguel y Salvador Balle.

PARTICIPACION EN PROYECTOS

- "Modelización, simulación y caracterización de dispositivos para comunicaciones ópticas por fibra", proyecto TIC93-0744-C04-01 de la CICYT (1993-94). Investigador principal: Prof. Maxi San Miguel .
- "Gigahertz and picosecond optics in semiconductor laser devices", proyecto CHRX-CT94-0594 del programa Human Capital and Mobility de la UE (1994-96). Investigador principal del grupo español: Prof. Maxi San Miguel.
- 'Estudio teórico y experimental de diodos láser para aplicaciones en tecnologías de la información y comunicaciones", proyecto TIC95-0563-C05-02 de la CICYT (1995-1998). Investigador principal: Dr. Salvador Balle.
- "Microlasers and QED", proyecto FMRX-CT96-0077 del programa Training and Mobility of Researchers de la UE (1996-2000). Investigador principal del grupo español: Prof. Maxi San Miguel.

ESTANCIAS EN CENTROS EXTRANJEROS

- Unité de Phys. Atomique et Moléculaire, Univ. Catholique de Louvaine, Bélgica, Julio–Septiembre, 1992. Programa ERASMUS. Investigador responsable: F. Brouillard.
- Departament of Electrical Engineering, Colorado State Univiversity, Colorado (USA), Noviembre–Diciembre, 1996. Programa CICYT FPI PN93. Investigador responsable: J. J. Rocca.

PUBLICACIONES

- J. Martín-Regalado, S. Balle, and N. B. Abraham, "Spatio-temporal dynamics of gain-guided semiconductor laser arrays". *IEEE J. of Quantum Electron.*, **32**(2), 257 (1996).
- J. Martín-Regalado, S. Balle, and N. B. Abraham, "Modeling spatio-temporal dynamics of gain-guided multistripe and broad area lasers". *IEE Proc. Optoelectron.*, **143**(1), 17 (1996).
- J. Martín-Regalado, S. Balle, and N. B. Abraham, "Spatio-temporal dynamics of gain-guided semiconductor laser arrays and broad area lasers", in *Physics and Simulation of Optoelectronic Devices IV*, W.W. Chow and M. Osinski, eds., SPIE Proc. **2693**, 369 (1996).
- J. Martín-Regalado, G. H. M. van Tartwijk, S. Balle, and M. San Miguel, "Mode control and pattern stabilization in broad-area lasers by optical feedback". *Phys. Rev. A* **54**(6), 5386 (1996).
- J. Martín-Regalado, M. San Miguel, N. B. Abraham, and F. Prati. "Polarization switching in quantum-well vertical-cavity surface-emitting lasers". *Optics Lett.*, **21**(5), 351 (1996).
- J. Martín-Regalado, M. San Miguel, N. B. Abraham, and F. Prati, "Polarization state selection and switching in VCSEL's", in *Physics and Simulation of Optoelectronic Devices IV*, W. W. Chow and M. Osinski, eds., SPIE Proc. **2693**, 213 (1996).
- J. Martín-Regalado, M. San Miguel, N. B. Abraham, F. Prati and G. Tissoni, "Polarization properties and transverse mode characteristics in quantum-well vertical-cavity surface-emitting lasers", in *Nonlinear Dynamics in Optical Systems.*, N.B. Abraham and Ya. I. Khanin, eds., SPIE Proc. **2792**, 136 (1996).

- C. Serrat, N. B. Abraham, M. San Miguel, R.Vilaseca, and J. Martín-Regalado. "Polarization dynamics in a vertical-cavity laser with an axial magnetic field", *Phys. Rev. A (Rapid Comm.)*, **53**(6), 3731 (1996).
- J. Martín-Regalado, M. San Miguel, N. B. Abraham, and F. Prati, "Polarization properties of vertical-cavity surface-emitting lasers", *IEEE J. of Quantum Electron.* **33**(5), 765 (1997).
- J. Martín-Regalado, S. Balle, and M. San Miguel, "Polarization and transverse-mode dynamics of gain-guided vertical-cavity surface-emitting lasers", *Optics Lett.* **22**(7), 460 (1997).
- J. Martín-Regalado, J. L. A. Chilla, J. J. Rocca, and P. Brusenbach, "Polarization switching in vertical-cavity surface emitting lasers observed at constant active region temperature", *Appl. Phys. Lett.*, **70**(25), 3350 (1997).
- J. Martín-Regalado, S. Balle, M. San Miguel, A. Valle, and L. Pesquera, "Polarization and transverse-mode selection in quantum-well vertical-cavity surface-emitting lasers: index- and gain-guided devices.", *Quantum and Semiclass. Opt.*, **9**, 1 (1997).
- H. van der Lem, J. Martín-Regalado, S. Balle, and C. Mirasso, "High-bit-rate generation of low-chirped pulses from vertical-cavity surface-emitting lasers via external axial magnetic field", to be published in *IEEE Photon. Technol. Lett.*.

PRESENTACIONES EN CONGRESOS (o=oral, p=poster)

- J. Martín-Regalado, M. San Miguel, N. B. Abraham, and F. Prati, "Polarization switching in QW vertical-cavity surface-emitting lasers" (p); J. Martín-Regalado, S. Balle, and N. B. Abraham, "Spatio-temporal dynamics of gain-guided semiconductor laser arrays" (p). **Semiconductor and Integrated Optoelectronics Conference (SIOE'95)**. *University of Cardiff, Cardiff, Reino Unido. 27-29 Marzo, 1995.*
- J. Martín-Regalado, M. San Miguel, N. B. Abraham, and F. Prati, "Polarization switching in QW vertical-cavity surface-emitting lasers" (o); F. Prati, G. Tissoni, L. A. Lugiato, J. Martín-Regalado, M. San Miguel, and N. B. Abraham, "Transverse and polarization effects in VCSEL's" (o); J. Martín-Regalado, S. Balle, and N. B. Abraham, "Spatio-temporal dynamics of gain-guided semiconductor laser arrays" (p). **Nonlinear Dynamics in Optical Systems (NDOS'95)**. *University of Rochester, Rochester, New York, USA. 5-7 Junio, 1995.*
- M. San Miguel, J. Martín-Regalado, N. B. Abraham, and F. Prati, "Polarization state selection and switching in vertical-cavity surface-emitting lasers" (o); N. B. Abraham, J. Martín-Regalado, and S. Balle, "Spatio-temporal dynamics of gain-guided semiconductor laser arrays" (o). **Integrated Optoelectronics OE/LASE'96 (SPIE's International Symposia)**. *San Jose Convention Center, San Jose, CA-USA. 27 Enero - 2 Febrero, 1996.*
- G. H. M. van Tartwijk, J. Martín-Regalado, S. Balle, and M. San Miguel "Mode control in broad area lasers by optical feedback" (o). **Integrated Photonics Research (IPR'96)**. *Boston, Massachusetts, USA. 29 Abril- 3 Mayo, 1996.*
- J. Martín-Regalado, C. Serrat, N. B. Abraham, M. San Miguel, and R.Vilaseca, "Dynamics of polarization states in a vertical-cavity surface-emitting semiconductor laser with an axial magnetic field" (o); J. Martín-Regalado, S. Balle, and M. San Miguel, "Polarization and transverse mode dynamics of gain-guided vertical-cavity surface-emitting lasers" (o). **European Conference on lasers and Electro-Optics/European Quantum Electronics Conference (CLEO /EUROPE -EQEC'96)**. *Hamburgo, Alemania. 8-13 Septiembre, 1996.*

- G. H. M. van Tartwijk, J. Martín-Regalado, S. Balle, and M. San Miguel "Control of spatio-temporal dynamics of broad-area lasers by weak optical feedback" (o). **X OSA Annual Meeting**. *University of Rochester, Rochester, New York, USA. 20-25 Octubre, 1996.*
- J. Martín-Regalado, S. Balle, and M. San Miguel, "Polarization and transverse mode properties of proton-implanted VCSELs" (o); A. Valle, L. Pesquera, J. Martín-Regalado, S. Balle, and M. San Miguel, "Polarization behaviour of index-guided vertical-cavity diodes" (o); J. Martín-Regalado, J. L. A. Chilla, J. J. Rocca, and P. Brusenbach, "Polarization switching in vertical-cavity surface-emitting lasers observed at constant active region temperature" (p). **Polarization effects in lasers and spectroscopy (PELS'97)**. *University of Toronto, Toronto, Canada. 26-28 May, 1997.*
- J. L. A. Chilla, J. Martín-Regalado, J. J. Rocca, and P. Brusenbach, "Polarization switching in vertical-cavity surface-emitting lasers observed at constant active region temperature" (o). **Device Research Conference (DRC'97)**. *Colorado State University, Fort Collins, Colorado, USA. 23-25 Junio, 1997.*

ASISTENCIA A OTROS CONGRESOS

- **Complexity and Chaos in Quantum Optics**. *Lille, Francia. 28-30 Marzo, 1994.*
- **European Conference on lasers and Electro-Optics/European Quantum Electronics Conference (CLEO /EUROPE -EQEC'94)**. *Amsterdam, Holanda. 28 Agosto - 2 Septiembre 1994.*
- **Joint Meeting of HCM Networks on Semiconductor lasers**. *Palma de Mallorca. 18-19 Abril 1996.*
- **Encuentro sobre Láseres de Semiconductor**. *Santander. 27-28 Junio 1996.*
- **HCM'97 Meeting**. *Santorini, Grecia. 16-18 Abril 1997.*
- **First workshop of the TMR Research Network: Microlasers and Cavity QED**. *Les Houches, Francia. 21-25 de Abril, 1997.*

CURSOS DE ESPECIALIZACION

- Postgrado en **Sistemas y redes de comunicaciones**. E.T.S.I. Telecomunicación de Madrid (UPM), 1993.
- *Universidad de Cantabria, cursos 94/95 y 95/96*: Optica integrada; Amplificación óptica; Introducción a la dinámica no-lineal de láseres; Introducción a los láseres de semiconductor; Láseres de semiconductor para comunicaciones ópticas; Advances in laser diodes for photonic applications; Láseres de pozo cuántico.

OTROS MERITOS Y CIRCUNSTANCIAS

- Referee de las revistas IEEE Journal of Quantum Electronics, Physical Review A, y Quantum and Semiclassical Optics.
- Usuario de equipos: PC, MAC, y UNIX workstations HP-9000/735 y Digital Alpha AXP 3000/500. Sistemas Operativos: DOS, Windows, y UNIX. Lenguajes de Programación: FORTRAN, C++ y BASIC.